

WELL-POSEDNESS AND NUMERICAL SOLUTION OF  
GENERALIZED STOKES-BRINKMAN EQUATIONS MODELING PCL  
FLUID IN HUMAN LUNGS



A THESIS SUBMITTED IN PARTIAL FULFILLMENT OF THE REQUIREMENT  
FOR THE DEGREE OF DOCTOR OF PHILOSOPHY IN APPLIED MATHEMATICS  
DEPARTMENT OF MATHEMATICS SCHOOL OF SCIENCE  
KING MONGKUT'S INSTITUTE OF TECHNOLOGY LADKRABANG  
2025

This material is reserved for educational use. **KMITL-2025-SC-D-001-031** is not allowed for commercial use.

Forbidden to modify the content, and cite the document when use.



COPYRIGHT 2025

SCHOOL OF SCIENCE

THESE MATERIALS ARE NOT TO BE USED FOR ANY COMMERCIAL USE.

Forbidden to modify the content, and cite the document when use.

|                       |                                                                                                                  |
|-----------------------|------------------------------------------------------------------------------------------------------------------|
| <b>Thesis Title</b>   | Well-Posedness and Numerical Solution of Generalized Stokes-Brinkman Equations Modeling PCL Fluid in Human Lungs |
| <b>Student Name</b>   | Miss Nisachon Kumankat                                                                                           |
| <b>Student ID</b>     | 63605007                                                                                                         |
| <b>Degree</b>         | Doctor of Philosophy (Applied Mathematics)                                                                       |
| <b>Department</b>     | Mathematics                                                                                                      |
| <b>Year</b>           | 2025                                                                                                             |
| <b>Thesis Advisor</b> | Assoc.Prof.Dr. Nachayadar Kamolmitisom                                                                           |

## Abstract

The mucociliary clearance system is an innate defense mechanism in the human respiratory tract, which plays a crucial role in protecting the airways from infections. The clearance system secretes mucus from the goblet cells scattering in the respiratory epithelium to trap foreign particles entering the airway, and then the mucus is removed out of the body by the movement of cilia residing under the mucus and above the epithelium cells. The layer containing cilia is called Periciliary layer (PCL). This layer also contains an incompressible Newtonian fluid called PCL fluid. The purpose of this research is to study the fluid flow in the two-dimensional PCL when fluid is driven by cilia movement rather than a pressure gradient. For the problem with self-propelled solid phases (cilia), we use a generalized Stokes equation for the free-fluid domain and the generalized Brinkman equation in a macroscopic scale for the porous medium. The models are derived with the assumption that the porosity is not a constant. The porosity in the mathematical model varies depending on the propagation of the solid phases. We apply a mixed finite element to the mathematical model. We prove the continuity and coercive properties of terms in the variational form and then prove the well-posedness of the discretized form of the generalized Stokes-Brinkman equations. Furthermore, we determine the velocity of the PCL fluid driven by the cilia movement in a porous domain using the generalized Brinkman equation in a macroscopic scale. The numerical domain is set up to be a shape of a fan blade which is similar to the motion of the cilia. A mixed finite element method is applied to discretize the mathematical models and the numerical solutions are provided in a two-dimensional domain. The system of equations can be applied to fluid flow propelled by moving solid phases.

**Keywords :** Generalized Stokes-Brinkman equations, Mixed finite element approach, Well-posedness, Varied porosity, Moving solid phase

Forbidden to modify the content, and cite the document when use.

## Acknowledgements

I would like to express my heartfelt gratitude to everyone who advised, helped, supported, and inspired me throughout my doctoral studies, resulting in the successful completion of this thesis.

First of all, I would like to express my sincere thanks to my thesis advisor, Assoc.Prof.Dr. Nachayadar Kamolmitisom, for her invaluable help and constant encouragement throughout the course of this research in my doctoral study. I am most grateful for her patience in teaching and providing endless advice, ideas, motivation, and enthusiasm with her positive energy. She taught me everything and she provided not only advice for research and studies but also advice for living. Her advice has been very helpful to me in the time of research and writing this thesis. I would not have achieved this far, and this thesis would not have been completed without all the support that I have always received from her.

Besides my advisor, I would also like to extend my sincere thanks to my thesis committee: Asst.Prof.Dr. Sukrawan Mavecha, Asst.Prof.Dr. Thawatchai Khumprapussorn, Asst.Prof.Dr. Puttha Sakkaplangkul and Asst.Prof.Dr. Jiraphan Suntornchost from Chulalongkorn University, for their valuable feedback, insightful comments, and challenging questions encouraged me to broaden my research perspective and deepen my understanding of the subject.

I am sincerely grateful for the financial support throughout my studies from the RA/TA graduate scholarship from the School of Science, King Mongkut's Institute of Technology Ladkrabang, giving me the opportunity to learn and prove myself in conducting independent research.

Not forget to thank the faculties, undergraduate and graduate students, and friends from the field of applied mathematics at KMITL for sharing good experiences and stories with me.

Finally, I most gratefully acknowledge my parents, my family and my friends for all their support and stand beside me no matter what problems I encountered, they never went anywhere and always continuously encouraged me throughout my years of study and the process of researching and writing this thesis. This accomplishment would not have been possible without them. Thank you.

Nisachon Kumankat

# Table of Contents

|                                                                                     | Page      |
|-------------------------------------------------------------------------------------|-----------|
| Abstract in English.....                                                            | i         |
| Acknowledgements.....                                                               | ii        |
| Table of Contents.....                                                              | iii       |
| List of Tables.....                                                                 | iv        |
| List of Figures.....                                                                | v         |
| <b>Chapter 1. Introduction.....</b>                                                 | <b>1</b>  |
| 1.1 Inception and Importance.....                                                   | 1         |
| 1.2 Objectives of the Study.....                                                    | 5         |
| 1.3 Scope of the Study.....                                                         | 5         |
| 1.4 Benefits of the Study.....                                                      | 5         |
| 1.5 Research Methodology.....                                                       | 5         |
| <b>Chapter 2. Fundamental Knowledge and literature review.....</b>                  | <b>7</b>  |
| 2.1 Fundamental definition and theorems.....                                        | 7         |
| 2.2 Hybrid Mixture Theory Method.....                                               | 14        |
| 2.3 Finite element method.....                                                      | 16        |
| 2.3.1 Weak formulation.....                                                         | 16        |
| 2.3.2 Methods of weighted residual.....                                             | 18        |
| 2.3.3 Elements and Shape functions.....                                             | 19        |
| 2.3.4 Isoparametric elements.....                                                   | 22        |
| 2.3.5 Mixed finite element method.....                                              | 26        |
| 2.4 Porosity and Permeability.....                                                  | 28        |
| 2.5 Literature Reviews.....                                                         | 29        |
| <b>Chapter 3. Generalized Stokes-Brinkman equations.....</b>                        | <b>32</b> |
| 3.1 Derivation of generalized Stokes equation.....                                  | 32        |
| 3.2 Derivation of generalized Brinkman equation.....                                | 35        |
| 3.3 Mathematical model.....                                                         | 37        |
| 3.4 Weak formulation of mathematical model.....                                     | 38        |
| 3.5 Well-posedness of generalized Stokes-Brinkman equations.....                    | 40        |
| 3.5.1 Continuity and coercivity.....                                                | 41        |
| 3.5.2 The existence and uniqueness of generalized Stokes-Brinkman<br>equations..... | 50        |
| <b>Chapter 4. Model Discretization and Boundary Conditions.....</b>                 | <b>55</b> |
| 4.1 Fan-blade shape domain.....                                                     | 55        |
| 4.2 Model Discretization.....                                                       | 56        |
| 4.3 Boundary Conditions.....                                                        | 59        |

This material is reserved for educational use only, not allowed for commercial use.

Forbidden to modify the content, and cite the document when use.

|                                                    |     |
|----------------------------------------------------|-----|
| <b>Chapter 5. Numerical Solutions</b> .....        | 62  |
| 5.1 Permeability, Cilia Velocity and Porosity..... | 62  |
| 5.1.1 Permeability.....                            | 62  |
| 5.1.2 Velocity of cilia.....                       | 63  |
| 5.1.3 Porosity .....                               | 64  |
| 5.2 Numerical Validation .....                     | 65  |
| 5.3 Numerical results .....                        | 67  |
| <b>Chapter 6. Conclusions</b> .....                | 77  |
| References .....                                   | 79  |
| Appendices .....                                   | 83  |
| Appendices A.....                                  | 84  |
| Appendices B.....                                  | 106 |
| Author Biography.....                              | 133 |



## List of Tables

| Table                                                                                                                                                                                                                                                                                                                                                                                                                                                                                     | Page |
|-------------------------------------------------------------------------------------------------------------------------------------------------------------------------------------------------------------------------------------------------------------------------------------------------------------------------------------------------------------------------------------------------------------------------------------------------------------------------------------------|------|
| 1.1 The research schedule.....                                                                                                                                                                                                                                                                                                                                                                                                                                                            | 6    |
| 3.1 The values of characteristic and constant variables in equation (3.5) in International System units.....                                                                                                                                                                                                                                                                                                                                                                              | 33   |
| 5.1 The coefficients of the eighth-order polynomial functions.....                                                                                                                                                                                                                                                                                                                                                                                                                        | 64   |
| 5.2 The $l_2$ -norm errors of the PCL velocity obtained from the different mesh refinements at the angle $\theta = 80^\circ$ .....                                                                                                                                                                                                                                                                                                                                                        | 67   |
| 5.3 The first-degree polynomial function: $p(\theta) = a_1\theta + a_2$ estimates the speed and the velocities $u_1$ at the tips of cilia for both cases of the boundary conditions, where $\theta$ is the angle in radians.....                                                                                                                                                                                                                                                          | 73   |
| 5.4 The eighth-degree polynomial function: $p(\theta) = a_1\theta^8 + a_2\theta^7 + a_3\theta^6 + a_4\theta^5 + a_5\theta^4 + a_6\theta^3 + a_7\theta^2 + a_8\theta + a_9$ estimates the speed and the velocities $u_1$ and $u_2$ at the tips of cilia for both cases of the boundary conditions, where $\theta$ is the angle in radians.....                                                                                                                                             | 73   |
| 5.5 The fifteenth-degree polynomial function: $p(\theta) = a_1\theta^{15} + a_2\theta^{14} + a_3\theta^{13} + a_4\theta^{12} + a_5\theta^{11} + a_6\theta^{10} + a_7\theta^9 + a_8\theta^8 + a_9\theta^7 + a_{10}\theta^6 + a_{11}\theta^5 + a_{12}\theta^4 + a_{13}\theta^3 + a_{14}\theta^2 + a_{15}\theta + a_{16}$ estimates the speed and the velocities $u_1$ and $u_2$ at the tips of cilia for both cases of the boundary conditions, where $\theta$ is the angle in radians..... | 74   |
| 5.6 $l_2$ -norm errors of the polynomial approximations of the velocity $u_1$ for both cases of the boundary conditions.....                                                                                                                                                                                                                                                                                                                                                              | 75   |
| 5.7 $l_2$ -norm errors of the polynomial approximations for both cases of the boundary conditions.....                                                                                                                                                                                                                                                                                                                                                                                    | 76   |
| 5.8 $l_2$ -norm errors of the polynomial approximations of the speed at the tips of cilia for both cases of the boundary conditions.....                                                                                                                                                                                                                                                                                                                                                  | 76   |

## List of Figures

| Figure                                                                                                                                                                                                                                                    | Page |
|-----------------------------------------------------------------------------------------------------------------------------------------------------------------------------------------------------------------------------------------------------------|------|
| 1.1 Left: Human respiratory system. Right: a portion of the trachea in the human respiratory tract. ....                                                                                                                                                  | 1    |
| 1.2 The layers of mucus and PCL when the cilia move forward and make angles $\theta$ to the horizontal plane. ....                                                                                                                                        | 2    |
| 1.3 (a) The cilia are perpendicular to the horizontal plane; (b) the cilia make an angle $\theta$ to the horizontal plane. ....                                                                                                                           | 3    |
| 1.4 The fan-blade shape of the porous domain on the $x_1x_2$ plane when cilia make angles with the horizontal plane. ....                                                                                                                                 | 4    |
| 2.1 (a) The domain with three linear elements; (b) A two-node linear element. ....                                                                                                                                                                        | 19   |
| 2.2 (a) The entire domain subdivided into smaller triangular elements; (b) A 3-node triangular element. ....                                                                                                                                              | 21   |
| 2.3 (a) Linear element and (b) quadratic element in both the physical coordinate system ( $x$ ) and the natural coordinate system ( $\xi$ ) ....                                                                                                          | 23   |
| 2.4 The linear triangular element in (a) the physical coordinate system ( $x, y$ ) and (b) the natural coordinate system ( $\xi, \eta$ ). ....                                                                                                            | 24   |
| 2.5 The quadratic triangular element in (a) the physical coordinate system ( $x, y$ ) and (b) the natural coordinate system ( $\xi, \eta$ ). ....                                                                                                         | 25   |
| 2.6 The influence of compaction on porosity and permeability of solid phase: (a) the rock, (b) compacted solid. ....                                                                                                                                      | 29   |
| 4.1 Left: the fan-blade shape of the porous domain on the $x_1x_2$ plane when cilia make angles with the horizontal plane. Right: the illustration of the length $\xi$ along cilia at the point $(x_1^a, x_2^a)$ and the the variable $\xi_{\max}$ . .... | 55   |
| 4.2 The boundary of our domain. ....                                                                                                                                                                                                                      | 59   |
| 5.1 The geometric cells of the periodic array of 5 cylinders in three dimensions. ....                                                                                                                                                                    | 62   |
| 5.2 Speed of cilia along the cilia length. ....                                                                                                                                                                                                           | 64   |
| 5.3 Generated mesh for the numerical domain. ....                                                                                                                                                                                                         | 65   |
| 5.4 The velocities of the PCL fluid obtained from four different mesh refinements at the angle $\theta = 80^\circ$ for the Case 1 boundary condition. The left graph is the velocity $u_1$ , while the right graph is the velocity $u_2$ . ....           | 66   |
| 5.5 The velocities of the PCL fluid obtained from four different mesh refinements at the angle $\theta = 80^\circ$ for the Case 2 boundary condition. The left graph is the velocity $u_1$ , while the right graph is the velocity $u_2$ . ....           | 67   |

|      |                                                                                                                                                                                                                                                                                                                        |    |
|------|------------------------------------------------------------------------------------------------------------------------------------------------------------------------------------------------------------------------------------------------------------------------------------------------------------------------|----|
| 5.6  | The velocities $u_1$ (left) and $u_2$ (right) of the PCL fluid for all angles. The first row shows the velocities for the Case 1 boundary condition while the second row shows the velocities for the Case 2 boundary condition..                                                                                      | 68 |
| 5.7  | The average velocities $u_1$ and $u_2$ of the PCL fluid. The top left shows the average velocity $u_1$ of Case 1, while the top right presents the average velocity $u_2$ of Case 1. The bottom left shows the average velocity $u_1$ of Case 2, while the bottom right presents the average velocity $u_2$ of Case 2. | 69 |
| 5.8  | The left figure shows the speed of the PCL fluid for the Case 1 boundary condition and the right figure presents the speed for the Case 2 boundary condition. ....                                                                                                                                                     | 70 |
| 5.9  | The speed of the PCL fluid at the tips of cilia for Case 1 boundary condition when $c_1 = c_2 = c_3 = c_4 = c$ , $c = 1, 10, 20, \dots, 50$ . ....                                                                                                                                                                     | 70 |
| 5.10 | The speed of the PCL fluid at the tips of cilia with different values of $c_i$ for $i = 1, 2, 3, 4$ .....                                                                                                                                                                                                              | 71 |
| 5.11 | The velocity $u_1$ of the PCL fluid at the tips of cilia for Case 1 boundary condition (left) and for Case 2 boundary condition (right).....                                                                                                                                                                           | 72 |
| 5.12 | The velocity $u_2$ of the PCL fluid at the tips of cilia for Case 1 boundary condition (left) and for Case 2 boundary condition (right).....                                                                                                                                                                           | 72 |
| 5.13 | The speed of the PCL fluid at the tips of cilia for Case 1 boundary condition (left) and for Case 2 boundary condition (right).....                                                                                                                                                                                    | 72 |

# Chapter 1

## Introduction

### 1.1 Inception and Importance

The respiratory system is one of the important systems for human survival, and the lungs are critical organs. It works by breathing air into the lungs through the nose and trachea. Breathing in not only brings in fresh air or oxygen, but also small particles contaminated with airborne pollutants such as PM 2.5, dust, or bacteria into the body, which humans cannot avoid. However, the human body has an innate immune system that plays an important role in protecting the body by secreting mucus from goblet cells to trap these contaminants and remove them via the movement of cilia. This mechanism is called mucociliary transport in the lungs. If mechanism is abnormal, it causes chronic airway diseases in humans such as asthma, pneumonia, and chronic bronchitis. As a result, we need to investigate changing the volume of the fluid to improve mucociliary transport out of the body. The important organelle that helps to remove mucus from the airway is cilia. Cilia are hair-like structures located on the surfaces of many organisms such as Paramecium, amoeba and complex multicellular organisms. The human body contains numerous cilia that can be found both inside the body and on the human skin. Cilia, for example, help to move eggs through the fallopian tubes into the uterus and move sperm in the reproductive systems [1]. Cilia help to pass food and waste through the digestive tract [2]. They also aid digestion and prevent intestine blockages [2]. Cilia in the respiratory system help to move mucus and foreign particles out of the lungs and airways [3]. They are self-propelled structures that move as metachronal motion. This protects the lungs and respiratory system from infection. This study focuses on the cilia found in the innate immune system in the human respiratory system, as illustrated in Figure 1.1.

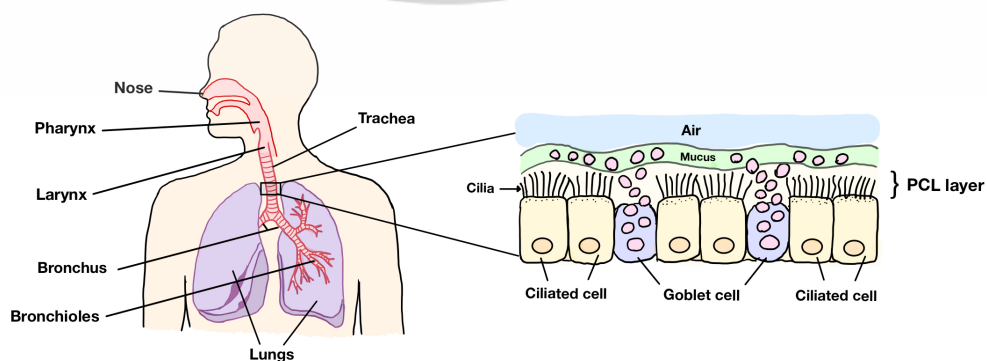


**Figure 1.1:** Left: Human respiratory system. Right: a portion of the trachea in the human respiratory tract.

Figure 1.1 illustrates the human respiratory system (left) and a portion of the trachea in the respiratory tract (right). The system consists of nose, pharynx, larynx, trachea, bronchus, bronchioles, and lungs. For closely inspecting the trachea, we can see that there are three main layers within the trachea: the periciliary layer (PCL), the mucus region, and the air at the top layer, the right figure. In the respiratory tract, cilia are found in the periciliary layer (PCL). This layer also contains fluid that is considered to be an incompressible fluid. The fluid in this layer is called the PCL fluid. The bottom of the PCL is comprised of goblet cells scattering among the ciliated cells. The ciliated cell is the cell membrane that the cilia reside on the top of the cell. The goblet cells contain mucus granules, which secrete mucus to trap strange particles entering the human body. After capturing foreign particles, mucus forms a layer at the tips of cilia. To prevent the accumulation of mucus in the lungs, cilia beat forward and backward producing metachronal waves, which fully expand during the forward stroke and then bend close to the epithelium before rotating back to the beginning of the forward stroke to push mucus out of the lungs. Above the mucus layer is the air row that is the path of bringing oxygen in and sending carbon dioxide out of the body. In this research, we focus on the fluid flow problem in the PCL where the fluid is moved by the movement of the cilia. That is the movement of bundles of cilia affects the fluid flow in the PCL. An example domain that gives more visual about the forward movement of cilia is represented in Figure 1.2.

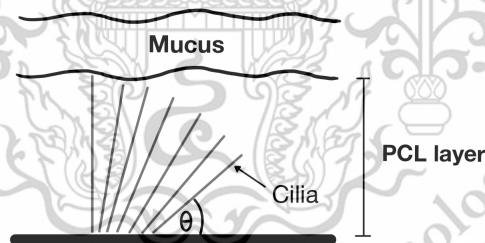


**Figure 1.2:** The layers of mucus and PCL when the cilia move forward and make angles  $\theta$  to the horizontal plane.

Figure 1.2 illustrates the effective stroke of cilia with angular movement of cilia. The angle  $\theta$  shows the angle that cilia make with the horizontal plane. The forward movement of cilia results in two different patterns of the domain in the PCL, as demonstrated in Figure 1.3. Figure 1.3 (a) shows that the cilia are perpendicular to the horizontal plane. In this pattern, the PCL consists of the PCL fluid and the solid phase or cilia, which is considered a porous medium ( $\Omega_p$ ). Figure 1.3 (b) shows that the cilia move forward and make an angle  $\theta$  to the horizontal plane that is less than  $90^\circ$ . The movement of cilia in this pattern causes a space between the tips of cilia and the mucus layer. Therefore, the PCL in Figure 1.3 (b) is divided into two domains: the domain containing

the cilia is called a porous domain ( $\Omega_p$ ), and the domain above the tips of cilia is called a free-fluid region ( $\Omega_f$ ). The domain  $\Omega_f$  contains only the PCL fluid without cilia.

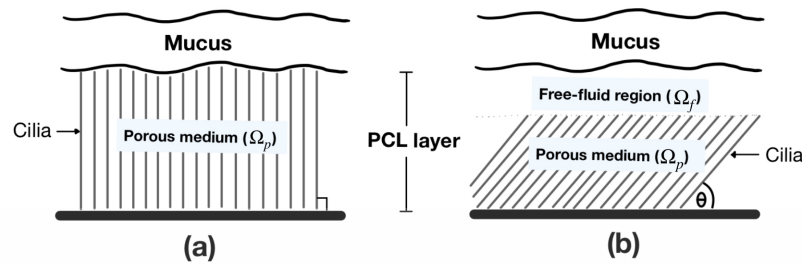


**Figure 1.3:** (a) The cilia are perpendicular to the horizontal plane; (b) the cilia make an angle  $\theta$  to the horizontal plane.

Because we consider a macroscopic scale where a bundle of cilia is considered instead of a single self-propelled cilium. The movement of cilia affects the motion of fluids in the nearby areas. If fluid flows through different domains, the mathematical models that used to describe the flow are also distinct. For a flow problem, typically, the Navier-Stokes or Stokes equation is applied in the free-fluid domain ( $\Omega_f$ ), while Darcy's Law or Brinkman equation is used in the porous domain ( $\Omega_p$ ). Note that a coupled free-fluid/porous-medium system of equations found in the usual literatures was derived assuming that porosity is a constant [4]. Unlike the usual problems, in this research, we develop the governing equations where the porosity is not a constant and the mathematical model can be used to predict the fluid flow in the PCL, which is close to the reality of the cilia movement. Our governing equations differ from the models in the usual literature because our model is derived with the assumption that the porosity is not a constant. The porosity in the mathematical model varies depending on the propagation of the solid phases or cilia.

The first goal of this research is to provide the generalized Stokes-Brinkman equations for slow flow with incompressible viscous fluid flowing through a free-fluid region and the adjacent porous medium. The generalized Brinkman equation is developed from the Hybrid Mixture Theory (HMT) [5, 6, 7]. The Hybrid Mixture Theory (HMT) is a technique for upscaling a multiphase flow by applying an averaging theorem to a microscale equation to obtain a macroscale equation. The macroscopic generalized Brinkman equation is more general than the Brinkman equation because it is derived from the conservation of momentum where the porosity in the equation is considered as a function of space. Therefore, the porosity is subject to a derivative operator, while the porosity in the Brinkman model has been used as a constant. Furthermore, we derive the generalized Stokes equation applied to the incompressible slow flow in the free-fluid region. Extra terms appearing in the generalized Stokes and macroscale generalized Brinkman equations aid in matching the shear stress at the free-fluid/porous-

medium interface. Since our model is different from typical Stokes-Brinkman equations in available research, we present the well-posedness of the generalized Stokes-Brinkman equations in a macroscopic scale by using a mixed finite element method and Lax-Milgram Theorem when the fluid is moved by the movement of solid phases and the permeability in the model is considered as a second-order tensor, not just a constant.

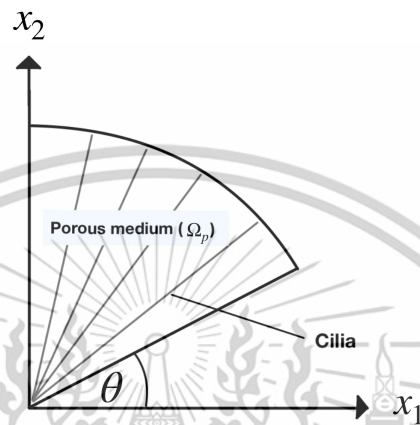


**Figure 1.4:** The fan-blade shape of the porous domain on the  $x_1x_2$  plane when cilia make angles with the horizontal plane.

The second goal of this research is to determine the velocity of the PCL fluid in the porous domain, which the fluid is driven by the beating of cilia. We use the generalized Brinkman equation on a macroscopic scale with varied porosity to predict the velocity of the PCL fluid. In this work, the numerical domain is set up to be the shape of a fan blade, resembling the wave pattern of cilia, as shown in Figure 1.4. Figure 1.4 shows our porous domain with angular movement of cilia. The angle  $\theta$  represents the angle that the cilia make with the horizontal plane. Since there are several angles  $\theta$  in the domain, the porosity in this work is considered as a function of the angle  $\theta$ , not a constant. This is unlike usual literatures that studied the numerical solutions of the Brinkman equation or the Stokes-Brinkman equations when the porosity was just a constant and they calculated the numerical results for a fixed angle  $\theta$  per one calculation on a rectangular domain. In fact, the angle  $\theta$  and the porosity should be varied in a numerical domain because of the metachronal waves of cilia. Therefore, this model designed closely approximates the actual beating pattern of cilia. A mixed finite element method of Taylor-Hood type is used to discretize the mathematical model and the numerical solutions are calculated in a two-dimensional domain.

## 1.2 Objectives of the Study

- 1) To derive the generalized Stokes-Brinkman equations on a macroscopic scale when the porosity is a function.
- 2) To prove the existence and uniqueness of the generalized Stokes-Brinkman equations for the numerical problem in a two-dimensional domain.
- 3) To use the mixed finite element method to discretize the mathematical model and calculate the numerical solutions in a two-dimensional domain.
- 4) To determine the velocity of the PCL fluid in a porous medium when fluid is driven by the cilia movement rather than a pressure gradient using the generalized Brinkman equation in a two-dimensional domain.

## 1.3 Scope of the Study

- 1) We study the velocity of PCL fluid in a two-dimensional domain in the PCL.
- 2) We consider the movement of bundles of cilia affecting the PCL fluid in the domain rather than individual cilia.
- 3) We assume that cilia move forward and make an angle from  $90^\circ$  to  $40^\circ$  with the horizontal plane.
- 4) We assume that cilia stop beating at  $\theta = 40^\circ$ .
- 5) We assume that the velocity of cilia is highest at the tips of cilia.
- 6) The variable of porosity in this study depends on space, not a constant.

## 1.4 Benefits of the Study

- 1) To obtain a new mathematical model of the fluid flow problem for flow through a free-fluid domain and an adjacent porous medium with varied porosity.
- 2) To obtain the well-posedness of the generalized Stokes-Brinkman equations.
- 3) To obtain the numerical results of the fluid flow problem that can be used for other researches.

## 1.5 Research Methodology

We plan the research as follows:

This material is reserved for educational use only, not allowed for commercial use.  
 Step 1: Study the fundamental definitions and theorem of the finite element method.  
 Forbidden to modify the content, and cite the document when use.

- Step 2: Study the mathematical model of the fluid flow problem for flow through a free-fluid domain and an adjacent porous medium.
- Step 3: Study the derivation and the well-posedness of the Stokes-Brinkman equations on a macroscopic scale with constant porosity.
- Step 4: Derive the generalized Stokes-Brinkman equations on a macroscopic scale when the porosity is a function.
- Step 5: Discretize the generalized Stokes-Brinkman equations in a two-dimensional by using a mixed finite element method.
- Step 6: Prove the well-posedness of generalized Stokes-Brinkman equations on a macroscopic scale with varied porosity in space in a two-dimensional.
- Step 7: Write and publish the first research paper.
- Step 8: Define the numerical domain and boundary conditions of our problem.
- Step 9: Use a mixed finite element method to discretize the generalized Brinkman equation and calculate the fluid velocities in a two-dimensional domain.
- Step 10: Write a program to find the numerical solutions.
- Step 11: Write and publish the second research paper and write a complete research report.

Table 1.1: The research schedule

| Activity | Time frame (month of year) |       |      |      |      |      |      |      |      |      |      |
|----------|----------------------------|-------|------|------|------|------|------|------|------|------|------|
|          | 2020                       |       | 2021 |      | 2022 |      | 2023 |      | 2024 |      | 2025 |
|          | 8-10                       | 11-12 | 1-6  | 7-12 | 1-6  | 7-12 | 1-6  | 7-12 | 1-6  | 7-12 | 1-6  |
| Step 1   |                            |       |      |      |      |      |      |      |      |      |      |
| Step 2   |                            |       |      |      |      |      |      |      |      |      |      |
| Step 3   |                            |       |      |      |      |      |      |      |      |      |      |
| Step 4   |                            |       |      |      |      |      |      |      |      |      |      |
| Step 5   |                            |       |      |      |      |      |      |      |      |      |      |
| Step 6   |                            |       |      |      |      |      |      |      |      |      |      |
| Step 7   |                            |       |      |      |      |      |      |      |      |      |      |
| Step 8   |                            |       |      |      |      |      |      |      |      |      |      |
| Step 9   |                            |       |      |      |      |      |      |      |      |      |      |
| Step 10  |                            |       |      |      |      |      |      |      |      |      |      |
| Step 11  |                            |       |      |      |      |      |      |      |      |      |      |

## Chapter 2

### Fundamental Knowledge and literature review

In this chapter, we provide the fundamental knowledge and concepts underlying the methods used in this research. We begin by introducing the notation, basic vector spaces, definitions and theorems used in proving the well-posedness of the equation, as described in Section 2.1. In Section 2.2, we discuss the Hybrid Mixture Theory (HMT), an upscaling technique that uses the averaging theorem to upscale equations from microscale to macroscale. Section 2.3 provides an overview of the Finite Element Method (FEM), a widely used numerical approach for solving partial differential equations in complex domains. In Section 2.4, we discuss the physical properties of porosity and permeability, which are critical in fluid flow through porous media. Finally, Section 2.5 presents a review of the relevant literatures on the methodologies and topics discussed in this research.

#### 2.1 Fundamental definition and theorems

This section introduces some notations and spaces, and present the preliminary definitions and theorems required to use in proving the well-posedness of our governing equation [8, 9, 10]. We begin by introducing the key notions of the gradient of a scalar field, the gradient of a vector field, and the divergence of a vector field in two-dimensional space. The definitions and illustrative examples provided here will serve as a basis for the methods and models used in this work.

##### 1. Gradient of a Scalar Field

The gradient of a scalar field is a fundamental concept in vector calculus. Given a scalar function  $f(x_1, x_2)$ , the gradient of  $f$ , denoted as  $\nabla f$ , is a vector field that points in the direction of the greatest rate of increase of the function. In two dimensions, the gradient is defined as:

$$\nabla f = \left( \frac{\partial}{\partial x_1}, \frac{\partial}{\partial x_2} \right) f = \left( \frac{\partial f}{\partial x_1}, \frac{\partial f}{\partial x_2} \right). \quad (2.1)$$

**Example:** Consider the scalar field  $f(x_1, x_2) = x_1^2 + x_2^2$  Its gradient is:

$$\nabla f = \left( \frac{\partial}{\partial x_1}(x_1^2 + x_2^2), \frac{\partial}{\partial x_2}(x_1^2 + x_2^2) \right) = (2x_1, 2x_2). \quad (2.2)$$

This means that at any point  $(x_1, x_2)$ , the gradient vector points radially outward from the origin, indicating that the value of  $f$  increases most rapidly in that direction.

##### 2. Gradient of a Vector Field

In contrast to the scalar field case, the "gradient" of a vector field refers not to a vector but to a matrix, specifically, the Jacobian matrix. Given a two-dimensional

This material is reserved for educational use only, not allowed for commercial use.

Forbidden to modify the content, and cite the document when use.

vector field:

$$\mathbf{v} = \begin{bmatrix} v_1(x_1, x_2) \\ v_2(x_1, x_2) \end{bmatrix}, \quad (2.3)$$

the gradient of vector  $\mathbf{v}$  is:

$$\nabla \mathbf{v} = \begin{bmatrix} \frac{\partial v_1}{\partial x_1} & \frac{\partial v_1}{\partial x_2} \\ \frac{\partial v_2}{\partial x_1} & \frac{\partial v_2}{\partial x_2} \end{bmatrix}. \quad (2.4)$$

This matrix contains all first-order partial derivatives and describes how the vector field changes in space.

**Example:** Let  $\mathbf{v} = (x_1x_2, x_2^2)$ . The gradient of vector  $\mathbf{v}$  is:

$$\nabla \mathbf{v} = \begin{bmatrix} \frac{\partial}{\partial x_1}(x_1x_2) & \frac{\partial}{\partial x_2}(x_1x_2) \\ \frac{\partial}{\partial x_1}(x_2^2) & \frac{\partial}{\partial x_2}(x_2^2) \end{bmatrix} = \begin{bmatrix} x_2 & x_1 \\ 0 & 2x_2 \end{bmatrix}. \quad (2.5)$$

This matrix provides local information about how the components of the vector field change with respect to both  $x_1$  and  $x_2$ .

### 3. Divergence of a Vector Field

The divergence of a vector field is a scalar quantity that measures the magnitude of a vector field's source or sink at a given point. Given a vector field:

$$\mathbf{v} = \begin{bmatrix} v_1(x_1, x_2) \\ v_2(x_1, x_2) \end{bmatrix}, \quad (2.6)$$

the divergence of  $\mathbf{v}$ , denoted by  $\nabla \cdot \mathbf{v}$ , is defined as:

$$\nabla \cdot \mathbf{v} = \left( \frac{\partial}{\partial x_1}, \frac{\partial}{\partial x_2} \right) \cdot (v_1, v_2) = \frac{\partial v_1}{\partial x_1} + \frac{\partial v_2}{\partial x_2}. \quad (2.7)$$

This operation takes the dot product of the del operator  $\nabla$  with the vector  $\mathbf{v}$ , resulting in a scalar field.

**Example:** Let the vector field be:  $\mathbf{v} = (x_1^2, -2x_2)$ . Then the divergence is:

$$\nabla \cdot \mathbf{v} = \frac{\partial}{\partial x_1}(x_1^2) + \frac{\partial}{\partial x_2}(-2x_2) = 2x_1 - 2. \quad (2.8)$$

This result tells us how the vector field is expanding or contracting at each point  $(x_1, x_2)$ . For instance, at the point  $(1, 0)$ , the divergence is  $2(1) - 2 = 0$ , indicating no net expansion or contraction at that specific location.

Next, we introduce the fundamental definitions utilized in this work as referenced in [10, 12, 11], starting with inner product.

**Definition 2.1.** Let  $V$  be a vector space. An inner product on  $V$  is a function:  $\langle \cdot, \cdot \rangle : V \times V \rightarrow \mathbb{R}$  that associates a real number  $\langle \mathbf{u}, \mathbf{v} \rangle$  with each pair of vectors in  $V$  in such a way that the following axioms are satisfied for all vectors  $\mathbf{u}, \mathbf{v}, \mathbf{w} \in V$  and all scalars  $k$ :

1.  $\langle \mathbf{u}, \mathbf{v} \rangle = \langle \mathbf{v}, \mathbf{u} \rangle$ .

Forbidden to modify the content, and cite the document when use.

2.  $\langle \mathbf{u} + \mathbf{v}, \mathbf{w} \rangle = \langle \mathbf{u}, \mathbf{w} \rangle + \langle \mathbf{v}, \mathbf{w} \rangle$ .
3.  $\langle k\mathbf{u}, \mathbf{v} \rangle = k\langle \mathbf{u}, \mathbf{v} \rangle$ .
4.  $\langle \mathbf{u}, \mathbf{u} \rangle \geq 0$  and  $\langle \mathbf{u}, \mathbf{u} \rangle = 0$  if and only if  $\mathbf{u} = 0$ .

**Definition 2.2.** A vector space  $V$  together with an inner product defined on it is called **inner-product space** and is denoted by  $(V, \langle \cdot, \cdot \rangle)$

**Definition 2.3.** If  $V$  is a real inner product space, then the norm of a vector  $\mathbf{v} \in V$  is defined by

$$\|\mathbf{v}\| := \sqrt{\langle \mathbf{v}, \mathbf{v} \rangle}. \quad (2.9)$$

**Definition 2.4 (Weak derivative).** We say that a given function  $f \in L^1_{loc}(\Omega)$  has a **weak derivative**,  $D_w^\alpha f$ , provided there exists a function  $g \in L^1_{loc}(\Omega)$  such that

$$\int_{\Omega} g(x)\phi(x)dx = (-1)^{|\alpha|} \int_{\Omega} f(x)\phi^{(\alpha)}(x)dx, \quad \forall \phi \in C_0^\infty(\Omega) \quad (2.10)$$

where  $C_0^\infty(\Omega)$  is the set of functions with compact support in  $\Omega$  and  $L^1_{loc}(\Omega) = \{f : f \in L^1(K) \quad \forall \text{ compact } K \subset \text{interior } \Omega\}$ . If such a  $g$  exists, we define  $D_w^\alpha f = g$ .

**Definition 2.5.** Let  $k$  be a non-negative integer, and  $f \in L^1_{loc}(\Omega)$ . Suppose that the weak derivatives  $D_w^\alpha f$  exist for all  $|\alpha| \leq k$ . Define the **Sobolev norm**

$$\|f\|_{W_p^k(\Omega)} = \left( \sum_{|\alpha| \leq k} \|D_w^\alpha f\|_{L^p(\Omega)}^p \right)^{1/p}, \quad (2.11)$$

in the case  $1 \leq p < \infty$ , and in the case  $p = \infty$

$$\|f\|_{W_\infty^k(\Omega)} := \max_{|\alpha| \leq k} \|D_w^\alpha f\|_{L^\infty(\Omega)}. \quad (2.12)$$

In either case, we define the **Sobolev spaces** via

$$W_p^k(\Omega) := \left\{ f \in L^1_{loc}(\Omega) : \|f\|_{W_p^k(\Omega)} < \infty \right\}. \quad (2.13)$$

**Definition 2.6.** Let  $(V, d)$  be a metric space. Then  $V$  is called **complete** if every Cauchy sequence  $\{v_n\} \subset V$ , there exists a point  $v \in V$  such that

$$\lim_{n \rightarrow \infty} v_n = v. \quad (2.14)$$

A Cauchy sequence is a sequence where the elements get arbitrarily close to each other as the sequence progresses:

$$\forall \varepsilon > 0, \exists N \in \mathbb{N} \quad \text{such that} \quad m > n \geq N \implies d(v_n, v_m) < \varepsilon. \quad (2.15)$$

**Definition 2.7.** Let  $(V, \langle \cdot, \cdot \rangle)$  be an inner-product space. If the associated normed linear space  $(V, \|\cdot\|)$  is complete, then  $(V, \langle \cdot, \cdot \rangle)$  is called a **Hilbert space**.

Forbidden to modify the content, and cite the document when use.

Note that when  $p = 2$ , Hilbert Space  $H^k(\Omega)$  is a special case of Sobolev Space  $W_2^k(\Omega)$ . That is

$$H^k(\Omega) := W_2^k(\Omega). \quad (2.16)$$

This is a Hilbert space with inner product:

$$\langle u, v \rangle_{H^k(\Omega)} = \sum_{|\alpha| \leq k} \int_{\Omega} D^{\alpha} u D^{\alpha} v \, dx. \quad (2.17)$$

**Definition 2.8** ( $L^p$  space). Let  $(\Omega, \mathcal{F}, \mu)$  is a measure space and  $1 < p < \infty$  on the set of all measurable functions  $f : \Omega \rightarrow \mathbb{R}$ . The **Lebesgue space**  $L^p$  is defined as:

$$L^p(\Omega) := \left\{ f : \Omega \rightarrow \mathbb{R} \mid \int_{\Omega} |f(x)|^p \, d\mu(x) < \infty \right\}. \quad (2.18)$$

This space is equipped with the  $L^p$ -norm, defined as:

$$\|f\|_{L^p(\Omega)} := \left( \int_{\Omega} |f(x)|^p \, d\mu(x) \right)^{1/p}. \quad (2.19)$$

**Definition 2.9.** The space  $L^2(\Omega)$ , a special case of  $L^p$  with  $p = 2$  is particularly important because it forms a Hilbert space. Define as

$$L^2(\Omega) := \left\{ f : \Omega \rightarrow \mathbb{R} \mid \int_{\Omega} |f(x)|^2 \, dx < \infty \right\}. \quad (2.20)$$

The norm in this space is given by:

$$\|f\|_{L^2(\Omega)} := \left( \int_{\Omega} |f(x)|^2 \, dx \right)^{1/2}, \quad (2.21)$$

and it admits the following inner product:

$$\langle u, v \rangle_{L^2_{\Omega}} = \int_{\Omega} f(x)g(x) \, dx, \quad \text{where } g : \Omega \rightarrow \mathbb{R}. \quad (2.22)$$

**Definition 2.10.** Let  $\Omega \in \mathbb{R}^n$  be an open set. The Sobolev space  $H^1$  is defined

$$H^1(\Omega) = \left\{ u \in L^2(\Omega) \mid \frac{\partial u}{\partial x_i} \in L^2(\Omega) \text{ for } i = 1, 2, \dots, n \right\}. \quad (2.23)$$

The norm on  $H^1(\Omega)$  combines the  $L^2$ -norm of the function and its gradient:

$$\|u\|_{H^1(\Omega)} = \left( \int_{\Omega} |u|^2 \, dx + \int_{\Omega} |\nabla u|^2 \, dx \right)^{1/2}, \quad (2.24)$$

and we define the inner product on  $H^1(\Omega)$ :

$$\langle u, v \rangle_{H^1} := \int_{\Omega} uv \, dx + \int_{\Omega} \nabla u \cdot \nabla v \, dx. \quad (2.25)$$

Let  $L^2(\Omega)$ ,  $H^1(\Omega)$ , and  $H_0^1(\Omega)$  be the Hilbert space, and  $L_0^2(\Omega)$  be the Sobolev space where  $\Omega$  is the domain. We define

$$L_0^2(\Omega) = \left\{ q \in L^2(\Omega) : \int_{\Omega} q \, d\Omega = 0 \right\}, \quad (2.26)$$

$$H_0^1(\Omega) = \left\{ \mathbf{w} \in H^1(\Omega) : \mathbf{w}|_{\partial\Omega} = 0 \right\}, \quad (2.27)$$

$$H_s^1(\Omega) = \left\{ \mathbf{w} \in H^1(\Omega) : \mathbf{w}|_{\partial\Omega} = \mathbf{s} \right\}, \quad (2.28)$$

$$H^{-1}(\Omega) = (H_0^1(\Omega))', \quad \text{the dual of } H_0^1(\Omega), \quad (2.29)$$

$$= \left\{ F : H_0^1(\Omega) \rightarrow \mathbb{R} \mid F \text{ is linear and continuous} \right\}, \quad (2.30)$$

$$V = \left\{ \mathbf{w} \in H^1(\Omega) : \mathbf{w}|_{\partial\Omega} = 0 \text{ and } \nabla \cdot \mathbf{w} = 0 \right\}, \quad (2.31)$$

$$V^\perp = \left\{ \mathbf{w}^\perp \in H_0^1(\Omega) : \int_{\Omega} \mathbf{w}^\perp \cdot \mathbf{w} = 0 \quad \forall \mathbf{w} \in V \right\}, \quad (2.32)$$

$$V^0 = \left\{ \mathbf{w}' \in H^{-1}(\Omega) : \langle \mathbf{w}', \mathbf{w} \rangle_{H^{-1}(\Omega) \times H_0^1(\Omega)} = 0 \quad \forall \mathbf{w} \in V \right\}, \quad (2.33)$$

where  $\langle \cdot, \cdot \rangle_{H^{-1}(\Omega) \times H_0^1(\Omega)}$  denotes the duality pairing between  $H^{-1}(\Omega)$  and  $H_0^1(\Omega)$ ,  $V^\perp$  denotes the orthogonal of  $V$  in  $H_0^1(\Omega)$  associated with the  $H^1(\Omega)$  seminorm  $|\cdot|_{H^1(\Omega)}$ , and  $V^0$  denotes the polar set of  $V$ . Notice that for  $n$  dimension,  $\mathbf{w} \in H^1(\Omega)^n$  and  $\nabla \mathbf{w} \in H^1(\Omega)^{n \times n}$ . In any case, for the sake of simplicity, we write  $\mathbf{w} \in H^1(\Omega)$  and the implication comes from the context of the surrounding sentences.

Next, we present the fundamental definitions, theorems, and lemmas required to use in proving the continuity and coercivity of Problems 3.1 and 3.2, [10, 12, 11, 13, 14]. We begin with the definitions of linear and bilinear forms, followed by the concepts of continuity and coercivity as presented in [10]. We then introduce the definitions of linear operators and their corresponding dual operators, as referenced in [43], as detailed below.

**Definition 2.11.** Let  $U$  be vector space over field  $\mathbb{F}$ . The function  $T : U \rightarrow \mathbb{F}$  is a **linear form** if it satisfies both of these conditions:

$$T(u + v) = T(u) + T(v), \quad \forall u, v \in U, \quad (2.34)$$

$$T(ku) = kT(u), \quad \forall u, v \in U, \forall k \in \mathbb{F}. \quad (2.35)$$

**Definition 2.12.** Let  $V$  be vector space over field  $\mathbb{F}$ . The function  $B : V \times V \rightarrow \mathbb{F}$  is called a **bilinear form** if it satisfies the following axioms:

$$B(\alpha u + \beta v, w) = \alpha B(u, w) + \beta B(v, w), \quad (2.36)$$

$$B(u, \alpha v + \beta w) = \alpha B(u, v) + \beta B(u, w), \quad (2.37)$$

for all  $u, v, w \in V$  and  $\alpha, \beta \in \mathbb{F}$ .

**Definition 2.13.** A bilinear form  $a(\cdot, \cdot)$  on a normed linear space  $H$  is said to be **bounded** (or **continuous**) if  $\exists C < \infty$  such that

$$|a(v, w)| \leq C \|v\|_H \|w\|_H \quad \forall v, w \in H \quad (2.38)$$

This material is reserved for educational use only, not allowed for commercial use.  
Forbidden to modify the content, and cite the document when use.

and coercive on  $V \subset H$  if  $\exists \alpha > 0$  such that

$$a(v, v) \geq \alpha \|v\|_H^2 \quad \forall v \in V \quad (2.39)$$

**Definition 2.14.** Let  $\mathbf{u}, \mathbf{w} \in H^1(\Omega)$  and  $q \in L_0^2(\Omega)$ . Define linear operators  $A : H_0^1(\Omega) \rightarrow H^{-1}(\Omega)$  and  $B : H_0^1(\Omega) \rightarrow L_0^2(\Omega)$  by

$$\langle A\mathbf{u}, \mathbf{w} \rangle_{H_0^1(\Omega) \times H^{-1}(\Omega)} := a(\mathbf{u}, \mathbf{w}), \quad \forall \mathbf{u}, \mathbf{w} \in H_0^1(\Omega), \quad (2.40)$$

$$\langle B\mathbf{u}, q \rangle_{H_0^1(\Omega) \times L_0^2(\Omega)} := b(\mathbf{u}, q), \quad \forall \mathbf{u} \in H_0^1(\Omega), \forall q \in L_0^2(\Omega). \quad (2.41)$$

Let  $B' \in \mathcal{L}(L_0^2(\Omega); H^{-1}(\Omega))$  be the dual operator of  $B$ . Then

$$\langle B'q, \mathbf{u} \rangle = \langle q, B\mathbf{u} \rangle := b(\mathbf{u}, q), \quad \forall \mathbf{u} \in H_0^1(\Omega), \forall q \in L_0^2(\Omega), \quad (2.42)$$

where the dual spaces of  $L_0^2(\Omega) = (L_0^2(\Omega))'$  and the dual spaces of  $H^{-1}(\Omega) = (H_0^1(\Omega))'$ .

The following theorems are used in the proofs of continuity and coercivity in Problems 3.1 and 3.2, as referenced in [10, 12].

**Theorem 2.15.** (*Minkowski's Inequality*) For  $1 \leq p \leq \infty$  and  $f, g \in L^p(\Omega)$ , we have

$$\|f + g\|_{L^p(\Omega)} \leq \|f\|_{L^p(\Omega)} + \|g\|_{L^p(\Omega)}. \quad (2.43)$$

**Theorem 2.16.** (*Hölder's Inequality*) For  $1 \leq p, q \leq \infty$  such that  $1 = 1/p + 1/q$ , if  $f \in L^p(\Omega)$  and  $g \in L^q(\Omega)$ , then  $fg \in L^1(\Omega)$  and

$$\|fg\|_{L^1(\Omega)} \leq \|f\|_{L^p(\Omega)} \|g\|_{L^q(\Omega)}. \quad (2.44)$$

**Theorem 2.17.** (*Cauchy-Schwarz's Inequality*) This is simply Hölder's inequality in the special case  $p = q = 2$ . If  $f, g \in L^2(\Omega)$ , then  $fg \in L^1(\Omega)$  and

$$\int_{\Omega} |f(x)g(x)| dx \leq \|f\|_{L^2(\Omega)} \|g\|_{L^2(\Omega)}, \quad (2.45)$$

for vectors  $\mathbf{v}, \mathbf{w} \in L^2(\Omega)$ , we also have

$$\int_{\Omega} |\mathbf{v} \cdot \mathbf{w}| \leq \|\mathbf{v}\|_{L^2(\Omega)} \|\mathbf{w}\|_{L^2(\Omega)}. \quad (2.46)$$

**Theorem 2.18.** (*Parallelogram Law*) Let  $\|\cdot\|$  be the norm associated with the inner product  $(\cdot, \cdot)$  on  $H$ . We have

$$\|u + w\|^2 + \|u - w\|^2 = 2(\|u\|^2 + \|w\|^2). \quad (2.47)$$

**Definition 2.19** (Semi-norms). For  $k$  a non-negative integer and  $f \in W_p^k(\Omega)$ , let

$$|f|_{W_p^k(\Omega)} = \left( \sum_{|\alpha|=k} \|D_w^\alpha f\|_{L^p(\Omega)}^p \right)^{1/p}, \quad (2.48)$$

in the case  $1 \leq p < \infty$ , and in the case  $p = \infty$

$$|f|_{W_\infty^k(\Omega)} = \max_{|\alpha|=k} \|D_w^\alpha f\|_{L^\infty(\Omega)}. \quad (2.49)$$

Forbidden to modify the content, and cite the document when use.

**Theorem 2.20.** (Poincarè inequality) If  $\Omega$  is connected and bounded at least in one direction, then for each integer  $m \geq 0$ , there exist a constant  $K = K(m, \Omega) > 0$  such that

$$\|w\|_{H^m(\Omega)} \leq K|w|_{H^m(\Omega)}, \quad \forall w \in H_0^m(\Omega), \quad (2.50)$$

or for space  $H_0^1(\Omega)$

$$\|w\|_{L^2(\Omega)} \leq K\|\nabla w\|_{L^2(\Omega)}, \quad \forall w \in H_0^1(\Omega). \quad (2.51)$$

Next, we introduce theorems which are important theorems used to prove the existence and uniqueness of the generalized Stokes-Brinkman equations in the section 3.5.2. The first theorem is the Lax-Milgram Theorem, which is one of the most important theorems used to prove the existence and uniqueness of solutions to the weak formulation of a mathematical model [10].

**Theorem 2.21.** [10] (Lax-Milgram) Let  $(H, (\cdot, \cdot))$  be a Hilbert space and  $a(\cdot, \cdot)$  be a continuous, coercive bilinear form on  $H$ . Then, for any a continuous linear functional  $L \in H'$ , there exists a unique  $u \in H$  such that

$$a(u, w) = L(w) \quad \forall w \in H. \quad (2.52)$$

The next theorem concerns the divergence operator, which is an isomorphism between  $L_0^2$  and  $V^\perp$ , and also establishes the Ladyzhenskaya–Babuška–Brezzi (LBB) condition, a key requirement for the stability of the mixed finite element method, as referenced in [13].

**Theorem 2.22.** Let  $\Omega$  be connected. Then

1. the operator **grad** is an isomorphism of  $L_0^2(\Omega)$  onto  $V^0$ ,
2. the operator **div** is an isomorphism of  $V^\perp$  onto  $L_0^2(\Omega)$ .

Therefore, there exists  $\beta > 0$  such that

$$\inf_{q \in L_0^2(\Omega)} \sup_{\mathbf{w} \in H_0^1(\Omega)} \frac{b(\mathbf{w}, q)}{\|\mathbf{w}\|_{H^1(\Omega)} \|q\|_{L^2(\Omega)}} \geq \beta > 0 \quad (2.53)$$

and for any  $q \in L_0^2(\Omega)$ , there exists a unique  $\mathbf{u} \in V^\perp \subset H_0^1(\Omega)$  satisfying

$$\|\mathbf{u}\|_{H^1(\Omega)} \leq \beta^{-1} \|q\|_{L^2(\Omega)}. \quad (2.54)$$

The following theorem presents the direct and inverse trace theorems for  $H^1(\Omega)$ , as stated in [14], while the subsequent lemma is essential for proving of the well-posedness of the generalized Stokes–Brinkman equations, as provided in [9].

**Theorem 2.23.** There exist positive constants  $Q_t$  and  $Q_s$  such that, for each  $\mathbf{v} \in H^1(\Omega)$ , its trace on  $\partial\Omega$  belongs to  $H^{1/2}(\partial\Omega)$  and

$$\|\mathbf{v}\|_{H^{1/2}(\partial\Omega)} \leq Q_t \|\mathbf{v}\|_{H^1(\Omega)}. \quad (2.55)$$

Conversely, for each given function  $\mathbf{s} \in H^{1/2}(\partial\Omega)$ , there exists  $\mathbf{u}_s \in H^1(\Omega)$  such that its trace on  $\partial\Omega$  coincides with  $\mathbf{s}$  and

$$\|\mathbf{u}_s\|_{H^1(\Omega)} \leq Q_s \|\mathbf{s}\|_{H^{1/2}(\partial\Omega)}, \quad (2.56)$$

where the space  $H^{1/2}(\Omega)$  is a Sobolev space of order 1/2, and is defined as

$$H^{1/2}(\Omega) = \left\{ u : \|u\|_{H^{1/2}(\Omega)}^2 = \|u\|_{L^2(\Omega)}^2 + |u|_{1/2}^2 < \infty \right\}, \quad (2.57)$$

where

$$|u|_{1/2}^2 = \int_{\Omega} \int_{\Omega} \frac{(u(\mathbf{x}) - u(\mathbf{y}))^2}{\|\mathbf{x} - \mathbf{y}\|^{d+1}} dx dy, \quad (2.58)$$

where  $d$  is the dimension.

**Lemma 2.24.** Suppose that  $\mathbf{f} \in H^{-1}(\Omega)$ ,  $f \in L^2(\Omega)$  and  $\mathbf{s} \in H^{1/2}(\partial\Omega)$ . Then there exist  $\mathbf{u}_s \in H^1(\Omega)$ ,  $Q_s > 0$  and  $\beta > 0$  such that

$$\mathbf{u}_s|_{\partial\Omega} = \mathbf{s} \quad \text{and} \quad \|\mathbf{u}_s\|_{H^1(\Omega)} \leq Q_s \|\mathbf{s}\|_{H^{1/2}(\partial\Omega)}, \quad (2.59)$$

$$\exists! \mathbf{u}_0 \in V^1 \subset H_0^1(\Omega) \quad \text{satisfying} \quad \nabla \cdot \mathbf{u}_0 = f - \nabla \cdot \mathbf{u}_s, \quad (2.60)$$

and

$$\|\mathbf{u}_0\|_{H^1(\Omega)} \leq \beta^{-1} \|f - \nabla \cdot \mathbf{u}_s\|_{L^2(\Omega)}. \quad (2.61)$$

Next section, we present upscaling procedure of the Hybrid Mixture Theory (HMT)

## 2.2 Hybrid Mixture Theory Method

In this section, we briefly present the upscaling procedure of the Hybrid Mixture Theory (HMT) [5, 6, 7], an upscaling technique used to derive multiphase flow equations such as the combination of solid and liquid phases. This method uses the averaging theorem to upscale equations from a microscale equation to a macroscale equation.

Let  $\delta V$  denote the representative elementary volume (REV), which is the smallest volume over which a measurement (such as porosity, permeability, or stress) can be carried out to produce a result that is representative of the macroscopic property. Given  $\delta V = \delta V_{\alpha} \cup \delta V_{\beta}$  where  $\delta V_{\alpha}$  and  $\delta V_{\beta}$  are the portions of the  $\delta V$  in phase  $\alpha$  and phase  $\beta$ , respectively. If the magnitude of REV is denoted by  $|\delta V|$ , then the volume fraction of phase  $\alpha$  can be written as

$$\varepsilon^{\alpha} = \frac{|\delta V_{\alpha}|}{|\delta V|} \quad \text{and} \quad \sum_{\alpha} \varepsilon^{\alpha} = 1. \quad (2.62)$$

The indicator function for phase  $\alpha$  is defined as

$$\gamma_{\alpha}(\mathbf{r}, t) = \begin{cases} 1 & \text{if } \mathbf{r} \in \delta V_{\alpha} \\ 0 & \text{if } \mathbf{r} \in \delta V_{\beta}, \quad \beta \neq \alpha. \end{cases} \quad (2.63)$$

Forbidden to modify the content, and cite the document when use.

To obtain the macroscale equations, the averaging theorems [7, 15] are applied to interchange the order of the partial derivatives and the integral, as follows

$$\frac{1}{|\delta V|} \int_{\delta V} \frac{\partial f}{\partial t} \gamma_\alpha dv(\xi) = \frac{\partial}{\partial t} \left[ \frac{1}{|\delta V|} \int_{\delta V} f \gamma_\alpha dv(\xi) \right] - \sum_{\beta \neq \alpha} \frac{1}{|\delta V|} \int_{\delta A_{\alpha\beta}} f \mathbf{w}_{\alpha\beta} \cdot \mathbf{n}_\alpha da(\xi), \quad (2.64)$$

$$\frac{1}{|\delta V|} \int_{\delta V} \nabla_x f \gamma_\alpha dv(\xi) = \nabla_x \left[ \frac{1}{|\delta V|} \int_{\delta V} f \gamma_\alpha dv(\xi) \right] + \sum_{\beta \neq \alpha} \frac{1}{|\delta V|} \int_{\delta A_{\delta\beta}} f \mathbf{n}_\alpha da(\xi), \quad (2.65)$$

where  $f$  is the quantities in the field equations,  $\delta A_{\alpha\beta}$  is the portion of the  $\alpha\beta$  interface within  $\delta V$ ,  $\mathbf{w}_{\alpha\beta}$  is the microscopic velocity of interface  $\alpha\beta$  and  $\mathbf{n}_\alpha$  is the outward unit normal vector to  $\delta V_\alpha$ .

Next, we show an example of deriving the macroscale conservation of mass equation using the HMT. We begin by considering the conservation of mass equation at the microscale

$$\frac{\partial \rho}{\partial t} + \nabla \cdot (\rho \mathbf{u}) = 0, \quad (2.66)$$

where  $\rho$  is the fluid density,  $t$  is time and  $\mathbf{u}$  is the velocity. Multiplying equation (2.66) by  $\gamma_\alpha$

$$\frac{\partial \rho}{\partial t} \gamma_\alpha + \nabla \cdot (\rho \mathbf{u}) \gamma_\alpha = 0, \quad (2.67)$$

integrating equation (2.67) over  $\delta V$  and then dividing by the volume  $|\delta V|$ , we have

$$\frac{1}{|\delta V|} \int_{\delta V} \frac{\partial \rho}{\partial t} \gamma_\alpha dv + \frac{1}{|\delta V|} \int_{\delta V} \nabla \cdot (\rho \mathbf{u}) \gamma_\alpha dv = 0. \quad (2.68)$$

By applying the averaging theorems given in equations (2.64) and (2.65) to each term in equation (2.68), we have

$$\frac{1}{|\delta V|} \int_{\delta V} \frac{\partial \rho}{\partial t} \gamma_\alpha dv = \frac{\partial}{\partial t} \left[ \frac{1}{|\delta V|} \int_{\delta V} \rho \gamma_\alpha dv \right] - \sum_{\beta \neq \alpha} \frac{1}{|\delta V|} \int_{\delta A_{\alpha\beta}} \rho \mathbf{w}_{\alpha\beta} \cdot \mathbf{n}_\alpha da, \quad (2.69)$$

and

$$\frac{1}{|\delta V|} \int_{\delta V} \nabla \cdot (\rho \mathbf{u}) \gamma_\alpha dv = \nabla \cdot \left[ \frac{1}{|\delta V|} \int_{\delta V} \rho \mathbf{u} \gamma_\alpha dv \right] + \sum_{\beta \neq \alpha} \frac{1}{|\delta V|} \int_{\delta A_{\delta\beta}} \rho \mathbf{u} \cdot \mathbf{n}_\alpha da. \quad (2.70)$$

Substituting equations (2.69) and (2.70) into equation (2.68), we have

$$\begin{aligned} \frac{\partial}{\partial t} \left[ \frac{1}{|\delta V|} \int_{\delta V} \rho \gamma_\alpha dv \right] - \sum_{\beta \neq \alpha} \frac{1}{|\delta V|} \int_{\delta A_{\alpha\beta}} \rho \mathbf{w}_{\alpha\beta} \cdot \mathbf{n}_\alpha da + \nabla \cdot \left[ \frac{1}{|\delta V|} \int_{\delta V} \rho \mathbf{u} \gamma_\alpha dv \right] \\ + \sum_{\beta \neq \alpha} \frac{1}{|\delta V|} \int_{\delta A_{\delta\beta}} \rho \mathbf{u} \cdot \mathbf{n}_\alpha da = 0. \end{aligned} \quad (2.71)$$

Rearranging equation (2.71) by moving the second and fourth terms into the right-hand side, we get

$$\frac{\partial}{\partial t} \left[ \frac{1}{|\delta V|} \int_{\delta V} \rho \gamma_\alpha dv \right] + \nabla \cdot \left[ \frac{1}{|\delta V|} \int_{\delta V} \rho \mathbf{u} \gamma_\alpha dv \right] = \sum_{\beta \neq \alpha} \frac{1}{|\delta V|} \int_{\delta A_{\alpha\beta}} \rho \mathbf{w}_{\alpha\beta} \cdot \mathbf{n}_\alpha da \quad (2.72)$$

This material is reserved for educational use only, not allowed for commercial use.

Forbidden to modify the content, and cite the document when use.

$$\frac{\partial}{\partial t} \left[ \frac{1}{|\delta V|} \int_{\delta V} \rho \gamma_\alpha dv \right] + \nabla \cdot \left[ \frac{1}{|\delta V|} \int_{\delta V} \rho \mathbf{u} \gamma_\alpha dv \right] = \sum_{\beta \neq \alpha} \frac{1}{|\delta V|} \int_{\delta A_{\delta \beta}} \rho (\mathbf{w}_{\alpha\beta} - \mathbf{u}) \cdot \mathbf{n}_\alpha da. \quad (2.73)$$

The macroscale conservation of mass, equation (2.73), can be rewritten as follows

$$\begin{aligned} \frac{\partial}{\partial t} \left[ \frac{|\delta V_\alpha|}{|\delta V|} \frac{1}{|\delta V_\alpha|} \int_{\delta V} \rho \gamma_\alpha dv \right] + \nabla \cdot \left[ \frac{\rho^\alpha |\delta V_\alpha|}{\rho^\alpha |\delta V_\alpha|} \frac{1}{|\delta V|} \int_{\delta V} \rho \mathbf{u} \gamma_\alpha dv \right] \\ = \sum_{\beta \neq \alpha} \frac{\rho^\alpha |\delta V_\alpha|}{\rho^\alpha |\delta V_\alpha|} \frac{1}{|\delta V|} \int_{\delta A_{\delta \beta}} \rho (\mathbf{w}_{\alpha\beta} - \mathbf{u}) \cdot \mathbf{n}_\alpha da, \end{aligned} \quad (2.74)$$

or

$$\begin{aligned} \frac{\partial}{\partial t} \left[ \frac{|\delta V_\alpha|}{|\delta V|} \frac{1}{|\delta V_\alpha|} \int_{\delta V} \rho \gamma_\alpha dv \right] + \nabla \cdot \left[ \frac{\rho^\alpha |\delta V_\alpha|}{|\delta V|} \frac{1}{\rho^\alpha |\delta V_\alpha|} \int_{\delta V} \rho \mathbf{u} \gamma_\alpha dv \right] \\ = \sum_{\beta \neq \alpha} \rho^\alpha \frac{|\delta V_\alpha|}{|\delta V|} \frac{1}{\rho^\alpha |\delta V_\alpha|} \int_{\delta A_{\delta \beta}} \rho (\mathbf{w}_{\alpha\beta} - \mathbf{u}) \cdot \mathbf{n}_\alpha da. \end{aligned} \quad (2.75)$$

Let  $\rho^\alpha$  be the macroscale density of phase  $\alpha$ ,  $\mathbf{u}^\alpha$  be the macroscale velocity of phase  $\alpha$ , and  $\hat{e}_\beta^\alpha$  be the rate of exchange of mass from phase  $\beta$  to phase  $\alpha$ . That is

$$\rho^\alpha = \frac{1}{|\delta V_\alpha|} \int_{\delta V} \rho \gamma_\alpha dv, \quad (2.76)$$

$$\mathbf{u}^\alpha = \frac{1}{\rho^\alpha |\delta V_\alpha|} \int_{\delta V} \rho \mathbf{u} \gamma_\alpha dv, \quad (2.77)$$

$$\hat{e}_\beta^\alpha = \frac{1}{\rho^\alpha |\delta V_\alpha|} \int_{\delta A_{\alpha\beta}} [\rho (\mathbf{w}_{\alpha\beta} - \mathbf{u})] \cdot \mathbf{n}_\alpha da. \quad (2.78)$$

Therefore, equation (2.75) becomes

$$\frac{\partial (\varepsilon^\alpha \rho^\alpha)}{\partial t} + \nabla \cdot (\varepsilon^\alpha \rho^\alpha \mathbf{u}^\alpha) = \sum_{\beta \neq \alpha} \varepsilon^\alpha \rho^\alpha \hat{e}_\beta^\alpha, \quad (2.79)$$

which is the macroscale conservation of mass.

## 2.3 Finite element method

In this section, we introduce the Finite Element Method (FEM) [16, 17], a powerful numerical technique widely used to solve partial differential equations (PDEs) that arise in various fields of engineering and applied sciences. The key idea is to divide the domain into smaller subdomains, called finite elements, which are simple geometric shapes. Within each element, the solution is approximated using shape functions. These local approximations are assembled into a global system of equations that models the behavior of the entire domain. We begin by introducing the weak formulation, followed by an overview of the methods of weighted residuals and shape functions. These foundations provide the basis of the finite element method. Finally, we provide a brief overview of discretization using the mixed finite element method for two-dimensional problems.

### 2.3.1 Weak formulation

In this subsection, we briefly introduce the concept of the weak formulation. This material is reserved for educational use only, not allowed for commercial use. The main idea of the weak form is to convert the differential equation into an integral. Forbidden to modify the content, and cite the document when use.

equation to reduce the computational load on the numerical algorithm in evaluating derivatives. Integration by parts reduces the order of differentiation to provide numerical benefits and generate natural boundary conditions for specifying fluxes at the boundaries, see detail in [16]. The process for generating the weak form is as follows:

1. Multiply the whole equation with a weight function and integrate the equation over the domain  $\Omega$ .
2. Integrate by parts in terms of any divergence or higher-order derivatives of the primary variable multiplied by a weight function and apply the divergence theorem to generate boundary integrals.

Next, we show an example to determine the weak formulation of the following equations of viscous fluid [18]. Let  $\Omega$  be a domain in  $\mathbb{R}^2$  with boundary  $\partial\Omega$  and the vector  $\mathbf{u} = (u_1, u_2)$ . Given the conservation of momentum

$$-\mu\Delta\mathbf{u} + \nabla p + \sigma\mathbf{u} - \mathbf{f} = \mathbf{0}, \quad (2.80)$$

and the conservation of mass

$$\nabla \cdot \mathbf{u} = 0, \quad (2.81)$$

where  $\mu$  is the viscosity of the fluid,  $\mathbf{u}$  is the velocity,  $p$  is the pressure,  $\sigma$  is constant and  $\mathbf{f}$  is the body force vector. In this problem, we want to find the variables  $\mathbf{u}$  and  $p$ . To obtain the weak form, the first step is to multiply the equation (2.80) and (2.81) by the weight functions  $\mathbf{w} \in H_0^1(\Omega)$  and  $Q \in L_0^2(\Omega)$ , respectively, and integrate over the element domain  $\Omega$ , we have

$$\int_{\Omega} \mathbf{w} \cdot (-\mu\Delta\mathbf{u} + \nabla p + \sigma\mathbf{u} - \mathbf{f}) d\Omega = 0, \quad (2.82)$$

$$\int_{\Omega} Q(\nabla \cdot \mathbf{u}) d\Omega = 0. \quad (2.83)$$

The vector forms of the equations (2.82) and (2.83) can be written in any coordinate system as shown below

$$\int_{\Omega} w_i \left( -\mu \frac{\partial^2 u_i}{\partial x_j^2} + \frac{\partial p}{\partial x_i} + \sigma u_i - f_i \right) d\Omega = 0, \quad (2.84)$$

$$\int_{\Omega} Q \frac{\partial u_i}{\partial x_i} d\Omega = 0. \quad (2.85)$$

In the second step, we integrate by parts the first two terms in equation (2.84), we have

$$\begin{aligned} - \int_{\Gamma} \mu w_i \frac{\partial u_i}{\partial x_j} n_j d\Gamma + \int_{\Omega} \frac{\partial w_i}{\partial x_j} \frac{\partial u_i}{\partial x_j} d\Omega + \int_{\Gamma} w_i p n_i d\Gamma - \int_{\Omega} \frac{\partial w_i}{\partial x_i} p d\Omega \\ + \int_{\Omega} (\sigma w_i u_i - w_i f_i) d\Omega = 0. \end{aligned} \quad (2.86)$$

We rearrange equation (2.86) as follows:

$$\int_{\Omega} \left( \frac{\partial w_i}{\partial x_j} \frac{\partial u_i}{\partial x_j} - \frac{\partial w_i}{\partial x_i} p + \sigma w_i u_i - w_i f_i \right) d\Omega + \int_{\Gamma} \left( -\mu w_i \frac{\partial u_i}{\partial x_j} n_j + w_i p n_i \right) d\Gamma = 0. \quad (2.87)$$

Then, we obtain the following integral statements :

$$\int_{\Omega} \left( \frac{\partial w_i}{\partial x_j} \frac{\partial u_i}{\partial x_j} - \frac{\partial w_i}{\partial x_i} p + \sigma w_i u_i - w_i f_i \right) d\Omega + \int_{\Gamma} \left( -\mu w_i \frac{\partial u_i}{\partial x_j} n_j + w_i p n_i \right) d\Gamma = 0, \quad (2.88)$$

$$\int_{\Omega} Q \frac{\partial u_i}{\partial x_i} d\Omega = 0. \quad (2.89)$$

This completes the weak form development.

Next, we present the methods used in the finite element method and introduce the weighted functions and shape functions commonly used in the finite element method in the following subsections. The method for solving the solutions of two-dimensional equations (2.88) and (2.89) is shown in Section 2.3.5.

### 2.3.2 Methods of weighted residual

In this subsection, we briefly introduce the methods of weighted residuals [16], which are efficient and commonly used approaches for obtaining approximate solutions of the differential governing equations given in the weak forms.

#### 1) Collocation Method:

For the collocation method, the Dirac delta function is used as the weight function, where the sampling point  $x_i$  must be within the domain. That is

$$w_i = \delta(x - x_i), \quad (2.90)$$

and the Dirac delta function has the property that

$$\delta(x - x_i) = \begin{cases} 1, & x = x_i \\ 0, & \text{otherwise} \end{cases}. \quad (2.91)$$

#### 2) Least Squares Method:

The weight functions for the Least Squares Method are the derivatives of the residual with respect to the unknown constants such that

$$w_i = \frac{\partial R}{\partial a_i}, \quad (2.92)$$

where  $R$  is a residue function and  $a_i$  is a unknown constants for  $i = 1, 2, \dots, n$ .

#### 3) Galerkin's Method:

Galerkin's method uses the weight functions that are identical to the shape functions. That is

$$w_i = \psi_i(x), \quad (2.93)$$

where  $\psi_i(x)$  is the shape functions.

### 2.3.3 Elements and Shape functions

In the finite element method, the domain is divided into small subregions called elements, such as triangles and quadrilaterals in two dimensions. Shape functions are mathematical constructs that interpolate solutions over an element based on its nodal values. They play a crucial role in approximating the field variables within each element. This subsection briefly presents an overview of the basic shape functions commonly used in the finite element method [16].

#### 1) Linear shape functions

The linear shape functions are commonly used in 1-dimensional finite element analysis. Figure 2.1 illustrates an example that a domain is composed of four nodes and three elements. Figure 2.1 (a) shows the entire domain divided into three linear elements, whereas Figure 2.1 (b) depicts any element within the domain where  $i = 1, 2, 3$ .

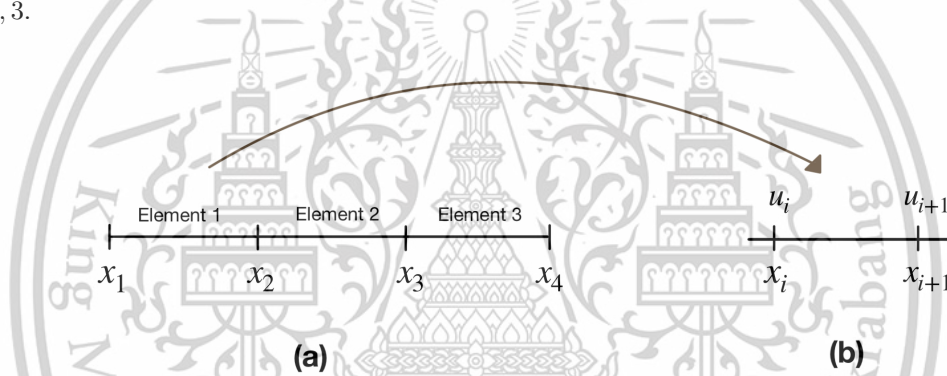


Figure 2.1: (a) The domain with three linear elements; (b) A two-node linear element.

Consider any element from the domain as shown in Figure 2.1 (b). Each element consists of two nodes, one at each end, corresponding to the coordinate values  $x_i$  and  $x_{i+1}$ , where  $i = 1, 2, 3$ , and the associated nodal variables  $u_i$  and  $u_{i+1}$ ,  $i = 1, 2, 3$ . For linear shape functions, the unknown trial function within the element is assumed to take the form

$$u = a_1 + a_2x, \quad (2.94)$$

where  $a_1$  and  $a_2$  are constants determined by the nodal values. The trial function in equation (2.94) can be expressed in terms of the nodal variables at each node. By substituting  $x_i$  and  $x_{i+1}$  into equation (2.94), we obtain the corresponding nodal values:

$$u(x_i) = u_i = a_1 + a_2x_i, \quad (2.95)$$

$$u(x_{i+1}) = u_{i+1} = a_1 + a_2x_{i+1}. \quad (2.96)$$

Solving equations (2.95) and (2.96) simultaneously for  $a_1$  and  $a_2$  yields:

$$a_1 = \frac{u_{i+1} - u_i}{x_{i+1} - x_i}, \quad (2.97)$$

$$a_2 = \frac{u_i x_{i+1} - u_{i+1} x_i}{x_{i+1} - x_i}. \quad (2.98)$$

Substituting equations (2.97) and (2.98) into the trial function in equation (2.94) and rearranging the resulting expression, we obtain

$$u = \psi_1(x)u_i + \psi_2(x)u_{i+1} = \begin{bmatrix} \psi_1(x) & \psi_2(x) \end{bmatrix} \begin{bmatrix} u_i \\ u_{i+1} \end{bmatrix}, \quad (2.99)$$

where  $\psi_1(x)$  and  $\psi_2(x)$  are the linear shape functions associated with nodes  $i$  and  $i + 1$ , respectively, defined by

$$\psi_1(x) = \frac{x_{i+1} - x}{x_{i+1} - x_i}, \quad (2.100)$$

$$\psi_2(x) = \frac{x - x_i}{x_{i+1} - x_i}. \quad (2.101)$$

The linear shape functions discussed above have two fundamental properties that hold for finite element shape functions:

1. Each shape function associated with node  $i$  has a value of one at node  $i$  and zero at all other nodes. That is,

$$\psi_1(x_i) = 1, \psi_1(x_{i+1}) = 0, \psi_2(x_i) = 0, \psi_2(x_{i+1}) = 1. \quad (2.102)$$

2. The sum of all shape functions is equal to one.

$$\psi_1(x) + \psi_2(x) = 1. \quad (2.103)$$

## 2) Linear triangular elements

For two-dimensional problems, the three-node triangular element, also referred to as a linear triangular element, is one of the simplest and most widely used element types. As illustrated in Figure 2.2, part (a) shows the domain subdivided into small triangular elements, while part (b) shows a 3-node triangular element within the domain. This element consists of three nodes located at the vertices of the triangle, each associated with coordinate values  $(x_i, y_i)$  and corresponding nodal variables  $u_i$ , for  $i = 1, 2, 3$ .

The interpolation of the nodal variable within the element is defined by a linear function of  $x$  and  $y$ :

$$u = b_1 + b_2x + b_3y = \begin{bmatrix} 1 & x & y \end{bmatrix} \begin{bmatrix} b_1 \\ b_2 \\ b_3 \end{bmatrix}, \quad (2.104)$$

This material is reserved for educational use only, not allowed for commercial use.

Forbidden to modify the content, and cite the document when use.

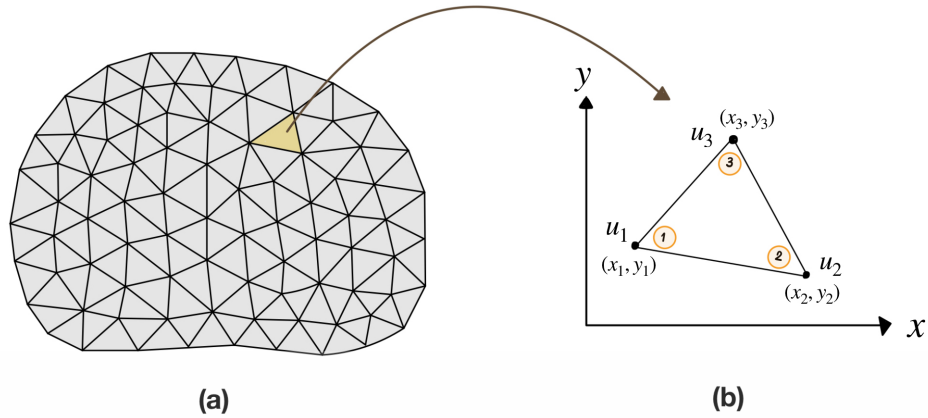


**Figure 2.2:** (a) The entire domain subdivided into smaller triangular elements; (b) A 3-node triangular element.

where  $b_1, b_2, b_3$  are constants determined from the nodal values. The interpolation function given in equation (2.104) can be expressed in terms of the nodal values at the three nodes. By substituting the coordinates  $(x_i, y_i)$ , where  $i = 1, 2, 3$ , into equation (2.104), we obtain the following matrix form:

$$\begin{bmatrix} u_1 \\ u_2 \\ u_3 \end{bmatrix} = \begin{bmatrix} 1 & x_1 & y_1 \\ 1 & x_2 & y_2 \\ 1 & x_3 & y_3 \end{bmatrix} \begin{bmatrix} b_1 \\ b_2 \\ b_3 \end{bmatrix} \quad (2.105)$$

Inverting the  $3 \times 3$  matrix in equation (2.105) and then rewriting it, we obtain the constants  $b_1, b_2$ , and  $b_3$  as

$$\begin{bmatrix} b_1 \\ b_2 \\ b_3 \end{bmatrix} = \frac{1}{2B} \begin{bmatrix} x_2y_3 - x_3y_2 & x_3y_1 - x_1y_3 & x_1y_2 - x_2y_1 \\ y_2 - y_3 & y_3 - y_1 & y_1 - y_2 \\ x_3 - x_2 & x_1 - x_3 & x_2 - x_1 \end{bmatrix} \begin{bmatrix} u_1 \\ u_2 \\ u_3 \end{bmatrix}, \quad (2.106)$$

where

$$B = \frac{1}{2} \det \begin{bmatrix} 1 & x_1 & y_1 \\ 1 & x_2 & y_2 \\ 1 & x_3 & y_3 \end{bmatrix}. \quad (2.107)$$

Substituting equation (2.106) into equation (2.104) and rearranging the resulting expression, we have

$$u = \psi_1(x, y)u_1 + \psi_2(x, y)u_2 + \psi_3(x, y)u_3, \quad (2.108)$$

where  $\psi_i(x, y)$  is the shape function of the 3-node triangle element and it is defined below:

$$\psi_1(x, y) = \frac{1}{2B} \left[ (x_2y_3 - x_3y_2) + (y_2 - y_3)x + (x_3 - x_2)y \right], \quad (2.109)$$

$$\psi_2(x, y) = \frac{1}{2B} \left[ (x_3y_1 - x_1y_3) + (y_3 - y_1)x + (x_1 - x_3)y \right], \quad (2.110)$$

$$\psi_3(x, y) = \frac{1}{2B} \left[ (x_1y_2 - x_2y_1) + (y_1 - y_2)x + (x_2 - x_1)y \right]. \quad (2.111)$$

These shape function also satisfy the conditions

$$\psi_i(x_j, y_j) = \begin{cases} 1 & \text{if } i = j \\ 0 & \text{if } i \neq j \end{cases}, \quad \text{and} \quad \sum_{i=1}^3 \psi_i(x, y) = 1. \quad (2.112)$$

In general, computing solutions using shape functions directly in terms of  $x, y$  for 2–dimensional or 3–dimensional problems in the finite element method, especially when unstructured meshes are involved, complicates the numerical integration process. As a result, most finite element methods calculate solutions using isoparametric elements because they simplify calculations and support complex shapes. In the next subsection, we introduce isoparametric elements in both one-dimensional and two-dimensional problems for the finite element method.

#### 2.3.4 Isoparametric elements

Isoparametric elements are widely used in the finite element method because they enable flexible and accurate modeling of complex geometries, support efficient numerical integration, and simplify implementation by using the same shape functions for both geometry and field interpolation. The concept of these elements is the use of a mathematical mapping between the natural coordinate system (denoted by  $\xi, \eta$ ) and physical coordinate system (denoted by  $x, y$ ). The mapping is accomplished through the use of shape functions, which are natural coordinate functions, see details in [16]. In this subsection, we provide a brief overview of linear and quadratic isoparametric elements in one and two dimensions.

##### 1) One-dimensional elements

We begin by considering one-dimensional isoparametric elements to discuss the fundamental characteristics of these elements. In the one-dimensional case, the natural coordinate is denoted by  $\xi$ , and the isoparametric element is defined over the standard domain  $\xi \in [-1, 1]$ . The shape functions for both linear and quadratic isoparametric elements in one dimension are illustrated in Figure 2.3. Figure 2.3 (a) illustrates the mapping of linear shape functions between the physical and natural coordinate systems. The top part of Figure 2.3 (a) shows the linear element in the physical coordinate system, with nodal coordinates  $x_1$  and  $x_2$ , and corresponding nodal values  $u_1$  and  $u_2$ . The bottom part of the figure shows the same element represented in the natural coordinate system, where the nodes are located at  $\xi = -1$  and  $\xi = 1$ . Similarly, the coordinate mapping for the quadratic shape functions is shown in Figure 2.3 (b). The quadratic isoparametric element consists of three nodes, located at  $\xi = -1$ ,  $\xi = 0$  and  $\xi = 1$ , as shown in the bottom part of Figure 2.3 (b).

The shape functions for the linear and quadratic isoparametric elements are defined in terms of the natural coordinate  $\xi$  as follows:

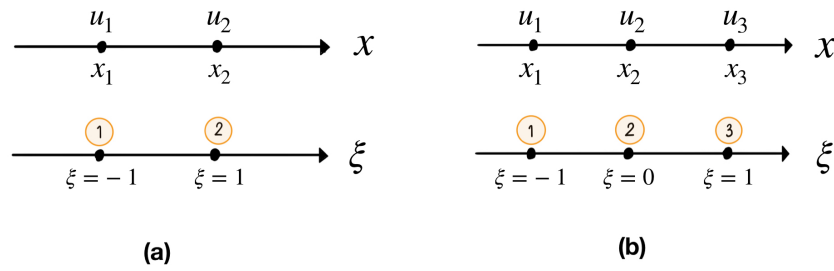


**Figure 2.3:** (a) Linear element and (b) quadratic element in both the physical coordinate system ( $x$ ) and the natural coordinate system ( $\xi$ )

1.1) *Linear isoparametric elements:*

$$\psi_1(\xi) = \frac{1 - \xi}{2}, \quad (2.113)$$

$$\psi_2(\xi) = \frac{1 + \xi}{2}. \quad (2.114)$$

1.2) *Quadratic isoparametric elements:*

$$\psi_1(\xi) = \frac{\xi^2 - \xi}{2}, \quad (2.115)$$

$$\psi_2(\xi) = 1 - \xi^2, \quad (2.116)$$

$$\psi_3(\xi) = \frac{\xi^2 + \xi}{2}. \quad (2.117)$$

The nodes in the natural coordinate system can be mapped to corresponding nodes in the physical coordinate system using the relation:

$$x = \sum_{i=1}^L \psi_i(\xi) x_i \quad (2.118)$$

and the nodal variable  $u$  can be interpolated using the same shape functions:

$$u = \sum_{i=1}^L \psi_i(\xi) u_i \quad (2.119)$$

where the constants  $L$  is the total number of nodes in the element,  $L = 2$  and  $L = 3$  for linear and quadratic isoparametric elements, respectively. The Jacobian for a one-dimensional element is defined as

$$J = \frac{dx}{d\xi} = \sum_{i=1}^L \frac{d\psi_i(\xi)}{d\xi} x_i, \quad (2.120)$$

and the differential transformation is given by

$$dx = |J| d\xi, \quad (2.121)$$

where  $|J|$  is the absolute value of the Jacobian, representing the scaling factor between the physical and natural coordinates.

This material is reserved for educational use only, not allowed for commercial use.

Forbidden to modify the content, and cite the document when use.

## 2) Triangular isoparametric elements

The basic characteristics of triangular isoparametric elements are discussed here. In a two-dimensional domain, the natural coordinates are denoted by  $\xi$  and  $\eta$ . The shape functions are defined in terms of the normalized natural domain, where  $\xi \in [0, 1]$  and  $\eta \in [0, 1]$ . For a linear triangular element, the shape functions in terms of the natural coordinates are:

$$\psi_1(\xi, \eta) = 1 - \xi - \eta, \quad (2.122)$$

$$\psi_2(\xi, \eta) = \xi, \quad (2.123)$$

$$\psi_3(\xi, \eta) = \eta, \quad (2.124)$$

where the nodes of this element are illustrated in Figure 2.4. The figure shows the mapping between the physical and natural coordinate systems of the linear triangular element, where part (a) shows the triangular shape function in the physical coordinate system with nodal coordinates  $(x_i, y_i)$  and corresponding nodal values  $u_i$ , for  $i = 1, 2, 3$ . Part (b) shows the same element in the natural coordinate system.

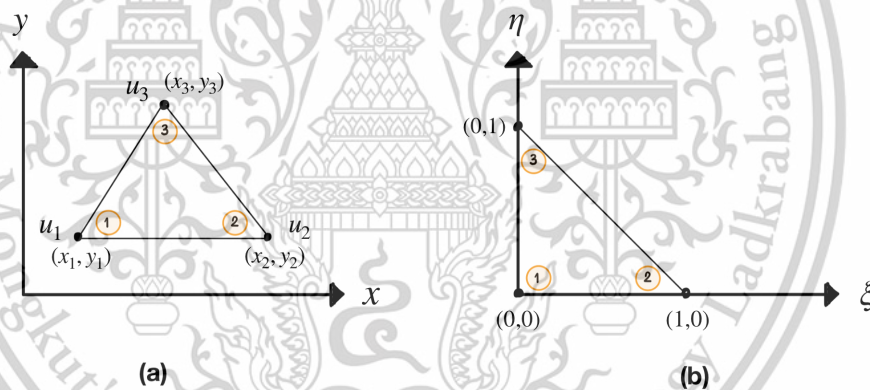


**Figure 2.4:** The linear triangular element in (a) the physical coordinate system  $(x, y)$  and (b) the natural coordinate system  $(\xi, \eta)$ .

Similarly, a general quadratic triangular element in the physical coordinate system, which consists of six nodes, can be mapped to a quadratic triangular element in the natural coordinate system, as illustrated in Figure 2.5. The shape functions of the quadratic triangular element are given by:

$$\psi_1(\xi, \eta) = (1 - \xi - \eta)(1 - 2\xi - 2\eta), \quad (2.125)$$

$$\psi_2(\xi, \eta) = \xi(2\xi - 1), \quad (2.126)$$

$$\psi_3(\xi, \eta) = \eta(2\eta - 1), \quad (2.127)$$

$$\psi_4(\xi, \eta) = 4\xi\eta, \quad (2.128)$$

$$\psi_5(\xi, \eta) = 4\eta(1 - \xi - \eta), \quad (2.129)$$

$$\psi_6(\xi, \eta) = 4\xi(1 - \xi - \eta). \quad (2.130)$$

This material is reserved for educational use only, not allowed for commercial use.

Forbidden to modify the content, and cite the document when use.

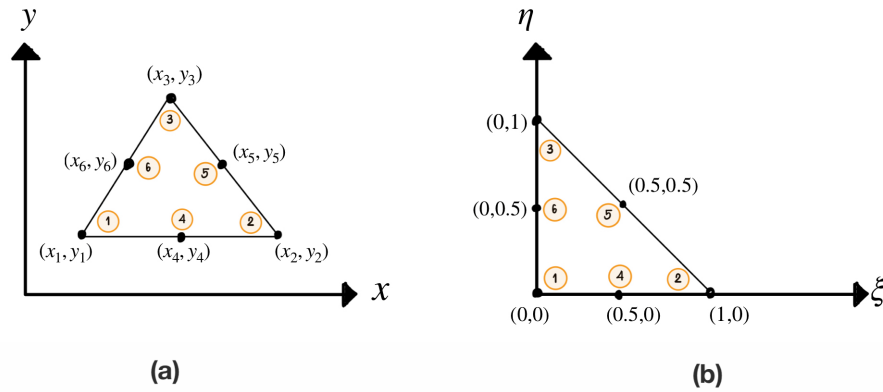


**Figure 2.5:** The quadratic triangular element in (a) the physical coordinate system  $(x, y)$  and (b) the natural coordinate system  $(\xi, \eta)$ .

The  $(\xi, \eta)$ -coordinates of any point in the natural domain are mapped to the  $(x, y)$ -coordinates in the physical domain through a mapping:

$$x(\xi, \eta) = \sum_{i=1}^M \psi_i(\xi, \eta)x_i, \tag{2.131}$$

$$y(\xi, \eta) = \sum_{i=1}^M \psi_i(\xi, \eta)y_i, \tag{2.132}$$

where  $M$  is the number of nodes of an element,  $M = 3$  for linear triangular elements and  $M = 6$  for quadratic triangular elements, and  $x_i$  and  $y_i$  are the coordinate values of  $i^{th}$  node in the physical domain, and  $\psi_i(\xi, \eta)$  is the shape function associated with the  $i^{th}$  node. The nodal variable  $u$  can be interpolated using the same shape functions:

$$u(\xi, \eta) = \sum_{i=1}^M \psi_i(\xi, \eta)u_i, \tag{2.133}$$

where  $u_i$  is the nodal variables at the  $i^{th}$  node.

To obtain the derivatives of the shape function with respect to  $x$  and  $y$ , we begin by using the chain rule

$$\frac{\partial}{\partial \xi} = \frac{\partial x}{\partial \xi} \frac{\partial}{\partial x} + \frac{\partial y}{\partial \xi} \frac{\partial}{\partial y} \tag{2.134}$$

$$\frac{\partial}{\partial \eta} = \frac{\partial x}{\partial \eta} \frac{\partial}{\partial x} + \frac{\partial y}{\partial \eta} \frac{\partial}{\partial y}. \tag{2.135}$$

Rewriting equations (2.134) and (2.135) in the matrix form, we have

$$\begin{Bmatrix} \frac{\partial}{\partial \xi} \\ \frac{\partial}{\partial \eta} \end{Bmatrix} = \begin{bmatrix} \frac{\partial x}{\partial \xi} & \frac{\partial y}{\partial \xi} \\ \frac{\partial x}{\partial \eta} & \frac{\partial y}{\partial \eta} \end{bmatrix} \begin{Bmatrix} \frac{\partial}{\partial x} \\ \frac{\partial}{\partial y} \end{Bmatrix}. \tag{2.136}$$

The square matrix on the right-hand side in equation (2.136) is referred to Jacobian matrix for the two dimensions and denoted as

$$[J] = \begin{bmatrix} \frac{\partial x}{\partial \xi} & \frac{\partial y}{\partial \xi} \\ \frac{\partial x}{\partial \eta} & \frac{\partial y}{\partial \eta} \end{bmatrix} = \begin{bmatrix} J_{11} & J_{12} \\ J_{21} & J_{22} \end{bmatrix}, \tag{2.137}$$

where the components in the Jacobian matrix are computed as follows

$$J_{11} = \frac{\partial x}{\partial \xi} = \sum_{i=1}^M \frac{\partial \psi_i(\xi, \eta)}{\partial \xi} x_i, \quad (2.138)$$

$$J_{12} = \frac{\partial y}{\partial \xi} = \sum_{i=1}^M \frac{\partial \psi_i(\xi, \eta)}{\partial \xi} y_i, \quad (2.139)$$

$$J_{21} = \frac{\partial x}{\partial \eta} = \sum_{i=1}^M \frac{\partial \psi_i(\xi, \eta)}{\partial \eta} x_i, \quad (2.140)$$

$$J_{22} = \frac{\partial y}{\partial \eta} = \sum_{i=1}^M \frac{\partial \psi_i(\xi, \eta)}{\partial \eta} y_i. \quad (2.141)$$

Inverse of the Jacobian matrix is denoted by

$$[R] = [J]^{-1} = \begin{bmatrix} R_{11} & R_{12} \\ R_{21} & R_{22} \end{bmatrix}. \quad (2.142)$$

Then, rewriting equation (2.136), we have

$$\begin{Bmatrix} \frac{\partial}{\partial x} \\ \frac{\partial}{\partial y} \end{Bmatrix} = [J]^{-1} \begin{Bmatrix} \frac{\partial}{\partial \xi} \\ \frac{\partial}{\partial \eta} \end{Bmatrix} = \begin{bmatrix} R_{11} & R_{12} \\ R_{21} & R_{22} \end{bmatrix} \begin{Bmatrix} \frac{\partial}{\partial \xi} \\ \frac{\partial}{\partial \eta} \end{Bmatrix}. \quad (2.143)$$

As a result, the derivatives of shape functions with respect to  $x$  and  $y$  can be denoted by

$$\begin{Bmatrix} \frac{\partial \psi_i(\xi, \eta)}{\partial x} \\ \frac{\partial \psi_i(\xi, \eta)}{\partial y} \end{Bmatrix} = \begin{bmatrix} R_{11} & R_{12} \\ R_{21} & R_{22} \end{bmatrix} \begin{Bmatrix} \frac{\partial \psi_i(\xi, \eta)}{\partial \xi} \\ \frac{\partial \psi_i(\xi, \eta)}{\partial \eta} \end{Bmatrix}. \quad (2.144)$$

The integration can be transformed from the physical coordinates to the natural coordinates using the Jacobian determinant, as expressed by

$$dxdy = |J| d\xi d\eta, \quad (2.145)$$

where  $|J|$  denotes the determinant of the Jacobian matrix.

### 2.3.5 Mixed finite element method

In this subsection, we briefly present the concept of the Mixed Finite Element Method [16], which is a variation of the standard finite element method used to solve partial differential equations (PDEs) with more than one unknown variable. Begin with the weak formulation given in equations (2.88) and (2.89) and then dividing the domain  $\Omega$  into  $N$  elements, i.e.,  $\Omega = \bigcup_e \Omega^e$  where  $\Omega^e$  be the element domains. This decomposition enables the integral over the entire domain  $\Omega$  to be written as the sum of integrals over each element domain  $\Omega^e$ , that is

$$\int_{\Omega} f(x) d\Omega = \sum_{e=1}^N \int_{\Omega^e} f(x) d\Omega^e, \quad (2.146)$$

This material is reserved for educational use only, not allowed for commercial use.

Forbidden to modify the content, and cite the document when use.

where  $N$  is the total number of elements. Applying equation (2.146) to equations (2.88) and (2.89), we obtain the equations

$$\sum_{e=1}^N \int_{\Omega^e} \left( \frac{\partial w_i}{\partial x_j} \frac{\partial u_i}{\partial x_j} - \frac{\partial w_i}{\partial x_i} p + \sigma w_i u_i - w_i f_i \right) d\Omega^e + \sum_{e=1}^N \int_{\Gamma^e} \left( -\mu w_i \frac{\partial u_i}{\partial x_j} n_j + w_i p n_i \right) d\Gamma^e = 0, \quad (2.147)$$

$$\sum_{e=1}^N \int_{\Omega^e} Q \frac{\partial u_j}{\partial x_j} d\Omega^e = 0. \quad (2.148)$$

To obtain the solutions using the mixed finite element method, the unknown variables  $u_i$  and  $p$  are approximated by the following expansions:

$$u_i(\mathbf{x}) = \sum_{m=1}^M \psi_m(x) u_i^m = \Psi^T \mathbf{U}_i, \quad (2.149)$$

$$p(\mathbf{x}) = \sum_{l=1}^L \phi_l(x) p_l = \Phi^T \mathbf{P}, \quad (2.150)$$

where  $i = 1, 2$ ,  $\psi_m \in H_0^1(\Omega)$  and  $\phi_l \in L_0^2(\Omega)$  are called a basis function, the vector  $\Psi$  and  $\Phi$  are their vector forms,  $\mathbf{U}_i$  and  $\mathbf{P}$  are the vectors of the velocity and pressure, respectively, the integer  $M$  and  $L$  are determined by the shape function and the superscript  $T$  is the transpose. By applying the Galerkin method described in Section 2.3.2, the weight functions  $w_i$  and  $Q$  are chosen to be the same as the corresponding shape functions, such that

$$w_i \approx \psi_m(x) \quad \text{and} \quad Q \approx \phi_l(x). \quad (2.151)$$

Substituting equations (2.149) and (2.150) into the weak form equation (2.147), we obtain the integration over each element as follows,

$$\begin{aligned} & \left( \int_{\Omega^e} \frac{\partial \Psi}{\partial x_j} \frac{\partial \Psi^T}{\partial x_j} d\Omega^e \right) \mathbf{U}_i - \left( \int_{\Omega^e} \frac{\partial \Psi}{\partial x_i} \Phi^T d\Omega^e \right) \mathbf{P} + \left( \int_{\Omega^e} \sigma \Psi \Psi^T d\Omega^e \right) \mathbf{U}_i \\ & = \int_{\Omega^e} \Psi f_i d\Omega^e + \int_{\Gamma^e} \left( -\mu \Psi \frac{\partial \Psi^T}{\partial x_j} \mathbf{U}_i n_j + \Psi \Phi \mathbf{P} n_i \right) d\Gamma^e. \end{aligned} \quad (2.152)$$

Similarly, substituting equation (2.149) into the weak form, equation (2.148), we have

$$\left( \int_{\Omega^e} \Phi \frac{\partial \Psi^T}{\partial x_j} d\Omega^e \right) \mathbf{U}_j = 0. \quad (2.153)$$

The equations (2.152) and (2.153) can be written as

$$\sum_{e=1}^N \left[ \mathbf{K}_{jj} \mathbf{U}_i - \mathbf{Q}_i \mathbf{P} + \mathbf{M} \mathbf{U}_i \right] = \sum_{e=1}^N \left[ \mathbf{F}_i \right], \quad (2.154)$$

$$\sum_{e=1}^N \left[ \mathbf{Q}_j^T \mathbf{U}_j \right] = 0, \quad (2.155)$$

where

$$\mathbf{K}_{jj} = \int_{\Omega^e} \frac{\partial \Psi}{\partial x_j} \frac{\partial \Psi^T}{\partial x_j} d\Omega^e, \quad (2.156)$$

$$\mathbf{Q}_i = \int_{\Omega^e} \frac{\partial \Psi}{\partial x_i} \Phi^T d\Omega^e, \quad (2.157)$$

$$\mathbf{M} = \int_{\Omega^e} \sigma \Psi \Psi^T d\Omega^e, \quad (2.158)$$

$$\mathbf{F}_i = \int_{\Omega^e} \Psi f_i d\Omega^e + \int_{\Gamma^e} \left( -\mu \Psi \frac{\partial \Psi^T}{\partial x_j} \mathbf{U}_i n_j + \Psi \Phi \mathbf{P} n_i \right) d\Gamma^e. \quad (2.159)$$

Rewriting equations (2.154) and (2.155) into the matrix form, for each element  $e$ , we have

$$\begin{bmatrix} \mathbf{K}_{jj} + \mathbf{M} & -\mathbf{Q}_i \\ \mathbf{Q}_j^T & 0 \end{bmatrix} \begin{Bmatrix} \mathbf{U}_i \\ \mathbf{P} \end{Bmatrix} = \begin{Bmatrix} \mathbf{F}_i \\ 0 \end{Bmatrix}. \quad (2.160)$$

Recall that the index  $i$  indicates the equation number, and the repeated index  $j$  indicates summation. For two-dimensional problems,  $i, j = 1, 2$ . Therefore, the equation (2.160) can be written in the element matrix form for two dimensions as follows:

$$\begin{bmatrix} \mathbf{K}_{11} + \mathbf{K}_{22} + \mathbf{M} & 0 & -\mathbf{Q}_1 \\ 0 & \mathbf{K}_{11} + \mathbf{K}_{22} + \mathbf{M} & -\mathbf{Q}_1 \\ -\mathbf{Q}_1^T & -\mathbf{Q}_2^T & 0 \end{bmatrix} \begin{Bmatrix} \mathbf{U}_1 \\ \mathbf{U}_2 \\ \mathbf{P} \end{Bmatrix} = \begin{Bmatrix} \mathbf{F}_1 \\ \mathbf{F}_2 \\ 0 \end{Bmatrix}, \quad (2.161)$$

which is called the mixed finite element model of equations (2.80) and (2.81).

## 2.4 Porosity and Permeability

This section introduces the porosity and the permeability, two fundamental physical properties of porous media that influence fluid flow behavior.

Porosity is a physical property of a material that describes the ratio of the volume of voids within the material to the total volume of the material. It is commonly used to quantify how much fluid exists in a porous media. In the context of fluid flow, the porosity is denoted by the symbol  $\varepsilon^l$  and can be calculated using the formula

$$\varepsilon^l = \frac{V_l}{V_t}, \quad (2.162)$$

where  $V_l$  is the volume of fluid (or voids) within the domain, and  $V_t$  is the total volume of the domain. As illustrated in Figure 2.6, where (a) and (b) show the domains consisting of fluid flowing through rock and compacted solid, respectively. Materials with high porosity, such as porous rock in Figure 2.6 (a), contain a large amount of empty space, which can store or allow fluids or gases to pass through. In contrast, materials with low porosity, like granite or compacted solid, have little void space, as seen in Figure 2.6 (b). While porosity indicates the amount of empty space in a porous material, it does not necessarily reflect how easily a fluid can flow through it. That ability is determined by another property called permeability.

Permeability is a physical property that measures the ability of a porous media to allow fluids to pass through it. Unlike porosity, which indicates how much fluid a material can hold, the permeability reflects how easily a fluid can move through the interconnected pore spaces within the material. It depends on factors such as pore size, shape, connectivity, and the viscosity of the fluid. Materials with high permeability, such as rock and gravel, allow fluid to move freely, while materials like compacted solid and clay have low permeability and restrict fluid movement, as shown in Figure 2.6. It can be observed that fluid flows more easily through the rock than through the

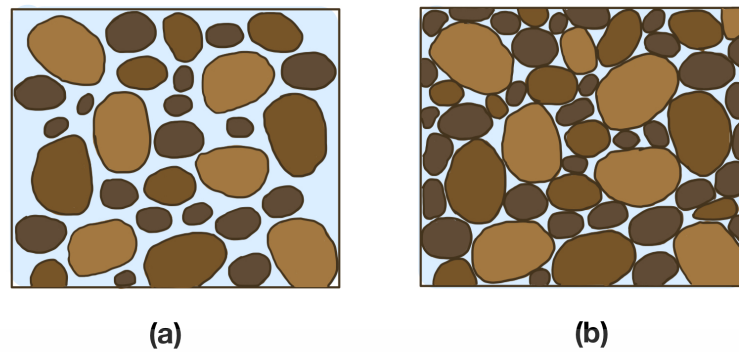


**Figure 2.6:** The influence of compaction on porosity and permeability of solid phase: (a) the rock, (b) compacted solid

compacted solid because the rock has more voids, resulting in higher permeability, as shown in Figure 2.6 (a). In contrast, the compacted solid domain offers greater fluid flow resistance because of its limited pore space, resulting in lower permeability, as shown in Figure 2.6 (b).

## 2.5 Literature Reviews

The problems involving the periciliary layer (PCL) and the mucus layer have been studied and investigated in both numerical and experimental studies by several researchers [19, 20, 21, 22, 23, 24, 25, 26, 27, 28]. For example, in part of the experimental studies, H. Matsui et al. [19] studied the movements of mucus and PCL fluid in human tracheobronchial epithelial cell cultures using conventional and confocal microscopy of fluorescent microspheres. They found that the PCL fluid and mucus move at similar rates,  $39.2 \pm 4.7$  and  $39.8 \pm 4.2 \mu\text{m/s}$ , respectively. U. Griesenbach et al. [22] established methods to measure the height of the PCL in lower airway biopsies in human and mice for both cystic fibrosis (CF) and non-cystic fibrosis (non-CF) cases. They discovered that the height of the PCL fluid was reduced in CF tissue. The mean height of the PCL in human CF and non-CF was  $4.52 \pm 0.47$  mm and  $5.60 \pm 0.28$  mm, respectively, while in mice, the CF and non-CF heights were  $4.10 \pm 0.09$  mm and  $4.70 \pm 0.13$  mm, respectively. In part of the numerical studies, P. Zhu et al. [23] proposed a 2-dimensional model to explore the migration law of particles and studied the transport velocity of mucus due to cilium beat in the PCL of the human respiratory tract using the immersed boundary-lattice Boltzmann method. P.G. Jayathilake [24] developed a three-dimensional numerical model to simulate human pulmonary cilia motion in the PCL and investigated the effects of the phase difference between cilia, the cilia beating frequency, the viscosity of PCL, the PCL height, and the ciliary length on the PCL motion. S.M. Vanaki et al. [25] studied the fluid flow characteristics of the PCL driven by cilia using the finite difference projection method with the immersed boundary method (BI). S.

Forbidden to modify the content, and cite the document when use.

Poopra and K. Wuttanachamsri [26] provide boundary conditions of velocity at the free-fluid/porous-medium interface, where the fluid in the PCL is moved due to the ciliary movement, using the asymptotic expansion method to one-dimensional macroscale Stokes-Brinkman equations.

For the fluid flow problems, there are several mathematical models used to describe the flow in the free-fluid, porous, or both domains [29, 30, 31, 32, 33, 34, 35, 36, 37, 38, 39, 40, 41, 42, 43, 44, 45, 46, 47, 48, 49, 50, 51, 52]. If fluid flows through different domains, then mathematical models used to describe the flow are also distinct. That is, the equations for the flow in the free-fluid region and flow in the porous domain are different. For example, K. Khanafer et al. [29] used Darcy's Law and Brinkman-extended Darcy to investigate the fluid flow inside the hollow fiber bundle of an artificial lung and applied the Navier-Stokes equation for the fluid flow outside the fiber bundle. H.B. Ly et al. [30] investigated the problem of fluid flow in coupling a free fluid domain and a porous medium using the Stokes and Darcy equations, respectively. F. Basirat et al. [32] predicted the flow and transport of gaseous CO<sub>2</sub> in a porous medium using the Darcy-Brinkman equation with commercial computational multiphysics software COMSOL which was based on the finite element method. S. Phaenchat and K. Wuttanachamsri [34] determined the velocity of the PCL fluid in a two-dimensional domain, employing the nonlinear Brinkman equation for the porous medium and the steady-state Navier-Stokes equation for the free-fluid region. These equations were solved using a mixed finite element method combined with Newton's method. K. Wuttanachamsri [35] found the velocity of the PCL fluid in a porous medium and presented the shape of the free boundary at the tips of cilia when the fluid was driven by cilia movement using a one-dimensional Brinkman equation with the Stefan problem. M. Conti and A. Giorgini [36] proved the existence and uniqueness of the Brinkman-Cahn-Hilliard system with logarithmic free energy density for the motion of binary fluids with different viscosities. E.S. Titi and S. Trabelsi [37] proved the existence and uniqueness of a three-dimensional Brinkman-Forchheimer-Benard equation for the flow of an incompressible fluid in a closed sample of a porous medium. For the study of a static solid phase, R. Ingram [38] developed a model for non-Darcian fluid flow under different boundary conditions by using the finite element discretization of the Brinkman equation. He proved that the discretized problem was well-posed and also demonstrated the existence and uniqueness of the solutions of the steady Navier-Stokes equation. P. Angot [39] presented the well-posedness of the Stokes-Brinkman equations with a family of jump embedded boundary conditions (J.E.B.C.) on an immersed interface. He also proved that the Stokes-Darcy equations with Beavers and Joseph conditions was well-posed by an asymptotic analysis. Furthermore, in P. Angot [40], he studied the well-posedness of the Stokes-Brinkman and Stokes-Darcy with new jump interface conditions. K. Chamsri [43] showed the well-posedness of the Stokes-

This material is reserved for educational use only, not allowed for commercial use.

Brinkman model for the case of moving solid phases, while the porosity was assumed to be a constant. For the numerical solution of the Stokes-Brinkman equations, W.R. Hwang and S.G. Advani [44] presented the numerical solutions of the Stokes-Brinkman equations in a parallel channel flow over a porous media by using a new finite-element scheme. Then, they also applied the same scheme to predict the effective permeability of dual scale fibrous media. N.O. Al-Atawi, et al [45] investigated the Stokes-Brinkman with the Beavers and Joseph slip conditions to find the velocity of the viscous flow along the articular surfaces between the joints using the finite volume method. S. Poopra and K. Wuttanachamsri [46] determined the velocity of the PCL fluid from the movement of the cilia in human lungs applying the asymptotic expansion method to the Stokes-Brinkman equations with the Beavers and Joseph boundary condition. K. Wuttanachamsri and L. Schreyer [50] determined the PCL fluid velocities due to the cilia beating in a three-dimensional domain using a mixed finite element method of Taylor-Hood type to the Stokes-Brinkman equations.

Most of the previous literatures had studied the well-posedness and numerical solutions of the Stokes-Brinkman equations when the fluid moved by the pressure gradient. Although some works considered the fluid velocity due to the movement of the solid phases, they still assumed that the porosity was just a constant. In this research, we focus on the problem of slow flow with an incompressible viscous fluid flowing through two distinct domains: a porous medium and an adjacent free-fluid region. The generalized Stokes-Brinkman equations are used to describe this problem, with the generalized Stokes used in the free-fluid region and the generalized Brinkman used in a porous medium, because these two models can be matched at the free-fluid/porous-medium interface. In this research, we provide the well-posedness of the generalized Stokes-Brinkman equations in a macroscopic scale for the free-fluid region and adjacent porous medium, when the fluid motion is driven by self-propelled solid phases. The model is derived under the assumption that the porosity is a function since the beginning of the derivation of the equation. We also determine the velocity of the PCL fluid in a porous medium by applying the mixed finite element method to the generalized Brinkman equation.

## Chapter 3

# Generalized Stokes-Brinkman equations

In this chapter, we present the derivation of the generalized Stokes-Brinkman equations. For the generalized Stokes equation, we start with the generalized Navier-Stokes equation and then use a nondimensionalization method to obtain the generalized Stokes equation. This is shown in Section 3.1. To derive the generalized Brinkman equation, we begin with a momentum equation obtained from Hybrid Mixture Theory (HMT) [5, 6, 7], an upscaling technique, and then use a nondimensionalization approach to have a macroscopic model in a porous medium, which is illustrated in Section 3.2. We rewrite our governing equations in Section 3.3 in order to summarize and use in the next chapter. The weak formulation of the generalized Stokes-Brinkman equations by using a mixed finite element method and the well-posedness of these equations are presented in Sections 3.4 and 3.5, respectively.

### 3.1 Derivation of generalized Stokes equation

In this section, we derive the generalized Stokes equation for the free-fluid region by using nondimensionalization method. To obtain the generalized Stokes equation, we begin with the generalized Navier-Stokes equation, which is attained by substituting a stress tensor (developed from entropy inequality held near equilibrium for a viscous fluid) into a momentum equation. The form of the generalized Navier-Stokes equation is [53]

$$\rho \frac{\partial \mathbf{u}}{\partial t} + \rho(\mathbf{u} \cdot \nabla \mathbf{u}) + \nabla p - (\lambda + \mu)\nabla(\nabla \cdot \mathbf{u}) - \mu \nabla \cdot \nabla \mathbf{u} - \rho \mathbf{g} = \mathbf{0}, \quad (3.1)$$

where  $\rho$  is density,  $t$  is time,  $\mathbf{u}$  is the velocity,  $p$  is pressure,  $\lambda$  is a constant,  $\mu$  is the dynamic viscosity and  $\mathbf{g}$  is gravity. To normalize the generalized Navier-Stokes equation (3.1), we define the following dimensionless variables :

$$\hat{\mathbf{u}} = \frac{\mathbf{u}}{u_0}, \quad \hat{p} = \frac{p}{p_0}, \quad \hat{\mathbf{g}} = \frac{\mathbf{g}}{g_0}, \quad \hat{\nabla} = L\nabla, \quad \hat{t} = ft, \quad (3.2)$$

where the scaling parameter  $u_0$  is the characteristic speed,  $p_0$  is the reference pressure,  $g_0$  is the gravitational acceleration,  $L$  is the characteristic length and  $f$  is the characteristic frequency. Next, we normalize the generalized Navier-Stokes equation, equation (3.1), with dimensionless variables, equation (3.2), and show that some terms in this equation can be neglected for our problem in the free-fluid domain. Substituting equation (3.2) into equation (3.1), we get

$$\rho \frac{\partial(\hat{\mathbf{u}}u_0)}{\partial\left(\frac{t}{f}\right)} + \rho\left(\hat{\mathbf{u}}u_0 \cdot \frac{\hat{\nabla}}{L}\hat{\mathbf{u}}u_0\right) + \frac{\hat{\nabla}}{L}\hat{p}p_0 - (\lambda + \mu)\frac{\hat{\nabla}}{L}\left(\frac{\hat{\nabla}}{L} \cdot \hat{\mathbf{u}}u_0\right) - \mu\frac{\hat{\nabla}}{L} \cdot \frac{\hat{\nabla}}{L}\hat{\mathbf{u}}u_0 - \rho\hat{\mathbf{g}}g_0 = \mathbf{0}, \quad (3.3)$$

Forbidden to modify the content, and cite the document when use.

or

$$\rho u_0 f \frac{\partial \hat{\mathbf{u}}}{\partial \hat{t}} + \frac{\rho u_0^2}{L} (\hat{\mathbf{u}} \cdot \hat{\nabla} \hat{\mathbf{u}}) + \frac{p_0}{L} \hat{\nabla} \hat{p} - \frac{(\lambda + \mu) u_0}{L^2} \hat{\nabla} (\hat{\nabla} \cdot \hat{\mathbf{u}}) - \frac{\mu u_0}{L^2} \hat{\nabla} \cdot \hat{\nabla} \hat{\mathbf{u}} - \rho g_0 \hat{\mathbf{g}} = \mathbf{0}. \quad (3.4)$$

Multiplying equation (3.4) by  $\frac{L^2}{\mu u_0}$  both sides, we have

$$\frac{\rho f L^2}{\mu} \frac{\partial \hat{\mathbf{u}}}{\partial \hat{t}} + \frac{\rho u_0 L}{\mu} (\hat{\mathbf{u}} \cdot \hat{\nabla} \hat{\mathbf{u}}) + \frac{p_0 L}{\mu u_0} \hat{\nabla} \hat{p} - \frac{(\lambda + \mu)}{\mu} \hat{\nabla} (\hat{\nabla} \cdot \hat{\mathbf{u}}) - \hat{\nabla} \cdot \hat{\nabla} \hat{\mathbf{u}} - \frac{\rho g_0 L^2}{\mu u_0} \hat{\mathbf{g}} = \mathbf{0}. \quad (3.5)$$

For our convenience, to calculate the coefficient values of equation (3.5), we let

$$\tilde{C}_1 = \frac{\rho f L^2}{\mu}, \quad \tilde{C}_2 = \frac{\rho u_0 L}{\mu}, \quad \tilde{C}_3 = \frac{p_0 L}{\mu u_0}, \quad (3.6)$$

$$\tilde{C}_4 = \frac{(\lambda + \mu)}{\mu}, \quad \tilde{C}_5 = 1, \quad \tilde{C}_6 = \frac{\rho g_0 L^2}{\mu u_0}, \quad (3.7)$$

and the equation (3.5) can be rewritten as

$$\tilde{C}_1 \frac{\partial \hat{\mathbf{u}}}{\partial \hat{t}} + \tilde{C}_2 (\hat{\mathbf{u}} \cdot \hat{\nabla} \hat{\mathbf{u}}) + \tilde{C}_3 \hat{\nabla} \hat{p} - \tilde{C}_4 \hat{\nabla} (\hat{\nabla} \cdot \hat{\mathbf{u}}) - \tilde{C}_5 \hat{\nabla} \cdot \hat{\nabla} \hat{\mathbf{u}} - \tilde{C}_6 \hat{\mathbf{g}} = \mathbf{0}. \quad (3.8)$$

To calculate the values of each coefficient in equations (3.6) and (3.7), we choose the characteristic length  $L$  is the highest length of cilia in the respiratory system [54], the reference  $f$  is the frequency of cilia beat in the human respiratory tract [55], the characteristic velocity  $u_0$  is the maximum speed of cilia for the effective stroke at temperature  $37^\circ\text{C}$ , the reference pressure  $p_0$  is the pressure in the human respiratory tract, which is about one [56],  $g_0$  is the Earth's gravity, and  $\rho$  and  $\mu$  are the density of water and dynamic viscosity at  $37^\circ\text{C}$ , respectively. The constant  $\lambda$  is set to be zero. The values of the characteristic parameters in International System (SI) units are shown in Table 3.1.

**Table 3.1:** The values of characteristic and constant variables in equation (3.5) in International System units.

| Variables | SI Units               | Values                  |
|-----------|------------------------|-------------------------|
| $L$       | m                      | $7 \times 10^{-6}$      |
| $f$       | 1/s                    | 10                      |
| $u_0$     | m/s                    | $2.5 \times 10^{-4}$    |
| $p_0$     | kg/(m·s <sup>2</sup> ) | 1                       |
| $g_0$     | m/s <sup>2</sup>       | 9.807                   |
| $\rho$    | kg/m <sup>3</sup>      | 993.3                   |
| $\mu$     | kg/(m·s)               | $0.6913 \times 10^{-3}$ |

Substituting the values from Table 3.1 into the coefficients in equations (3.6) and (3.7),

we obtain the coefficients

$$\tilde{C}_1 = \frac{\rho f L^2}{\mu} = 7.0406 \times 10^{-4}, \quad (3.9)$$

$$\tilde{C}_2 = \frac{\rho u_0 L}{\mu} = 2.5 \times 10^{-3}, \quad (3.10)$$

$$\tilde{C}_3 = \frac{p_0 L}{\mu u_0} = 40.5034, \quad (3.11)$$

$$\tilde{C}_4 = \frac{(\lambda + \mu)}{\mu} = 1, \quad (3.12)$$

$$\tilde{C}_5 = 1, \quad (3.13)$$

$$\tilde{C}_6 = \frac{\rho g_0 L^2}{\mu u_0} = 2.7619. \quad (3.14)$$

We can see that the coefficients  $\tilde{C}_1$  and  $\tilde{C}_2$  are comparatively small compared with the others. Therefore, we neglect the first and second terms, the unsteady and nonlinear terms in the equation, and then equation (3.1) becomes

$$\nabla p - (\lambda + \mu)\nabla(\nabla \cdot \mathbf{u}) - \mu\nabla \cdot \nabla \mathbf{u} - \rho \mathbf{g} = \mathbf{0}, \quad (3.15)$$

or

$$\nabla p - \lambda\nabla(\nabla \cdot \mathbf{u}) - \mu\nabla(\nabla \cdot \mathbf{u}) - \mu\nabla \cdot \nabla \mathbf{u} - \rho \mathbf{g} = \mathbf{0}. \quad (3.16)$$

In this research, we assume that the velocity  $\mathbf{u}$  in a two dimension is smooth enough so that the order of the derivative can be interchanged,

$$\frac{\partial}{\partial x} \left( \frac{\partial \mathbf{u}}{\partial y} \right) = \frac{\partial}{\partial y} \left( \frac{\partial \mathbf{u}}{\partial x} \right). \quad (3.17)$$

Then, we obtain

$$\nabla(\nabla \cdot \mathbf{u}) = \nabla \cdot (\nabla \mathbf{u})^T. \quad (3.18)$$

Substituting equation (3.18) into the third term of equation (3.16), we have

$$\nabla p - \lambda\nabla(\nabla \cdot \mathbf{u}) - \mu\nabla \cdot (\nabla \mathbf{u})^T - \mu\nabla \cdot \nabla \mathbf{u} - \rho \mathbf{g} = \mathbf{0}, \quad (3.19)$$

or

$$\nabla p - \lambda\nabla(\nabla \cdot \mathbf{u}) - \mu\nabla \cdot (\nabla \mathbf{u} + (\nabla \mathbf{u})^T) - \rho \mathbf{g} = \mathbf{0}. \quad (3.20)$$

Since the rate of deformation for the liquid phase is defined by

$$\mathbf{d} = \frac{1}{2}(\nabla \mathbf{u} + (\nabla \mathbf{u})^T). \quad (3.21)$$

Then, the equation (3.20) can be rewritten as

$$\nabla p - \lambda\nabla(\nabla \cdot \mathbf{u}) - \mu\nabla \cdot (2\mathbf{d}) - \rho \mathbf{g} = \mathbf{0}, \quad (3.22)$$

$$\nabla p - \lambda\nabla(\nabla \cdot \mathbf{u}) - \nabla \cdot (2\mu\mathbf{d}) - \rho \mathbf{g} = \mathbf{0}. \quad (3.23)$$

Notice that if  $\lambda = 0$ , then equation (3.23) becomes

$$\nabla p - \nabla \cdot (2\mu\mathbf{d}) - \rho \mathbf{g} = \mathbf{0}, \quad (3.24)$$

which is the generalized Stokes equation. If the matrix  $\nabla \mathbf{u}$  is symmetric, then  $\mathbf{d}$  becomes  $\nabla \mathbf{u}$ . Then equation (3.24) is the Stokes equation :

This material is reserved for educational use only, not allowed for commercial use.

$$\nabla p - 2\mu\nabla \cdot \nabla \mathbf{u} - \rho \mathbf{g} = \mathbf{0}. \quad (3.25)$$

Forbidden to modify the content, and cite the document when use.

### 3.2 Derivation of generalized Brinkman equation

In this section, we show the derivation of the generalized Brinkman equation in a macroscopic scale derived by using Hybrid Mixture Theory (HMT) and nondimensionalization. Hybrid Mixture Theory is an upscaling technique used to derive multiphase equations such as the combination of solid and liquid phases. This method uses the averaging theorem to upscale equations from a microscale equation to a macroscale equation [5]. In this study, we focus on developing a model for fluid flow due to the movement of self-propelled solid phases. Here, we follow the procedure provided in [4]. We start with the multiphase equation upscaled from the conservation of momentum [4] when the porosity is a function, not a constant:

$$\varepsilon^l \rho^l \frac{D^l \mathbf{u}^l}{Dt} + \varepsilon^l \nabla p + p \nabla \varepsilon^l - \nabla \cdot (\varepsilon^l 2\mu \mathbf{d}^l) - \varepsilon^l \rho^l \mathbf{g}^l = p \nabla \varepsilon^l - \varepsilon^l \mathbf{R} \cdot (\mathbf{u}^l - \mathbf{u}^s), \quad (3.26)$$

where the variables  $l$  and  $s$  mean the liquid and solid phases, respectively. The function  $\varepsilon^l$  is the porosity which is a variable in space,  $\mathbf{d}^l = 0.5 (\nabla \mathbf{u}^l + (\nabla \mathbf{u}^l)^T)$  is the rate of deformation tensor,  $\mathbf{R}$  is a second-order tensor,  $\mathbf{u}^l$  and  $\mathbf{u}^s$  are the velocity of liquid and solid phases, respectively. Subtracting  $p \nabla \varepsilon^l$  from both sides in equation (3.26), we have

$$\varepsilon^l \rho^l \frac{D^l \mathbf{u}^l}{Dt} + \varepsilon^l \nabla p - \nabla \cdot (\varepsilon^l 2\mu \mathbf{d}^l) - \varepsilon^l \rho^l \mathbf{g}^l = -\varepsilon^l \mathbf{R} \cdot (\mathbf{u}^l - \mathbf{u}^s), \quad (3.27)$$

and dividing both sides by  $\varepsilon^l$ , we have

$$\rho^l \frac{D^l \mathbf{u}^l}{Dt} + \nabla p - \frac{1}{\varepsilon^l} \nabla \cdot (\varepsilon^l 2\mu \mathbf{d}^l) - \rho \mathbf{g} = -\mathbf{R} \cdot (\mathbf{u}^l - \mathbf{u}^s). \quad (3.28)$$

From the definition of the material time derivative for liquid phase [4]:

$$\frac{D^l}{Dt} = \frac{\partial}{\partial t} + \mathbf{u}^l \cdot \nabla, \quad (3.29)$$

we have

$$\frac{D^l \mathbf{u}^l}{Dt} = \frac{\partial \mathbf{u}^l}{\partial t} + \mathbf{u}^l \cdot \nabla \mathbf{u}^l. \quad (3.30)$$

Substituting equation (3.30) and taking  $\mathbf{R} = \mu \varepsilon^l \mathbf{k}^{-1}$  into equation (3.28), where  $\mathbf{k}^{-1}$  is the inverse of the permeability tensor, we have

$$\rho \left( \frac{\partial \mathbf{u}^l}{\partial t} + \mathbf{u}^l \cdot \nabla \mathbf{u}^l \right) + \nabla p - \frac{1}{\varepsilon^l} \nabla \cdot (\varepsilon^l 2\mu \mathbf{d}^l) - \rho \mathbf{g} = -\mu \varepsilon^l \mathbf{k}^{-1} \cdot (\mathbf{u}^l - \mathbf{u}^s). \quad (3.31)$$

Rearranging the terms in equation (3.31), we get

$$\rho \left( \frac{\partial \mathbf{u}^l}{\partial t} + \mathbf{u}^l \cdot \nabla \mathbf{u}^l \right) + \mu \mathbf{k}^{-1} \cdot (\varepsilon^l \mathbf{u}^l - \varepsilon^l \mathbf{u}^s) + \nabla p - \frac{\mu}{\varepsilon^l} \nabla \cdot (2\varepsilon^l \mathbf{d}^l) = \rho \mathbf{g}, \quad (3.32)$$

which is the conservation of momentum for liquid phase. Since  $\mathbf{d}^l = 0.5 (\nabla \mathbf{u}^l + (\nabla \mathbf{u}^l)^T)$ , the equation (3.32) can be rewritten as

$$\rho \left( \frac{\partial \mathbf{u}^l}{\partial t} + \mathbf{u}^l \cdot \nabla \mathbf{u}^l \right) + \mu \mathbf{k}^{-1} \cdot (\varepsilon^l \mathbf{u}^l - \varepsilon^l \mathbf{u}^s) + \nabla p - \frac{\mu}{\varepsilon^l} \nabla \cdot (\varepsilon^l (\nabla \mathbf{u}^l + (\nabla \mathbf{u}^l)^T)) = \rho \mathbf{g}, \quad (3.33)$$

This material is reserved for educational use only, not allowed for commercial use.

or

$$\rho \frac{\partial \mathbf{u}^l}{\partial t} + \rho (\mathbf{u}^l \cdot \nabla \mathbf{u}^l) + \mu \mathbf{k}^{-1} \cdot (\varepsilon^l \mathbf{u}^l - \varepsilon^l \mathbf{u}^s) + \nabla p - \frac{\mu}{\varepsilon^l} \nabla \cdot (\varepsilon^l (\nabla \mathbf{u}^l + (\nabla \mathbf{u}^l)^T)) = \rho \mathbf{g}. \quad (3.34)$$

Next, we normalize equation (3.34) and show that some term can be neglected for our problem in the porous medium. We use the same characteristic parameters as in the previous section and define the nondimensional variables as

$$\hat{\mathbf{u}}^l = \frac{\mathbf{u}^l}{u_0}, \quad \hat{\mathbf{u}}^s = \frac{\mathbf{u}^s}{u_0}, \quad \hat{p} = \frac{p}{p_0}, \quad (3.35)$$

$$\hat{\mathbf{g}} = \frac{\mathbf{g}}{g_0}, \quad \hat{\nabla} = L \nabla, \quad \hat{t} = ft. \quad (3.36)$$

Substituting equations (3.35) and (3.36) into equation (3.34), we have

$$\rho f u_0 \frac{\partial \hat{\mathbf{u}}^l}{\partial \hat{t}} + \frac{\rho u_0^2}{L} (\hat{\mathbf{u}}^l \cdot \hat{\nabla} \hat{\mathbf{u}}^l) + u_0 \mu \mathbf{k}^{-1} \cdot (\varepsilon^l \hat{\mathbf{u}}^l - \varepsilon^l \hat{\mathbf{u}}^s) + \frac{p_0}{L} \hat{\nabla} \hat{p} - \frac{u_0 \mu}{\varepsilon^l L^2} \hat{\nabla} \cdot (\varepsilon^l (\hat{\nabla} \hat{\mathbf{u}}^l + (\hat{\nabla} \hat{\mathbf{u}}^l)^T)) = \rho g_0 \hat{\mathbf{g}}. \quad (3.37)$$

Multiplying equation (3.37) by  $\frac{\mathbf{k}}{\mu u_0}$  both sides, we have

$$\frac{\mathbf{k} \rho f}{\mu} \frac{\partial \hat{\mathbf{u}}^l}{\partial \hat{t}} + \frac{\mathbf{k} \rho u_0}{\mu L} (\hat{\mathbf{u}}^l \cdot \hat{\nabla} \hat{\mathbf{u}}^l) + (\varepsilon^l \hat{\mathbf{u}}^l - \varepsilon^l \hat{\mathbf{u}}^s) + \frac{\mathbf{k} p_0}{\mu u_0 L} \hat{\nabla} \hat{p} - \frac{\mathbf{k}}{\varepsilon^l L^2} \hat{\nabla} \cdot (\varepsilon^l (\hat{\nabla} \hat{\mathbf{u}}^l + (\hat{\nabla} \hat{\mathbf{u}}^l)^T)) = \frac{\mathbf{k} \rho g_0}{\mu u_0} \hat{\mathbf{g}}. \quad (3.38)$$

For our convenience to calculate the coefficient values of equation (3.38), we rewrite equation (3.38) as

$$\tilde{C}_7 \frac{\partial \hat{\mathbf{u}}^l}{\partial \hat{t}} + \tilde{C}_8 (\hat{\mathbf{u}}^l \cdot \hat{\nabla} \hat{\mathbf{u}}^l) + \tilde{C}_9 (\varepsilon^l \hat{\mathbf{u}}^l - \varepsilon^l \hat{\mathbf{u}}^s) + \tilde{C}_{10} \hat{\nabla} \hat{p} - \tilde{C}_{11} \hat{\nabla} \cdot (\varepsilon^l (\hat{\nabla} \hat{\mathbf{u}}^l + (\hat{\nabla} \hat{\mathbf{u}}^l)^T)) = \tilde{C}_{12} \hat{\mathbf{g}}, \quad (3.39)$$

where we define

$$\tilde{C}_7 = \frac{\mathbf{k} \rho f}{\mu}, \quad \tilde{C}_8 = \frac{\mathbf{k} \rho u_0}{\mu L}, \quad \tilde{C}_9 = 1, \quad (3.40)$$

$$\tilde{C}_{10} = \frac{\mathbf{k} p_0}{\mu u_0 L}, \quad \tilde{C}_{11} = \frac{\mathbf{k}}{\varepsilon^l L^2}, \quad \tilde{C}_{12} = \frac{\mathbf{k} \rho g_0}{\mu u_0}. \quad (3.41)$$

Using the values in Table 3.1 to calculate the coefficients  $\tilde{C}_7$  to  $\tilde{C}_{12}$  with the permeability  $\mathbf{k} = 10^{-14} \text{ m}^2$  and porosity  $\varepsilon^l = 1$ , which are the maximum values employed from [57], we obtain the values of the coefficients as

$$\tilde{C}_7 = \frac{\mathbf{k} \rho f}{\mu} = 1.4369 \times 10^{-7}, \quad (3.42)$$

$$\tilde{C}_8 = \frac{\mathbf{k} \rho u_0}{\mu L} = 5.1316 \times 10^{-7}, \quad (3.43)$$

$$\tilde{C}_9 = 1, \quad (3.44)$$

$$\tilde{C}_{10} = \frac{\mathbf{k} p_0}{\mu u_0 L} = 8.3 \times 10^{-3}, \quad (3.45)$$

$$\tilde{C}_{11} = \frac{\mathbf{k}}{\varepsilon^l L^2} = 2.0408 \times 10^{-4}, \quad (3.46)$$

$$\tilde{C}_{12} = \frac{\mathbf{k} \rho g_0}{\mu u_0} = 5.6365 \times 10^{-4}. \quad (3.47)$$

This material is reserved for educational use only, not allowed for commercial use.

Forbidden to modify the content, and cite the document when use.

Considering the values of the coefficients  $\tilde{C}_7$  to  $\tilde{C}_{12}$ , we neglect the first two terms in equation (3.39), the time-dependent and nonlinear terms, because they are significantly smaller than the others. Therefore, equation (3.32) becomes

$$\mu \mathbf{k}^{-1} \cdot (\varepsilon^l \mathbf{u}^l - \varepsilon^l \mathbf{u}^s) + \nabla p - \frac{\mu}{\varepsilon^l} \nabla \cdot (2\varepsilon^l \mathbf{d}^l) = \rho \mathbf{g}, \quad (3.48)$$

which is called the generalized Brinkman equation in a macroscopic scale. Notice that the equation (3.48) is different from the Brinkman in literatures [58], which is

$$\mu \mathbf{k}^{-1} \cdot \varepsilon^l \mathbf{u}^l + \nabla p - \mu \Delta \mathbf{u}^l = \rho \mathbf{g}. \quad (3.49)$$

Our model starts with the macroscale momentum equation that the porosity is a function and cannot be moved out of the derivative as usually used in researches. The porosity in the third term in equation (3.48) cannot be canceled out with the denominator. Moreover, the first-order derivative of the rate of deformation times with the porosity in equation (3.48) cannot be changed to be the second-order derivative of the velocity as shown in equation (3.49). It may seem that the difference is not much but finding the numerical results of equation (3.48) are more complicated than equation (3.49) including the proof of the well-posedness of the equation.

Notice that the generalized Brinkman equation in the macroscopic scale, equation (3.48), has a good engagement with the generalized Stokes equation (3.24). Notice that if there are no solid phases in the adjacent free-fluid domain, the porosity becomes one, and the permeability tends to infinity in this region, then the first term in equation (3.48) is disappeared and then the generalized Brinkman equation, equation (3.48) becomes generalized Stokes equation, equation (3.24). Thus, the solutions in these two layers can be matched in the transition zone at the free-fluid/porous-medium interface by using the generalized Stokes-Brinkman equations. The mathematical model is summarized in the next section.

### 3.3 Mathematical model

In this section, we summarize the mathematical model derived in Sections 3.1 and 3.2. The models in both the free-fluid layer and porous medium consist of two unknowns, which are the velocity  $\mathbf{u}^l$  and the pressure  $p$ . Therefore, in each domain, we need one more equation which is a continuity equation obtained from the conservation of mass. Since the fluid flow is caused by the movement of bundle of solid phases, we employ the continuity equation for two-phase flow in the porous medium derived by HMT [59, 60], which is

$$\nabla \cdot (\varepsilon^l \mathbf{u}^l) = f, \quad (3.50)$$

where  $f = -\dot{\varepsilon}^l / (1 - \varepsilon^l) + \nabla \cdot (\varepsilon^l \mathbf{u}^s)$  and  $\dot{\varepsilon}^l = \partial \varepsilon^l / \partial t + \mathbf{u}^s \cdot \nabla \varepsilon^l$  is the material time derivative of the porosity with respect to the solid phase. Let  $\Omega = \Omega_p \cup \Omega_f$  be our domain and  $\partial \Omega$

is the boundary of the domain where  $\Omega_p$  is a porous medium and  $\Omega_f$  is the free-fluid domain. From equations (3.48) and (3.50), we have

$$\mu \mathbf{k}^{-1} \cdot (\varepsilon^l \mathbf{u}^l - \varepsilon^l \mathbf{u}^s) - \frac{\mu}{\varepsilon^l} \nabla \cdot (2\varepsilon^l \mathbf{d}^l) + \nabla p = \rho \mathbf{g}, \quad (3.51)$$

$$\nabla \cdot (\varepsilon^l \mathbf{u}^l) = f, \quad (3.52)$$

which is the generalized Stokes-Brinkman equations with varied porosity in space. Define the vectors

$$\mathbf{u} = \varepsilon^l \mathbf{u}^l \quad \text{and} \quad \mathbf{f} = \rho \mathbf{g} + \mu \mathbf{k}^{-1} \cdot \varepsilon^l \mathbf{u}^s. \quad (3.53)$$

Substituting equation (3.53) into the equations (3.51) and (3.52), the mathematical models used in a porous domain  $\Omega_p$  can be rewritten as

$$\mu \mathbf{k}^{-1} \cdot \mathbf{u} - \frac{\mu}{\varepsilon^l} \nabla \cdot (2\varepsilon^l \mathbf{d}^l) + \nabla p = \mathbf{f} \quad \text{in } \Omega_p, \quad (3.54)$$

$$\nabla \cdot \mathbf{u} = f \quad \text{in } \Omega_p. \quad (3.55)$$

For the free-fluid domain  $\Omega_f$ , the flow is considered incompressible. Because of no solid phase in this domain, we have no source term  $f$  and no permeability  $\mathbf{k}$  and the porosity  $\varepsilon^l$  becomes one in this domain. Therefore, the system of equations used in the free-fluid region  $\Omega_f$  is

$$-\mu \nabla \cdot (2\mathbf{d}^l) + \nabla p = 0 \quad \text{in } \Omega_f, \quad (3.56)$$

$$\nabla \cdot \mathbf{u} = 0 \quad \text{in } \Omega_f. \quad (3.57)$$

The mathematical model, the generalized Stokes-Brinkman equations, used in this work are now provided. Before we proof the well-posedness of the generalized Stokes-Brinkman equations, we present the weak formulation of these equations in the next section.

### 3.4 Weak formulation of mathematical model

In this section, we present the weak formulation of the generalized Stokes-Brinkman equations in a 2-dimensional domain by using a mixed finite element method. The weak formulation is the lower-order integral equations obtained from multiplying the higher-order differential equation by a weight function, then integrating over the domain and after that applying the Green's identity, which is integration by parts in one dimension, to the integral equation. We begin with the generalized Stokes-Brinkman equations, equations (3.54) and (3.55), in the indicial notation for 2 dimension,

$$\mu k_{ij}^{-1} u_j - \frac{\mu}{\varepsilon^l} \frac{\partial}{\partial x_j} (2\varepsilon^l d_{ij}^l) + \frac{\partial p}{\partial x_i} = f_i, \quad \text{in } \Omega \quad (3.58)$$

$$\frac{\partial u_j}{\partial x_j} = f, \quad \text{in } \Omega \quad (3.59)$$

for  $i, j = 1, 2$ . The index  $i$  indicates the number of equations and the repeated index  $j$  indicates summation. Let  $H^1(\Omega)$  be the Hilbert space and  $L_0^2(\Omega)$  be the Sobolev space

defined in Section 2.1. That is

$$L_0^2(\Omega) = \left\{ q \in L^2(\Omega) : \int_{\Omega} q \, d\Omega = 0 \right\} \text{ and } H_0^1(\Omega) = \left\{ \mathbf{w} \in H^1(\Omega) : \mathbf{w}|_{\partial\Omega} = 0 \right\}. \quad (3.60)$$

We first provide the weak formulation of equation (3.58). To obtain the weak formulation, we multiply equation (3.58) by a weight function  $w_i \in H_0^1(\Omega)$  and then integrate over the domain  $\Omega$  both sides. Therefore, equation (3.58) becomes

$$\int_{\Omega} \mu k_{ij}^{-1} u_j w_i \, d\Omega - \int_{\Omega} \frac{\mu}{\varepsilon^l} \frac{\partial}{\partial x_j} (2\varepsilon^l d_{ij}^l) w_i \, d\Omega + \int_{\Omega} \frac{\partial p}{\partial x_i} w_i \, d\Omega = \int_{\Omega} f_i w_i \, d\Omega. \quad (3.61)$$

Applying the Green's first identity to the second and third terms on the left hand side of equation (3.61), we have

$$\begin{aligned} \int_{\Omega} \mu k_{ij}^{-1} u_j w_i \, d\Omega + \int_{\Omega} 2\mu \varepsilon^l d_{ij}^l \frac{\partial}{\partial x_j} \left( \frac{w_i}{\varepsilon^l} \right) \, d\Omega - \int_{\Omega} \frac{\partial w_i}{\partial x_i} p \, d\Omega \\ = \int_{\Omega} f_i w_i \, d\Omega + \int_{\Gamma} 2\mu d_{ij}^l w_i n_j \, d\Gamma - \int_{\Gamma} p w_i n_i \, d\Gamma, \end{aligned} \quad (3.62)$$

where  $n_i$  is the outward unit normal vector,  $i = 1, 2$ , and  $\Gamma$  is the boundary of the domain. Using the property that the weight function is zero at the boundary, we have

$$\int_{\Omega} \mu k_{ij}^{-1} u_j w_i \, d\Omega + \int_{\Omega} 2\mu \varepsilon^l d_{ij}^l \frac{\partial}{\partial x_j} \left( \frac{w_i}{\varepsilon^l} \right) \, d\Omega - \int_{\Omega} \frac{\partial w_i}{\partial x_i} p \, d\Omega = \int_{\Omega} f_i w_i \, d\Omega. \quad (3.63)$$

Substituting  $d_{ij}^l = 0.5 \left[ \frac{\partial}{\partial x_j} \left( \frac{u_i}{\varepsilon^l} \right) + \frac{\partial}{\partial x_i} \left( \frac{u_j}{\varepsilon^l} \right) \right]$  into equation (3.63) and rearranging the terms, we obtain the weak formulation of equation (3.58), which is

$$\begin{aligned} \int_{\Omega} \mu k_{ij}^{-1} u_j w_i \, d\Omega + \int_{\Omega} \mu \varepsilon^l \frac{\partial}{\partial x_j} \left( \frac{u_i}{\varepsilon^l} \right) \frac{\partial}{\partial x_j} \left( \frac{w_i}{\varepsilon^l} \right) \, d\Omega + \int_{\Omega} \mu \varepsilon^l \frac{\partial}{\partial x_i} \left( \frac{u_j}{\varepsilon^l} \right) \frac{\partial}{\partial x_j} \left( \frac{w_i}{\varepsilon^l} \right) \, d\Omega \\ - \int_{\Omega} \frac{\partial w_i}{\partial x_i} p \, d\Omega = \int_{\Omega} f_i w_i \, d\Omega. \end{aligned} \quad (3.64)$$

The equation (3.64) can be written in the vector form as follows

$$\begin{aligned} \int_{\Omega} \mu (\mathbf{k}^{-1} \cdot \mathbf{u}) \cdot \mathbf{w} \, d\Omega + \int_{\Omega} \mu \varepsilon^l \nabla \left( \frac{\mathbf{u}}{\varepsilon^l} \right) : \nabla \left( \frac{\mathbf{w}}{\varepsilon^l} \right) \, d\Omega + \int_{\Omega} \mu \varepsilon^l \left( \nabla \left( \frac{\mathbf{u}}{\varepsilon^l} \right) \right)^T : \nabla \left( \frac{\mathbf{w}}{\varepsilon^l} \right) \, d\Omega \\ - \int_{\Omega} (\nabla \cdot \mathbf{w}) p \, d\Omega = \int_{\Omega} \mathbf{f} \cdot \mathbf{w} \, d\Omega. \end{aligned} \quad (3.65)$$

To obtain the weak formulation of the continuity equation (3.59), we apply the same process as we have done with the equation (3.58). Multiplying a weight function  $q \in L_0^2(\Omega)$  to equation (3.59) and then integrating the equation over the domain  $\Omega$  both sides, we have

$$\int_{\Omega} \frac{\partial u_j}{\partial x_j} q \, d\Omega = \int_{\Omega} f q \, d\Omega. \quad (3.66)$$

The equation (3.66) can be written in the vector form as follows

$$\int_{\Omega} (\nabla \cdot \mathbf{u}) q \, d\Omega = \int_{\Omega} f q \, d\Omega, \quad (3.67)$$

which is the weak formulation of the continuity equation. We have now derived the weak formulation of the generalized Stokes-Brinkman equations.

In the next section, we use the Lax-Milgram theorem to show that the well-posedness of the generalized Stokes-Brinkman equations.

### 3.5 Well-posedness of generalized Stokes-Brinkman equations

In this section, we show the well-posedness of the generalized Stokes-Brinkman equations using the Lax-Milgram theorem. To present the well-posedness, we begin with the weak formulation of the mathematical model, equations (3.65) and (3.67), which were provided in the previous section. These equations can be expressed in terms of linear and bilinear functionals as follows.

**Problem 3.1.** The weak form of the generalized Stokes-Brinkman equations is to find  $\mathbf{u} \in H_s^1(\Omega)$  and  $p \in L_0^2(\Omega)$  such that

$$a(\mathbf{u}, \mathbf{w}) + b(\mathbf{w}, p) = c_1(\mathbf{w}), \quad \forall \mathbf{w} \in H_0^1(\Omega), \quad (3.68)$$

$$b(\mathbf{u}, q) = c_2(q), \quad \forall q \in L_0^2(\Omega), \quad (3.69)$$

where we define the linear and bilinear functionals as

$$a(\mathbf{u}, \mathbf{w}) = \int_{\Omega} \mu(\mathbf{k}^{-1} \cdot \mathbf{u}) \cdot \mathbf{w} + \int_{\Omega} \mu \varepsilon^l \nabla \left( \frac{\mathbf{u}}{\varepsilon^l} \right) : \nabla \left( \frac{\mathbf{w}}{\varepsilon^l} \right) + \int_{\Omega} \mu \varepsilon^l \left( \nabla \left( \frac{\mathbf{u}}{\varepsilon^l} \right) \right)^T : \nabla \left( \frac{\mathbf{w}}{\varepsilon^l} \right), \quad (3.70)$$

$$b(\mathbf{u}, q) = - \int_{\Omega} (\nabla \cdot \mathbf{u}) q, \quad (3.71)$$

$$c_1(\mathbf{w}) = \langle \mathbf{f}, \mathbf{w} \rangle_{H^{-1}(\Omega) \times H_0^1(\Omega)}, \quad (3.72)$$

$$c_2(q) = - \int_{\Omega} f q, \quad (3.73)$$

the space  $H_s^1(\Omega) = \{\mathbf{w} \in H^1(\Omega) : \mathbf{w}|_{\partial\Omega} = \mathbf{s}\}$  and  $\langle \cdot, \cdot \rangle$  is the duality pairing.

Applying the linear operators in the definition 2.14, the linear and bilinear functionals in Problem 3.1 can be written in the form of a linear operator as in Problem 3.2.

**Problem 3.2.** Let  $A : H_0^1(\Omega) \rightarrow H^{-1}(\Omega)$  and  $B : H_0^1(\Omega) \rightarrow L_0^2(\Omega)$  are linear operators. Find  $\mathbf{u} \in H_s^1(\Omega)$ ,  $p \in L_0^2(\Omega)$  such that

$$A\mathbf{u} + B'p = \mathbf{f} \quad \text{in } H^{-1}(\Omega), \quad (3.74)$$

$$B\mathbf{u} = f \quad \text{in } L_0^2(\Omega), \quad (3.75)$$

where

$$\|\mathbf{f}\|_{H^{-1}(\Omega)} = \sup_{\mathbf{w} \in H_0^1(\Omega), \mathbf{w} \neq 0} \frac{\langle \mathbf{f}, \mathbf{w} \rangle_{H^{-1}(\Omega) \times H_0^1(\Omega)}}{\|\mathbf{w}\|_{H^1(\Omega)}}, \quad (3.76)$$

the norm  $\|\cdot\|_{H^1(\Omega)}$  denotes the standard norm on the space  $H^1(\Omega)$  and the function  $\mathbf{u}^s$  in  $\mathbf{f}$  is a bounded continuous function.

Next, we show that the linear and bilinear functionals in Problem 3.1 are continuous and coercive, that will be used to prove the existence and uniqueness of the generalized Stokes-Brinkman equations in Section 3.5.2.

Forbidden to modify the content, and cite the document when use.

### 3.5.1 Continuity and coercivity

In this section, we show that the linear and bilinear functionals in Problem 3.1 are continuous and coercive. These properties are necessary to prove the existence and uniqueness of the governing equations. We first proof the continuity as shown in Theorem 3.3.

**Theorem 3.3.** *The linear functionals  $c_1(\mathbf{w})$ ,  $c_2(q)$  and bilinear functionals  $a(\cdot, \cdot)$ ,  $b(\cdot, \cdot)$  are continuous. In particular,*

$$c_1(\mathbf{w}) \leq \|\mathbf{f}\|_{H^{-1}(\Omega)} \|\mathbf{w}\|_{H^1(\Omega)}, \quad \forall \mathbf{w} \in H^1(\Omega), \quad (3.77)$$

$$c_2(q) \leq \|f\|_{L^2(\Omega)} \|q\|_{L^2(\Omega)}, \quad \forall q \in L^2(\Omega), \quad (3.78)$$

$$b(\mathbf{u}, q) \leq \sqrt{n} \|\mathbf{u}\|_{H^1(\Omega)} \|q\|_{L^2(\Omega)}, \quad \forall \mathbf{u} \in H^1(\Omega), \forall q \in L^2(\Omega), \quad (3.79)$$

$$a(\mathbf{u}, \mathbf{w}) \leq Q_\alpha \|\mathbf{u}\|_{H^1(\Omega)} \|\mathbf{w}\|_{H^1(\Omega)}, \quad \forall \mathbf{u}, \mathbf{w} \in H^1(\Omega), \quad (3.80)$$

where  $n$  is the dimensional number and

$$Q_\alpha = 2 \max\{\sqrt{6}\mu \max_{1 \leq i, j \leq 2} |k_{ij}^{-1}|, 2\mu / \|\varepsilon^l\|_{H^1(\Omega)}\}.$$

**Proof.** First, we show that  $c_1(\mathbf{w})$  and  $c_2(q)$  are linear. Let  $\mathbf{u}, \mathbf{v} \in H^1(\Omega)$  and  $\alpha, \beta$  are constants, we have

$$\begin{aligned} c_1(\alpha\mathbf{u} + \beta\mathbf{v}) &= \int_{\Omega} \mathbf{f} \cdot (\alpha\mathbf{u} + \beta\mathbf{v}) \, d\Omega \\ &= \int_{\Omega} ((\mathbf{f} \cdot \alpha\mathbf{u}) + (\mathbf{f} \cdot \beta\mathbf{v})) \, d\Omega \\ &= \int_{\Omega} \mathbf{f} \cdot \alpha\mathbf{u} \, d\Omega + \int_{\Omega} \mathbf{f} \cdot \beta\mathbf{v} \, d\Omega \\ &= \alpha \int_{\Omega} \mathbf{f} \cdot \mathbf{u} \, d\Omega + \beta \int_{\Omega} \mathbf{f} \cdot \mathbf{v} \, d\Omega \\ &= \alpha c_1(\mathbf{u}) + \beta c_1(\mathbf{v}). \end{aligned}$$

Hence,  $c_1(\mathbf{w})$  is linear function. For the linearity of  $c_2(q)$ , let  $q_1, q_2 \in L^2(\Omega)$  and  $\alpha, \beta$  are constants, we have

$$\begin{aligned} c_2(\alpha q_1 + \beta q_2) &= - \int_{\Omega} f(\alpha q_1 + \beta q_2) \, d\Omega \\ &= - \int_{\Omega} (f(\alpha q_1) + f(\beta q_2)) \, d\Omega \\ &= - \int_{\Omega} f(\alpha q_1) \, d\Omega - \int_{\Omega} f(\beta q_2) \, d\Omega \\ &= -\alpha \int_{\Omega} f q_1 \, d\Omega - \beta \int_{\Omega} f q_2 \, d\Omega \\ &= \alpha c_2(q_1) + \beta c_2(q_2). \end{aligned}$$

Then,  $c_2(q)$  is a linear function. Next, we show that  $b(\mathbf{u}, q)$  and  $a(\mathbf{u}, \mathbf{w})$  are bilinear

functions. Let  $\mathbf{u}, \mathbf{v}, \mathbf{w} \in H^1(\Omega)$ ,  $q_1, q_2 \in L^2(\Omega)$  and  $\alpha, \beta$  are constants, we have

$$\begin{aligned}
 b(\alpha\mathbf{u} + \beta\mathbf{v}, q_1) &= - \int_{\Omega} (\nabla \cdot (\alpha\mathbf{u} + \beta\mathbf{v})) q_1 d\Omega \\
 &= - \int_{\Omega} (\nabla \cdot (\alpha\mathbf{u}) + \nabla \cdot (\beta\mathbf{v})) q_1 d\Omega \\
 &= - \int_{\Omega} (\nabla \cdot \alpha\mathbf{u}) q_1 d\Omega - \int_{\Omega} (\nabla \cdot \beta\mathbf{v}) q_1 d\Omega \\
 &= -\alpha \int_{\Omega} (\nabla \cdot \mathbf{u}) q_1 d\Omega - \beta \int_{\Omega} (\nabla \cdot \mathbf{v}) q_1 d\Omega \\
 &= \alpha b(\mathbf{u}, q_1) + \beta b(\mathbf{v}, q_1),
 \end{aligned}$$

and

$$\begin{aligned}
 b(\mathbf{u}, \alpha q_1 + \beta q_2) &= - \int_{\Omega} (\nabla \cdot \mathbf{u})(\alpha q_1 + \beta q_2) d\Omega \\
 &= - \int_{\Omega} [(\nabla \cdot \mathbf{u})\alpha q_1 + (\nabla \cdot \mathbf{u})\beta q_2] d\Omega \\
 &= - \int_{\Omega} (\nabla \cdot \mathbf{u})\alpha q_1 d\Omega - \int_{\Omega} (\nabla \cdot \mathbf{u})\beta q_2 d\Omega \\
 &= -\alpha \int_{\Omega} (\nabla \cdot \mathbf{u}) q_1 d\Omega - \beta \int_{\Omega} (\nabla \cdot \mathbf{u}) q_2 d\Omega \\
 &= \alpha b(\mathbf{u}, q_1) + \beta b(\mathbf{u}, q_2).
 \end{aligned}$$

Hence,  $b(\mathbf{u}, q)$  is a bilinear function. For the bilinearity of  $a(\mathbf{u}, \mathbf{w})$  becomes

$$\begin{aligned}
 a(\alpha\mathbf{u} + \beta\mathbf{v}, \mathbf{w}) &= \int_{\Omega} \mu(\mathbf{k}^{-1} \cdot (\alpha\mathbf{u} + \beta\mathbf{v})) \cdot \mathbf{w} d\Omega + \int_{\Omega} \mu \varepsilon^l \nabla \left( \frac{\alpha\mathbf{u} + \beta\mathbf{v}}{\varepsilon^l} \right) : \nabla \left( \frac{\mathbf{w}}{\varepsilon^l} \right) d\Omega \\
 &\quad + \int_{\Omega} \mu \varepsilon^l \left( \nabla \left( \frac{\alpha\mathbf{u} + \beta\mathbf{v}}{\varepsilon^l} \right) \right)^T : \nabla \left( \frac{\mathbf{w}}{\varepsilon^l} \right) d\Omega \\
 &= \int_{\Omega} \mu(\mathbf{k}^{-1} \cdot \alpha\mathbf{u} + \mathbf{k}^{-1} \cdot \beta\mathbf{v}) \cdot \mathbf{w} d\Omega + \int_{\Omega} \mu \varepsilon^l \left[ \nabla \left( \frac{\alpha\mathbf{u}}{\varepsilon^l} \right) + \nabla \left( \frac{\beta\mathbf{v}}{\varepsilon^l} \right) \right] : \nabla \left( \frac{\mathbf{w}}{\varepsilon^l} \right) d\Omega \\
 &\quad + \int_{\Omega} \mu \varepsilon^l \left[ \nabla \left( \frac{\alpha\mathbf{u}}{\varepsilon^l} \right) + \nabla \left( \frac{\beta\mathbf{v}}{\varepsilon^l} \right) \right]^T : \nabla \left( \frac{\mathbf{w}}{\varepsilon^l} \right) d\Omega \\
 &= \int_{\Omega} \mu(\mathbf{k}^{-1} \cdot \alpha\mathbf{u}) \cdot \mathbf{w} d\Omega + \int_{\Omega} \mu(\mathbf{k}^{-1} \cdot \beta\mathbf{v}) \cdot \mathbf{w} d\Omega + \int_{\Omega} \mu \varepsilon^l \nabla \left( \frac{\alpha\mathbf{u}}{\varepsilon^l} \right) : \nabla \left( \frac{\mathbf{w}}{\varepsilon^l} \right) d\Omega \\
 &\quad + \int_{\Omega} \mu \varepsilon^l \nabla \left( \frac{\beta\mathbf{v}}{\varepsilon^l} \right) : \nabla \left( \frac{\mathbf{w}}{\varepsilon^l} \right) d\Omega + \int_{\Omega} \mu \varepsilon^l \left( \nabla \left( \frac{\alpha\mathbf{u}}{\varepsilon^l} \right) \right)^T : \nabla \left( \frac{\mathbf{w}}{\varepsilon^l} \right) d\Omega \\
 &\quad + \int_{\Omega} \mu \varepsilon^l \left( \nabla \left( \frac{\beta\mathbf{v}}{\varepsilon^l} \right) \right)^T : \nabla \left( \frac{\mathbf{w}}{\varepsilon^l} \right) d\Omega \\
 &= \alpha \int_{\Omega} \mu(\mathbf{k}^{-1} \cdot \mathbf{u}) \cdot \mathbf{w} d\Omega + \beta \int_{\Omega} \mu(\mathbf{k}^{-1} \cdot \mathbf{v}) \cdot \mathbf{w} d\Omega + \alpha \int_{\Omega} \mu \varepsilon^l \nabla \left( \frac{\mathbf{u}}{\varepsilon^l} \right) : \nabla \left( \frac{\mathbf{w}}{\varepsilon^l} \right) d\Omega \\
 &\quad + \beta \int_{\Omega} \mu \varepsilon^l \nabla \left( \frac{\mathbf{v}}{\varepsilon^l} \right) : \nabla \left( \frac{\mathbf{w}}{\varepsilon^l} \right) d\Omega + \alpha \int_{\Omega} \mu \varepsilon^l \left( \nabla \left( \frac{\mathbf{u}}{\varepsilon^l} \right) \right)^T : \nabla \left( \frac{\mathbf{w}}{\varepsilon^l} \right) d\Omega \\
 &\quad + \beta \int_{\Omega} \mu \varepsilon^l \left( \nabla \left( \frac{\mathbf{v}}{\varepsilon^l} \right) \right)^T : \nabla \left( \frac{\mathbf{w}}{\varepsilon^l} \right) d\Omega \\
 &= \alpha \left[ \int_{\Omega} \mu(\mathbf{k}^{-1} \cdot \mathbf{u}) \cdot \mathbf{w} d\Omega + \int_{\Omega} \mu \varepsilon^l \nabla \left( \frac{\mathbf{u}}{\varepsilon^l} \right) : \nabla \left( \frac{\mathbf{w}}{\varepsilon^l} \right) d\Omega \right. \\
 &\quad \left. + \int_{\Omega} \mu \varepsilon^l \left( \nabla \left( \frac{\mathbf{u}}{\varepsilon^l} \right) \right)^T : \nabla \left( \frac{\mathbf{w}}{\varepsilon^l} \right) d\Omega \right] + \beta \left[ \int_{\Omega} \mu(\mathbf{k}^{-1} \cdot \mathbf{v}) \cdot \mathbf{w} d\Omega \right. \\
 &\quad \left. + \int_{\Omega} \mu \varepsilon^l \nabla \left( \frac{\mathbf{v}}{\varepsilon^l} \right) : \nabla \left( \frac{\mathbf{w}}{\varepsilon^l} \right) d\Omega + \int_{\Omega} \mu \varepsilon^l \left( \nabla \left( \frac{\mathbf{v}}{\varepsilon^l} \right) \right)^T : \nabla \left( \frac{\mathbf{w}}{\varepsilon^l} \right) d\Omega \right] \\
 &= \alpha a(\mathbf{u}, \mathbf{w}) + \beta a(\mathbf{v}, \mathbf{w}),
 \end{aligned}$$

This material is reserved for educational use only, not allowed for commercial use.

Forbidden to modify the content, and cite the document when use.

and

$$\begin{aligned}
a(\mathbf{u}, \alpha\mathbf{v} + \beta\mathbf{w}) &= \int_{\Omega} \mu(\mathbf{k}^{-1} \cdot \mathbf{u}) \cdot (\alpha\mathbf{v} + \beta\mathbf{w}) d\Omega + \int_{\Omega} \mu\varepsilon^l \nabla \left( \frac{\mathbf{u}}{\varepsilon^l} \right) : \nabla \left( \frac{\alpha\mathbf{v} + \beta\mathbf{w}}{\varepsilon^l} \right) d\Omega \\
&\quad + \int_{\Omega} \mu\varepsilon^l \left( \nabla \left( \frac{\mathbf{u}}{\varepsilon^l} \right) \right)^T : \nabla \left( \frac{\alpha\mathbf{v} + \beta\mathbf{w}}{\varepsilon^l} \right) d\Omega \\
&= \int_{\Omega} [\mu(\mathbf{k}^{-1} \cdot \mathbf{u}) \cdot \alpha\mathbf{v} + \mu(\mathbf{k}^{-1} \cdot \mathbf{u}) \cdot \beta\mathbf{w}] d\Omega \\
&\quad + \int_{\Omega} \mu\varepsilon^l \nabla \left( \frac{\mathbf{u}}{\varepsilon^l} \right) : \left[ \nabla \left( \frac{\alpha\mathbf{v}}{\varepsilon^l} \right) + \nabla \left( \frac{\beta\mathbf{w}}{\varepsilon^l} \right) \right] d\Omega \\
&\quad + \int_{\Omega} \mu\varepsilon^l \left( \nabla \left( \frac{\mathbf{u}}{\varepsilon^l} \right) \right)^T : \left[ \nabla \left( \frac{\alpha\mathbf{v}}{\varepsilon^l} \right) + \nabla \left( \frac{\beta\mathbf{w}}{\varepsilon^l} \right) \right] d\Omega \\
&= \int_{\Omega} \mu(\mathbf{k}^{-1} \cdot \mathbf{u}) \cdot \alpha\mathbf{v} d\Omega + \int_{\Omega} \mu(\mathbf{k}^{-1} \cdot \mathbf{u}) \cdot \beta\mathbf{w} d\Omega + \int_{\Omega} \mu\varepsilon^l \nabla \left( \frac{\mathbf{u}}{\varepsilon^l} \right) : \nabla \left( \frac{\alpha\mathbf{v}}{\varepsilon^l} \right) d\Omega \\
&\quad + \int_{\Omega} \mu\varepsilon^l \nabla \left( \frac{\mathbf{u}}{\varepsilon^l} \right) : \nabla \left( \frac{\beta\mathbf{w}}{\varepsilon^l} \right) d\Omega + \int_{\Omega} \mu\varepsilon^l \left( \nabla \left( \frac{\mathbf{u}}{\varepsilon^l} \right) \right)^T : \nabla \left( \frac{\alpha\mathbf{v}}{\varepsilon^l} \right) d\Omega \\
&\quad + \int_{\Omega} \mu\varepsilon^l \left( \nabla \left( \frac{\mathbf{u}}{\varepsilon^l} \right) \right)^T : \nabla \left( \frac{\beta\mathbf{w}}{\varepsilon^l} \right) d\Omega \\
&= \alpha \int_{\Omega} \mu(\mathbf{k}^{-1} \cdot \mathbf{u}) \cdot \mathbf{v} d\Omega + \beta \int_{\Omega} \mu(\mathbf{k}^{-1} \cdot \mathbf{u}) \cdot \mathbf{w} d\Omega + \alpha \int_{\Omega} \mu\varepsilon^l \nabla \left( \frac{\mathbf{u}}{\varepsilon^l} \right) : \nabla \left( \frac{\mathbf{v}}{\varepsilon^l} \right) d\Omega \\
&\quad + \beta \int_{\Omega} \mu\varepsilon^l \nabla \left( \frac{\mathbf{u}}{\varepsilon^l} \right) : \nabla \left( \frac{\mathbf{w}}{\varepsilon^l} \right) d\Omega + \alpha \int_{\Omega} \mu\varepsilon^l \left( \nabla \left( \frac{\mathbf{u}}{\varepsilon^l} \right) \right)^T : \nabla \left( \frac{\mathbf{v}}{\varepsilon^l} \right) d\Omega \\
&\quad + \beta \int_{\Omega} \mu\varepsilon^l \left( \nabla \left( \frac{\mathbf{u}}{\varepsilon^l} \right) \right)^T : \nabla \left( \frac{\mathbf{w}}{\varepsilon^l} \right) d\Omega \\
&= \alpha \left[ \int_{\Omega} \mu(\mathbf{k}^{-1} \cdot \mathbf{u}) \cdot \mathbf{v} d\Omega + \int_{\Omega} \mu\varepsilon^l \nabla \left( \frac{\mathbf{u}}{\varepsilon^l} \right) : \nabla \left( \frac{\mathbf{v}}{\varepsilon^l} \right) d\Omega \right. \\
&\quad \left. + \int_{\Omega} \mu\varepsilon^l \left( \nabla \left( \frac{\mathbf{u}}{\varepsilon^l} \right) \right)^T : \nabla \left( \frac{\mathbf{v}}{\varepsilon^l} \right) d\Omega \right] + \beta \left[ \int_{\Omega} \mu(\mathbf{k}^{-1} \cdot \mathbf{u}) \cdot \mathbf{w} d\Omega \right. \\
&\quad \left. + \int_{\Omega} \mu\varepsilon^l \nabla \left( \frac{\mathbf{u}}{\varepsilon^l} \right) : \nabla \left( \frac{\mathbf{w}}{\varepsilon^l} \right) d\Omega + \int_{\Omega} \mu\varepsilon^l \left( \nabla \left( \frac{\mathbf{u}}{\varepsilon^l} \right) \right)^T : \nabla \left( \frac{\mathbf{w}}{\varepsilon^l} \right) d\Omega \right] \\
&= \alpha a(\mathbf{u}, \mathbf{v}) + \beta a(\mathbf{u}, \mathbf{w}).
\end{aligned}$$

Hence,  $a(\mathbf{u}, \mathbf{w})$  is a bilinear function.

Next, we show the continuity of them. Let  $\mathbf{u}, \mathbf{w} \in H^1(\Omega)$  and  $q \in L^2(\Omega)$ . We first show the continuity of  $c_1(\mathbf{w})$ , then

$$\begin{aligned}
|c_1(\mathbf{w})| &= \left| \langle \mathbf{f}, \mathbf{w} \rangle_{H^{-1}(\Omega) \times H_0^1(\Omega)} \right| \\
&= \left| \frac{\langle \mathbf{f}, \mathbf{w} \rangle_{H^{-1}(\Omega) \times H_0^1(\Omega)}}{\|\mathbf{w}\|_{H^1(\Omega)}} \|\mathbf{w}\|_{H^1(\Omega)} \right| \\
&\leq \left| \sup_{\mathbf{w} \in H_0^1(\Omega), \mathbf{w} \neq 0} \frac{\langle \mathbf{f}, \mathbf{w} \rangle_{H^{-1}(\Omega) \times H_0^1(\Omega)}}{\|\mathbf{w}\|_{H^1(\Omega)}} \|\mathbf{w}\|_{H^1(\Omega)} \right| \\
&= \|\mathbf{f}\|_{H^{-1}(\Omega)} \|\mathbf{w}\|_{H^1(\Omega)},
\end{aligned}$$

where we apply the definition of norm on the space  $H^{-1}(\Omega)$ , equation (3.76), at the inequality. For the continuity of  $c_2(q)$ , we have

$$\begin{aligned}
|c_2(q)| &= \left| - \int_{\Omega} fg \, d\Omega \right| \\
&= \left| \int_{\Omega} fg \, d\Omega \right|
\end{aligned}$$

This material is reserved for educational use only, not allowed for commercial use.

Forbidden to modify the content, and cite the document when use.

where we apply Cauchy-Schwarz's inequality, Theorem 2.17, at inequality. For the continuity of  $b(\mathbf{u}, q)$ , we have

$$\begin{aligned} |b(\mathbf{u}, q)| &= \left| - \int_{\Omega} (\nabla \cdot \mathbf{u}) q \, d\Omega \right| \\ &= \left| \int_{\Omega} (\nabla \cdot \mathbf{u}) q \, d\Omega \right| \\ &\leq \|\nabla \cdot \mathbf{u}\|_{L^2(\Omega)} \|q\|_{L^2(\Omega)} \\ &\leq \sqrt{n} \|\mathbf{u}\|_{H^1(\Omega)} \|q\|_{L^2(\Omega)}, \end{aligned}$$

where we apply Cauchy-Schwarz's inequality, Theorem 2.17, for the first inequality and use the fact that  $\|\nabla \cdot \mathbf{u}\|_{L^2(\Omega)} \leq \sqrt{n} \|\mathbf{u}\|_{H^1(\Omega)}$  provided in [9] for the last inequality.

To prove the continuity of  $a(\mathbf{u}, \mathbf{w})$  in a two-dimensional domain, let  $\mathbf{u} = (u_1, u_2)$  and  $\mathbf{w} = (w_1, w_2)$ , we first consider

$$\begin{aligned} \|\mathbf{k}^{-1} \cdot \mathbf{u}\|_{L^2(\Omega)}^2 &= \int_{\Omega} (k_{ij}^{-1} u_j)^2 \, d\Omega \\ &= \int_{\Omega} (k_{11}^{-1} u_1 + k_{12}^{-1} u_2)^2 \, d\Omega + \int_{\Omega} (k_{21}^{-1} u_1 + k_{22}^{-1} u_2)^2 \, d\Omega \\ &\leq \int_{\Omega} [(k_{11}^{-1} u_1)^2 + |2k_{11}^{-1} k_{12}^{-1} u_1 u_2| + (k_{12}^{-1} u_2)^2 \\ &\quad + (k_{21}^{-1} u_1)^2 + |2k_{21}^{-1} k_{22}^{-1} u_1 u_2| + (k_{22}^{-1} u_2)^2] \, d\Omega \\ &\leq 2 \max_{1 \leq i, j \leq 2} |k_{ij}^{-1}|^2 \int_{\Omega} (2u_1^2 + 2u_2^2 + 2|u_1 u_2|) \, d\Omega \\ &= 4 \max_{1 \leq i, j \leq 2} |k_{ij}^{-1}|^2 \int_{\Omega} (u_1^2 + u_2^2 + |u_1 u_2|) \, d\Omega \\ &\leq 4 \max_{1 \leq i, j \leq 2} |k_{ij}^{-1}|^2 \int_{\Omega} (u_1^2 + u_2^2 + \frac{|u_1|^2}{2} + \frac{|u_2|^2}{2}) \, d\Omega \\ &= 4 \max_{1 \leq i, j \leq 2} |k_{ij}^{-1}|^2 \int_{\Omega} (\frac{3u_1^2}{2} + \frac{3u_2^2}{2}) \, d\Omega \\ &= 6 \max_{1 \leq i, j \leq 2} |k_{ij}^{-1}|^2 \int_{\Omega} (u_1^2 + u_2^2) \, d\Omega \\ &= 6 \max_{1 \leq i, j \leq 2} |k_{ij}^{-1}|^2 \|\mathbf{u}\|_{L^2(\Omega)}^2, \end{aligned}$$

where Young's inequality  $ab \leq \frac{a^p}{p} + \frac{b^q}{q}$  where  $a, b \geq 0, p, q > 0$  and  $\frac{1}{p} + \frac{1}{q} = 1$  is applied at the third inequality. Therefore,

$$\|\mathbf{k}^{-1} \cdot \mathbf{u}\|_{L^2(\Omega)} \leq \sqrt{6} \max_{1 \leq i, j \leq 2} |k_{ij}^{-1}| \|\mathbf{u}\|_{L^2(\Omega)}. \quad (3.81)$$

Next, we employ the inequality 3.81 to complete the proof of the continuity of  $a(\mathbf{u}, \mathbf{w})$ . Then, from equation (3.70), we have

$$\begin{aligned} |a(\mathbf{u}, \mathbf{w})| &= \left| \int_{\Omega} \mu(\mathbf{k}^{-1} \cdot \mathbf{u}) \cdot \mathbf{w} + \int_{\Omega} \mu \varepsilon^l \nabla \left( \frac{\mathbf{u}}{\varepsilon^l} \right) : \nabla \left( \frac{\mathbf{w}}{\varepsilon^l} \right) + \int_{\Omega} \mu \varepsilon^l \left( \nabla \left( \frac{\mathbf{u}}{\varepsilon^l} \right) \right)^T : \nabla \left( \frac{\mathbf{w}}{\varepsilon^l} \right) \right| \\ &\leq \left| \int_{\Omega} \mu(\mathbf{k}^{-1} \cdot \mathbf{u}) \cdot \mathbf{w} \right| + \left| \int_{\Omega} \mu \varepsilon^l \nabla \left( \frac{\mathbf{u}}{\varepsilon^l} \right) : \nabla \left( \frac{\mathbf{w}}{\varepsilon^l} \right) \right| + \left| \int_{\Omega} \mu \varepsilon^l \left( \nabla \left( \frac{\mathbf{u}}{\varepsilon^l} \right) \right)^T : \nabla \left( \frac{\mathbf{w}}{\varepsilon^l} \right) \right| \\ &\leq \mu \|\mathbf{k}^{-1} \cdot \mathbf{u}\|_{L^2(\Omega)} \|\mathbf{w}\|_{L^2(\Omega)} + \mu \left\| \varepsilon^l \nabla \left( \frac{\mathbf{u}}{\varepsilon^l} \right) \right\|_{L^2(\Omega)} \left\| \nabla \left( \frac{\mathbf{w}}{\varepsilon^l} \right) \right\|_{L^2(\Omega)} \\ &\quad + \mu \left\| \varepsilon^l \left( \nabla \left( \frac{\mathbf{u}}{\varepsilon^l} \right) \right)^T \right\|_{L^2(\Omega)} \left\| \nabla \left( \frac{\mathbf{w}}{\varepsilon^l} \right) \right\|_{L^2(\Omega)} \end{aligned}$$

This material is not allowed for commercial use.

Forbidden to modify the content, and cite the document when use.

$$\begin{aligned}
&\leq \sqrt{6}\mu \max_{1 \leq i, j \leq 2} |k_{ij}^{-1}| \|\mathbf{u}\|_{L^2(\Omega)} \|\mathbf{w}\|_{L^2(\Omega)} + \mu \|\varepsilon^l\|_{L^2(\Omega)} \left\| \nabla \left( \frac{\mathbf{u}}{\varepsilon^l} \right) \right\|_{L^2(\Omega)} \left\| \nabla \left( \frac{\mathbf{w}}{\varepsilon^l} \right) \right\|_{L^2(\Omega)} \\
&\quad + \mu \|\varepsilon^l\|_{L^2(\Omega)} \left\| \left( \nabla \left( \frac{\mathbf{u}}{\varepsilon^l} \right) \right)^T \right\|_{L^2(\Omega)} \left\| \nabla \left( \frac{\mathbf{w}}{\varepsilon^l} \right) \right\|_{L^2(\Omega)} \\
&= \sqrt{6}\mu \max_{1 \leq i, j \leq 2} |k_{ij}^{-1}| \|\mathbf{u}\|_{L^2(\Omega)} \|\mathbf{w}\|_{L^2(\Omega)} + \mu \|\varepsilon^l\|_{L^2(\Omega)} \left\| \nabla \left( \frac{\mathbf{u}}{\varepsilon^l} \right) \right\|_{L^2(\Omega)} \left\| \nabla \left( \frac{\mathbf{w}}{\varepsilon^l} \right) \right\|_{L^2(\Omega)} \\
&\quad + \mu \|\varepsilon^l\|_{L^2(\Omega)} \left\| \nabla \left( \frac{\mathbf{u}}{\varepsilon^l} \right) \right\|_{L^2(\Omega)} \left\| \nabla \left( \frac{\mathbf{w}}{\varepsilon^l} \right) \right\|_{L^2(\Omega)} \\
&= \sqrt{6}\mu \max_{1 \leq i, j \leq 2} |k_{ij}^{-1}| \|\mathbf{u}\|_{L^2(\Omega)} \|\mathbf{w}\|_{L^2(\Omega)} + 2\mu \|\varepsilon^l\|_{L^2(\Omega)} \left\| \nabla \left( \frac{\mathbf{u}}{\varepsilon^l} \right) \right\|_{L^2(\Omega)} \left\| \nabla \left( \frac{\mathbf{w}}{\varepsilon^l} \right) \right\|_{L^2(\Omega)} \\
&\leq \sqrt{6}\mu \max_{1 \leq i, j \leq 2} |k_{ij}^{-1}| \|\mathbf{u}\|_{H^1(\Omega)} \|\mathbf{w}\|_{H^1(\Omega)} + 2\mu \|\varepsilon^l\|_{L^2(\Omega)} \left\| \frac{\mathbf{u}}{\varepsilon^l} \right\|_{H^1(\Omega)} \left\| \frac{\mathbf{w}}{\varepsilon^l} \right\|_{H^1(\Omega)} \\
&\leq \sqrt{6}\mu \max_{1 \leq i, j \leq 2} |k_{ij}^{-1}| \|\mathbf{u}\|_{H^1(\Omega)} \|\mathbf{w}\|_{H^1(\Omega)} + 2\mu \|\varepsilon^l\|_{L^2(\Omega)} \frac{\|\mathbf{u}\|_{H^1(\Omega)}}{\|\varepsilon^l\|_{H^1(\Omega)}} \frac{\|\mathbf{w}\|_{H^1(\Omega)}}{\|\varepsilon^l\|_{H^1(\Omega)}} \\
&\leq \sqrt{6}\mu \max_{1 \leq i, j \leq 2} |k_{ij}^{-1}| \|\mathbf{u}\|_{H^1(\Omega)} \|\mathbf{w}\|_{H^1(\Omega)} + \frac{2\mu}{\|\varepsilon^l\|_{H^1(\Omega)}} \|\mathbf{u}\|_{H^1(\Omega)} \|\mathbf{w}\|_{H^1(\Omega)} \\
&\leq 2 \max \left\{ \sqrt{6}\mu \max_{1 \leq i, j \leq 2} |k_{ij}^{-1}|, \frac{2\mu}{\|\varepsilon^l\|_{H^1(\Omega)}} \right\} \|\mathbf{u}\|_{H^1(\Omega)} \|\mathbf{w}\|_{H^1(\Omega)} \\
&= Q_a \|\mathbf{u}\|_{H^1(\Omega)} \|\mathbf{w}\|_{H^1(\Omega)},
\end{aligned}$$

where  $Q_a = 2 \max \left\{ \sqrt{6}\mu \max_{1 \leq i, j \leq 2} |k_{ij}^{-1}|, \frac{2\mu}{\|\varepsilon^l\|_{H^1(\Omega)}} \right\}$ . We apply the triangular inequality for the first inequality, and apply the Cauchy-Schwarz's inequality, Theorem 2.17, for each term in the second inequality. The inequality given in equation (3.81) [43] is applied to the first term of the third inequality and the Hölder's inequality, Theorem 2.16, is applied to the second and third terms of the third inequality. For the second equation, we use the fact that  $\|\nabla u\| = \|(\nabla u)^T\|$  and rearranging the terms. We apply the inequality:

$$\|u\|_{L^2(\Omega)} \leq \|u\|_{H^1(\Omega)} \quad \text{and} \quad \|\nabla u\|_{L^2(\Omega)} \leq \|u\|_{H^1(\Omega)}, \quad (3.82)$$

for the fourth inequality. For the sixth inequality, we use the fact that  $\|\cdot\|_{L^2(\Omega)} \leq \|\cdot\|_{H^1(\Omega)}$  so  $\frac{\|\cdot\|_{L^2(\Omega)}}{\|\cdot\|_{H^1(\Omega)}} \leq 1$ . Therefore,  $a(\mathbf{u}, \mathbf{w})$  is continuous.  $\square$

To show that the bilinear form  $a(\cdot, \cdot)$  is coercive, we begin by examining the term  $(\mathbf{k}^{-1} \cdot \mathbf{w}) \cdot \mathbf{w}$  for 2-dimensions, which is provided in [9]. Let  $\mathbf{w} = (w_1, w_2)$ , we have

$$\begin{aligned}
(\mathbf{k}^{-1} \cdot \mathbf{w}) \cdot \mathbf{w} &= k_{ij}^{-1} w_j w_i \\
&= k_{11}^{-1} w_1^2 + k_{12}^{-1} w_2 w_1 + k_{21}^{-1} w_1 w_2 + k_{22}^{-1} w_2^2 \\
&= k_{11}^{-1} w_1^2 + k_{22}^{-1} w_2^2 + 2k_{12}^{-1} w_1 w_2,
\end{aligned}$$

where  $\mathbf{k}^{-1}$  is symmetric. Note that  $(\mathbf{k}^{-1} \cdot \mathbf{w}) \cdot \mathbf{w} = \mathbf{w}^T \mathbf{k}^{-1} \mathbf{w}$  as matrix multiplication where  $T$  is the transpose. Since in our problem  $\mathbf{k}^{-1}$  is a positive definite matrix and its diagonal entries are positive numbers. Then the terms  $k_{11}^{-1} w_1^2 + k_{22}^{-1} w_2^2 > 0$  where  $\mathbf{w} > 0$ .

We now focus on the term  $2k_{12}^2 w_1 w_2$ . If  $2k_{12}^2 w_1 w_2 \geq 0$ , it's easy to see that

$$\begin{aligned}
 (\mathbf{k}^{-1} \cdot \mathbf{w}) \cdot \mathbf{w} &= k_{11}^{-1} w_1^2 + k_{22}^{-1} w_2^2 + 2k_{12}^{-1} w_1 w_2 \\
 &\geq k_{11}^{-1} w_1^2 + k_{22}^{-1} w_2^2 \\
 &\geq \min \{k_{11}^{-1}, k_{22}^{-1}\} (w_1^2 + w_2^2) \\
 &= Q_k (w_1^2 + w_2^2),
 \end{aligned}$$

where  $Q_k = \min \{k_{11}^{-1}, k_{22}^{-1}\} > 0$ . If  $2k_{12}^2 w_1 w_2 < 0$ , the analysis can be divided into two distinct cases:

Case 1:  $k_{12}^{-1} > 0$  and  $w_1 w_2 < 0$ .

We have

$$\begin{aligned}
 (\mathbf{k}^{-1} \cdot \mathbf{w}) \cdot \mathbf{w} &= k_{11}^{-1} w_1^2 + k_{22}^{-1} w_2^2 - 2k_{12}^{-1} w_1 w_2 \\
 &= k_{11}^{-1} w_1^2 + k_{22}^{-1} w_2^2 - 2k_{12}^{-1} |w_1 w_2| \\
 &= k_{11}^{-1} w_1^2 + k_{22}^{-1} w_2^2 - 2k_{12}^{-1} |w_1| |w_2| \\
 &\geq k_{11}^{-1} w_1^2 + k_{22}^{-1} w_2^2 - 2k_{12}^{-1} \left( \frac{|w_1|^2}{2} + \frac{|w_2|^2}{2} \right) \\
 &= k_{11}^{-1} w_1^2 + k_{22}^{-1} w_2^2 - k_{12}^{-1} (|w_1|^2 + |w_2|^2) \\
 &= (k_{11}^{-1} - k_{12}^{-1}) w_1^2 + (k_{22}^{-1} - k_{12}^{-1}) w_2^2 \\
 &\geq \min \{ (k_{11}^{-1} - k_{12}^{-1}), (k_{22}^{-1} - k_{12}^{-1}) \} (w_1^2 + w_2^2) \\
 &= Q_k (w_1^2 + w_2^2),
 \end{aligned}$$

where  $Q_k = \min \{ (k_{11}^{-1} - k_{12}^{-1}), (k_{22}^{-1} - k_{12}^{-1}) \} > 0$  because  $\mathbf{k}^{-1}$  is diagonally dominant and we apply Young's inequality:  $ab < \frac{a^2}{2} + \frac{b^2}{2}$  where  $a, b > 0$  at the first inequality. Therefore,  $(\mathbf{k}^{-1} \cdot \mathbf{w}) \cdot \mathbf{w} > Q_k (w_1^2 + w_2^2)$ .

Case 2:  $k_{12}^{-1} < 0$  and  $w_1 w_2 > 0$ .

Since  $\mathbf{k}^{-1}$  is bounded,  $\exists Q_b > 0$  such that  $k_{12}^{-1} = -Q_b$ .

Thus,

$$\begin{aligned}
 (\mathbf{k}^{-1} \cdot \mathbf{w}) \cdot \mathbf{w} &= k_{11}^{-1} w_1^2 + k_{22}^{-1} w_2^2 - 2Q_b w_1 w_2 \\
 &= k_{11}^{-1} w_1^2 + k_{22}^{-1} w_2^2 - 2Q_b |w_1 w_2| \\
 &= k_{11}^{-1} w_1^2 + k_{22}^{-1} w_2^2 - 2Q_b |w_1| |w_2| \\
 &\geq k_{11}^{-1} w_1^2 + k_{22}^{-1} w_2^2 - 2Q_b \left( \frac{|w_1|^2}{2} + \frac{|w_2|^2}{2} \right) \\
 &= k_{11}^{-1} w_1^2 + k_{22}^{-1} w_2^2 - Q_b (|w_1|^2 + |w_2|^2) \\
 &= (k_{11}^{-1} - Q_b) w_1^2 + (k_{22}^{-1} - Q_b) w_2^2 \\
 &\geq \min \{ (k_{11}^{-1} - Q_b), (k_{22}^{-1} - Q_b) \} (w_1^2 + w_2^2) \\
 &= Q_k (w_1^2 + w_2^2),
 \end{aligned}$$

where  $Q_k = \min \{ (k_{11}^{-1} - Q_b), (k_{22}^{-1} - Q_b) \} > 0$  because  $Q_b$  is less than the diagonal entries of  $\mathbf{k}^{-1}$ . The Young's inequality is applied at the first inequality.

Therefore,  $(\mathbf{k}^{-1} \cdot \mathbf{w}) \cdot \mathbf{w} > Q_k (w_1^2 + w_2^2)$ .

From all of cases above, we have

$$\exists Q_k > 0, \quad (\mathbf{k}^{-1} \cdot \mathbf{w}) \cdot \mathbf{w} > Q_k (w_1^2 + w_2^2). \quad (3.83)$$

Integrating both sides, we obtain

$$\begin{aligned} \int_{\Omega} (\mathbf{k}^{-1} \cdot \mathbf{w}) \cdot \mathbf{w} \, d\Omega &\geq Q_k \int_{\Omega} (w_1^2 + w_2^2) \, d\Omega \\ &= Q_k \int_{\Omega} \mathbf{w}^2 \, d\Omega \\ &= Q_k \|\mathbf{W}\|_{L^2(\Omega)}^2. \end{aligned} \quad (3.84)$$

Next, we provide the proofs of Lemma 3.4 and 3.5, which will be used in the proof of coercivity given in Theorem 3.6.

**Lemma 3.4.** Let  $\varepsilon^l : \mathbb{R} \rightarrow (0, 1]$  be a real-valued function. Suppose there exist  $m, M > 0$  such that for all  $x \in \mathbb{R}$ ,

$$m \leq \varepsilon^l(x) \leq M. \quad (3.85)$$

Then there exists  $h \in \mathbb{N}$  such that for all  $x \in \mathbb{R}$ , we have

$$\varepsilon^l(x) \geq \frac{1}{h}. \quad (3.86)$$

**Proof.** Let  $\varepsilon^l : \mathbb{R} \rightarrow (0, 1]$  be a real-valued function and  $0 < \varepsilon^l \leq 1$ . Since  $m, M > 0$  such that

$$0 < m \leq \varepsilon^l(x) \leq M \leq 1, \quad (3.87)$$

for all  $x \in \mathbb{R}$ , by Archimedean property, there exists  $h \in \mathbb{N}$  such that

$$\frac{1}{h} \leq m \leq \varepsilon^l(x) \quad (3.88)$$

for all  $x \in \mathbb{R}$ . Hence,  $\varepsilon^l(x) \geq \frac{1}{h}$  for all  $x \in \mathbb{R}$ .  $\square$

**Lemma 3.5.** Let  $\mathbf{w} \in H^1(\Omega)$ . Then

$$\int_{\Omega} \mu \varepsilon^l \nabla \mathbf{W} : \nabla \mathbf{W} \, d\Omega + \int_{\Omega} \mu \varepsilon^l (\nabla \mathbf{W})^T : \nabla \mathbf{W} \, d\Omega \geq \frac{\mu \sqrt{|\mathbf{V}|}}{2h^2} \|\nabla \mathbf{W} + (\nabla \mathbf{W})^T\|_{L^2(\Omega)}^2, \quad (3.89)$$

for some natural number  $h$ .

**Proof.** Let  $\mathbf{W} \in H^1(\Omega)$ . Then

$$\begin{aligned} \int_{\Omega} \mu \varepsilon^l \nabla \mathbf{W} : \nabla \mathbf{W} \, d\Omega + \int_{\Omega} \mu \varepsilon^l (\nabla \mathbf{W})^T : \nabla \mathbf{W} \, d\Omega &= \int_{\Omega} \mu \varepsilon^l [\nabla \mathbf{W} : \nabla \mathbf{W} + (\nabla \mathbf{W})^T : \nabla \mathbf{W}] \, d\Omega \\ &= \mu \int_{\Omega} \varepsilon^l [\nabla \mathbf{W} + (\nabla \mathbf{W})^T] : \nabla \mathbf{W} \, d\Omega \\ &= 2\mu \int_{\Omega} \varepsilon^l \frac{1}{2} [\nabla \mathbf{W} + (\nabla \mathbf{W})^T] : \nabla \mathbf{W} \, d\Omega \\ &= 2\mu \int_{\Omega} \varepsilon^l \mathbf{D} : \nabla \mathbf{W} \, d\Omega \\ &= 2\mu \int_{\Omega} \varepsilon^l D_{ij} \frac{\partial W_i}{\partial x_j} \, d\Omega \end{aligned}$$

$$\begin{aligned}
&= 2\mu \int_{\Omega} \varepsilon^l \left( D_{11} \frac{\partial W_1}{\partial x_1} + D_{12} \frac{\partial W_1}{\partial x_2} + D_{21} \frac{\partial W_2}{\partial x_1} + D_{22} \frac{\partial W_2}{\partial x_2} \right) d\Omega \\
&= 2\mu \int_{\Omega} \varepsilon^l \left( D_{11}^2 + D_{12} \left( \frac{\partial W_1}{\partial x_2} + \frac{\partial W_2}{\partial x_1} \right) + D_{22}^2 \right) d\Omega \\
&= 2\mu \int_{\Omega} \varepsilon^l \left( D_{11}^2 + 2D_{12} \frac{1}{2} \left( \frac{\partial W_1}{\partial x_2} + \frac{\partial W_2}{\partial x_1} \right) + D_{22}^2 \right) d\Omega \\
&= 2\mu \int_{\Omega} \varepsilon^l (D_{11}^2 + 2D_{12}^2 + D_{22}^2) d\Omega \\
&= 2\mu \int_{\Omega} \varepsilon^l (D_{11}^2 + D_{12}^2 + D_{21}^2 + D_{22}^2) d\Omega \\
&\geq 2\mu \int_{\Omega} (\varepsilon^l)^2 (D_{11}^2 + D_{12}^2 + D_{21}^2 + D_{22}^2) d\Omega \\
&= 2\mu \left( \int_{\Omega} (\varepsilon^l D_{11})^2 d\Omega + \int_{\Omega} (\varepsilon^l D_{12})^2 d\Omega + \int_{\Omega} (\varepsilon^l D_{21})^2 d\Omega + \int_{\Omega} (\varepsilon^l D_{22})^2 d\Omega \right) \\
&= 2\mu \left( \|\varepsilon^l D_{11}\|_{L^2(\Omega)}^2 + \|\varepsilon^l D_{12}\|_{L^2(\Omega)}^2 + \|\varepsilon^l D_{21}\|_{L^2(\Omega)}^2 + \|\varepsilon^l D_{22}\|_{L^2(\Omega)}^2 \right) \\
&\geq 2\mu \left( \|(\varepsilon^l D_{11})^2\|_{L^2(\Omega)} + \|(\varepsilon^l D_{12})^2\|_{L^2(\Omega)} + \|(\varepsilon^l D_{21})^2\|_{L^2(\Omega)} + \|(\varepsilon^l D_{22})^2\|_{L^2(\Omega)} \right) \\
&\geq 2\mu \|(\varepsilon^l D_{11})^2 + (\varepsilon^l D_{12})^2 + (\varepsilon^l D_{21})^2 + (\varepsilon^l D_{22})^2\|_{L^2(\Omega)} \\
&= 2\mu \left\| |\varepsilon^l D_{11}|^2 + |\varepsilon^l D_{12}|^2 + |\varepsilon^l D_{21}|^2 + |\varepsilon^l D_{22}|^2 \right\|_{L^2(\Omega)} \\
&= 2\mu \left\| \sum_{i=1}^2 \sum_{j=1}^2 |\varepsilon^l D_{ij}|^2 \right\|_{L^2(\Omega)} \\
&\geq 2\mu \left\| (\sigma_{\max}(\varepsilon^l \mathbf{D}))^2 \right\|_{L^2(\Omega)} \\
&= 2\mu \left( \int_{\Omega} (\sigma_{\max}(\varepsilon^l \mathbf{D}))^4 d\Omega \right)^{\frac{1}{2}} \\
&= 2\mu \left( (\sigma_{\max}(\varepsilon^l \mathbf{D}))^4 \int_{\Omega} 1 d\Omega \right)^{\frac{1}{2}} \\
&= 2\mu \left( (\sigma_{\max}(\varepsilon^l \mathbf{D}))^4 |V| \right)^{\frac{1}{2}} \\
&= 2\mu \sqrt{|V|} (\sigma_{\max}(\varepsilon^l \mathbf{D}))^2 \\
&= 2\mu \sqrt{|V|} \|\varepsilon^l \mathbf{D}\|_{L^2(\Omega)}^2 \\
&= 2\mu \sqrt{|V|} \left\| \frac{\varepsilon^l}{2} (\nabla \mathbf{W} + (\nabla \mathbf{W})^T) \right\|_{L^2(\Omega)}^2 \\
&\geq 2\mu \sqrt{|V|} \left\| \frac{1}{2h} (\nabla \mathbf{W} + (\nabla \mathbf{W})^T) \right\|_{L^2(\Omega)}^2 \\
&= \frac{\mu \sqrt{|V|}}{2h^2} \|\nabla \mathbf{W} + (\nabla \mathbf{W})^T\|_{L^2(\Omega)}^2,
\end{aligned}$$

where  $\mathbf{D} = \frac{1}{2}(\nabla \mathbf{W} + (\nabla \mathbf{W})^T)$  is symmetric with the indicial notation  $D_{ij} = \frac{1}{2} \left( \frac{\partial W_i}{\partial x_j} + \frac{\partial W_j}{\partial x_i} \right)$ . The variable  $D_{ij}$  is considered to be real number for all  $i, j = 1, 2$  and  $|V|$  is the volume of the domain  $\Omega$ . For the first inequality, we use the fact that the porosity  $\varepsilon^l \leq 1$ . For the second and third inequalities, we apply the Hölder's inequality, Theorem 2.16, and Minkowski's inequality, Theorem 2.15, respectively. For the fourth inequality, we apply

the spectral norm of a matrix  $\mathbf{E}$ , [62], i.e.

$$\|\mathbf{E}\|_{L^2(\Omega)} = \sigma_{\max}(\mathbf{E}) \leq \left( \sum_{i=1}^m \sum_{j=1}^s |e_{ij}|^2 \right)^{\frac{1}{2}}, \quad (3.90)$$

where  $\sigma_{\max}(\mathbf{E})$  represents the largest singular value of a matrix  $\mathbf{E}$ , and  $s$  and  $m$  are the dimensional numbers. For the last inequality, we use Lemma 3.4. Hence, the proof is complete.  $\square$

Next, we show the coercivity of the bilinear functional  $a(\cdot, \cdot)$ .

**Theorem 3.6.** *The bilinear functionals  $a(\cdot, \cdot)$  is coercive such that*

$$a(\mathbf{w}, \mathbf{w}) \geq Q_c \|\mathbf{w}\|_{H^1(\Omega)}^2, \quad \forall \mathbf{w} \in H^1(\Omega), \quad (3.91)$$

where  $Q_c = \min \left\{ \mu Q_k, \frac{\mu \sqrt{|V|}}{h^2 K} (N-1)^2 \right\}$  and  $Q_k$  is a positive number.

**Proof.** Let  $\mathbf{w} \in H^1(\Omega)$  and  $\mathbf{W} = \frac{\mathbf{w}}{\varepsilon^l}$ . Then

$$\begin{aligned} a(\mathbf{w}, \mathbf{w}) &= \int_{\Omega} \mu (\mathbf{k}^{-1} \cdot \mathbf{w}) \cdot \mathbf{w} d\Omega + \int_{\Omega} \mu \varepsilon^l \nabla \left( \frac{\mathbf{w}}{\varepsilon^l} \right) : \nabla \left( \frac{\mathbf{w}}{\varepsilon^l} \right) d\Omega + \int_{\Omega} \mu \varepsilon^l \left( \nabla \left( \frac{\mathbf{w}}{\varepsilon^l} \right) \right)^T : \nabla \left( \frac{\mathbf{w}}{\varepsilon^l} \right) d\Omega \\ &= \int_{\Omega} \mu (\mathbf{k}^{-1} \cdot \mathbf{w}) \cdot \mathbf{w} d\Omega + \int_{\Omega} \mu \varepsilon^l \nabla \mathbf{W} : \nabla \mathbf{W} d\Omega + \int_{\Omega} \mu \varepsilon^l (\nabla \mathbf{W})^T : \nabla \mathbf{W} d\Omega \\ &\geq \mu Q_k \|\mathbf{w}\|_{L^2(\Omega)}^2 + \frac{\mu \sqrt{|V|}}{2h^2} \|\nabla \mathbf{W} + (\nabla \mathbf{W})^T\|_{L^2(\Omega)}^2 \\ &= \mu Q_k \|\mathbf{w}\|_{L^2(\Omega)}^2 + \frac{\mu \sqrt{|V|}}{2h^2} \left( \|\nabla \mathbf{W} + (\nabla \mathbf{W})^T\|_{L^2(\Omega)}^2 + \|\nabla \mathbf{W} - (\nabla \mathbf{W})^T\|_{L^2(\Omega)}^2 \right) \\ &\geq \mu Q_k \|\mathbf{w}\|_{L^2(\Omega)}^2 + \frac{\mu \sqrt{|V|}}{2h^2} \left[ 2\|\nabla \mathbf{W}\|_{L^2(\Omega)}^2 + 2\|(\nabla \mathbf{W})^T\|_{L^2(\Omega)}^2 \right. \\ &\quad \left. - \left( \|\nabla \mathbf{W}\|_{L^2(\Omega)}^2 + \|(\nabla \mathbf{W})^T\|_{L^2(\Omega)}^2 \right) \right] \\ &= \mu Q_k \|\mathbf{w}\|_{L^2(\Omega)}^2 + \frac{\mu \sqrt{|V|}}{2h^2} \left( \|\nabla \mathbf{W}\|_{L^2(\Omega)}^2 + \|(\nabla \mathbf{W})^T\|_{L^2(\Omega)}^2 \right) \\ &\geq \mu Q_k \|\mathbf{w}\|_{L^2(\Omega)}^2 + \frac{\mu \sqrt{|V|}}{h^2} \|\nabla \mathbf{W}\|_{L^2(\Omega)}^2 \\ &= \mu Q_k \|\mathbf{w}\|_{L^2(\Omega)}^2 + \frac{\mu \sqrt{|V|}}{h^2} |\mathbf{W}|_{H^1(\Omega)}^2 \\ &= \mu Q_k \|\mathbf{w}\|_{L^2(\Omega)}^2 + \frac{\mu \sqrt{|V|}}{h^2} \left| \frac{\mathbf{w}}{\varepsilon^l} \right|_{H^1(\Omega)}^2 \\ &\geq \mu Q_k \|\mathbf{w}\|_{L^2(\Omega)}^2 + \frac{\mu \sqrt{|V|}}{h^2 K} \left\| \frac{\mathbf{w}}{\varepsilon^l} \right\|_{H^1(\Omega)}^2 \\ &\geq \mu Q_k \|\mathbf{w}\|_{L^2(\Omega)}^2 + \frac{\mu \sqrt{|V|}}{h^2 K} \|(N-1)\mathbf{w}\|_{H^1(\Omega)}^2 \\ &= \mu Q_k \|\mathbf{w}\|_{L^2(\Omega)}^2 + \frac{\mu \sqrt{|V|}}{h^2 K} (N-1)^2 \|\mathbf{w}\|_{H^1(\Omega)}^2 \end{aligned}$$

This material is reserved for educational use only, not allowed for commercial use.

Forbidden to modify the content, and cite the document when use.

$$\begin{aligned}
&\geq \min \left\{ \mu Q_k, \frac{\mu \sqrt{|V|}}{h^2 K} (N-1)^2 \right\} \left( \|\mathbf{w}\|_{L^2(\Omega)}^2 + \|\mathbf{w}\|_{H^1(\Omega)}^2 \right) \\
&\geq \min \left\{ \mu Q_k, \frac{\mu \sqrt{|V|}}{h^2 K} (N-1)^2 \right\} \|\mathbf{w}\|_{H^1(\Omega)}^2 \\
&= Q_c \|\mathbf{w}\|_{H^1(\Omega)}^2,
\end{aligned}$$

where  $Q_c = \min \left\{ \mu Q_k, \frac{\mu \sqrt{|V|}}{h^2 K} (N-1)^2 \right\} > 0$ . The property [43], equation (3.84),

$$\int_{\Omega} (\mathbf{k}^{-1} \cdot \mathbf{w}) \cdot \mathbf{w} \geq Q_k \|\mathbf{w}\|_{L^2(\Omega)}^2 \quad \text{where } Q_k > 0, \quad (3.92)$$

and equation (3.89) are used in the first inequality. Parallelogram law [10], Theorem 2.18, and the fact that  $\|\mathbf{u} - \mathbf{w}\|^2 \leq \|\mathbf{u}\|^2 + \|\mathbf{w}\|^2$  are applied to the second inequality. Poincaré inequality, Theorem 2.20, [10] is applied to the fourth inequality. By Archimedean property [61]:  $\forall r \in \mathbb{R}, \exists N \in \mathbb{N}$  such that  $N - 1 \leq r \leq N$ . Since  $0 < \varepsilon^l \leq 1$ ,  $\frac{1}{\varepsilon^l} \in \mathbb{R}$ . Then  $\exists N \in \mathbb{N}$  such that  $N - 1 \leq \frac{1}{\varepsilon^l} \leq N$ . So this is applied at the fifth inequality. Hence, the proof of the coercivity of the bilinear form  $a(\mathbf{w}, \mathbf{w})$  is complete.  $\square$

### 3.5.2 The existence and uniqueness of generalized Stokes-Brinkman equations

In this section, we provide the proof of the existence and uniqueness of the generalized Stokes-Brinkman equations. Before illustrating the proof of the well-posedness, we present the following proposition.

**Proposition 3.7.** *Let  $f \in L^2(\Omega)$  and  $\mathbf{s} \in H^{1/2}(\partial\Omega)$ . Then there exist  $\mathbf{u}_s \in H^1(\Omega)$  and a unique  $\mathbf{u}_0 \in V^\perp$  such that*

$$\|\mathbf{u}_s + \mathbf{u}_0\|_{H^1(\Omega)} \leq \frac{1}{\beta} \|f\|_{L^2(\Omega)} + \left(1 + \frac{\sqrt{n}}{\beta}\right) Q_s \|\mathbf{s}\|_{H^{1/2}(\partial\Omega)}, \quad (3.93)$$

where  $n$  is the dimensional number,  $\beta$  and  $Q_s$  are positive constants.

**Proof.** Let  $f \in L^2(\Omega)$  and  $\mathbf{s} \in H^{1/2}(\partial\Omega)$ . From Lemma 2.24, there exist  $\mathbf{u}_s \in H^1(\Omega)$  and  $Q_s > 0$  such that

$$\mathbf{u}_s|_{\partial\Omega} = \mathbf{s} \quad \text{and} \quad \|\mathbf{u}_s\|_{H^1(\Omega)} \leq Q_s \|\mathbf{s}\|_{H^{1/2}(\partial\Omega)}, \quad (3.94)$$

and there exist a unique  $\mathbf{u}_0 \in V^\perp \subset H_0^1(\Omega)$  and  $\beta > 0$  such that

$$\nabla \cdot \mathbf{u}_0 = f - \nabla \cdot \mathbf{u}_s \quad \text{and} \quad \|\mathbf{u}_0\|_{H^1(\Omega)} \leq \beta^{-1} \|f - \nabla \cdot \mathbf{u}_s\|_{L^2(\Omega)}. \quad (3.95)$$

Next, we show that  $\mathbf{u}_s + \mathbf{u}_0$  is bounded as follows.

$$\begin{aligned}
\|\mathbf{u}_s + \mathbf{u}_0\|_{H^1(\Omega)} &\leq \|\mathbf{u}_s\|_{H^1(\Omega)} + \|\mathbf{u}_0\|_{H^1(\Omega)} \\
&\leq Q_s \|\mathbf{s}\|_{H^{1/2}(\partial\Omega)} + \frac{1}{\beta} \|f - \nabla \cdot \mathbf{u}_s\|_{L^2(\Omega)} \\
&\leq Q_s \|\mathbf{s}\|_{H^{1/2}(\partial\Omega)} + \frac{1}{\beta} \|f\|_{L^2(\Omega)} + \frac{1}{\beta} \|\nabla \cdot \mathbf{u}_s\|_{L^2(\Omega)}
\end{aligned}$$

This material is reserved for educational use only, not allowed for commercial use.

Forbidden to modify the content, and cite the document when use.

$$\begin{aligned}
&\leq Q_s \|\mathbf{s}\|_{H^{1/2}(\partial\Omega)} + \frac{1}{\beta} \|f\|_{L^2(\Omega)} + \frac{\sqrt{n}}{\beta} \|\mathbf{u}_s\|_{H^1(\Omega)} \\
&\leq Q_s \|\mathbf{s}\|_{H^{1/2}(\partial\Omega)} + \frac{1}{\beta} \|f\|_{L^2(\Omega)} + \frac{\sqrt{n}}{\beta} Q_s \|\mathbf{s}\|_{H^{1/2}(\partial\Omega)} \\
&= \frac{1}{\beta} \|f\|_{L^2(\Omega)} + \left(1 + \frac{\sqrt{n}}{\beta}\right) Q_s \|\mathbf{s}\|_{H^{1/2}(\partial\Omega)},
\end{aligned}$$

where equations (3.94) and (3.95) are applied to the second inequality and Minkowski's inequality, Theorem 2.15, is applied at the third inequality. For the fourth inequality, we use the fact that [9] :  $\|\nabla \cdot \phi\|_{L^2(\Omega)} \leq \sqrt{n} \|\phi\|_{H^1(\Omega)}$ ,  $n$  is the dimensional number. For the last inequality, we use equation (3.94).  $\square$

Next, we show the theorem of the well-posedness of the generalized Stokes-Brinkman equations.

**Theorem 3.8.** (*Well-posedness of the generalized Stokes-Brinkman equations*)

Let  $\mathbf{f} \in H^{-1}(\Omega)$ ,  $f \in L^2(\Omega)$  and  $\mathbf{s} \in H^{1/2}(\partial\Omega)$ . There exists a unique  $\mathbf{u} \in H_s^1(\Omega)$  and  $p \in L_0^2(\Omega)$  satisfying Problem 3.1. Moreover,

$$\|\mathbf{u}\|_{H^1(\Omega)} \leq \frac{1}{Q_c} \|\mathbf{f}\|_{H^{-1}(\Omega)} + \left(1 + \frac{Q_a}{Q_c}\right) \|\hat{\mathbf{u}}\|_{H^1(\Omega)}, \quad (3.96)$$

$$\|p\|_{L^2(\Omega)} \leq \frac{1}{\beta} \|\mathbf{f}\|_{H^{-1}(\Omega)} + \frac{1}{\beta} Q_a \|\mathbf{u}\|_{H^1(\Omega)}, \quad (3.97)$$

where  $\hat{\mathbf{u}} = \mathbf{u}_s + \mathbf{u}_0$ ,  $\beta > 0$  as presented in Proposition 3.7, and  $Q_a$  and  $Q_c$  are defined in Theorem 3.3 and Theorem 3.6, respectively.

**Proof.** Let  $\mathbf{f} \in H^{-1}(\Omega)$ ,  $f \in L^2(\Omega)$  and  $\mathbf{s} \in H^{1/2}(\partial\Omega)$ . From proposition 3.7, we have  $\mathbf{u}_s \in H^1(\Omega)$  and  $\mathbf{u}_0 \in V^\perp \subset H_0^1(\Omega)$  such that

$$\mathbf{u}_s|_{\partial\Omega} = \mathbf{s} \quad \text{and} \quad \nabla \cdot \mathbf{u}_0 = f - \nabla \cdot \mathbf{u}_s. \quad (3.98)$$

Let  $\hat{\mathbf{u}} = \mathbf{u}_s + \mathbf{u}_0$  and  $L(\mathbf{w}) = c_1(\mathbf{w}) - a(\hat{\mathbf{u}}, \mathbf{w})$  for any  $\mathbf{w} \in V$ . From Theorem 3.3, we can see that  $c_1(\cdot)$  and  $a(\cdot, \cdot)$  are linear and bilinear functions, respectively. Then,  $L(\cdot)$  is a linear function. Moreover, the continuities of  $c_1(\cdot)$  and  $a(\cdot, \cdot)$  along with the coercivity of  $a(\cdot, \cdot)$  implies that  $L(\cdot)$  is a continuous function. By applying the Lax-Milgram theorem, there exists a unique  $\tilde{\mathbf{u}} \in V \subset H_0^1(\Omega)$  such that

$$a(\tilde{\mathbf{u}}, \mathbf{w}) = L(\mathbf{w}). \quad (3.99)$$

Let  $\mathbf{u} = \tilde{\mathbf{u}} + \hat{\mathbf{u}} = \tilde{\mathbf{u}} + \mathbf{u}_s + \mathbf{u}_0$ . Then

$$\begin{aligned}
\mathbf{u}|_{\partial\Omega} &= \tilde{\mathbf{u}}|_{\partial\Omega} + \mathbf{u}_s|_{\partial\Omega} + \mathbf{u}_0|_{\partial\Omega} \\
&= \mathbf{0} + \mathbf{s} + \mathbf{0} \\
&= \mathbf{s},
\end{aligned}$$

because  $\tilde{\mathbf{u}} \in V \subset H_0^1(\Omega)$ , and  $\mathbf{u}_0 \in V^\perp \subset H_0^1(\Omega)$ . Therefore, there exists  $\mathbf{u} \in H_s^1(\Omega)$ . This material is reserved for educational use only, not allowed for commercial use.

Next, we show the uniqueness of  $\mathbf{u}$ . Since  $a(\tilde{\mathbf{u}}, \mathbf{w}) = L(\mathbf{w}) = c_1(\mathbf{w}) - a(\hat{\mathbf{u}}, \mathbf{w})$ , by using the bilinear property of  $a(\cdot, \cdot)$ , we have

$$a(\mathbf{u}, \mathbf{w}) = a(\tilde{\mathbf{u}} + \hat{\mathbf{u}}, \mathbf{w}) = c_1(\mathbf{w}). \quad (3.100)$$

Suppose that  $\mathbf{u}_1$  and  $\mathbf{u}_2$  are two such solutions satisfying

$$a(\mathbf{u}_1, \mathbf{w}) = c_1(\mathbf{w}) \text{ and } a(\mathbf{u}_2, \mathbf{w}) = c_1(\mathbf{w}). \quad (3.101)$$

Therefore,

$$\begin{aligned} a(\mathbf{u}_1, \mathbf{w}) &= a(\mathbf{u}_2, \mathbf{w}) \\ a(\mathbf{u}_1, \mathbf{w}) - a(\mathbf{u}_2, \mathbf{w}) &= 0 \\ a(\mathbf{u}_1 - \mathbf{u}_2, \mathbf{w}) &= 0. \end{aligned} \quad (3.102)$$

Then, substituting  $\mathbf{w} = \mathbf{u}_1 - \mathbf{u}_2$  in equation (3.102), we get

$$0 = a(\mathbf{u}_1 - \mathbf{u}_2, \mathbf{u}_1 - \mathbf{u}_2) \geq Q_c \|\mathbf{u}_1 - \mathbf{u}_2\|_{H^1(\Omega)}^2 \geq 0,$$

where we apply the coercivity of  $a(\cdot, \cdot)$ , Theorem 3.6, at the first inequality. Since, the constant  $Q_c > 0$ , it implies that  $\|\mathbf{u}_1 - \mathbf{u}_2\|_{H^1(\Omega)} = 0$ . Then  $\mathbf{u}_1 = \mathbf{u}_2$ . Therefore,  $\mathbf{u}$  is unique satisfying  $a(\mathbf{u}, \mathbf{w}) = c_1(\mathbf{w})$ , for all  $\mathbf{w} \in V$ .

Next, we show that  $\mathbf{u} = \tilde{\mathbf{u}} + \mathbf{u}_s + \mathbf{u}_0$  satisfies the continuity equation. Since  $\tilde{\mathbf{u}} \in V$ ,  $\nabla \cdot \tilde{\mathbf{u}} = 0$ . Then,

$$\begin{aligned} \nabla \cdot \mathbf{u} &= \nabla \cdot (\tilde{\mathbf{u}} + \mathbf{u}_s + \mathbf{u}_0) \\ &= \nabla \cdot \tilde{\mathbf{u}} + \nabla \cdot \mathbf{u}_s + \nabla \cdot \mathbf{u}_0 \\ &= 0 + \nabla \cdot \mathbf{u}_s + f - \nabla \cdot \mathbf{u}_s \\ &= f, \end{aligned}$$

where  $\nabla \cdot \mathbf{u}_0 = f - \nabla \cdot \mathbf{u}_s$  is applied at the third equality. Hence,  $\mathbf{u}$  satisfies the continuity equation.

To prove the existence and uniqueness of  $p \in L_0^2(\Omega)$ . Define  $L_1$  such that  $\langle L_1, \mathbf{w} \rangle = c_1(\mathbf{w})$ . Then, from equation (3.100), we have

$$\begin{aligned} a(\tilde{\mathbf{u}}, \mathbf{w}) &= c_1(\mathbf{w}) - a(\hat{\mathbf{u}}, \mathbf{w}) \\ 0 &= c_1(\mathbf{w}) - a(\tilde{\mathbf{u}}, \mathbf{w}) - a(\hat{\mathbf{u}}, \mathbf{w}), \quad \forall \mathbf{w} \in V. \end{aligned} \quad (3.103)$$

By the definition of the linear operator, Definition 2.14, we can rewrite equation (3.103) in operator notation as  $L_1 - A\tilde{\mathbf{u}} - A\hat{\mathbf{u}} = 0$ . Then  $L_1 - A\tilde{\mathbf{u}} - A\hat{\mathbf{u}} \in V^0$ , where  $V^0$  is the polar set of  $V$ . Given  $B' : L_0^2(\Omega) \rightarrow V^0$  is an isomorphism **grad** operator. Thus, from Theorem 2.22 and the property of isomorphism, there exists a unique  $p \in L_0^2(\Omega)$  such that

$$B'p = L_1 - A\tilde{\mathbf{u}} - A\hat{\mathbf{u}}$$

$$B'p = L_1 - A(\tilde{\mathbf{u}} + \hat{\mathbf{u}})$$

$$B'p = L_1 - A\mathbf{u}$$

$$A\mathbf{u} + B'p = L_1.$$

This material is reserved for educational use only, not allowed for commercial use.

Forbidden to modify the content, and cite the document when use.

Then,  $A\mathbf{u} + B'p = L_1 = \mathbf{f}$ . Therefore, there exists a unique  $\mathbf{u} \in H_s^1(\Omega)$  and  $p \in L_0^2(\Omega)$  satisfying Problem 3.1 and Problem 3.2.

Next, we show that the variables  $\mathbf{u}$  and  $p$  are bounded. We first illustrate that  $\tilde{\mathbf{u}}$  is bounded. Employing equation (3.91), we have

$$\begin{aligned} Q_c \|\tilde{\mathbf{u}}\|_{H^1(\Omega)}^2 &\leq a(\tilde{\mathbf{u}}, \tilde{\mathbf{u}}) \\ &= c_1(\tilde{\mathbf{u}}) - a(\hat{\mathbf{u}}, \tilde{\mathbf{u}}) \\ &\leq \|\mathbf{f}\|_{H^{-1}(\Omega)} \|\tilde{\mathbf{u}}\|_{H^1(\Omega)} + Q_a \|\hat{\mathbf{u}}\|_{H^1(\Omega)} \|\tilde{\mathbf{u}}\|_{H^1(\Omega)}, \end{aligned} \quad (3.104)$$

where the second inequality is obtained from Theorem 3.3. Dividing both sides of Eq. (3.104) by  $\|\tilde{\mathbf{u}}\|_{H^1(\Omega)}$  and  $Q_c$ , we get

$$\|\tilde{\mathbf{u}}\|_{H^1(\Omega)} \leq \frac{1}{Q_c} \|\mathbf{f}\|_{H^{-1}(\Omega)} + \frac{Q_a}{Q_c} \|\hat{\mathbf{u}}\|_{H^1(\Omega)}. \quad (3.105)$$

Thus,

$$\begin{aligned} \|\mathbf{u}\|_{H^1(\Omega)} &= \|\tilde{\mathbf{u}} + \hat{\mathbf{u}}\|_{H^1(\Omega)} \\ &\leq \|\tilde{\mathbf{u}}\|_{H^1(\Omega)} + \|\hat{\mathbf{u}}\|_{H^1(\Omega)} \\ &\leq \frac{1}{Q_c} \|\mathbf{f}\|_{H^{-1}(\Omega)} + \frac{Q_a}{Q_c} \|\hat{\mathbf{u}}\|_{H^1(\Omega)} + \|\hat{\mathbf{u}}\|_{H^1(\Omega)} \\ &= \frac{1}{Q_c} \|\mathbf{f}\|_{H^{-1}(\Omega)} + \left(1 + \frac{Q_a}{Q_c}\right) \|\hat{\mathbf{u}}\|_{H^1(\Omega)}. \end{aligned}$$

Therefore, the variable  $\mathbf{u}$  is bounded. To show that  $p$  is bounded, we first employ equation (3.68):

$$\begin{aligned} b(\mathbf{w}, p) &= c_1(\mathbf{w}) - a(\mathbf{u}, \mathbf{w}) \\ &\leq \|\mathbf{f}\|_{H^{-1}(\Omega)} \|\mathbf{w}\|_{H^1(\Omega)} + Q_a \|\mathbf{u}\|_{H^1(\Omega)} \|\mathbf{w}\|_{H^1(\Omega)}, \end{aligned} \quad (3.106)$$

where equations (3.77) and (3.80) are applied to the inequality. Since

$$\sup_{\mathbf{w} \in H_0^1(\Omega)} \frac{b(\mathbf{w}, p)}{\|\mathbf{w}\|_{H^1(\Omega)} \|p\|_{L^2(\Omega)}}$$

is independent of  $p$ , from equation (2.53),

$$\begin{aligned} \|p\|_{L^2(\Omega)}^{-1} \sup_{\mathbf{w} \in H_0^1(\Omega)} \frac{b(\mathbf{w}, p)}{\|\mathbf{w}\|_{H^1(\Omega)}} &= \sup_{\mathbf{w} \in H_0^1(\Omega)} \frac{b(\mathbf{w}, p)}{\|\mathbf{w}\|_{H^1(\Omega)} \|p\|_{L^2(\Omega)}} \\ &\geq \inf_{p \in L_0^2(\Omega)} \sup_{\mathbf{w} \in H_0^1(\Omega)} \frac{b(\mathbf{w}, p)}{\|\mathbf{w}\|_{H^1(\Omega)} \|p\|_{L^2(\Omega)}} \geq \beta > 0. \end{aligned} \quad (3.107)$$

Rearranging equation (3.107), we obtain that

$$\begin{aligned} \|p\|_{L^2(\Omega)} &\leq \frac{1}{\beta} \sup_{\mathbf{w} \in H_0^1(\Omega)} \frac{b(\mathbf{w}, p)}{\|\mathbf{w}\|_{H^1(\Omega)}} \\ &= \frac{1}{\beta} \sup_{\mathbf{w} \in H_0^1(\Omega)} \frac{c_1(\mathbf{w}) - a(\mathbf{u}, \mathbf{w})}{\|\mathbf{w}\|_{H^1(\Omega)}} \\ &\leq \frac{1}{\beta} \sup_{\mathbf{w} \in H_0^1(\Omega)} \left( \frac{\|\mathbf{f}\|_{H^{-1}(\Omega)} \|\mathbf{w}\|_{H^1(\Omega)} + Q_a \|\mathbf{u}\|_{H^1(\Omega)} \|\mathbf{w}\|_{H^1(\Omega)}}{\|\mathbf{w}\|_{H^1(\Omega)}} \right) \end{aligned}$$

This material is reserved for educational use only, not allowed for commercial use.

Forbidden to modify the content, and cite the document when use.

Since  $\|\mathbf{f}\|_{H^{-1}(\Omega)} + Q_a\|\mathbf{u}\|_{H^1(\Omega)}$  is independent of  $\mathbf{w} \in H_0^1(\Omega)$ ,

$$\sup_{\mathbf{w} \in H_0^1(\Omega)} (\|\mathbf{f}\|_{H^{-1}(\Omega)} + Q_a\|\mathbf{u}\|_{H^1(\Omega)}) = \|\mathbf{f}\|_{H^{-1}(\Omega)} + Q_a\|\mathbf{u}\|_{H^1(\Omega)}.$$

Therefore,

$$\|p\|_{L^2(\Omega)} \leq \frac{1}{\beta} (\|\mathbf{f}\|_{H^{-1}(\Omega)} + Q_a\|\mathbf{u}\|_{H^1(\Omega)}).$$

Hence, the proof of the existence and uniqueness of the generalized Stokes-Brinkman equations is complete.  $\square$



## Chapter 4

### Model Discretization and Boundary Conditions

In this chapter, we present the process of discretizing the governing equations and applying the boundary conditions used to determine the velocity of the PCL fluid. In Section 4.1, we first introduces the fan-blade-shaped porous domain employed for the numerical simulations. In Section 4.2, we apply a mixed finite element method of the Taylor-Hood type to discretize the governing equations. In Section 4.3, we present the boundary conditions implemented in this study.

#### 4.1 Fan-blade shape domain

In order to determine the velocity of the PCL fluid, we first introduce the numerical domain used to find the numerical solutions in this section. We define the numerical domain in the shape of a fan blade, resembling the wave pattern of cilia, as shown on the left side of Figure 4.1, where the cilia are monitored as rigid cylinders because they have long and thin lines. Based on our information, this shape of the domain was not studied in the previous literatures. The model designed is more closely to the actual beating pattern of cilia that the cilia rotate as a clockwise pattern moving from left to right around their base. The movement of cilia generates the leftward flow of the PCL fluid. Figure 4.1 on the left shows our numerical porous domain with angular movement of cilia. The angle  $\theta$  represents the angle that the cilia make with the horizontal plane. The variable  $\xi$  is the dimensionless length along cilia, which is

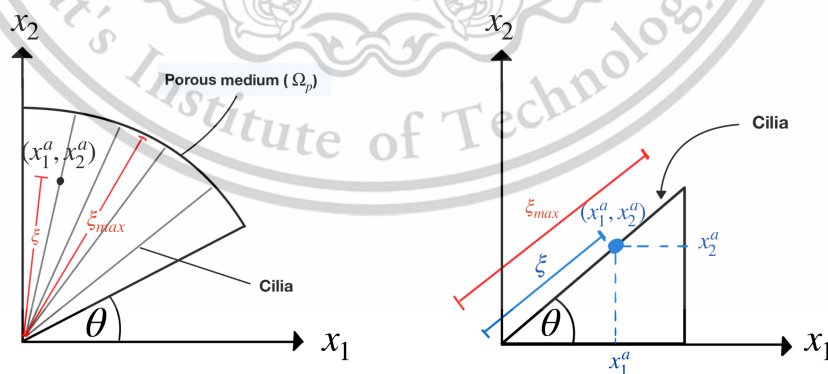


**Figure 4.1:** Left: the fan-blade shape of the porous domain on the  $x_1x_2$  plane when cilia make angles with the horizontal plane. Right: the illustration of the length  $\xi$  along cilia at the point  $(x_1^a, x_2^a)$  and the the variable  $\xi_{max}$ .

the distance from the roots of the cilia to a point  $(x_1^a, x_2^a)$  on the cilia divided by the length of the cilia which is approximately  $7.5 \mu\text{m}$  [63]. Figure 4.1 on the right shows that at each point  $(x_1^a, x_2^a)$  on the cilia, we can calculate the variable  $\xi$  by using the

formula  $\xi = x_2^a / \sin \theta$ , the angle  $\theta = \arctan(x_2^a / x_1^a)$  and the variable  $\xi_{\max}$  represents the dimensionless length of the cilia, which is one.

Because we consider the motion of bundles of cilia affecting the movement of the PCL fluid in the fan-blade shape of the porous domain, we use the generalized Brinkman equation on a macroscopic scale to predict the velocity of the PCL fluid. The mathematical model used to obtain the numerical solutions is derived in Section 3.2. Recall the generalized Brinkman and continuity equations for the porous domain,

$$\mu \mathbf{k}^{-1} \cdot \mathbf{u} - \frac{\mu}{\varepsilon^l} \nabla \cdot (2\varepsilon^l \mathbf{d}^l) + \nabla p = \rho \mathbf{g} + \mu \mathbf{k}^{-1} \cdot \varepsilon^l \mathbf{u}^s \quad \text{in } \Omega_p, \quad (4.1)$$

$$\nabla \cdot \mathbf{u} = f \quad \text{in } \Omega_p. \quad (4.2)$$

The unknowns of the system of equations are the fluid velocity  $\mathbf{u}$  and the pressure  $p$ . Before we calculate the numerical results, we provide the discretized form of our governing equations using a mixed finite element method in the next section.

## 4.2 Model Discretization

In this section, we present the discretization of the generalized Brinkman equations using a mixed finite element method. We start with the weak formulation equation (3.62) presented in Section 3.4. That is

$$\begin{aligned} \int_{\Omega_p} \mu k_{ij}^{-1} w_i u_j d\Omega_p + \int_{\Omega_p} 2\mu \varepsilon^l \frac{\partial}{\partial x_j} \left( \frac{w_i}{\varepsilon^l} \right) d_{ij}^l d\Omega_p - \int_{\Omega_p} \frac{\partial w_i}{\partial x_i} p d\Omega_p \\ = \int_{\Omega_p} w_i f_i d\Omega_p + \int_{\Gamma_p} 2\mu w_i d_{ij}^l n_j d\Gamma_p - \int_{\Gamma_p} p w_i n_i d\Gamma_p, \end{aligned} \quad (4.3)$$

where  $\Omega_p$  is the domain of the porous medium and  $\Gamma_p$  is the boundary of the domain  $\Omega_p$ . Substituting  $d_{ij}^l = 0.5 \left[ \frac{\partial}{\partial x_j} \left( \frac{u_i}{\varepsilon^l} \right) + \frac{\partial}{\partial x_i} \left( \frac{u_j}{\varepsilon^l} \right) \right]$  and  $f_i = \rho g_i + \mu \varepsilon^l k_{ij}^{-1} u_j^s$  into equation (4.3), and rearranging the terms, we have

$$\begin{aligned} \int_{\Omega_p} \mu k_{ij}^{-1} w_i u_j d\Omega_p + \int_{\Omega_p} \mu \varepsilon^l \frac{\partial}{\partial x_j} \left( \frac{w_i}{\varepsilon^l} \right) \frac{\partial}{\partial x_j} \left( \frac{u_i}{\varepsilon^l} \right) d\Omega_p + \int_{\Omega_p} \mu \varepsilon^l \frac{\partial}{\partial x_j} \left( \frac{w_i}{\varepsilon^l} \right) \frac{\partial}{\partial x_i} \left( \frac{u_j}{\varepsilon^l} \right) d\Omega_p - \int_{\Omega_p} \frac{\partial w_i}{\partial x_i} p d\Omega_p \\ = \int_{\Omega_p} w_i (\rho g_i + \mu \varepsilon^l k_{ij}^{-1} u_j^s) d\Omega_p + \int_{\Gamma_p} \mu w_i \frac{\partial}{\partial x_j} \left( \frac{u_i}{\varepsilon^l} \right) n_j d\Gamma_p + \int_{\Gamma_p} \mu w_i \frac{\partial}{\partial x_i} \left( \frac{u_j}{\varepsilon^l} \right) n_j d\Gamma_p - \int_{\Gamma_p} w_i p n_i d\Gamma_p. \end{aligned} \quad (4.4)$$

Similarly, the weak formulation of the continuity equation is

$$\int_{\Omega_p} q \frac{\partial u_j}{\partial x_j} d\Omega_p = \int_{\Omega_p} q f d\Omega_p. \quad (4.5)$$

Substituting  $f = \frac{-\varepsilon^l}{1-\varepsilon^l} + \frac{\partial}{\partial x_j} (\varepsilon^l u_j^s)$  into equation (4.5), we have

$$\int_{\Omega_p} q \frac{\partial u_j}{\partial x_j} d\Omega_p = \int_{\Omega_p} q \left( \frac{-\varepsilon^l}{1-\varepsilon^l} + \frac{\partial}{\partial x_j} (\varepsilon^l u_j^s) \right) d\Omega_p. \quad (4.6)$$

Considering the term  $\varepsilon^l$  in equation (4.6), which is the material time derivative of the porosity with respect to the solid phase, we have

$$\frac{\partial \varepsilon^l}{\partial t} = \frac{\partial \varepsilon^l}{\partial t} + \mathbf{u}^s \cdot \nabla \varepsilon^l = \frac{\partial \varepsilon^l}{\partial \theta} \frac{\partial \theta}{\partial t} + u_j^s \frac{\partial \varepsilon^l}{\partial x_j}. \quad (4.7)$$

Forbidden to modify the content, and cite the document when use.

Using the angular velocity to determine  $\frac{\partial \theta}{\partial t}$ , we obtain  $\frac{\partial \theta}{\partial t} = \frac{-|u^s|}{\xi}$  [50]. Then

$$\dot{\varepsilon}^l = \frac{-|u^s|}{\xi} \frac{\partial \varepsilon^l}{\partial \theta} + u_j^s \frac{\partial \varepsilon^l}{\partial x_j}, \quad (4.8)$$

where  $|u^s|$  is the speed of the solid velocity. Substituting equation (4.8) into equation (4.6) and applying the product rule to the last term of equation (4.6), we obtain

$$-\int_{\Omega_p} q \frac{\partial u_j}{\partial x_j} d\Omega_p = -\int_{\Omega_p} q \left( \frac{|u^s|}{\xi(1-\varepsilon^l)} \frac{\partial \varepsilon^l}{\partial \theta} - \frac{\varepsilon^l}{(1-\varepsilon^l)} u_j^s \frac{\partial \varepsilon^l}{\partial x_j} + \varepsilon^l \frac{\partial u_j^s}{\partial x_j} \right) d\Omega_p, \quad (4.9)$$

where we multiply  $(-1)$  both sides of the weak formulation in order to obtain the symmetric form of the stiffness matrix equation (4.28), shown below.

Next, we discretize the domain  $\Omega_p$  into triangular elements and approximate the velocity and the pressure within each element using basis functions from the spaces  $U_h$  and  $H_h$ , respectively, defined below. Let  $T_h$  be a triangulation of the domain  $\Omega$  and we define the finite-dimensional subspaces of  $H^1(\Omega)$  and  $L_0^2(\Omega)$  as [10]

$$U_h = \left\{ u \in H^1(\Omega) : u|_K \text{ is quadratic, } \forall K \in T_h \right\}, \quad (4.10)$$

$$H_h = \left\{ q \in L_0^2(\Omega) : q|_K \text{ is linear, } \forall K \in T_h \right\}, \quad (4.11)$$

respectively. Since  $\mathbf{u} = (u_1, u_2)$ ,  $\mathbf{u} \in U_h \times U_h$ . The solutions  $(u_1, u_2, p) \in U_h \times U_h \times H_h$  is approximated by the expansions of the forms

$$u_i(\mathbf{x}) = \sum_{m=1}^M \psi_m(\mathbf{x}) u_i^m = \Psi^T \mathbf{U}_i, \quad (4.12)$$

$$p(\mathbf{x}) = \sum_{l=1}^L \phi_l(\mathbf{x}) p_l = \Phi^T \mathbf{P}, \quad (4.13)$$

where  $i = 1, 2$ ,  $\mathbf{x} = (x_1, x_2)$ ,  $\psi_m \in H_0^1(\Omega)$  and  $\phi_l \in L_0^2(\Omega)$  are the basis functions, the vector  $\Psi$  and  $\Phi$  are their vector forms,  $\mathbf{U}_1, \mathbf{U}_2$  and  $\mathbf{P}$  are vectors of the velocities and pressure, respectively, and the superscript  $T$  represents the transpose. The constants  $M$  and  $L$  are integers determined by the interpolation functions. For a triangular element, in this work, we use a quadratic function for the velocities  $u_i$  ( $M = 6$ ) and a linear function for the pressure  $p$  ( $L = 3$ ). By applying the Galerkin method, the weight functions  $w_i$  and  $q$  are chosen to be the same as the corresponding shape functions. That is

$$w_i \approx \Psi \quad \text{and} \quad q \approx \Phi. \quad (4.14)$$

Substituting equations (4.12)–(4.14) into equations (4.4) and (4.9), we have

$$\begin{aligned} & \mu k_{ij}^{-1} \left( \int_{\Omega_p} \Psi \Psi^T d\Omega_p \right) \mathbf{U}_j + \mu \left( \int_{\Omega_p} \varepsilon^l \frac{\partial}{\partial x_j} \left( \frac{\Psi}{\varepsilon^l} \right) \frac{\partial}{\partial x_j} \left( \frac{\Psi^T}{\varepsilon^l} \right) d\Omega_p \right) \mathbf{U}_i \\ & + \mu \left( \int_{\Omega_p} \varepsilon^l \frac{\partial}{\partial x_j} \left( \frac{\Psi}{\varepsilon^l} \right) \frac{\partial}{\partial x_i} \left( \frac{\Psi^T}{\varepsilon^l} \right) d\Omega_p \right) \mathbf{U}_j - \left( \int_{\Omega_p} \frac{\partial \Psi}{\partial x_i} \Phi^T d\Omega_p \right) \mathbf{P} \\ & = \int_{\Omega_p} \Psi (\rho g_i + \mu \varepsilon^l k_{ij}^{-1} u_j^s) d\Omega_p + \mu \left( \int_{\Gamma_p} \Psi \frac{\partial}{\partial x_j} \left( \frac{\Psi^T}{\varepsilon^l} \right) n_j d\Gamma_p \right) \mathbf{U}_i \\ & + \mu \left( \int_{\Gamma_p} \Psi \frac{\partial}{\partial x_i} \left( \frac{\Psi^T}{\varepsilon^l} \right) n_j d\Gamma_p \right) \mathbf{U}_j - \left( \int_{\Gamma_p} \Psi \Phi^T n_i d\Gamma_p \right) \mathbf{P}, \end{aligned} \quad (4.15)$$

and

$$-\left(\int_{\Omega_p} \Phi \frac{\partial \Psi^T}{\partial x_j} d\Omega_p\right) \mathbf{U}_j = -\int_{\Omega_p} \Phi \left( \frac{|u^s|}{\xi(1-\varepsilon^l)} \frac{\partial \varepsilon^l}{\partial \theta} - \frac{\varepsilon^l}{(1-\varepsilon^l)} u_j^s \frac{\partial \varepsilon^l}{\partial x_j} + \varepsilon^l \frac{\partial u_j^s}{\partial x_j} \right) d\Omega_p. \quad (4.16)$$

Let  $\Omega^e$  be the element domains such that  $\Omega = \bigcup_e \Omega^e$ , where the interiors of the elements do not overlap. This decomposition enables the integral over the entire domain  $\Omega$  to be written as the sum of integrals over each element domain  $\Omega^e$ , that is

$$\int_{\Omega} f(x) d\Omega = \sum_{e=1}^n \int_{\Omega^e} f(x) d\Omega^e, \quad (4.17)$$

where  $n$  is the total number of elements. Applying equation (4.17) to every integral term in equations (4.15) and (4.16), we obtain the equations

$$\begin{aligned} & \sum_{e=1}^n \left[ \mu k_{ij}^{-1} \left( \int_{\Omega_p^e} \Psi \Psi^T d\Omega_p^e \right) \mathbf{U}_j \right] + \sum_{e=1}^n \left[ \mu \left( \int_{\Omega_p^e} \varepsilon^l \frac{\partial}{\partial x_j} \left( \frac{\Psi}{\varepsilon^l} \right) \frac{\partial}{\partial x_j} \left( \frac{\Psi^T}{\varepsilon^l} \right) d\Omega_p^e \right) \mathbf{U}_i \right] \\ & + \sum_{e=1}^n \left[ \mu \left( \int_{\Omega_p^e} \varepsilon^l \frac{\partial}{\partial x_j} \left( \frac{\Psi}{\varepsilon^l} \right) \frac{\partial}{\partial x_i} \left( \frac{\Psi^T}{\varepsilon^l} \right) d\Omega_p^e \right) \mathbf{U}_j \right] - \sum_{e=1}^n \left[ \left( \int_{\Omega_p^e} \frac{\partial \Psi}{\partial x_i} \Phi^T d\Omega_p^e \right) \mathbf{P} \right] \\ & = \sum_{e=1}^n \left[ \int_{\Omega_p^e} \Psi (\rho g_i + \mu \varepsilon^l k_{ij}^{-1} u_j^s) d\Omega_p^e \right] + \sum_{e=1}^n \left[ \mu \left( \int_{\Gamma_p^e} \Psi \frac{\partial}{\partial x_j} \left( \frac{\Psi^T}{\varepsilon^l} \right) n_j d\Gamma_p^e \right) \mathbf{U}_i \right] \\ & + \sum_{e=1}^n \left[ \mu \left( \int_{\Gamma_p^e} \Psi \frac{\partial}{\partial x_i} \left( \frac{\Psi^T}{\varepsilon^l} \right) n_j d\Gamma_p^e \right) \mathbf{U}_j \right] - \sum_{e=1}^n \left[ \left( \int_{\Gamma_p^e} \Psi \Phi^T n_i d\Gamma_p^e \right) \mathbf{P} \right], \end{aligned} \quad (4.18)$$

and

$$\sum_{e=1}^n \left[ -\left( \int_{\Omega_p^e} \Phi \frac{\partial \Psi^T}{\partial x_j} d\Omega_p^e \right) \mathbf{U}_j \right] = \sum_{e=1}^n \left[ -\int_{\Omega_p^e} \Phi \left( \frac{|u^s|}{\xi(1-\varepsilon^l)} \frac{\partial \varepsilon^l}{\partial \theta} - \frac{\varepsilon^l}{(1-\varepsilon^l)} u_j^s \frac{\partial \varepsilon^l}{\partial x_j} + \varepsilon^l \frac{\partial u_j^s}{\partial x_j} \right) d\Omega_p^e \right]. \quad (4.19)$$

The equations (4.18) and (4.19) can be written in the form

$$\sum_{e=1}^n \left[ -(\mu k_{ij}^{-1} \hat{\mathbf{A}} + \mu \hat{\mathbf{D}}_{ij}) \mathbf{U}_j + \mu \hat{\mathbf{K}}_{jj} \mathbf{U}_i - \hat{\mathbf{Q}}_i^T \mathbf{P} \right] = \sum_{e=1}^n \left[ \hat{\mathbf{F}}_i \right], \quad (4.20)$$

$$\sum_{e=1}^n \left[ -\hat{\mathbf{Q}}_j \mathbf{U}_j \right] = \sum_{e=1}^n \left[ \hat{\mathbf{F}}_3 \right], \quad (4.21)$$

where

$$\hat{\mathbf{A}} = \int_{\Omega_p^e} \Psi \Psi^T d\Omega_p^e, \quad (4.22)$$

$$\hat{\mathbf{K}}_{jj} = \int_{\Omega_p^e} \varepsilon^l \frac{\partial}{\partial x_j} \left( \frac{\Psi}{\varepsilon^l} \right) \frac{\partial}{\partial x_j} \left( \frac{\Psi^T}{\varepsilon^l} \right) d\Omega_p^e, \quad (4.23)$$

$$\hat{\mathbf{D}}_{ij} = \int_{\Omega_p^e} \varepsilon^l \frac{\partial}{\partial x_j} \left( \frac{\Psi}{\varepsilon^l} \right) \frac{\partial}{\partial x_i} \left( \frac{\Psi^T}{\varepsilon^l} \right) d\Omega_p^e, \quad (4.24)$$

$$\hat{\mathbf{Q}}_i^T = \int_{\Omega_p^e} \frac{\partial \Psi}{\partial x_i} \Phi^T d\Omega_p^e, \quad (4.25)$$

$$\begin{aligned} \hat{\mathbf{F}}_i &= \int_{\Omega_p^e} \Psi (\rho g_i + \mu \varepsilon^l k_{ij}^{-1} u_j^s) d\Omega_p^e + \mu \left( \int_{\Gamma_p^e} \Psi \frac{\partial}{\partial x_j} \left( \frac{\Psi^T}{\varepsilon^l} \right) n_j d\Gamma_p^e \right) \mathbf{U}_i \\ &+ \mu \left( \int_{\Gamma_p^e} \Psi \frac{\partial}{\partial x_i} \left( \frac{\Psi^T}{\varepsilon^l} \right) n_j d\Gamma_p^e \right) \mathbf{U}_j - \left( \int_{\Gamma_p^e} \Psi \Phi^T n_i d\Gamma_p^e \right) \mathbf{P}, \quad i = 1, 2, \end{aligned} \quad (4.26)$$

$$\hat{\mathbf{F}}_3 = -\int_{\Omega_p^e} \Phi \left( \frac{|u^s|}{\xi(1-\varepsilon^l)} \frac{\partial \varepsilon^l}{\partial \theta} - \frac{\varepsilon^l}{(1-\varepsilon^l)} u_j^s \frac{\partial \varepsilon^l}{\partial x_j} + \varepsilon^l \frac{\partial u_j^s}{\partial x_j} \right) d\Omega_p^e. \quad (4.27)$$

Forbidden to modify the content, and cite the document when use.

Rewriting equations (4.20) and (4.21) into matrix form for each element  $e$ , we have the element matrix of the system of equations (4.20) and (4.21) in 2 dimension as follows,

$$\begin{pmatrix} \mu \left( k_{11}^{-1} \hat{\mathbf{A}} + \hat{\mathbf{D}}_{11} + \hat{\mathbf{K}}_{11} + \hat{\mathbf{K}}_{22} \right) & \mu \left( k_{12}^{-1} \hat{\mathbf{A}} + \hat{\mathbf{D}}_{12} \right) & -\hat{\mathbf{Q}}_1^T \\ \mu \left( k_{21}^{-1} \hat{\mathbf{A}} + \hat{\mathbf{D}}_{21} \right) & \mu \left( k_{22}^{-1} \hat{\mathbf{A}} + \hat{\mathbf{D}}_{22} + \hat{\mathbf{K}}_{11} + \hat{\mathbf{K}}_{22} \right) & -\hat{\mathbf{Q}}_2^T \\ -\hat{\mathbf{Q}}_1 & -\hat{\mathbf{Q}}_2 & 0 \end{pmatrix} \begin{pmatrix} \mathbf{U}_1 \\ \mathbf{U}_2 \\ \mathbf{P} \end{pmatrix} = \begin{pmatrix} \hat{\mathbf{F}}_1 \\ \hat{\mathbf{F}}_2 \\ \hat{\mathbf{F}}_3 \end{pmatrix}. \quad (4.28)$$

To bring back to equations (4.20) and (4.21), the local element matrices are assembled to a global matrix in order to get the numerical solution. In the next section, we present the boundary conditions used in this study.

### 4.3 Boundary Conditions

In this work, we consider the forward stroke of cilia moving from the angle  $\theta = 90^\circ$  to  $40^\circ$ . The numerical domain and the boundaries are shown in Figure 4.2. The variable  $x_1^b$  is the length that  $\xi_{\max}$  is projected on the  $x_1$  axis when the cilia make the angle  $\theta = 40^\circ$  with the horizontal plane. Then  $x_1^b = \cos 40^\circ$  and  $0 \leq x_2 \leq 1$ . The variables  $\Gamma_i, i = 1, 2, 3$ , are the boundaries of the domain  $\Omega_p$  and  $\Gamma_p = \Gamma_1 \cup \Gamma_2 \cup \Gamma_3$ . We let  $\mathbf{u} = (u_1, u_2)$  be the velocity vector, where  $u_1$  is the velocity in the rightward direction and  $u_2$  is the velocity in the upward direction, in which the velocity these directions are considered to be positive numbers. If the cilia move in the downward direction, the velocity  $u_2$  becomes negative. At the boundary  $\Gamma_1$ , we let the fluid velocity be equal to the velocity of the cilia, provide in Section 5.1.2, when the angle  $\theta = 90^\circ$ . Since, from the experimental data [20], the cilia move forward rapidly and stop moving at  $\theta = 40^\circ$  approximately before having the reverse movement, in this work, we assume that the velocity of the cilia is zero at  $\theta = 40^\circ$ . So the velocity at the boundary  $\Gamma_3$  is zero. For the boundary condition at  $\Gamma_2$ , since no one really knows the condition at  $\Gamma_2$ , we consider two cases for this problem.

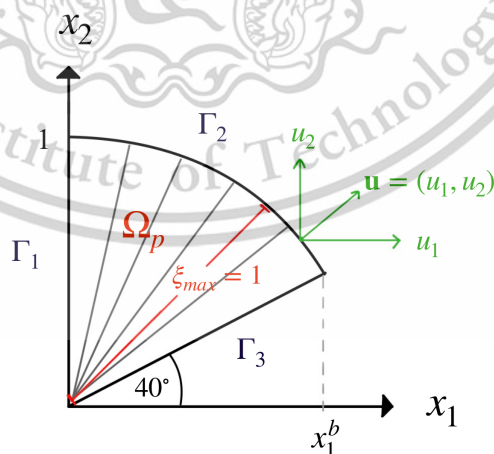


Figure 4.2: The boundary of our domain.

Case 1: We employ the boundary conditions from [35], where they have determined the velocity at the tips of cilia when the cilia move forward and backward. They provide that the rate of change of the fluid velocities with respect to  $x_1$  and  $x_2$  depends on the exponential

function of the angle  $\theta$ . So our boundary conditions at  $\Gamma_1, \Gamma_2$  and  $\Gamma_3$  are

$$u_1(0, x_2) = u^s(x_2), \quad \text{at } \Gamma_1 \quad (4.29)$$

$$\frac{\partial u_1}{\partial x_1} = c_1 e^\theta, \quad \frac{\partial u_1}{\partial x_2} = c_2 e^\theta, \quad \frac{\partial u_2}{\partial x_1} = c_3 e^\theta, \quad \frac{\partial u_2}{\partial x_2} = c_4 e^\theta, \quad \text{at } \Gamma_2 \quad (4.30)$$

$$u_1(x_1, x_2) = u_2(x_1, x_2) = 0, \quad \text{at } \Gamma_3 \quad (4.31)$$

where  $c_1, c_2, c_3$  and  $c_4$  are constants.

Case 2: We assume that boundary conditions at  $\Gamma_2$  are unknown. So to obtain the numerical solution, the velocities  $u_1$  and  $u_2$  at  $\Gamma_2$  are moved to the left-hand side of the equation, used to find the numerical solution, in order to determine  $u_1$  and  $u_2$  at  $\Gamma_2$ .

Next, we show the procedure for applying the boundary conditions for Case 1 and Case 2 into the discretized equations, equation (4.28), provided in the previous section. We begin by considering the terms of the boundary integral appearing in equation (4.4). For simplicity, we define  $\hat{f}_i$  as the boundary integral terms for each element, as follows

$$\hat{f}_i = \int_{\Gamma_p^e} \mu w_i \frac{\partial}{\partial x_j} \left( \frac{u_i}{\varepsilon^l} \right) n_j d\Gamma_p^e + \int_{\Gamma_p^e} \mu w_i \frac{\partial}{\partial x_i} \left( \frac{u_j}{\varepsilon^l} \right) n_j d\Gamma_p^e - \int_{\Gamma_p^e} w_i p n_i d\Gamma_p^e, \quad (4.32)$$

$$= \int_{\Gamma_p^e} \mu w_i \left( \frac{\partial}{\partial x_j} \left( \frac{u_i}{\varepsilon^l} \right) n_j + \frac{\partial}{\partial x_i} \left( \frac{u_j}{\varepsilon^l} \right) n_j \right) d\Gamma_p^e - \int_{\Gamma_p^e} w_i p n_i d\Gamma_p^e, \quad (4.33)$$

where the index  $i$  indicates the number of equations and the repeated index  $j$  indicates summation,  $i, j = 1, 2$ . Substituting the index  $i = 1$  and  $j = 1, 2$  into equation (4.33), we obtain

$$\begin{aligned} \hat{f}_1 &= \int_{\Gamma_p^e} \mu w_1 \left( \frac{\partial}{\partial x_1} \left( \frac{u_1}{\varepsilon^l} \right) n_1 + \frac{\partial}{\partial x_2} \left( \frac{u_1}{\varepsilon^l} \right) n_2 + \frac{\partial}{\partial x_1} \left( \frac{u_1}{\varepsilon^l} \right) n_1 + \frac{\partial}{\partial x_1} \left( \frac{u_2}{\varepsilon^l} \right) n_2 \right) d\Gamma_p^e - \int_{\Gamma_p^e} w_1 p n_1 d\Gamma_p^e, \\ &= \int_{\Gamma_p^e} \mu w_1 \left( 2 \frac{\partial}{\partial x_1} \left( \frac{u_1}{\varepsilon^l} \right) n_1 + \frac{\partial}{\partial x_2} \left( \frac{u_1}{\varepsilon^l} \right) n_2 + \frac{\partial}{\partial x_1} \left( \frac{u_2}{\varepsilon^l} \right) n_2 \right) d\Gamma_p^e - \int_{\Gamma_p^e} w_1 p n_1 d\Gamma_p^e, \end{aligned} \quad (4.34)$$

and, similarly, substituting the index  $i = 2$  and  $j = 1, 2$  into equation (4.33), we obtain

$$\begin{aligned} \hat{f}_2 &= \int_{\Gamma_p^e} \mu w_2 \left( \frac{\partial}{\partial x_1} \left( \frac{u_2}{\varepsilon^l} \right) n_1 + \frac{\partial}{\partial x_2} \left( \frac{u_2}{\varepsilon^l} \right) n_2 + \frac{\partial}{\partial x_2} \left( \frac{u_1}{\varepsilon^l} \right) n_1 + \frac{\partial}{\partial x_2} \left( \frac{u_2}{\varepsilon^l} \right) n_2 \right) d\Gamma_p^e - \int_{\Gamma_p^e} w_2 p n_2 d\Gamma_p^e, \\ &= \int_{\Gamma_p^e} \mu w_2 \left( \frac{\partial}{\partial x_1} \left( \frac{u_2}{\varepsilon^l} \right) n_1 + 2 \frac{\partial}{\partial x_2} \left( \frac{u_2}{\varepsilon^l} \right) n_2 + \frac{\partial}{\partial x_2} \left( \frac{u_1}{\varepsilon^l} \right) n_1 \right) d\Gamma_p^e - \int_{\Gamma_p^e} w_2 p n_2 d\Gamma_p^e. \end{aligned} \quad (4.35)$$

We given by the outward unit normal vector,  $\mathbf{n} = (n_1, n_2)$ , at the boundaries  $\Gamma_1, \Gamma_2$ , and  $\Gamma_3$  used in this work as follows. On boundary  $\Gamma_1$ , the outward unit normal vector is constant:

$$\mathbf{n} = (-1, 0), \quad (4.36)$$

which points directly to the left along the negative  $x_1$ -axis. On boundaries  $\Gamma_2$  and  $\Gamma_3$ , the outward unit normal vector is:

$$\mathbf{n} = \left( \frac{\Delta x_2}{\sqrt{(\Delta x_1)^2 + (\Delta x_2)^2}}, \frac{-\Delta x_1}{\sqrt{(\Delta x_1)^2 + (\Delta x_2)^2}} \right), \quad (4.37)$$

which is calculated based on the perpendicular direction to the edge segment defined by  $(\Delta x_1, \Delta x_2)$ , and normalized to have unit length. The symbols  $\Delta x_1$  and  $\Delta x_2$  denote the difference between two adjacent nodes along the boundary segment for each element in the  $x_1$ -direction and the  $x_2$ -direction, respectively.

For Case 1, we apply the boundary conditions given in equations (4.29)–(4.31) to equations (4.34) and (4.35), yielding the following results;

at  $\Gamma_1$ :

$$\hat{f}_1 = \int_{\Gamma_1^e} w_1 p \, d\Gamma_1^e, \quad (4.38)$$

$$\hat{f}_2 = - \int_{\Gamma_1^e} \mu w_2 \frac{\partial}{\partial x_1} \left( \frac{u_2}{\varepsilon} \right) \, d\Gamma_1^e, \quad (4.39)$$

at  $\Gamma_2$ :

$$\hat{f}_1 = \int_{\Gamma_2^e} \frac{\mu}{\varepsilon} w_1 \left( 2c_1 e^\theta n_1 + c_2 e^\theta n_2 + c_3 e^\theta n_2 \right) \, d\Gamma_2^e - \int_{\Gamma_2^e} w_1 p n_1 \, d\Gamma_2^e, \quad (4.40)$$

$$\hat{f}_2 = \int_{\Gamma_2^e} \frac{\mu}{\varepsilon} w_2 \left( c_3 e^\theta n_1 + 2c_4 e^\theta n_2 + c_2 e^\theta n_1 \right) \, d\Gamma_2^e - \int_{\Gamma_2^e} w_2 p n_2 \, d\Gamma_2^e, \quad (4.41)$$

at  $\Gamma_3$ :

$$\hat{f}_1 = - \int_{\Gamma_3^e} w_1 p n_1 \, d\Gamma_3^e, \quad (4.42)$$

$$\hat{f}_2 = - \int_{\Gamma_3^e} w_2 p n_2 \, d\Gamma_3^e. \quad (4.43)$$

So to obtain the numerical solution of Case 1, we apply the boundary conditions given in equations (4.38) - (4.43) to the element matrix system, equation (4.28).

For Case 2, since the boundary conditions at  $\Gamma_1$  and  $\Gamma_3$  are assumed to be the same as boundary conditions in Case 1, we apply the same equations to these boundaries. At  $\Gamma_2$ , the boundary conditions are assumed to be unknown, so we have:

$$\hat{f}_1 = \int_{\Gamma_2^e} \mu w_1 \left( 2 \frac{\partial}{\partial x_1} \left( \frac{u_1}{\varepsilon^l} \right) n_1 + \frac{\partial}{\partial x_2} \left( \frac{u_1}{\varepsilon^l} \right) n_2 + \frac{\partial}{\partial x_1} \left( \frac{u_2}{\varepsilon^l} \right) n_2 \right) \, d\Gamma_2^e - \int_{\Gamma_2^e} w_1 p n_1 \, d\Gamma_2^e, \quad (4.44)$$

$$\hat{f}_2 = \int_{\Gamma_2^e} \mu w_2 \left( \frac{\partial}{\partial x_1} \left( \frac{u_2}{\varepsilon^l} \right) n_1 + 2 \frac{\partial}{\partial x_2} \left( \frac{u_2}{\varepsilon^l} \right) n_2 + \frac{\partial}{\partial x_2} \left( \frac{u_1}{\varepsilon^l} \right) n_1 \right) \, d\Gamma_2^e - \int_{\Gamma_2^e} w_2 p n_2 \, d\Gamma_2^e. \quad (4.45)$$

In the same process, we apply the boundary conditions given in equations (4.38)–(4.39), (4.42)–(4.43), and (4.44)–(4.45) to the element matrix system in equation (4.28) to obtain the numerical solution for Case 2. Note that the terms involving  $u_1$ ,  $u_2$  and  $p$  for both cases are moved to the left-hand side of the equation to be incorporated into the matrix system in equation (4.28), in order to determine the numerical solution.

At this point, we have presented the discretized form of our mathematical model along with the boundary conditions for Case 1 and Case 2. In the next chapter, we will present the numerical results for both cases using a mixed finite element method of the Taylor–Hood type.

# Chapter 5

## Numerical Solutions

In this chapter, we present the velocity of the PCL fluid due to the forward stroke of the cilia in the porous medium, computed using the generalized Brinkman equation. The results are computed from our own code using MATLAB program. Before we illustrated the numerical results, we provide the permeability, velocity of cilia and porosity used in our program in Section 5.1. The validation of the numerical solutions using the discretized model is presented in Section 5.2. The numerical solutions of the generalized Brinkman equation and the continuity equation is illustrated in Section 5.3.

### 5.1 Permeability, Cilia Velocity and Porosity

Regarding the numerical calculation, the values of the permeability, cilia velocity, and porosity that we use in our program are provided in this section.

#### 5.1.1 Permeability

For the permeability, we employ the values of the permeability tensor from [57], where they have calculated the permeability tensor when an array of rigid cylinders are parallel to each other and has a constant length as shown in Figure 5.1. Figure 5.1 shows the parallel cylinders making the angle  $90^\circ$  to the horizontal plane, which is imitated from [57]. The cylinders are represented as cilia in this work. They have provided the permeability tensor when the parallel array of cylinders make angles  $\theta, 26^\circ \leq \theta \leq 90^\circ$ , to the horizontal plane in the fourth-order polynomial form, which is

$$\hat{k}_{ij} = a_1 z^4 + a_2 z^3 \theta + a_3 z^3 + a_4 z^2 \theta^2 + a_5 z^2 \theta + a_6 z^2 + a_7 z \theta^3 + a_8 z \theta^2 + a_9 z \theta + a_{10} z + a_{11} \theta^4 + a_{12} \theta^3 + a_{13} \theta^2 + a_{14} \theta + a_{15}, \quad (5.1)$$

where  $i, j = 1, 2, 3$ , the coefficients  $a_k, k = 1, 2, \dots, 15$ , are given in Table 3 in [57], and  $z = r/d$ , where  $r$  is the cross-sectional radius of a cylinder and  $d$  is the distance between cylinders.

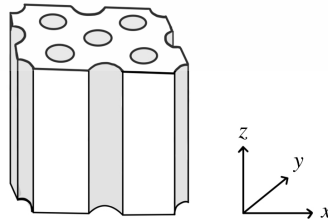


**Figure 5.1:** The geometric cells of the periodic array of 5 cylinders in three dimensions.

Note that in 3 dimensions the permeability

$$\hat{\mathbf{k}} = \begin{pmatrix} \hat{k}_{11} & \hat{k}_{12} & \hat{k}_{13} \\ \hat{k}_{21} & \hat{k}_{22} & \hat{k}_{23} \\ \hat{k}_{31} & \hat{k}_{32} & \hat{k}_{33} \end{pmatrix}. \quad (5.2)$$

So the coefficients  $a_k$ ,  $k = 1, 2, \dots, 15$ , are different for each  $\hat{k}_{ij}$ ,  $i, j = 1, 2, 3$ . In this work, we consider the 2-dimensional problem, where the cilia move in  $x_1$  and  $x_2$  directions, which are  $x$  and  $z$  in Figure 5.1. So the permeability used in our code comes from the first and third rows and columns of equation (5.2). That is our permeability

$$\mathbf{k} = \begin{pmatrix} k_{11} & k_{12} \\ k_{21} & k_{22} \end{pmatrix} = \begin{pmatrix} \hat{k}_{11} & \hat{k}_{13} \\ \hat{k}_{31} & \hat{k}_{33} \end{pmatrix}. \quad (5.3)$$

Since  $\hat{\mathbf{k}}$  is symmetric,  $k_{12} = k_{21}$ . Based on laboratory data of cilia in human lungs that provided in [64], the radius of cilia is  $0.1 \mu\text{m}$  and the distance between cilia is  $0.3 \mu\text{m}$ . Then substituting  $z = 1/3$  and  $\theta = \arctan(x_2/x_1)$  into equation (5.1), we obtain  $k_{11}, k_{12} = k_{21}$  and  $k_{22}$ , which will be used in Sections 5.2 and 5.3.

### 5.1.2 Velocity of cilia

We provide the solid velocity  $\mathbf{u}^s$  used in this study employed from [50, 20]. In [20] they experimentally provide the speed of cilia in lungs when cilia make angles  $40^\circ$  to  $140^\circ$  approximately with the horizontal plane. Next, Wuttanachamsri and Schreyer [50] convert the cilia speed into a polynomial form. The solid speed is approximated in the form of the eighth-order polynomial functions where the coefficients  $a_i$ ,  $i = 1, 2, \dots, 8$  for the angles  $50^\circ, 60^\circ, 70^\circ, 80^\circ$  and  $90^\circ$  are given in Table 1 in [50]. That is the speed of cilia

$$s = a_1 \xi^8 + a_2 \xi^7 + a_3 \xi^6 + a_4 \xi^5 + a_5 \xi^4 + a_6 \xi^3 + a_7 \xi^2 + a_8 \xi, \quad (5.4)$$

where  $\xi$  is the distance along cilia as shown in Figure 4.1. The variable  $s$  in equation (5.4) represents the solid speed along the cilia. To find the speed of the cilia at each point  $(x_1, x_2)$ , we substitute  $\xi = x_2/\sin\theta$  into the polynomial approximation (5.4). Because we consider the 2-dimensional domain, let the cilia velocity  $\mathbf{u}^s = (u_1^s, u_2^s)$ . The components in  $x_1$ -direction and  $x_2$ -direction of the cilia velocity are  $u_1^s = s \sin\theta$  and  $u_2^s = -s \cos\theta$ , respectively.

From [20], they experimentally provide that for the forward stroke of cilia, the cilia stop beating at  $\theta = 40^\circ$  approximately. In this research, we assume the cilia start at  $\theta = 90^\circ$ , move forward with decreasing angle, and stop beating at  $\theta = 40^\circ$ . Because the angles used in this study are 5 degrees apart, we determine the cilia speed at the angles  $85^\circ, 75^\circ, \dots, 45^\circ$  by averaging the cilia speed of two adjacent angles. For example, we calculate the cilia speed at  $\theta = 85^\circ$  by averaging the cilia speed at  $\theta = 80^\circ$  and  $\theta = 90^\circ$ . We provide the coefficients of equation (5.4) at  $\theta = 45^\circ, 55^\circ, 65^\circ, 75^\circ$  and  $85^\circ$  in Table 5.1 and the speed profiles of the angles are represented in Figure 5.2. Table 5.1 illustrates the coefficients  $a_i$ ,  $i = 1, 2, \dots, 8$  of the terms of the polynomial in equation (5.4) which are not provided in [50]. Figure 5.2 illustrates the speed along cilia from the roots to the tips of cilia from the angle  $\theta = 40^\circ$  to  $90^\circ$ . The black line is the velocity at  $\theta = 40^\circ, 50^\circ, 60^\circ, 70^\circ, 80^\circ$  and  $90^\circ$  presented in [50], and the red line is the speed at  $\theta = 45^\circ, 55^\circ, 65^\circ, 75^\circ$  and  $85^\circ$  and also we show the speed at  $\theta = 42.5^\circ, 47.5^\circ, 52.5^\circ, \dots, 87.5^\circ$  as illustrated by the green

line. The speed of the cilia is maximum at the angle  $\theta = 90^\circ$  and the speed is reduced when the angle  $\theta$  decreases until the cilia speed equals to zero at  $\theta = 40^\circ$ .

**Table 5.1:** The coefficients of the eighth-order polynomial functions.

| Coefficients | Degree        |             |             |             |             |            |
|--------------|---------------|-------------|-------------|-------------|-------------|------------|
|              | $\times 10^5$ | $45^\circ$  | $55^\circ$  | $65^\circ$  | $75^\circ$  | $85^\circ$ |
| $a_1$        | 0.12489999    | 0.32704999  | -0.04719999 | -0.43174999 | -0.45169999 |            |
| $a_2$        | -0.53904999   | -1.37844999 | 0.22399999  | 1.84774999  | 1.89174999  |            |
| $a_3$        | 0.96449999    | 2.39729999  | -0.42229999 | -3.23804999 | -3.24839999 |            |
| $a_4$        | -0.92294999   | -2.22019999 | 0.40379999  | 2.98859999  | 2.94744999  |            |
| $a_5$        | 0.50664999    | 1.17564999  | -0.20744999 | -1.55564999 | -1.51859999 |            |
| $a_6$        | -0.15784999   | -0.35264999 | 0.05579999  | 0.45169999  | 0.44124999  |            |
| $a_7$        | 0.02519999    | 0.05444999  | -0.00659999 | -0.06549999 | -0.06434999 |            |
| $a_8$        | -0.00114999   | -0.00234999 | 0.00124999  | 0.00464999  | 0.00469999  |            |

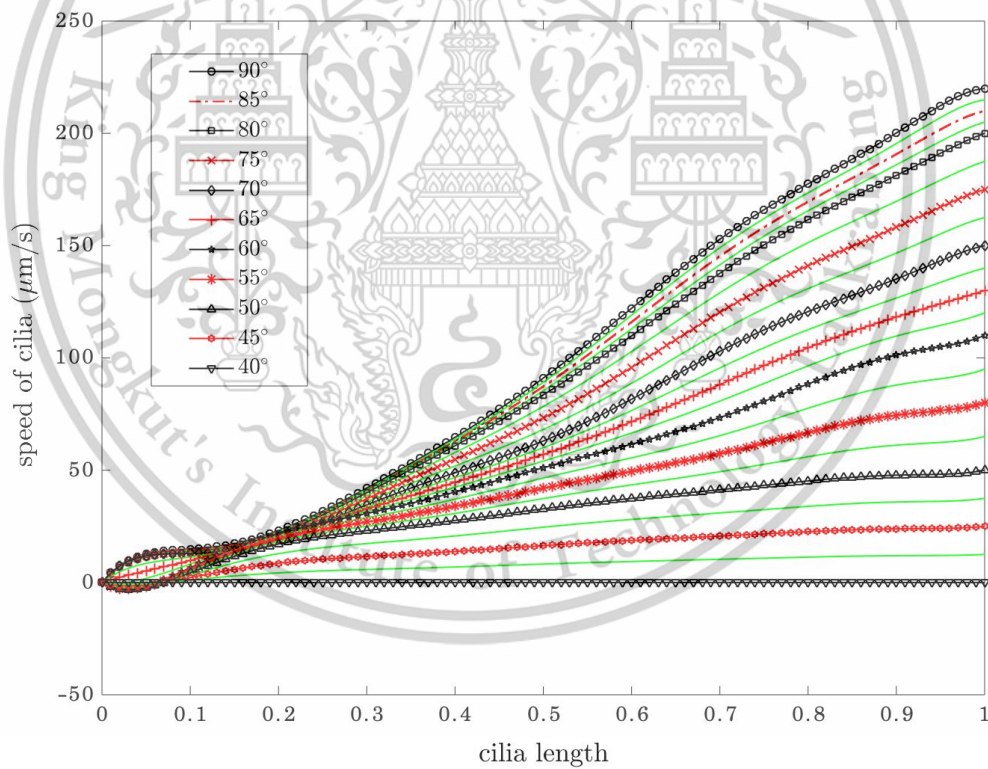


**Figure 5.2:** Speed of cilia along the cilia length.

### 5.1.3 Porosity

For the value of the porosity  $\epsilon^l$ , we employ the value from [50], where they provide the porosity of an parallel array of cilia making  $\theta = 90^\circ, 80^\circ, \dots, 40^\circ$  with horizontal plane in a cell domain. They approximate the porosity from [57] and present the porosity in a polynomial form.

Forbidden to modify the content, and cite the document when use.

The fifth-degree polynomial function provided in [50] is

$$\varepsilon^I(\theta) = 0.5223\theta^5 - 3.0283\theta^4 + 7.0630\theta^3 - 8.4987\theta^2 + 5.5056\theta - 0.8627, \quad (5.5)$$

where  $\theta$  is the angle that cilia make with the horizontal plane given in radians. The values of other variables that are used in the code and the validation of the numerical solutions are presented in the next section. The numerical results of the velocities of the PCL fluid are provided in Section 5.3.

## 5.2 Numerical Validation

Before we provide our numerical results, we first validate our numerical solutions by using the discretized model provided in Section 4.2, equation (4.28). For this validation, we begin with the two-dimensional numerical domain, as shown in Figure 4.2. The domain is in the shape of a portion of a quarter circle. After that we apply mesh generator Netgen [65] to generate triangular mesh, as shown in Figure 5.3. Figure 5.3 shows the example of our generated mesh with 5 degrees apart. To validate the numerical result, we use four different mesh refinements. The four discretized domains consist of 30, 45, 270, and 704 elements. For the constant variables, we let  $\mu = 3 \times 10^{-6} \text{ g}/(\mu\text{m}\cdot\text{s})$ ,  $\rho = 992.2 \times 10^{-15} \text{ g}/\mu\text{m}^3$ , the gravity  $g = 9.81 \times 10^6 \mu\text{m}/\text{s}^2$  and the coefficient values  $c_1 = c_2 = c_3 = c_4 = 1$  in equation (4.30). For the shape functions, we use quadratic triangular elements for the velocity and linear triangular elements for the pressure, confirming the stability of the method known as the Taylor-Hood elements [66]. Therefore, in equations (3.18) and (3.19),  $M = 6$  and  $L = 3$ .

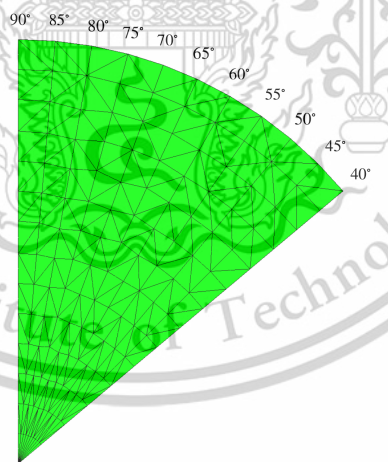


**Figure 5.3:** Generated mesh for the numerical domain.

Next, we clarify the value of the inverse of the permeability tensor,  $\mathbf{k}^{-1}$ , used in our program. Because the polynomial function (5.1) used to approximate the permeability tensor is the function that depends on  $\theta$ , for each  $k_{ij}$  where  $i, j = 1, 2$ , we have 6 values per one element. In this work, for each element, we average the 6 values of each  $k_{ij}$  and use the average value of each  $k_{ij}$  to find the numerical solutions. We then compute the inverse of the matrix  $\mathbf{k}$  to obtain  $k_{ij}^{-1}$  for each element.

This method is used for the solid velocity, we approximate the solid velocity in equations (4.26) and (4.27)

as

$$\mathbf{u}_j^s(\mathbf{x}) = \sum_{m=1}^M \psi_m(\mathbf{x})(u_j^s)_m = \Psi^T \mathbf{U}_j^s. \quad (5.6)$$

where  $\mathbf{U}_j^s$  is the vector of solid velocities  $(u_j^s)_m$ ,  $m = 1, \dots, M$ ,  $j = 1, 2$ .

For the porosity, we use the same process of calculating the permeability tensor to compute the value of the porosity  $\varepsilon^l$  because the porosity  $\varepsilon^l$  is a function that depends on  $\theta$ . That is we use the average value of the porosity  $\varepsilon^l$  for each element to find the numerical solutions. For the term  $\frac{\partial \varepsilon^l}{\partial x_j}$  in equation (4.27), to compute the numerical solution, we approximate the derivative of the porosity as

$$\frac{\partial \varepsilon^l(\mathbf{x})}{\partial x_j} = \sum_{m=1}^M \frac{\partial \psi_m^T(\mathbf{x})}{\partial x_j} \varepsilon_m^l = \frac{\partial \Psi^T}{\partial x_j} \Upsilon^l, \quad (5.7)$$

where  $\Upsilon^l$  is the vector value of  $\varepsilon^l$ , consisting of six nodes per element. These values will be substituted into equation (4.28) to calculate the numerical solutions.

To validate the code, we choose to present the velocity profile of the PCL fluid when  $\theta = 80^\circ$ . Since, in our work, we consider 2 cases of the boundary conditions, we provide our numerical results for the two cases. Figures 5.4 and 5.5 illustrate the PCL velocities for Case 1 and Case 2 boundary conditions, respectively. In both figures, the left graph shows the velocity  $u_1$  and the right graph presents  $u_2$ . The blue, orange, yellow, and purple lines represent the velocity of the PCL fluid obtained from the grid refinements containing 30, 45, 270, and 704 elements, respectively. In both figures, the numerical solutions obtained from the coarser grids converge to the numerical solutions obtained from the finest grid. Table 5.2 presents the  $l_2$ -norm errors of the velocities  $u_1$  and  $u_2$  of the PCL fluid at the angle  $\theta = 80^\circ$ , compared to the solutions obtained from the finest grid, 704 elements. The results show that the errors decrease as the number of elements increases, illustrating the convergence of the numerical solutions.

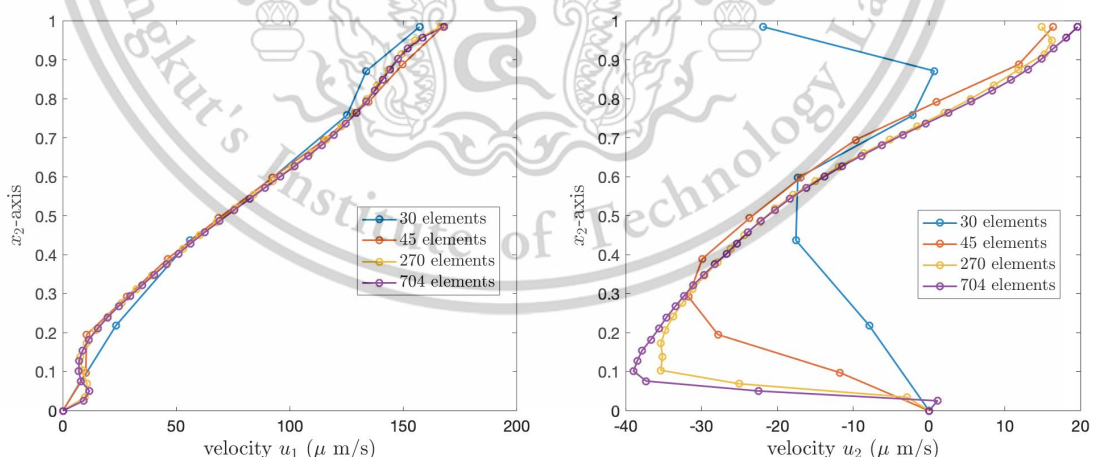


**Figure 5.4:** The velocities of the PCL fluid obtained from four different mesh refinements at the angle  $\theta = 80^\circ$  for the Case 1 boundary condition. The left graph is the velocity  $u_1$ , while the right graph is the velocity  $u_2$ .

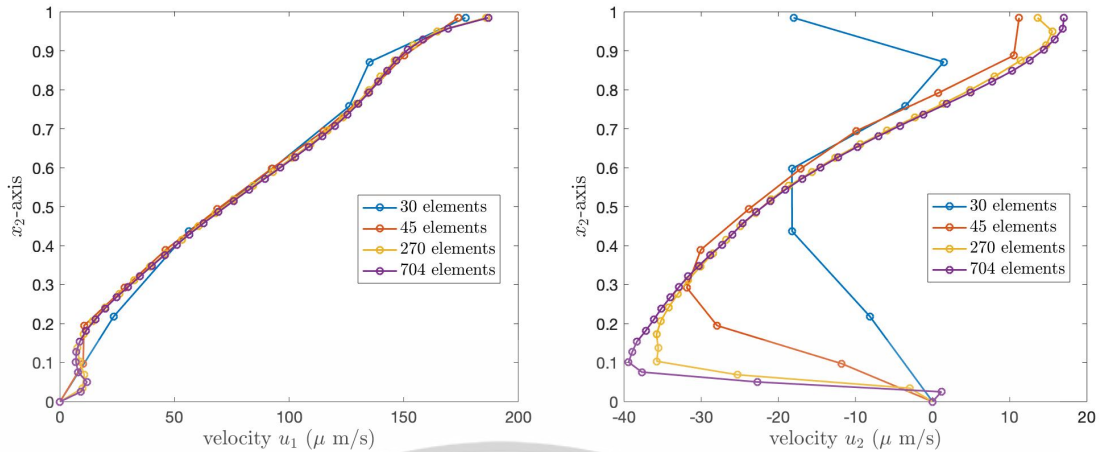


**Figure 5.5:** The velocities of the PCL fluid obtained from four different mesh refinements at the angle  $\theta = 80^\circ$  for the Case 2 boundary condition. The left graph is the velocity  $u_1$ , while the right graph is the velocity  $u_2$ .

**Table 5.2:** The  $l_2$ -norm errors of the PCL velocity obtained from the different mesh refinements at the angle  $\theta = 80^\circ$ .

| number of elements | $l_2$ -norm errors |         |         |         |
|--------------------|--------------------|---------|---------|---------|
|                    | Case 1             |         | Case 2  |         |
|                    | $u_1$              | $u_2$   | $u_1$   | $u_2$   |
| 30                 | 17.8755            | 52.3543 | 18.1664 | 47.3204 |
| 45                 | 8.8341             | 30.1146 | 15.3896 | 30.7428 |
| 270                | 8.8134             | 15.1360 | 9.7240  | 14.8701 |

### 5.3 Numerical results

The numerical solutions of the generalized Brinkman equation and the continuity equation, equations (4.1)-(4.2), are presented in this section. We use the 2-dimensional finite element method to determine the velocities of the PCL fluid propelled by moving cilia in the porous medium. We present the velocity of the PCL fluid when cilia make angle  $90^\circ$  to  $40^\circ$  to the horizontal plane. Two cases of the boundary conditions are considered. The values of the dynamic viscosity, fluid density, gravity and the coefficients  $c_i$ ,  $i = 1, 2, 3, 4$ , are the same as in Section 5.2.

We use the triangular mesh with 270 elements and 579 points generated by Netgen [65] as shown in Figure 5.3. The numerical domain  $\Omega$  is divided into 10 subdomains. The first subdomain starts from the leftmost vertical line, at  $\theta = 90^\circ$ , to the inclined line, at  $\theta = 85^\circ$ . The second subdomain is next to the right of the first subdomain starting from  $\theta = 85^\circ$  to  $\theta = 80^\circ$ . Continuing the process until reaching  $\theta = 40^\circ$ , we have 10 different subdomains. By using the mixed finite element method of Taylor-Hood type, we obtain the numerical results which are illustrated in Figure 5.6. The first row of Figure 5.6 shows the velocities of the PCL fluid using the Case 1 boundary condition. The top left graph represents the velocity  $u_1$  in the  $x_1$  direction, while the top right graph presents the velocity  $u_2$  in the  $x_2$  direction. The velocity of the PCL

fluid decreases when the angle decreases. This is affected from the velocity of cilia, see Figure 5.2. The velocity  $u_1$  is highest when  $\theta = 90^\circ$ , and the velocity is zero at  $\theta = 40^\circ$  because the velocity of cilia is highest at  $\theta = 90^\circ$  and the cilia stop beating at  $\theta = 40^\circ$ . For the velocity  $u_2$ , when the angle decreases the velocity  $u_2$  at the tips of cilia decreases from  $110.74$  to  $-36.64 \mu\text{m/s}$  and then increases slightly until the velocity approaches zero at  $\theta = 40^\circ$ . The velocity  $u_2$  is negative because for the forward bend direction of cilia, the vertical velocity changes from the positive to the negative direction. The second row of Figure 5.6 illustrates the velocities  $u_1$  and  $u_2$  of the PCL fluid under the Case 2 boundary condition for the angles ranging from  $\theta = 90^\circ$  to  $40^\circ$ . The bottom left graph presents the velocity  $u_1$  and the bottom right graph represents the velocity  $u_2$ . In this case, we assume that the boundary condition at  $\Gamma_2$ , at the tips of the cilia, is unknown. Similarly as in Case 1, the velocity  $u_1$  of the PCL fluid reduces as the angles decrease, and the maximum velocity of the PCL fluid occurs at the tips of cilia. The difference of  $u_1$  between Case 1 and Case 2 is that the velocity at the tips of cilia in Case 2 appears like a wave, moving up and down at the free interface. Similarly as in Case 1, the velocity  $u_2$  is highest at the tips of cilia at  $\theta = 90^\circ$ . As the angle decreases, the velocity  $u_2$  at the tips of cilia reduces from  $90.39$  to  $-37.06 \mu\text{m/s}$  before gradually increasing in the positive direction until it reaches zero at  $\theta = 40^\circ$ . We also observe that the velocity  $u_2$  at the tips of cilia in this case is smaller than the velocity  $u_2$  in Case 1 for all angles.

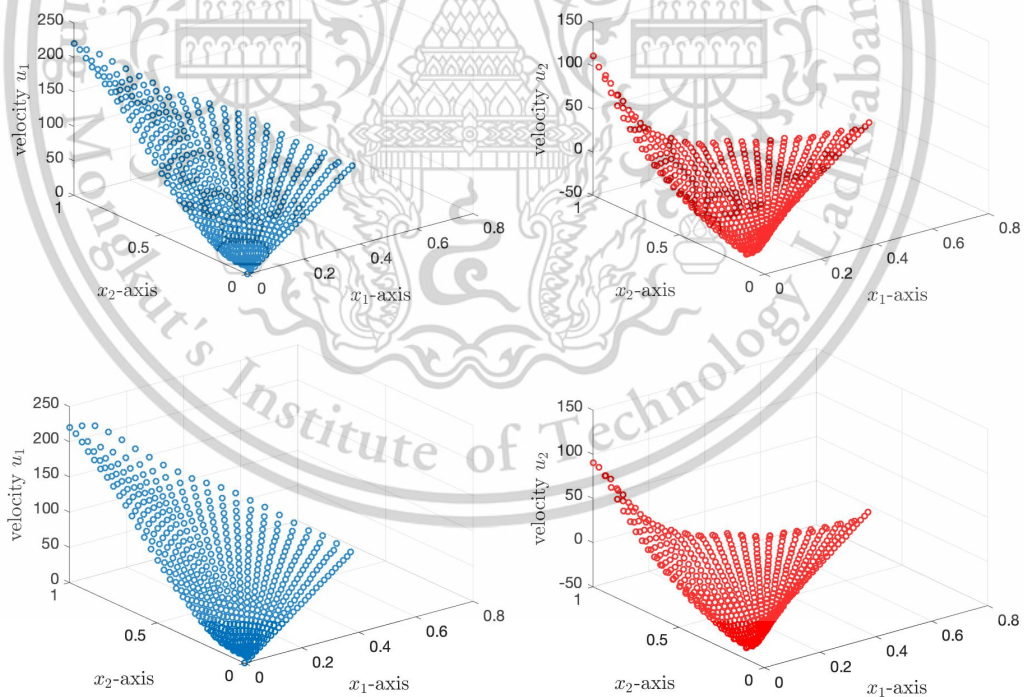


**Figure 5.6:** The velocities  $u_1$  (left) and  $u_2$  (right) of the PCL fluid for all angles. The first row shows the velocities for the Case 1 boundary condition while the second row shows the velocities for the Case 2 boundary condition.

Next, we average the velocities  $u_1$  and  $u_2$  of the PCL fluid over the  $x_1$ -axis. The first row of Figure 5.7 shows the average velocities of the PCL fluid for the Case 1 boundary condition, Forbidden to modify the content, and cite the document when use.

while the second row illustrates the average velocities of the PCL fluid for the Case 2 boundary condition. The top left graph shows the average velocity of  $u_1$ , while the top right graph shows the average velocity of  $u_2$ . The average velocities of  $u_1$  and  $u_2$  are almost the same for both cases. For the velocity  $u_2$ , near the root of cilia, the velocity has negative value and the velocity gradually increases to positive value along the cilia until the tips of cilia. The highest average velocities are at the tips of cilia for all cases. The mean velocities of  $u_1$  for Case 1 and Case 2 are 46.55 and 47.26  $\mu\text{m/s}$ , respectively. The mean velocities of  $u_2$  for Case 1 and Case 2 are  $-13.95$  and  $-14.57$   $\mu\text{m/s}$ , respectively. The mean velocities for both cases of  $u_1$  are close to the velocity of the PCL fluid obtained from an experimental data [19]. They studied the movements of PCL and mucus in human tracheobronchial epithelial cell cultures using conventional and confocal microscopy of fluorescent microspheres. They found that the PCL fluid and mucus move at similar rates,  $39.2 \pm 4.7$  and  $39.8 \pm 4.2$   $\mu\text{m/s}$ , respectively, which is close to our mean velocity  $u_1$  for both cases.



**Figure 5.7:** The average velocities  $u_1$  and  $u_2$  of the PCL fluid. The top left shows the average velocity  $u_1$  of Case 1, while the top right presents the average velocity  $u_2$  of Case 1. The bottom left shows the average velocity  $u_1$  of Case 2, while the bottom right presents the average velocity  $u_2$  of Case 2.

Figure 5.8 shows the speed of the PCL fluid of the both cases of the boundary conditions. The left and right graphs illustrate the speed of the PCL fluid for the Case 1 and Case 2, respectively. The shapes of the graphs for both cases are similar to the velocity  $u_1$  except at the bottom of the representations. The difference comes from the effect of the negative value  $u_2$  near the root of cilia. It shows that the velocity  $u_1$  is more impactful to the PCL-fluid movement than  $u_2$ .

Forbidden to modify the content, and cite the document when use.

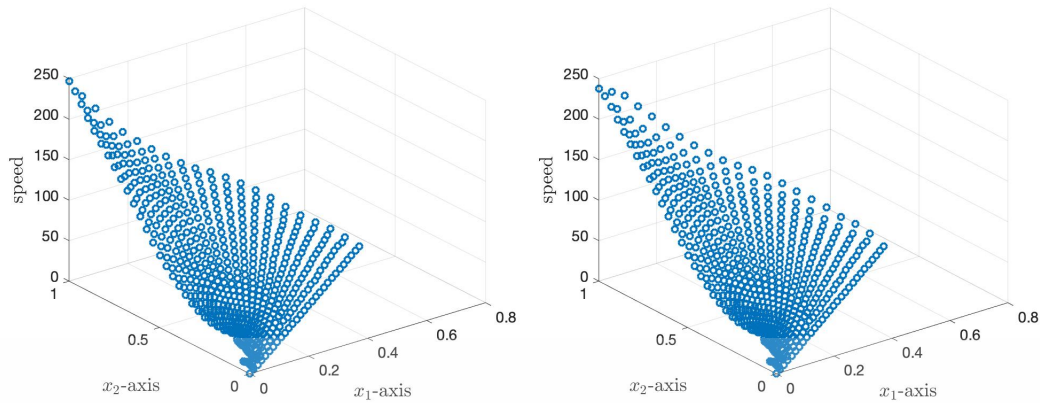


**Figure 5.8:** The left figure shows the speed of the PCL fluid for the Case 1 boundary condition and the right figure presents the speed for the Case 2 boundary condition.

Next, we study the speed of the PCL fluid at the tips of cilia for different constants  $c_i$ ,  $i = 1, 2, 3, 4$ , which are the coefficients in the boundary condition at  $\Gamma_2$  of Case 1. In the previous numerical results, we use  $c_i = 1$  for all  $i$ . For other values of  $c_i$ ,  $i = 1, 2, 3, 4$ , we present the speed of the PCL fluid at the tips of cilia in Figures 5.9 and 5.10. Figure 5.9 shows the speed at the tips of cilia when  $c_1 = c_2 = c_3 = c_4 = c$ , where  $c = 1, 10, 20, 30, 40, 50$ . From the graph, it can be observed that the different values of  $c_i$  result in slight variations in speed. Figure 5.10 illustrates the speed of the PCL fluid at the tips of cilia when the values of  $c_i$ ,  $i = 1, 2, 3, 4$ , are not equal. We also present the speed of the PCL fluid at the tips of cilia for Case 2 in order to compare the speed for Case 1 and Case 2 with different value of  $c_i$ ,  $i = 1, 2, 3, 4$ . From the graph, we observe that the red and yellow lines are closed to the line of Case 2. We also found that, despite different values of  $c_i$ , the shapes of all speed profiles in Figures 5.9 and 5.10 are similar.

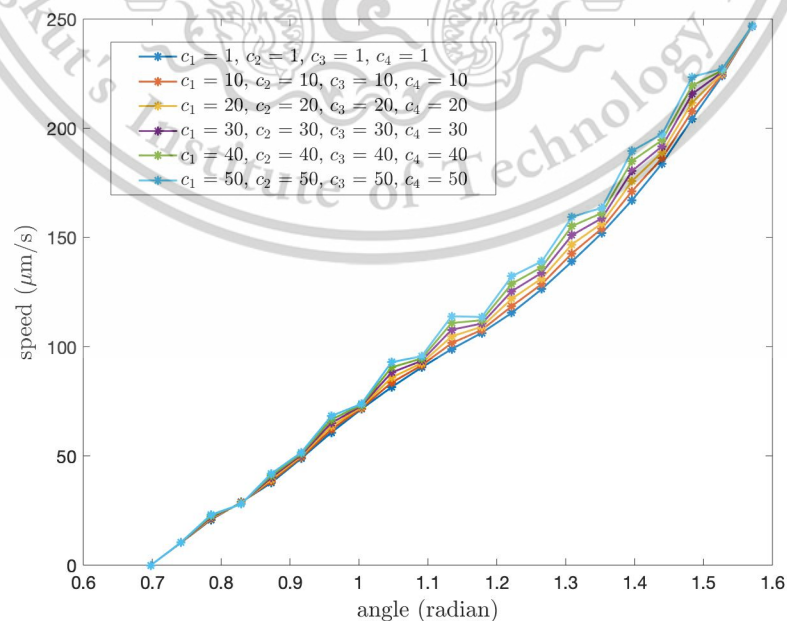


**Figure 5.9:** The speed of the PCL fluid at the tips of cilia for Case 1 boundary condition when  $c_1 = c_2 = c_3 = c_4 = c$ ,  $c = 1, 10, 20, \dots, 50$ .

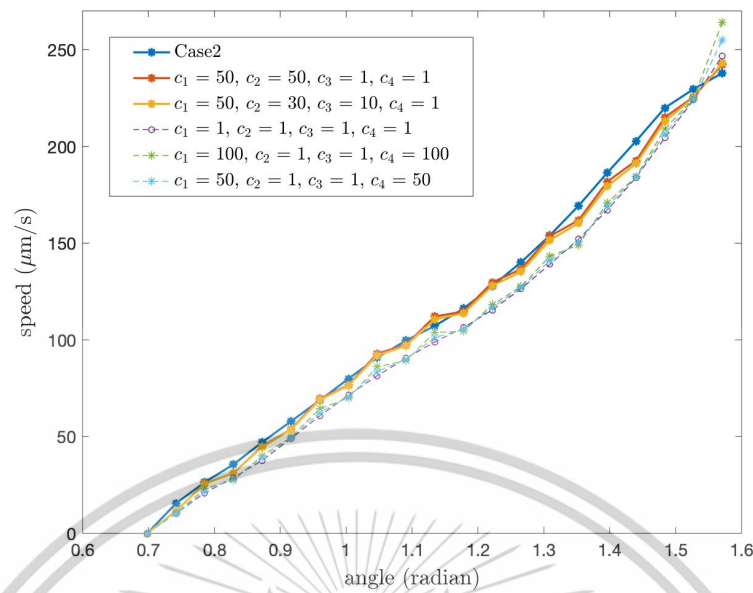


**Figure 5.10:** The speed of the PCL fluid at the tips of cilia with different values of  $c_i$  for  $i = 1, 2, 3, 4$ .

Because the velocity of the PCL fluid at the tips of cilia affects the velocity of mucus and the thickness of mucus can cause lung diseases, we focus on the velocity at the tips of cilia. We provide polynomial approximations of the velocities  $u_1$  and  $u_2$ , as well as the speed of the PCL fluid at the tips of cilia for both cases of the boundary conditions illustrated in Figures 5.11 – 5.13. We use  $c_1 = c_2 = c_3 = c_4 = 1$ . Here, we provide the polynomial approximations of degrees 1, 8, and 15 for the velocities  $u_1$  and the speed at the tips of cilia because the velocity  $u_1$  and the speed profiles at the tips of cilia can be approximated by straight lines with an acceptable error and sometime it is convenient to use the first degree polynomials for some problems. The polynomial approximations of degrees 8 and 15 are provided for  $u_2$ . In these figures, the horizontal axis represents the angle, measured in radians, ranging from  $40^\circ$  to  $90^\circ$ . The green, magenta and blue lines represent the polynomial approximations of degrees 1, 8 and 15, respectively. Figure 5.11 shows the velocity  $u_1$  of the PCL fluid at the tips of cilia and its polynomial approximations for Case 1 (left) and Case 2 (right) boundary conditions. We find that the velocity  $u_1$  at the tips of cilia in both cases increase as the angle  $\theta$  increases from  $40^\circ$  to  $90^\circ$  and the maximum velocity occurs at the angle  $\theta = 90^\circ$ .

Figure 5.12 illustrates the velocity  $u_2$  of the PCL fluid at the tips of cilia and its polynomial approximations for both cases of the boundary conditions. The velocity  $u_2$  for the Case 1 boundary condition (left) is greater than the velocity  $u_2$  for the Case 2 boundary condition (right), especially at  $\theta = 90^\circ$ . Although the shapes of the graphs in both cases have similar shapes, the values of the velocity  $u_2$  are different. The velocity  $u_2$  is maximum at  $\theta = 90^\circ$ , then it decreases as the angle decreases until  $\theta = 60^\circ$ . Then the velocity increases until it reaches zero at  $\theta = 40^\circ$ .

Figure 5.13 shows the speed of the PCL fluid at the tips of cilia and the first, eighth- and fifteenth-degree polynomial approximations for Case 1 (left) and Case 2 (right) boundary conditions. We see that the shapes of the speeds at the tips of cilia are similar to the shapes of the velocity  $u_1$  for both cases, see Figure 5.11. This means the velocity  $u_1$  affects the motion of the PCL fluid more than the velocity  $u_2$ .

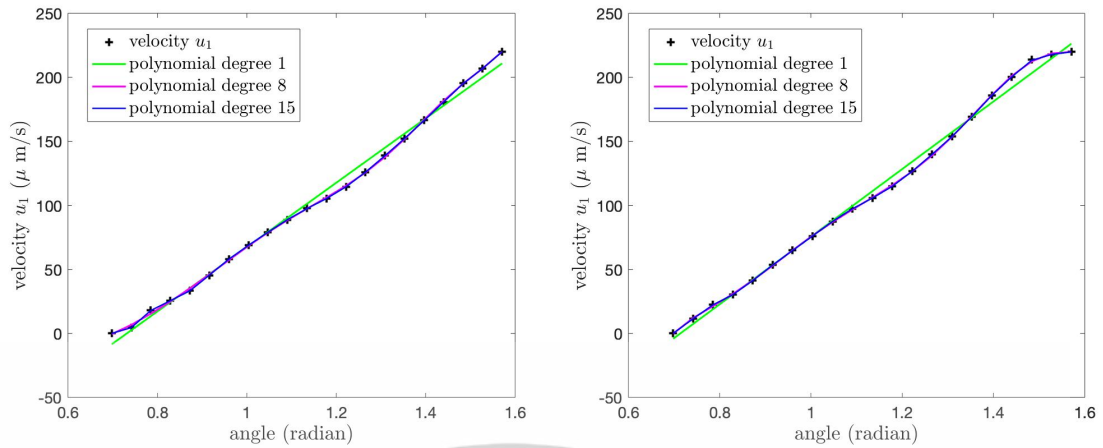


Figure 5.11: The velocity  $u_1$  of the PCL fluid at the tips of cilia for Case 1 boundary condition (left) and for Case 2 boundary condition (right).

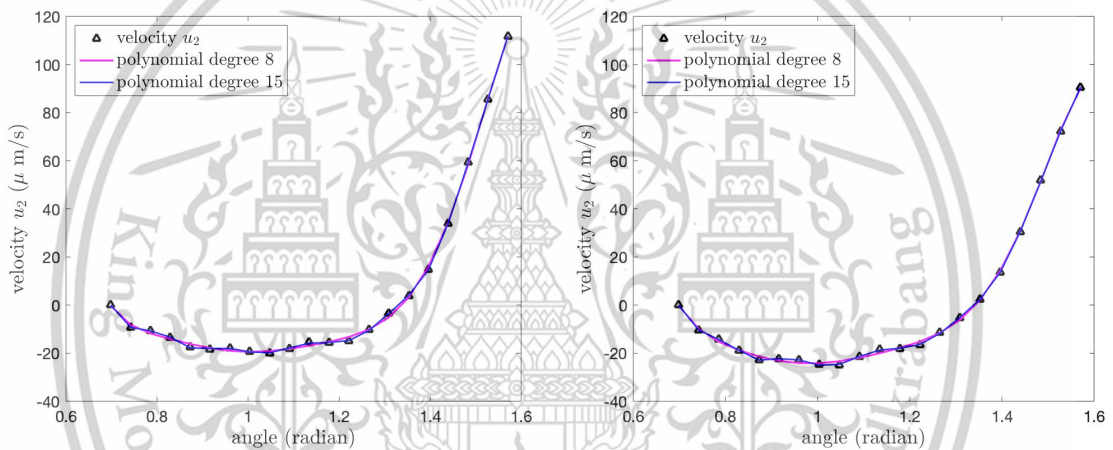


Figure 5.12: The velocity  $u_2$  of the PCL fluid at the tips of cilia for Case 1 boundary condition (left) and for Case 2 boundary condition (right).

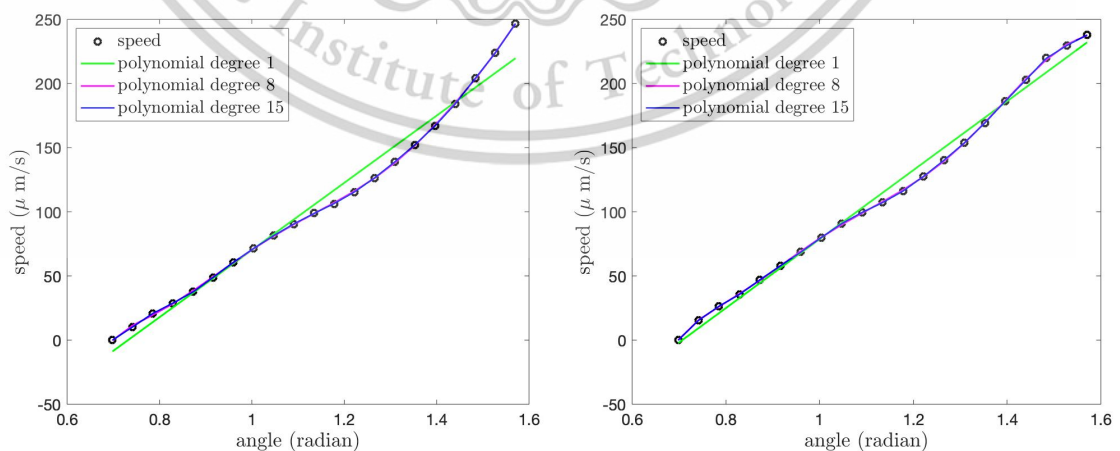


Figure 5.13: The speed of the PCL fluid at the tips of cilia for Case 1 boundary condition (left) and for Case 2 boundary condition (right).

This material is reserved for educational use only, not allowed for commercial use.

Forbidden to modify the content, and cite the document when use.

From physical perspectives, the PCL fluid appears to move similarly to the motion of the cilia. That is the velocity of the PCL fluid increases progressively from the base to the tips of cilia. As the cilia angle decreases, indicating greater bending, the fluid velocity at the tips also decreases, implying that propulsion efficiency is reduced during the motion. Since cilia are self-propelled organelles that move forth speedily and back gently, they perform their power stroke to move fluids and then they gradually back to their starting position, which is slower than the forward stroke. This pattern of acceleration and deceleration repeats periodically due to the nature of cilia. As a result, the PCL fluid moves faster when the cilia are upright (effective stroke), slows down during the bending, and then accelerates again when the cilia are in the upright position, resulting in a pulsatile flow pattern similar to metachronal waves.

The polynomial functions and their coefficients are given in Tables 5.3, 5.3 and 5.3. Table 5.3 illustrates the coefficients of the first-degree polynomial function. Tables 5.3 and 5.3 show the coefficients of the eighth-and fifteenth-degree polynomial functions, respectively.

**Table 5.3:** The first-degree polynomial function:  $p(\theta) = a_1\theta + a_2$  estimates the speed and the velocities  $u_1$  at the tips of cilia for both cases of the boundary conditions, where  $\theta$  is the angle in radians.

| coefficients | Case 1              |                | Case 2      |                |
|--------------|---------------------|----------------|-------------|----------------|
|              | $10^2 \times$ speed | velocity $u_1$ | speed       | velocity $u_1$ |
| $a_1$        | 2.61877889          | 2.51367073     | 2.68644586  | 2.64005346     |
| $a_2$        | -1.91617185         | -1.83969272    | -1.89878036 | -1.88461055    |

**Table 5.4:** The eighth-degree polynomial function:  $p(\theta) = a_1\theta^8 + a_2\theta^7 + a_3\theta^6 + a_4\theta^5 + a_5\theta^4 + a_6\theta^3 + a_7\theta^2 + a_8\theta + a_9$  estimates the speed and the velocities  $u_1$  and  $u_2$  at the tips of cilia for both cases of the boundary conditions, where  $\theta$  is the angle in radians.

| coefficients | Case 1              |                    |                    |
|--------------|---------------------|--------------------|--------------------|
|              | $10^6 \times$ speed | $u_1$              | $u_2$              |
| $a_1$        | -0.012734118271167  | 0.057378313095743  | 0.008776158423867  |
| $a_2$        | 0.135670026652116   | -0.500821282568611 | -0.107483926304666 |
| $a_3$        | -0.617877401645130  | 1.885859004719336  | 0.527199931990443  |
| $a_4$        | 1.572260187763733   | -4.001363507459469 | -1.393202912554586 |
| $a_5$        | -2.445640591057800  | 5.233621138954125  | 2.203387221815350  |
| $a_6$        | 2.381652851245531   | -4.323269305568677 | -2.155213357695548 |
| $a_7$        | -1.418299927611897  | 2.204332823035274  | 1.280981336161525  |
| $a_8$        | 0.472589132393864   | -0.634706944987602 | -0.424880299024707 |
| $a_9$        | -0.067549690623399  | 0.079037225239463  | 0.060416408378815  |

| coefficients  |                    | Case 2             |                    |
|---------------|--------------------|--------------------|--------------------|
| $10^6 \times$ | speed              | $u_1$              | $u_2$              |
| $a_1$         | -0.010939237329981 | 0.015621983213058  | 0.008379732732943  |
| $a_2$         | 0.124622237256656  | -0.112413273633599 | -0.100340169104345 |
| $a_3$         | -0.597329420016729 | 0.319219155174230  | 0.484478291821826  |
| $a_4$         | 1.580853921698133  | -0.425346939699839 | -1.264833543315435 |
| $a_5$         | -2.535184997493686 | 0.184504901777252  | 1.980693486623330  |
| $a_6$         | 2.529299675528232  | 0.190169061295289  | -1.921683695840503 |
| $a_7$         | -1.536399388702010 | -0.289319521303333 | 1.134790516797084  |
| $a_8$         | 0.520744248609177  | 0.143704103345063  | -0.374654504988026 |
| $a_9$         | -0.075587763208465 | -0.026064000222104 | 0.053145691955595  |

**Table 5.5:** The fifteenth-degree polynomial function:  $p(\theta) = a_1\theta^{15} + a_2\theta^{14} + a_3\theta^{13} + a_4\theta^{12} + a_5\theta^{11} + a_6\theta^{10} + a_7\theta^9 + a_8\theta^8 + a_9\theta^7 + a_{10}\theta^6 + a_{11}\theta^5 + a_{12}\theta^4 + a_{13}\theta^3 + a_{14}\theta^2 + a_{15}\theta + a_{16}$  estimates the speed and the velocities  $u_1$  and  $u_2$  at the tips of cilia for both cases of the boundary conditions, where  $\theta$  is the angle in radians.

| coefficients     |                    | Case 1             |                    |
|------------------|--------------------|--------------------|--------------------|
| $10^{13} \times$ | speed              | $u_1$              | $u_2$              |
| $a_1$            | 0.000148633026563  | 0.000238695384065  | 0.000026480736805  |
| $a_2$            | -0.002550402419714 | -0.004115644913638 | -0.000605547516345 |
| $a_3$            | 0.020326208989479  | 0.032955135924412  | 0.006026245594933  |
| $a_4$            | -0.099800320623606 | -0.162544503017583 | -0.035447475762319 |
| $a_5$            | 0.337572785098084  | 0.552225554160010  | 0.139568160750811  |
| $a_6$            | -0.833149607242801 | -1.368720582565515 | -0.392545818489031 |
| $a_7$            | 1.549823716319571  | 2.556522729178357  | 0.818652144300971  |
| $a_8$            | -2.212460020243270 | -3.663952619805488 | -1.293279880109145 |
| $a_9$            | 2.443567136385676  | 4.061961701798492  | 1.563966870703912  |
| $a_{10}$         | -2.087818866919695 | -3.483132513082045 | -1.450226545717761 |
| $a_{11}$         | 1.368634146361897  | 2.291168271604290  | 1.024021239349936  |
| $a_{12}$         | -0.675937881127803 | -1.135256083953165 | -0.541256467049189 |
| $a_{13}$         | 0.243443136497010  | 0.410133386662197  | 0.207457763075095  |
| $a_{14}$         | -0.060357509441902 | -0.101981304210337 | -0.054469949954978 |
| $a_{15}$         | 0.009211069453411  | 0.015605585109138  | 0.008764590893595  |
| $a_{16}$         | -0.000652224105843 | -0.001107808266398 | -0.000651810809226 |

| coefficients | Case 2             |                    |                    |
|--------------|--------------------|--------------------|--------------------|
|              | $10^{13} \times$   | speed              | $u_1$              |
| $a_1$        | 0.000161729298700  | 0.000296703434881  | 0.000331043699638  |
| $a_2$        | -0.002663547237013 | -0.004991231500699 | -0.005772032762279 |
| $a_3$        | 0.020339099732280  | 0.038977801794141  | 0.046722649194728  |
| $a_4$        | -0.095508127683471 | -0.187426343684253 | -0.232891653324938 |
| $a_5$        | 0.308374706749317  | 0.620563020263077  | 0.799355226552687  |
| $a_6$        | -0.725042308960541 | -1.498477240355366 | -2.000992476154122 |
| $a_7$        | 1.282121070283650  | 2.725929439835820  | 3.773595128776208  |
| $a_8$        | -1.736005918233114 | -3.803798599185942 | -5.458846767793530 |
| $a_9$        | 1.814220029861536  | 4.104776739782694  | 6.106696174312163  |
| $a_{10}$     | -1.462981962075676 | -3.425342914369116 | -5.282486588179633 |
| $a_{11}$     | 0.902659332059763  | 2.192185648577189  | 3.504347199487991  |
| $a_{12}$     | -0.418360013949618 | -1.056619726773176 | -1.750716165522668 |
| $a_{13}$     | 0.140946840215663  | 0.371266424291172  | 0.637552371208520  |
| $a_{14}$     | -0.032574870988444 | -0.089776224139980 | -0.159766249185166 |
| $a_{15}$     | 0.004616166473962  | 0.013358553374243  | 0.024633814653303  |
| $a_{16}$     | -0.000302225539089 | -0.000922051337170 | -0.001761674965389 |

The  $l_2$ -norm errors of the polynomial approximations of the velocity  $u_1$  are presented in Table 5.6. Table 5.6 shows the errors of the first-, eighth- and fifteenth-degree polynomials. When the degree of the polynomial increases, the error decreases. Although the 15th-degree polynomials provide the best fitting, we also present the lower order approximations because in some cases, one may need only a rough estimate.

**Table 5.6:**  $l_2$ -norm errors of the polynomial approximations of the velocity  $u_1$  for both cases of the boundary conditions.

| order of polynomial | $l_2$ -norm errors of Case 1 | $l_2$ -norm errors of Case 2 |
|---------------------|------------------------------|------------------------------|
| 1                   | 23.37590758                  | 22.60410473                  |
| 8                   | 4.49732994                   | 2.54515053                   |
| 15                  | 0.77551149                   | 0.67652906                   |

The  $l_2$ -norm errors of the polynomials approximating  $u_2$  are shown in Table 5.7. In Table 5.7, we present the errors of the eighth- and fifteenth-order polynomials. The 15th-order approximation has better error than the 8th-order polynomial but we also present both of them here because the smaller degree of the polynomial may be useful for some rough study cases.

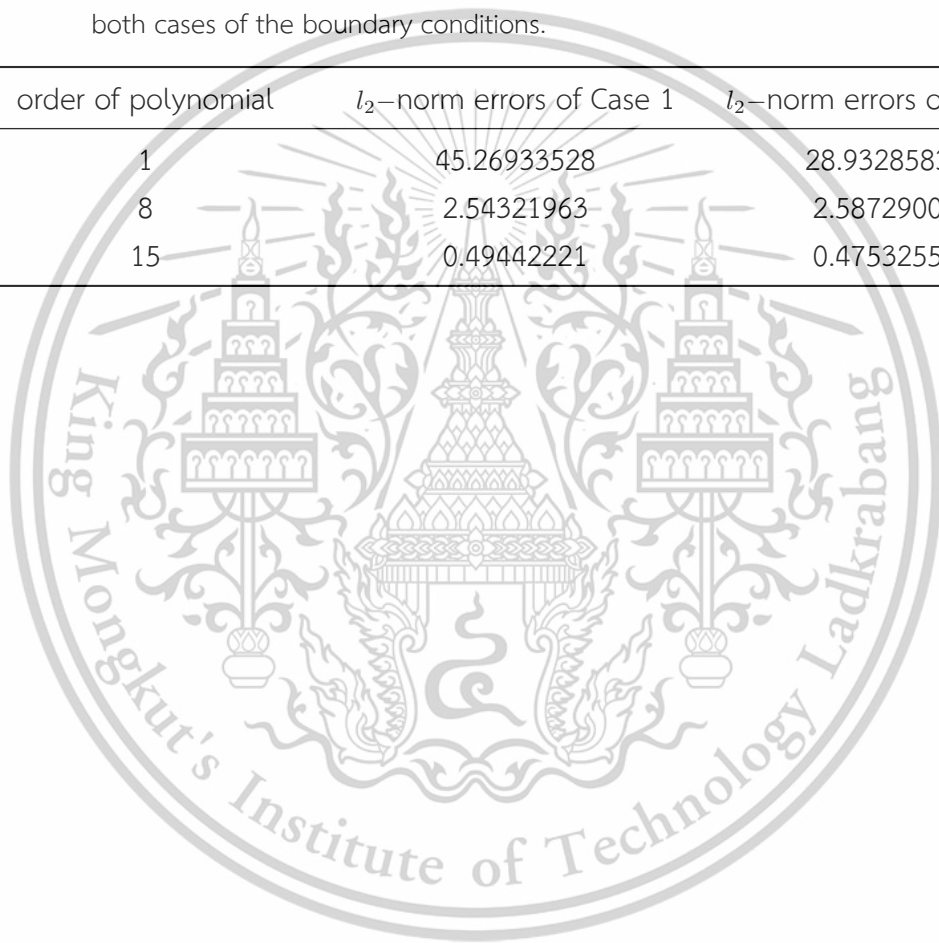
**Table 5.7:**  $l_2$ -norm errors of the polynomial approximations for both cases of the boundary conditions.

| order of polynomial | $l_2$ -norm errors of Case 1 | $l_2$ -norm errors of Case 2 |
|---------------------|------------------------------|------------------------------|
| 8                   | 4.22075638                   | 3.90055486                   |
| 15                  | 0.84113482                   | 1.05561499                   |

The  $l_2$ -norm errors of the polynomial approximations of the speed at the tips of cilia are provided in Table 5.8. The errors are small for the 15th-order approximation.

**Table 5.8:**  $l_2$ -norm errors of the polynomial approximations of the speed at the tips of cilia for both cases of the boundary conditions.

| order of polynomial | $l_2$ -norm errors of Case 1 | $l_2$ -norm errors of Case 2 |
|---------------------|------------------------------|------------------------------|
| 1                   | 45.26933528                  | 28.93285837                  |
| 8                   | 2.54321963                   | 2.58729001                   |
| 15                  | 0.49442221                   | 0.47532558                   |



# Chapter 6

## Conclusions

In this research, we study a two-dimensional fluid flow problem in the periciliary layer (PCL) in the respiratory system in human lungs. We focus on the fluid moved by self-propelled bundles of solid phase rather than by a pressure gradient. The PCL consists of a solid phase, known as cilia, and a fluid phase, represented by an incompressible Newtonian fluid called PCL fluid. When the cilia move forward, the PCL is divided into two adjacent domains: a porous medium, consisting of both cilia and PCL fluid, and a free-fluid region, containing only the PCL fluid. This study is divided into two main parts: an analytical investigation and a numerical investigation. The process and results of both parts of the study are summarized below.

In the analytical part, we developed a mathematical model for fluid flow in the PCL. For the porous medium, we apply a non-dimensionalization scheme to the macroscale multiphase equation derived from an upscaling technique called Hybrid Mixture Theory (HMT) to obtain the generalized Brinkman equation. Our model is more general than the Brinkman equation in the literature because the porosity in our equation is considered as a function since the beginning of the derivation. Then, our model in the porous medium conserves the reality of the problem. In the free-fluid region, we start with the generalized Navier-Stokes equation and use the non-dimensionalization method to derive the generalized Stokes equation. Our generalized Brinkman and generalized Stokes equations can be matched at the free-fluid/porous-medium interface. We name them as the generalized Stokes-Brinkman equations. We show that the discretized form of the mathematical model is a well-posed system with the use of a mixed finite element method. The weak formulation of the generalized Stokes-Brinkman equations is rewritten in linear and bilinear functional structures. We show that the bilinear form  $a(\cdot, \cdot)$  is continuous and coercive. Then, we present the well-posedness of the generalized Stokes-Brinkman equations in the last theorem.

In the numerical investigation part, we determine the velocity of the PCL fluid in the porous medium using the generalized Brinkman equation on a macroscopic scale with varied porosity for one fixed numerical domain. The numerical domain is designed to be a shape of a fan blade, imitating the actual beating pattern of cilia. The shape of the domain used in this study is closer to the pattern of the motion of cilia than the rectangular domain used in the previous literatures. For the rectangular domain, authors have considered only one angle  $\theta$  for one fixed numerical domain. So the porosity in their works was only a constant. In this work, our domain is designed to be aligned with the rotational movement of cilia, that the cilia rotate around their roots. Therefore, the porosity used in the fan-blade domain is varied depending on the angle  $\theta$  that the cilia make with the horizontal plane. We employ the mixed finite element method of Taylor-Hood type to discretize the mathematical model and find the numerical solutions in the 2-dimensional domain. We consider the forward movement of cilia making the angle  $90^\circ$  to  $40^\circ$  with the horizontal plane. We provide the velocities  $u_1, u_2$  and the speed at the tips of cilia because it affects the velocity of mucus and then mucus thickness, which can cause the diseases in the respiratory system in human lungs. At the tips of cilia, the velocity  $u$  is the Case

1 boundary condition is lower than the velocity  $u_1$  for the Case 2 about 8.86%. Therefore, the boundary condition of Case 1 at the tips of cilia, which is expressed in the explicit form and it is easy to apply to problems, may be used as a boundary condition at the free interface not only in this problem but also in other problems that are similar to this one, if the percentage difference is in an acceptable range of the problems. We provide the velocities and the speed of the PCL fluid for different values of  $c_i$  so that they can be a guideline for those interested in applying this research to their works. We also present the first-, eighth- and fifteenth-order polynomial functions for the velocities  $u_1$  and  $u_2$ , as well as the speed at the tips of the cilia in order to apply to future work and other similar efforts.

The system of equations can be useful for more complexity of a real problem in a macroscopic scale than a typical Stokes-Brinkman equation. If the velocity of the solid phases in our governing equations is neglected, the system of equations can be applied to fluid flow problems with immobile solids, such as natural rice fields or trees, glass rods, engine filters, filter pads, and underground oil. In future work, we will predict the PCL fluid velocity with full forward stroke of cilia from the angles  $130^\circ$  to  $40^\circ$  [20], as well as extending the problem to two domains: a porous medium and an adjacent free-fluid region. We will use the result from this study as a lower boundary condition in order to find the mucus velocity.



# References

- [1] Lyons, R.A.; Saridogan, E.; Djahanbakhch, O. The reproductive significance of human Fallopian tube cilia. *Hum. Reprod. Update.* **2006**, *12*, 363–372.
- [2] Pechenik, J.A. *Biology of the Invertebrates*, 4th ed., Tufts University: McGraw-Hill, 1976.
- [3] Bustamante-Marin, X.M.; Ostrowski, L.E. Cilia and mucociliary clearance. *Cold Spring Harbor Perspect. Biol.* **2017**, *9*, a028241.
- [4] Wuttanachamsri, K.; Schreyer, L. Effects of cilia movement on fluid velocity: I model of fluid flow due to a moving solid in a porous media framework. *Transp. Porous Media* **2021**, *136*, 699–714.
- [5] Cushman, J.H.; Bennethum, L.S.; Hu, B.X. A primer on upscaling tools for porous media. *Adv. Water Resour.* **2002**, *25*, 1043–1067.
- [6] Bennethum, L.S. Multiscale, hybrid mixture theory for swelling systems with interfaces, Lecture Note, University of Colorado: Denver, CO, USA, 2007.
- [7] Bennethum, L.S.; Cushman, J.H. Multiscale, hybrid mixture theory for swelling systems—I: balance laws. *Int. J. Eng. Sci.* **1996**, *34*, 125–145.
- [8] Braess, D. *Finite Elements: Theory, Fast Solvers, and Applications in Elasticity Theory*, 3rd ed. Cambridge: Cambridge University Press, New York, 2007.
- [9] Chamsri, K. Modeling the flow of PCL fluid due to the movement of lung cilia. Ph.D. Thesis, University of Colorado, Denver, CO, USA, 2012.
- [10] Brenner, S.C. *The Mathematical Theory of Finite Element Methods*, 2nd ed., Springer-Verlag, New York, NY, USA, 2002.
- [11] Brezzi, F.; Fortin, M. *Mixed and Hybrid Finite Element Methods*, Springer: New York, United States, 1991.
- [12] Girault, V.; Raviart, P. *Finite Element Methods for Navier-Stokes Equations: Theory and Algorithms*, Springer: Berlin/Heidelberg, Germany, 1986.
- [13] Arfken, G.B.; Weber, H.J.; Harris, F.E. *Mathematical Methods for Physicists*, 7rd ed.; Academic Press: Cambridge, United States, 2012.
- [14] Dyakonov, E.G.; McCormick, S. *Optimization in Solving Elliptic Problems*, CRC Press: Boca Raton, United States, 1996.
- [15] Dormieux, L.; Kondo, D.; Ulm, Franz-Josef. *Microporomechanics*, John Wiley and Sons, Ltd, 2006.
- [16] Reddy, J.N; Gartling, D.K. *The Finite Element Method in Heat Transfer and Fluid Dynamics*, CRC press, 2010.
- [17] Kwon, Young W.; Bang, Hyochoong *The Finite Element Method using Matlab*, CRC press, 2018.
- [18] Lamichhane, B.P. A new finite element method for Darcy-Stokes-Brinkman equations. *ISRN Computational Mathematics* **2013**, *3*, 1–4.

This material is provided for educational use only, not allowed for commercial use.

Forbidden to modify the content, and cite the document when use.

- [19] Matsui, H.; Randell, S.H.; Peretti, S.W.; Davis, C.W.; Boucher, R.C. Coordinated clearance of periciliary liquid and mucus from airway surfaces. *J. Clin. Invest.* **1998**, *102*, 1125–1131.
- [20] Sears, P.R.; Thompson, K.; Knowles, M.R.; Davis, C.W. Human airway ciliary dynamics, *Am. J. Physiol. Lung Cell. Mol. Physiol.* **2012**, *304*, 170–183.
- [21] Matsui, H.; Grubb, B.; Tarran, R.; Randell, S.; Gatzky, J.; Davis, C.; Boucher, R. Evidence for Periciliary Liquid Layer Depletion, Not Abnormal Ion Composition, in the Pathogenesis of Cystic Fibrosis Airways Disease. *cell* **1998**, *95*, 1005–1015.
- [22] Griesenbach, U.; Soussi, S.; Larsen, M.B.; Casamayor, I.; Dewar, A.; Regamey, N.; Bush, A.; Shah, P.L.; Davies, J.C.; Alton, E.W.F.W. Quantification of Periciliary Fluid Height in Human Airway Biopsies Is Feasible, but Not Suitable as a Biomarker. *Am. J. Respir. Cell Mol. Biol.* **2011**, *44*, 309–315.
- [23] Zhu, P.; Chen, D.; Xu, Y. Simulation study on the mass transport in PCL based on the ciliated dynamic system of the respiratory tract. *J. Phys.: Conf. Ser.* **2019**, *1300*, 012068.
- [24] Jayathilake, P.G.; Tan, Z.; Le, D.V.; Lee, H.P.; Khoo, B.C. Three-dimensional numerical simulations of human pulmonary cilia in the periciliary liquid layer by the immersed boundary method. *Comput. Fluids* **2012**, *67*, 130–137.
- [25] Vanaki, S.M.; Holmes, D.; Jayathilake, P.G.; Brown, R. Three-Dimensional Numerical Analysis of Periciliary Liquid Layer: Ciliary Abnormalities in Respiratory Diseases. *Appl. Sci.* **2019**, *9*, 4033.
- [26] Poopra, S. and Wuttanachamsri, K. On the asymptotic boundary condition at the free-fluid/porous-medium interface in periciliary layer due to the ciliary movement, *Math. Probl. Eng.* **2022**, *2022*, 1–12.
- [27] Sedaghat, M.H.; Sadrizadeh, S.; Abouali, O. Three-dimensional simulation of mucociliary clearance under the ciliary abnormalities, *J. Nonnewton. Fluid Mech.* **2023**, *316*, 105029.
- [28] Milosevic, M.; Stojanovic, D.B.; Simic, V.; Grkovic, M.; Bjelovic, M.; Uskokovic, P.S. et al. Preparation and modeling of three-layered PCL/PLGA/PCL fibrous scaffolds for prolonged drug release. *Sci. Rep.* **2020**, *10*, 11126
- [29] Khanafer, K.; Cook, K.; Marafie, A. The role of porous media in modeling fluid flow within hollow fiber membranes of the total artificial lung. *J. Porous Media* **2012**, *15*, 113–122.
- [30] Ly, H.-B.; Nguyen, H.-L.; Do, M.-N. Finite element modeling of fluid flow in fractured porous media using unified approach. *Vietnam J. Earth Sciences.* **2020**, *43*, 13–22.
- [31] Lesinigo, M.; D'Angelo, C.; Quarteroni, A. A multiscale Darcy-Brinkman model for fluid flow in fractured porous media. *Numer. Math.* **2011**, *117*, 717–752.
- [32] Basirat, F.; Sharma, P.; Fagerlund, F.; Niemi, A. Experimental and modeling investigation of CO<sub>2</sub> flow and transport in a coupled domain of porous media and free flow. *Int. J. Greenh. Gas Control.* **2015**, *42*, 461–470.
- [33] Oangwatcharaparkan, N. and Wuttanachamsri, K. The flow in periciliary layer in human lungs with Navier-Stokes-Brinkman equations. *Tamkang J. Math.* **2023**, *54*, 107–120.
- [34] Phaenchat, S. and Wuttanachamsri, K. Two-dimensional nonlinear Brinkman and steady-state Navier-Stokes equations for fluid flow in PCL. *Partial Differ. Equ. Appl. Math.* **2024**, *12*, 100961.

- [35] Wuttanachamsri, K. Free interfaces at the tips of the cilia in the one-dimensional periciliary layer. *Mathematics* **2020**, *8*, 1961.
- [36] Conti, M.; Giorgini, A. Well-posedness for the Brinkman–Cahn–Hilliard system with unmatched viscosities. *J. Differ. Equ.* **2020**, *268*, 6350–6384.
- [37] Titi, E.S. and Trabelsi, S. Global well-posedness of a three-dimensional Brinkman–Forchheimer–Bénard convection model in porous media. *math. AP.* **2022**, arXiv:2204.03531.
- [38] Ingram, R. Finite element approximation of nonsolenoidal, viscous flows around porous and solid obstacles. *SIAM J. Numer. Anal.* **2011**, *49*, 491–520.
- [39] Angot, P. On the well-posed coupling between free fluid and porous viscous flows. *Appl. Math. Lett.* **2011**, *24*, 803–810.
- [40] Angot, P. Well-posed Stokes/Brinkman and Stokes/Darcy coupling revisited with new jump interface conditions. *ESAIM: Math. Model. Numer. Anal.* **2018**, *52*, 1875–1911.
- [41] Kohr, M.; Sekhar, G.P.R.; Ului, E.M.; Wendland, W.L. Two-dimensional Stokes–Brinkman cell model – a boundary integral formulation. *Appl. Anal.* **2011**, *91*, 251–275.
- [42] Koroleva, Y. Qualitative properties of the solution to Brinkman–Stokes system modelling a filtration process. *Math. Stat.* **2017**, *5*, 143 - 150.
- [43] Chamsri, K. Formulation of a well-posed Stokes–Brinkman problem with a permeability tensor. *J. Math.* **2014**, *1*, 1–7.
- [44] Hwang, W.R. and Advani, S.G. Numerical simulations of Stokes–Brinkman equations for permeability prediction of dual scale fibrous porous media. *Phys Fluids.* **2010**, *22*, 113101.
- [45] Al-Atawi, N.O.; Hasnain, S.; Saqib, M.; Mashat, D.S. Significance of Brinkman and Stokes system conjuncture in human knee joint. *Sci. Rep* **2022**, *12*, 18992.
- [46] Poopra, S. and Wuttanachamsri, K. The velocity of PCL fluid in human lungs with beaver and Joseph boundary condition by using asymptotic expansion method. *Mathematics* **2019**, *7*, 567.
- [47] Kasamwan, T.; Wuttanachamsri, K. Unsteady one-dimensional flow in PCL with Stokes–Brinkman equations. The 9<sup>th</sup> Phayao Research Conference, Thailand, **2020**, 1935–1950.
- [48] Oangwatcharaparkan, N.; Wuttanachamsri, K. Solutions of flow over periciliary layer using finite difference and n-dimensional Newton–Raphson methods. *J. Science Ladkrabang* **2020**, *29*, 16–30.
- [49] Phaenchat, S.; Wuttanachamsri, K. On the one-dimensional nonlinear Stokes–Brinkman equations for modeling flow in PCL. The 24<sup>th</sup> Annual Meeting in Mathematics, Thailand, **2019**, 167–175.
- [50] Wuttanachamsri, K.; Schreyer, L. Effects of cilia movement on fluid velocity: II numerical solutions over a fixed domain, *Transp. Porous Media* **2020**, *134*, 471–489.
- [51] Patiño, I.D.; Power, H.; Nieto-Londoño, C.; Flórez, W.F. Stokes–Brinkman formulation for prediction of void formation in dual-scale fibrous reinforcements: a BEM/DR–BEM simulation. *Comput. Mech.* **2017**, *59*, 555–577.

This material is reserved for educational use only, not allowed for commercial use.

Forbidden to modify the content, and cite the document when use.

- [52] Mardanov, R.F.; Zaripov, S.K.; Sharafutdinov, V.F.; Dunnett, S.J. A Stokes–Brinkman model of the fluid flow in a periodic cell with a porous body using the boundary element method. *Eng. Anal. Bound. Elem.* **2018**, *88*, 54–63.
- [53] Bennethum, L.S. Notes for Introduction to Continuum Mechanics. *Continuum Mechanics Class Lecture*, 2011.
- [54] Tilley, A.E.; Walters, M.S.; Shaykhiev, R.; Crystal, R.G. Cilia Dysfunction in Lung Disease. *Annu. Rev. Physiol.* **2015**, *77*, 379–406.
- [55] Smith, C.M.; Djakow, J.; Free, R.C.; Djakow, P.; Lonnen, R.; Williams, G.; Pohunek, P.; Hirst, R.A.; Easton, A.J.; Andrew, P.W.; O’Callaghan, C. CiliaFA: A Research Tool for Automated, High-Throughput Measurement of Ciliary Beat Frequency Using Freely Available Software. *Cilia* **2012**, *1*, 1–14.
- [56] Chovancov’a, M.; Elcner, J. The Pressure Gradient in the Human Respiratory Tract. *EPJ Web Conf.* **2014**, *67*, 2–6.
- [57] Chamsri, K.; Bennethum, L.S. Permeability of fluid flow through a periodic array of cylinders. *Appl. Math. Model.* **2015**, *39*, 244–254.
- [58] Karageorghis, A.; Lesnic, D.; Marin, L. The Method of Fundamental Solutions for Brinkman Flows. Part II. Interior Domains. *J. Eng. Math.* **2021**, *127*, 1–16.
- [59] Weinstein, T.F. Three-phase hybrid mixture theory for swelling drug delivery systems. Ph.D. Thesis, University of Colorado, Denver, CO, USA, 2005.
- [60] Weinstein, T.F.; Bennethum, L.S. On the Derivation of the Transport Equation for Swelling Porous Materials with Finite Deformation. *Int. J. Eng. Sci.* **2006**, *44(18–19)*, 1408–1422.
- [61] Bartle, R.G.; Sherbert, D.R. *Introduction to Real Analysis*, 4rd ed.; Wiley: New York, USA, 2011.
- [62] Horn, R.A.; Johnson, C.R. *Matrix analysis*, 2rd ed.; Cambridge University Press: Cambridge, 2012.
- [63] Sleight, M.A. Ciliary adaptations for the propulsion of mucus, *Biorheology* **1990**, *27*, 527–532.
- [64] ICRP. *Measurement: Human Respiratory Tract Model for Radiological Protection*; ICRP Publication 66. Ann. ICRP; ICRB: Ottawa, ON, Canada, 1994; Volume 24, pp. 1–3.
- [65] Schöberl, J. NETGEN An advancing front 2D/3D-mesh generator based on abstract rules, *Comput. Visual. Sci.* **1997**, *1*, 41–52.
- [66] Woodfield, J.; Alvarez, M.; Gómez-Vargas, B.; Ruiz-Baier, R. Stability and finite element approximation of phase change models for natural convection in porous media, *J. Comput. Appl. Math.* **2019**, *360*, 117–137.



Appendices

This material is reserved for educational use only, not allowed for commercial use.

Forbidden to modify the content, and cite the document when use.

# Appendix A

Well-posedness of generalized Stokes-Brinkman equations modeling moving solid phases



This material is reserved for educational use only, not allowed for commercial use.

Forbidden to modify the content, and cite the document when use.



*Research article*

## Well-posedness of generalized Stokes-Brinkman equations modeling moving solid phases

Nisachon Kumankat and Kanognudge Wuttanachamsri\*

Department of Mathematics, School of Science, King Mongkut's Institute of Technology Ladkrabang, Bangkok 10520, Thailand

\* **Correspondence:** Email: kanognudge.wu@kmitl.ac.th.

**Abstract:** Fluid flow through a free-fluid region and the adjacent porous medium has been studied in various problems, such as water flow in rice fields. For the problem with self-propelled solid phases, we provide a generalized Stokes equation for the free-fluid domain and the Brinkman equation in a macroscopic scale due to the movement of self-propelled solid phases rather than a single solid in the porous medium. The model is derived with the assumption that the porosity is not a constant. The porosity in the mathematical model varies depending on the propagation of the solid phases. These two models can be matched at the free-fluid/porous-medium interface and are developed for real world problems. We show the proof of the well-posedness of the discretized form of the weak formulation obtained from applying a mixed finite element scheme to the generalized Stokes-Brinkman equations. The proofs of the continuity and coercive property of the linear and bilinear functionals in the discretized equation are illustrated. We present the existence and uniqueness of the generalized Stokes-Brinkman equations for the numerical problem in two dimensions. The system of equations can be applied to fluid flow propelled by moving solid phases, such as mucus flow in the trachea.

**Keywords:** generalized Stokes-Brinkman equations; finite element approach; well-posedness; varied porosity; permeability tensor

### 1. Introduction

Fluid flow problems have considerable attention from researchers and appear in many applications such as engineering, industry, biomedical sciences and other areas. The fluid flow problems are investigated in both theoretical and applied research, among which is the study of flow through a free-fluid domain and an adjacent porous medium. For example, Basirata et al. [1] studied the CO<sub>2</sub> gas flow in a porous medium and free air above it. Oangwatcharaparkan and Wuttanachamsri [2] studied the fluid flow in a periciliary layer (PCL) in the human respiratory system where the mucus

layer was on the top of a porous layer. In this research, we focus on fluid flow problems in which the fluid is moved by self-propelled solid phases rather than a pressure gradient. That is, the movement of solids affects the fluid flow whether the fluid is in the same layer as the solid phases or above the solid phases. An example domain that illustrates the regions of interest is represented in Figure 1.

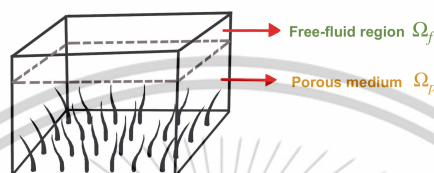


**Figure 1.** Sample layers of a free-fluid region residing above an adjacent porous medium.

Figure 1 shows a sampling domain consisting of two regions: the layer composed of fluid and self-propelled solid phases, which is considered as a porous medium,  $\Omega_p$ , and a free-fluid region,  $\Omega_f$ , residing on the porous medium. In this study, we consider a macroscopic flow where a bundle of solid phases is considered instead of a single self-propelled solid. The locomotion of solids affects the movement of fluids in the nearby areas. If fluid flows through different domains, then mathematical models are also distinct. That is, the equations for the flow above the porous medium and flow in the porous domain are different.

There are several mathematical models used to describe problems of this type [3–11]. Khanafer et al. [3] used Darcy's Law and Brinkman-extended Darcy to investigate the fluid flow inside the hollow fiber bundle of an artificial lung and applied the Navier-Stokes equation for the fluid flow outside the fiber bundle. Ly et al. [4] investigated the problem of fluid flow in coupling a free fluid domain and a porous medium using the Stokes and Darcy equations, respectively. Wuttanachamsri and Schreyer [5] used the Stokes-Brinkman equations to compute the fluid velocities due to the self-propelled solid phases in a three-dimensional domain. Poopra and Wuttanachamsri [6] considered the fluid flow in the periciliary layer (PCL) in human lungs by using the Stokes-Brinkman equations with the Beavers and Joseph boundary condition. Wuttanachamsri [7] used Stokes-Brinkman equations in one dimension with the Stefan problem to estimate the free interface between a porous medium and an adjacent free-fluid region. The well-posedness of the system of the Stokes-Brinkman equations is also provided for both moving or static solid phase [12–16]. For the study of a static solid phase, Ingram [12] applied a finite element discretization to the Brinkman equation and demonstrated that the discretized problem was well-posed. Angot [13] studied the well-posedness of the Stokes-Brinkman and Stokes-Darcy with new jump interface conditions. Chamsri [14] showed the well-posedness of the Stokes-Brinkman model for the case of moving solid phase, while the porosity was assumed to be a constant.

Unlike the usual problems, in this research, we use generalized Stokes-Brinkman equations, where the Brinkman model is developed from the Hybrid Mixture Theory (HMT) [17]. The HMT is a technique for upscaling a multiphase flow by applying an averaging theorem to a microscale equation to obtain a macroscale equation [18, 19]. The macroscopic Brinkman equation is distinct from the models in the above literature because it is derived from the conservation of momentum, where the porosity in the equation is considered as a function of space. Therefore, the porosity is subject to a

derivative operator, while the porosity in the Brinkman model in the available research is outside the derivative, although the porosity has been used as a function of space. Our model, the macroscopic Brinkman model, can be used for a bundle of self-propelled solid phases instead of a single solid for fluid flow in a porous medium. In addition, we derive the generalized Stokes equation to apply to the incompressible slow flow in the domain of the free-fluid region next to the porous medium. Extra terms appearing in the generalized Stokes and macroscale Brinkman equations aid to match shear stress at the free-fluid/porous-medium interface. Since our model differs from typical Stokes-Brinkman equations in available research, the well-posedness of the generalized Stokes-Brinkman equations in a macroscopic scale when the fluid is moved by self-propelled solid phases is provided, and the permeability in the model is considered as a second-order tensor, not just a constant.

In Section 2, we derive the generalized Stokes-Brinkman equations. In order to present the well-posedness of the discretized form of the mathematical model using a mixed finite element technique, in Section 3, we present the weak formulation of the governing equations as well as the discretized form of the generalized Stokes-Brinkman equations. In Section 4, the continuity and coercivity of linear and bilinear functionals in the discretized system of equations are presented. The well-posedness of the generalized Stokes-Brinkman equations is illustrated in Section 5. The conclusion is drawn in Section 6. The fundamental definitions, theorems and lemmas proved in available literature and books, which are used in the proof of the well-posedness of the discretized equations, are provided in the Appendix.

## 2. Generalized Stokes-Brinkman equations

In this section, we present the derivation of our governing equations. For the generalized Stokes equation, we start with the generalized Navier-Stokes equation and then use a nondimensionalization method to obtain the generalized Stokes equation. This is shown in Section 2.1. To derive the Brinkman equation, we begin with a momentum equation obtained from Hybrid Mixture Theory (HMT) [19], an upscaling technique, and then use a nondimensionalization approach to have a macroscopic model in a porous medium, which is illustrated in Section 2.2. We rewrite our governing equations in Section 2.3 in order to summarize and use them in the next sections.

### 2.1. Derivation of generalized Stokes equation

To obtain the generalized Stokes equation, we start with the generalized Navier-Stokes equation, which is attained from substituting a stress tensor, developed from entropy inequality holding near equilibrium for a viscous fluid, into a momentum equation. The generalized Navier-Stokes equation is [20]

$$\rho \frac{\partial \mathbf{u}}{\partial t} + \rho(\mathbf{u} \cdot \nabla \mathbf{u}) + \nabla p - (\lambda + \mu)\nabla(\nabla \cdot \mathbf{u}) - \mu \nabla \cdot \nabla \mathbf{u} - \rho \mathbf{g} = \mathbf{0}, \quad (2.1)$$

where  $\rho$  is density,  $t$  is time,  $\mathbf{u}$  is the velocity,  $p$  is pressure,  $\lambda$  is a constant,  $\mu$  is the dynamic viscosity, and  $\mathbf{g}$  is gravity. The generalized Navier-Stokes equation, Eq (2.1), is normalized with dimensionless variables, and we get

$$\rho \mu_0 f \frac{\partial \widehat{\mathbf{u}}}{\partial t} + \frac{\rho \mu_0^2}{L} (\widehat{\mathbf{u}} \cdot \widehat{\nabla} \widehat{\mathbf{u}}) + \frac{p_0}{L} \widehat{\nabla} \widehat{p} - \frac{(\lambda + \mu) \mu_0}{L^2} \widehat{\nabla}(\widehat{\nabla} \cdot \widehat{\mathbf{u}}) - \frac{\mu \mu_0}{L^2} \widehat{\nabla} \cdot \widehat{\nabla} \widehat{\mathbf{u}} - \rho g_0 \widehat{\mathbf{g}} = \mathbf{0}, \quad (2.2)$$

where the characteristic parameter  $L$  is the characteristic length;  $f$  is the characteristic frequency;  $u_0$  is the characteristic speed;  $p_0$  is the reference pressure;  $g_0$  is the gravitational acceleration. Multiplying Eq (2.2) by  $\frac{L^2}{\mu u_0}$  on both sides, we have

$$\frac{\rho f L^2}{\mu} \frac{\partial \widehat{\mathbf{u}}}{\partial t} + \frac{\rho u_0 L}{\mu} (\widehat{\mathbf{u}} \cdot \widehat{\nabla} \widehat{\mathbf{u}}) + \frac{p_0 L}{\mu u_0} \widehat{\nabla} \widehat{p} - \frac{(\lambda + \mu)}{\mu} \widehat{\nabla} (\widehat{\nabla} \cdot \widehat{\mathbf{u}}) - \widehat{\nabla} \cdot \widehat{\nabla} \widehat{\mathbf{u}} - \frac{\rho g_0 L^2}{\mu u_0} \widehat{\mathbf{g}} = \mathbf{0}. \quad (2.3)$$

Next, we calculate the coefficients in Eq (2.3), where the values of the characteristic variables and other variables in International System (SI) units are shown in Table 1. The characteristic length is the highest length of cilia in the respiratory system [21], the reference  $f$  is the frequency of cilia beat in the human respiratory tract [22], the characteristic velocity  $u_0$  is the maximum speed of cilia for the effective stroke at temperature  $37^\circ\text{C}$ , the reference pressure  $p_0$  is the pressure in the human respiratory tract, which is about one [23],  $g_0$  is the Earth's gravity, and  $\rho$  and  $\mu$  are the density of water and dynamic viscosity at  $37^\circ\text{C}$ , respectively. The constant  $\lambda$  is set equal to zero. The values of the coefficients are shown in Table 2.

**Table 1.** The values of characteristic and constant variables in Eq (2.3) in International System units.

| Variables | $L$                | $f$ | $u_0$                | $p_0$                  | $g_0$            | $\rho$            | $\mu$                   |
|-----------|--------------------|-----|----------------------|------------------------|------------------|-------------------|-------------------------|
| SI Units  | m                  | 1/s | m/s                  | kg/(m·s <sup>2</sup> ) | m/s <sup>2</sup> | kg/m <sup>3</sup> | kg/(m·s)                |
| Values    | $7 \times 10^{-6}$ | 10  | $2.5 \times 10^{-4}$ | 1                      | 9.807            | 993.3             | $0.6913 \times 10^{-3}$ |

**Table 2.** The values of the coefficients in Eq (2.3).

| Coefficients | $\frac{\rho f L^2}{\mu}$ | $\frac{\rho u_0 L}{\mu}$ | $\frac{p_0 L}{\mu u_0}$ | $\frac{\lambda + \mu}{\mu}$ | $\frac{\rho g_0 L^2}{\mu u_0}$ |
|--------------|--------------------------|--------------------------|-------------------------|-----------------------------|--------------------------------|
| Values       | $7.0406 \times 10^{-4}$  | $2.5 \times 10^{-3}$     | 40.5034                 | 1                           | 2.7619                         |

From Table 2, the coefficients of the first two terms in Eq (2.3) are comparatively small compared with the others. Therefore, the unsteady and nonlinear terms in the equation are neglected, and then Eq (2.3) becomes

$$\nabla p - (\lambda + \mu) \nabla (\nabla \cdot \mathbf{u}) - \mu \nabla \cdot \nabla \mathbf{u} - \rho \mathbf{g} = \mathbf{0}. \quad (2.4)$$

In this work, we assume that the velocity  $\mathbf{u}$  in two dimensions is smooth enough that the order of the derivative can be interchanged, that is,  $\frac{\partial}{\partial x} \frac{\partial \mathbf{u}}{\partial y} = \frac{\partial}{\partial y} \frac{\partial \mathbf{u}}{\partial x}$ . Then, we obtain

$$\nabla (\nabla \cdot \mathbf{u}) = \nabla \cdot (\nabla \mathbf{u})^T. \quad (2.5)$$

Substituting Eq (2.5) into the second term of Eq (2.4), we have

$$\nabla p - \lambda \nabla (\nabla \cdot \mathbf{u}) - \mu \nabla \cdot (\nabla \mathbf{u})^T - \mu \nabla \cdot \nabla \mathbf{u} - \rho \mathbf{g} = \mathbf{0}, \quad (2.6)$$

or

$$\nabla p - \lambda \nabla (\nabla \cdot \mathbf{u}) - \mu \nabla \cdot (\nabla \mathbf{u} + (\nabla \mathbf{u})^T) - \rho \mathbf{g} = \mathbf{0}. \quad (2.7)$$

Since the rate of deformation for the liquid phase  $\mathbf{d} = \frac{1}{2}(\nabla\mathbf{u} + (\nabla\mathbf{u})^T)$ , we rewrite Eq (2.7) as

$$\nabla p - \lambda \nabla(\nabla \cdot \mathbf{u}) - \nabla \cdot (2\mu\mathbf{d}) - \rho\mathbf{g} = \mathbf{0}. \tag{2.8}$$

Notice that if  $\lambda = 0$ , then Eq (2.8) becomes

$$\nabla p - \nabla \cdot (2\mu\mathbf{d}) - \rho\mathbf{g} = \mathbf{0}, \tag{2.9}$$

which is the generalized Stokes equation. If the matrix  $\nabla\mathbf{u}$  is symmetric, then Eq (2.9) is the following Stokes equation:

$$\nabla p - 2\mu\Delta\mathbf{u} - \rho\mathbf{g} = \mathbf{0}. \tag{2.10}$$

2.2. Derivation of the Brinkman equation

In this section, we show the derivation of the Brinkman equation in a macroscopic scale derived using Hybrid Mixture Theory (HMT). HMT is an upscaling technique used to derive multiphase equations such as the combination of solid and liquid phases. This method uses the averaging theorem to upscale equations from a microscale equation to a macroscale equation [19]. In this study, we focus on developing a model for fluid flow due to the movement of self-propelled solid phases. Here, we follow the procedure provided in [18]. We begin with the multiphase equation upscaled from the conservation of momentum [18] when the porosity is a function, not a constant:

$$\varepsilon^l \rho^l \frac{D^l \mathbf{u}^l}{Dt} + \varepsilon^l \nabla p + p \nabla \varepsilon^l - \nabla \cdot (\varepsilon^l 2\mu \mathbf{d}^l) - \varepsilon^l \rho^l \mathbf{g}^l = p \nabla \varepsilon^l - \varepsilon^l \mathbf{R} \cdot (\mathbf{u}^l - \mathbf{u}^s), \tag{2.11}$$

where  $l$  and  $s$  mean the liquid and solid phases, respectively. The function  $\varepsilon^l$  is the porosity, which is a variable in space;  $\mathbf{d}^l = 0.5(\nabla\mathbf{u}^l + (\nabla\mathbf{u}^l)^T)$  is the rate of deformation tensor;  $\mathbf{R}$  is a second-order tensor;  $\mathbf{u}^l$  and  $\mathbf{u}^s$  are the velocities of liquid and solid phases, respectively. Substituting  $\mathbf{R} = \mu \varepsilon^l \mathbf{k}^{-1}$ , where  $\mathbf{k}^{-1}$  is the inverse of the permeability tensor, and taking  $\frac{D^l \mathbf{u}^l}{Dt} = \frac{\partial \mathbf{u}^l}{\partial t} + \mathbf{u}^l \cdot \nabla \mathbf{u}^l$  into Eq (2.11), subtracting from both sides by  $p \nabla \varepsilon^l$  and dividing by  $\varepsilon^l$  on both sides, we have

$$\rho \left( \frac{\partial \mathbf{u}^l}{\partial t} + \mathbf{u}^l \cdot \nabla \mathbf{u}^l \right) + \mu \mathbf{k}^{-1} \cdot (\varepsilon^l \mathbf{u}^l - \varepsilon^l \mathbf{u}^s) + \nabla p - \frac{\mu}{\varepsilon^l} \nabla \cdot (2\varepsilon^l \mathbf{d}^l) = \rho \mathbf{g}. \tag{2.12}$$

Then, we normalize Eq (2.12). We use the same characteristic parameters as in the previous subsection. The dimensionless form of Eq (2.12) is

$$\frac{\mathbf{k}\rho f}{\mu} \frac{\partial \widehat{\mathbf{u}}^l}{\partial \widehat{t}} + \frac{\mathbf{k}\rho u_0}{\mu L} (\widehat{\mathbf{u}}^l \cdot \widehat{\nabla} \widehat{\mathbf{u}}^l) + (\varepsilon^l \widehat{\mathbf{u}}^l - \varepsilon^l \widehat{\mathbf{u}}^s) + \frac{\mathbf{k}p_0}{\mu u_0 L} \widehat{\nabla} \widehat{p} - \frac{\mathbf{k}}{\varepsilon^l L^2} \widehat{\nabla} \cdot (2\varepsilon^l \widehat{\mathbf{d}}^l) = \frac{\mathbf{k}\rho g_0}{\mu u_0} \widehat{\mathbf{g}}. \tag{2.13}$$

Using the values in Table 1 to calculate the coefficients in Eq (2.13) with the permeability  $k = 10^{-14} \text{ m}^2$  and porosity  $\varepsilon^l = 1$ , which are the maximum values employed from [24], we obtain the values of the coefficients as illustrated in Table 3.

Table 3. The values of the coefficients in Eq (2.13).

| Coefficients | $\frac{\mathbf{k}\rho f}{\mu}$ | $\frac{\mathbf{k}\rho u_0}{\mu L}$ | $\frac{\mathbf{k}p_0}{\mu u_0 L}$ | $\frac{\mathbf{k}}{\varepsilon^l L^2}$ | $\frac{\mathbf{k}\rho g_0}{\mu u_0}$ |
|--------------|--------------------------------|------------------------------------|-----------------------------------|----------------------------------------|--------------------------------------|
| Values       | $1.4369 \times 10^{-7}$        | $5.1316 \times 10^{-7}$            | $8.3 \times 10^{-3}$              | $2.0408 \times 10^{-4}$                | $5.6365 \times 10^{-4}$              |

From the calculation demonstrated in Table 3, we neglect the first two terms in Eq (2.13), the time-dependent and nonlinear terms, because these expressions are significantly small in comparison with others. Therefore, Eq (2.12) becomes

$$\mu \mathbf{k}^{-1} \cdot (\varepsilon^l \mathbf{u}^l - \varepsilon^l \mathbf{u}^s) + \nabla p - \frac{\mu}{\varepsilon^l} \nabla \cdot (2\varepsilon^l \mathbf{d}^l) = \rho \mathbf{g}, \quad (2.14)$$

which is called the Brinkman equation in a macroscopic scale. Notice that the macroscale Brinkman equation is distinct from the Brinkman in literature such as in [25],

$$\mu \mathbf{k}^{-1} \cdot \varepsilon^l \mathbf{u}^l + \nabla p - \mu \Delta \mathbf{u}^l = \rho \mathbf{g}, \quad (2.15)$$

because our model starts with the momentum equation that the porosity is a function and cannot be moved out of the derivative as a constant, as usually used in research. The porosity in the parentheses in the third term in Eq (2.14) cannot be canceled out with the denominator. Moreover, the first-order derivative of the rate of deformation times the porosity in Eq (2.14) cannot be changed to be the second-order derivative of the velocity as shown in Eq (2.15). It may seem that the difference is not much, but finding the numerical results of Eq (2.14) is more complicated than for Eq (2.15), including the proof of the well-posedness of the equation.

Notice that the Brinkman equation in the macroscopic scale, Eq (2.14), has a good engagement with the generalized Stokes equation, Eq (2.9). Because there are no solid phases in the adjacent free-fluid domain, the porosity becomes one, and the permeability tends to infinity in this region. Therefore, the first term in Eq (2.14) disappears, and then the Brinkman equation, Eq (2.14), becomes generalized Stokes equation, Eq (2.9). Thus, the solutions in these two layers can be matched in the transition zone at the free-fluid/porous-medium interface by using the generalized Stokes-Brinkman model. The mathematical model is summarized in the next section.

### 2.3. Governing equations

The models for a problem of this kind are summarized in this section. The models in both free-fluid layer and porous medium consist of two unknowns, which are the velocity  $\mathbf{u}^l$  and the pressure  $p$ . Therefore, in each region, we need one more equation, which is a continuity equation obtained from conservation of mass. Since a bundle of self-propelled solid phases effects the fluid flow, we employ the continuity equation for two-phase flow in the porous medium derived by HMT [26, 27], which is

$$\nabla \cdot (\varepsilon^l \mathbf{u}^l) = f, \quad (2.16)$$

where  $f = -\dot{\varepsilon}^l / (1 - \varepsilon^l) + \nabla \cdot (\varepsilon^l \mathbf{u}^s)$  and  $\dot{\varepsilon}^l = \partial \varepsilon^l / \partial t + \mathbf{u}^s \cdot \nabla \varepsilon^l$ . Let  $\Omega = \Omega_p \cup \Omega_f$  be our domain, and  $\partial \Omega$  is the boundary of the domain. Define the vectors

$$\mathbf{u} = \varepsilon^l \mathbf{u}^l \quad \text{and} \quad \mathbf{f} = \rho \mathbf{g} + \mu \mathbf{k}^{-1} \cdot \varepsilon^l \mathbf{u}^s. \quad (2.17)$$

From Eqs (2.14), (2.16) and (2.17), the system of equations used in domain  $\Omega_p$  is

$$\mu \mathbf{k}^{-1} \cdot \mathbf{u} - \frac{\mu}{\varepsilon^l} \nabla \cdot (2\varepsilon^l \mathbf{d}^l) + \nabla p = \mathbf{f} \quad \text{in } \Omega_p, \quad (2.18)$$

$$\nabla \cdot \mathbf{u} = f \quad \text{in } \Omega_p. \quad (2.19)$$

For the free-fluid domain  $\Omega_f$ , the flow is considered incompressible. Then, the divergence of velocity is zero. Therefore, in domain  $\Omega_f$ , we have the system of equations

$$-\mu \nabla \cdot (2\varepsilon^l \mathbf{d}^l) + \nabla p = 0 \quad \text{in } \Omega_f, \quad (2.20)$$

$$\nabla \cdot \mathbf{u} = 0 \quad \text{in } \Omega_f. \quad (2.21)$$

Before we prove the well-posedness of the generalized Stokes-Brinkman equations, Eqs (2.18) and (2.19), in the next section we provide the discretized form of the governing equations by using a finite element method.

### 3. Discretized model

In this section, we first formulate the weak formulation of the generalized Stokes-Brinkman equations, Eqs (2.18) and (2.19), by using a mixed finite element method. To obtain the weak form of Eq (2.18), we multiply a weight function  $\mathbf{w} \in H_0^1(\Omega)$  and integrate Eq (2.18) over the domain  $\Omega$  on both sides, and we have

$$\int_{\Omega} \mu(\mathbf{k}^{-1} \cdot \mathbf{u}) \cdot \mathbf{w} - \int_{\Omega} \frac{\mu}{\varepsilon^l} (\nabla \cdot (2\varepsilon^l \mathbf{d}^l)) \cdot \mathbf{w} + \int_{\Omega} \nabla p \cdot \mathbf{w} = \int_{\Omega} \mathbf{f} \cdot \mathbf{w}. \quad (3.1)$$

Applying Green's first identity to the second and third terms on the left hand side of Eq (3.1) and using the property that the weight function is zero at the boundary, we have

$$\int_{\Omega} \mu(\mathbf{k}^{-1} \cdot \mathbf{u}) \cdot \mathbf{w} + \int_{\Omega} 2\mu\varepsilon^l \mathbf{d}^l : \nabla \left( \frac{\mathbf{w}}{\varepsilon^l} \right) - \int_{\Omega} (\nabla \cdot \mathbf{w}) p = \int_{\Omega} \mathbf{f} \cdot \mathbf{w}. \quad (3.2)$$

Substituting  $\mathbf{d}^l = 0.5 \left[ \nabla \left( \frac{\mathbf{u}}{\varepsilon^l} \right) + \left( \nabla \left( \frac{\mathbf{u}}{\varepsilon^l} \right) \right)^T \right]$  into Eq (3.2), we obtain the weak formulation of Eq (2.18), which is

$$\int_{\Omega} \mu(\mathbf{k}^{-1} \cdot \mathbf{u}) \cdot \mathbf{w} + \int_{\Omega} \mu\varepsilon^l \nabla \left( \frac{\mathbf{u}}{\varepsilon^l} \right) : \nabla \left( \frac{\mathbf{w}}{\varepsilon^l} \right) + \int_{\Omega} \mu\varepsilon^l \left( \nabla \left( \frac{\mathbf{u}}{\varepsilon^l} \right) \right)^T : \nabla \left( \frac{\mathbf{w}}{\varepsilon^l} \right) - \int_{\Omega} (\nabla \cdot \mathbf{w}) p = \int_{\Omega} \mathbf{f} \cdot \mathbf{w}. \quad (3.3)$$

Similarly, multiplying both sides of Eq (2.19) by another weight function  $q \in L_0^2(\Omega)$  and integrating both sides, we obtain the weak formulation of Eq (2.19):

$$\int_{\Omega} (\nabla \cdot \mathbf{u}) q = \int_{\Omega} f q. \quad (3.4)$$

The weak formulation of the generalized Stokes-Brinkman equations can be written in linear and bilinear functionals as follows.

**Problem 1.** The weak form of the generalized Stokes-Brinkman equations is to find  $\mathbf{u} \in H_0^1(\Omega)$  and  $p \in L_0^2(\Omega)$  such that

$$a(\mathbf{u}, \mathbf{w}) + b(\mathbf{w}, p) = c_1(\mathbf{w}), \quad \forall \mathbf{w} \in H_0^1(\Omega), \quad (3.5)$$

$$b(\mathbf{u}, q) = c_2(q), \quad \forall q \in L_0^2(\Omega), \quad (3.6)$$

where the linear and bilinear functionals are defined as

$$a(\mathbf{u}, \mathbf{w}) = \int_{\Omega} \mu(\mathbf{k}^{-1} \cdot \mathbf{u}) \cdot \mathbf{w} + \int_{\Omega} \mu \varepsilon^l \nabla \left( \frac{\mathbf{u}}{\varepsilon^l} \right) : \nabla \left( \frac{\mathbf{w}}{\varepsilon^l} \right) + \int_{\Omega} \mu \varepsilon^l \left( \nabla \left( \frac{\mathbf{u}}{\varepsilon^l} \right) \right)^T : \nabla \left( \frac{\mathbf{w}}{\varepsilon^l} \right), \quad (3.7)$$

$$b(\mathbf{u}, q) = - \int_{\Omega} (\nabla \cdot \mathbf{u}) q, \quad (3.8)$$

$$c_1(\mathbf{w}) = \langle \mathbf{f}, \mathbf{w} \rangle_{H^{-1}(\Omega) \times H_0^1(\Omega)}, \quad (3.9)$$

$$c_2(q) = - \int_{\Omega} f q, \quad (3.10)$$

where the space  $H_s^1(\Omega) = \{\mathbf{w} \in H^1(\Omega) : \mathbf{w}|_{\partial\Omega} = \mathbf{s}\}$ , and  $\langle \cdot, \cdot \rangle$  is the duality pairing.

Notice that the space  $L_0^2(\Omega)$  is used instead of  $L^2(\Omega)$  because the system of Eqs (2.18) and (2.19) demonstrates pressure up to an additive constant; see [28] on page 157 for details. The linear and bilinear functionals in Problem 1 can be written in the form of a linear operator as in Problem 2 (the definition of the linear operator is in the Appendix).

**Problem 2.** Let  $A : H_0^1(\Omega) \rightarrow H^{-1}(\Omega)$  and  $B : H_0^1(\Omega) \rightarrow L_0^2(\Omega)$  be linear operators. Find  $\mathbf{u} \in H_s^1(\Omega)$ ,  $p \in L_0^2(\Omega)$  such that

$$A\mathbf{u} + B^* p = \mathbf{f} \text{ in } H^{-1}(\Omega), \quad (3.11)$$

$$B\mathbf{u} = f \text{ in } L_0^2(\Omega), \quad (3.12)$$

where

$$\|\mathbf{f}\|_{H^{-1}(\Omega)} = \sup_{\mathbf{w} \in H_0^1(\Omega), \mathbf{w} \neq 0} \frac{\langle \mathbf{f}, \mathbf{w} \rangle_{H^{-1}(\Omega) \times H_0^1(\Omega)}}{\|\mathbf{w}\|_{H^1(\Omega)}}, \quad (3.13)$$

the norm  $\|\cdot\|_{H^1(\Omega)}$  denotes the standard norm on the space  $H^1(\Omega)$ , and the function  $\mathbf{u}^s$  in  $\mathbf{f}$  is a bounded continuous function.

Next, we show that the linear and bilinear functionals in Problem 1 are continuous and coercive, and that will be used to prove the existence and uniqueness of the generalized Stokes-Brinkman equations in Section 5.

#### 4. Continuity and coercivity of linear and bilinear functionals

In this section, we show that the linear and bilinear functionals in Problem 1 are continuous and coercive. These properties are necessary to prove the existence and uniqueness of the governing equations. We first proof the continuity as shown in Theorem 4.1.

**Theorem 4.1.** The linear functionals  $c_1(\mathbf{w}), c_2(q)$  and bilinear functionals  $a(\cdot, \cdot), b(\cdot, \cdot)$  are continuous. In particular,

$$c_1(\mathbf{w}) \leq \|\mathbf{f}\|_{H^{-1}(\Omega)} \|\mathbf{w}\|_{H^1(\Omega)}, \quad \forall \mathbf{w} \in H^1(\Omega), \quad (4.1)$$

$$c_2(q) \leq \|f\|_{L^2(\Omega)} \|q\|_{L^2(\Omega)}, \quad \forall q \in L^2(\Omega), \quad (4.2)$$

$$b(\mathbf{u}, q) \leq \sqrt{n} \|\mathbf{u}\|_{H^1(\Omega)} \|q\|_{L^2(\Omega)}, \quad \forall \mathbf{u} \in H^1(\Omega), \forall q \in L^2(\Omega), \quad (4.3)$$

$$a(\mathbf{u}, \mathbf{w}) \leq Q_a \|\mathbf{u}\|_{H^1(\Omega)} \|\mathbf{w}\|_{H^1(\Omega)}, \quad \forall \mathbf{u}, \mathbf{w} \in H^1(\Omega), \quad (4.4)$$

where  $n$  is the dimensional number, and

$$Q_a = \max\{\sqrt{6}\mu \max_{1 \leq i, j \leq 2} |k_{ij}^{-1}|, 2\mu / \|\varepsilon'\|_{H^1(\Omega)}\}.$$

*Proof.* It is obvious that  $c_1(\mathbf{w})$  and  $c_2(q)$  are linear functionals, and  $a(\mathbf{u}, \mathbf{w})$  and  $b(\mathbf{u}, q)$  are bilinear functionals. Next, we show the continuity of  $c_1(\mathbf{w})$ . Let  $\mathbf{w} \in H^1(\Omega)$ . Then,

$$\begin{aligned} |c_1(\mathbf{w})| &= \left| \langle \mathbf{f}, \mathbf{w} \rangle_{H^{-1}(\Omega) \times H_0^1(\Omega)} \right| \\ &= \left| \frac{\langle \mathbf{f}, \mathbf{w} \rangle_{H^{-1}(\Omega) \times H_0^1(\Omega)}}{\|\mathbf{w}\|_{H^1(\Omega)}} \|\mathbf{w}\|_{H^1(\Omega)} \right| \\ &\leq \|\mathbf{f}\|_{H^{-1}(\Omega)} \|\mathbf{w}\|_{H^1(\Omega)}, \end{aligned}$$

where we apply the definition of norm on the space  $H^{-1}(\Omega)$ , Eq (3.13), at the inequality. The proof of the continuities of  $c_2(q)$  and  $b(\mathbf{u}, q)$  has been shown in [16]. Next, we show the continuity of  $a(\mathbf{u}, \mathbf{w})$  in a two-dimensional domain. Define  $\mathbf{u} = (u_1, u_2)$  and  $\mathbf{w} = (w_1, w_2)$ . Then, from Eq (3.7), we have

$$\begin{aligned} |a(\mathbf{u}, \mathbf{w})| &= \left| \int_{\Omega} \mu(\mathbf{k}^{-1} \cdot \mathbf{u}) \cdot \mathbf{w} + \int_{\Omega} \mu \varepsilon' \nabla \left( \frac{\mathbf{u}}{\varepsilon'} \right) : \nabla \left( \frac{\mathbf{w}}{\varepsilon'} \right) + \int_{\Omega} \mu \varepsilon' \left( \nabla \left( \frac{\mathbf{u}}{\varepsilon'} \right) \right)^T : \nabla \left( \frac{\mathbf{w}}{\varepsilon'} \right) \right| \\ &\leq \left| \int_{\Omega} \mu(\mathbf{k}^{-1} \cdot \mathbf{u}) \cdot \mathbf{w} \right| + \left| \int_{\Omega} \mu \varepsilon' \nabla \left( \frac{\mathbf{u}}{\varepsilon'} \right) : \nabla \left( \frac{\mathbf{w}}{\varepsilon'} \right) \right| + \left| \int_{\Omega} \mu \varepsilon' \left( \nabla \left( \frac{\mathbf{u}}{\varepsilon'} \right) \right)^T : \nabla \left( \frac{\mathbf{w}}{\varepsilon'} \right) \right| \\ &\leq \mu \|\mathbf{k}^{-1} \cdot \mathbf{u}\|_{L^2(\Omega)} \|\mathbf{w}\|_{L^2(\Omega)} + \mu \left\| \varepsilon' \nabla \left( \frac{\mathbf{u}}{\varepsilon'} \right) \right\|_{L^2(\Omega)} \left\| \nabla \left( \frac{\mathbf{w}}{\varepsilon'} \right) \right\|_{L^2(\Omega)} \\ &\quad + \mu \left\| \varepsilon' \left( \nabla \left( \frac{\mathbf{u}}{\varepsilon'} \right) \right)^T \right\|_{L^2(\Omega)} \left\| \nabla \left( \frac{\mathbf{w}}{\varepsilon'} \right) \right\|_{L^2(\Omega)} \\ &\leq \sqrt{6}\mu \max_{1 \leq i, j \leq 2} |k_{ij}^{-1}| \|\mathbf{u}\|_{L^2(\Omega)} \|\mathbf{w}\|_{L^2(\Omega)} + \mu \|\varepsilon'\|_{L^2(\Omega)} \left\| \nabla \left( \frac{\mathbf{u}}{\varepsilon'} \right) \right\|_{L^2(\Omega)} \left\| \nabla \left( \frac{\mathbf{w}}{\varepsilon'} \right) \right\|_{L^2(\Omega)} \\ &\quad + \mu \|\varepsilon'\|_{L^2(\Omega)} \left\| \left( \nabla \left( \frac{\mathbf{u}}{\varepsilon'} \right) \right)^T \right\|_{L^2(\Omega)} \left\| \nabla \left( \frac{\mathbf{w}}{\varepsilon'} \right) \right\|_{L^2(\Omega)} \\ &= \sqrt{6}\mu \max_{1 \leq i, j \leq 2} |k_{ij}^{-1}| \|\mathbf{u}\|_{L^2(\Omega)} \|\mathbf{w}\|_{L^2(\Omega)} + 2\mu \|\varepsilon'\|_{L^2(\Omega)} \left\| \nabla \left( \frac{\mathbf{u}}{\varepsilon'} \right) \right\|_{L^2(\Omega)} \left\| \nabla \left( \frac{\mathbf{w}}{\varepsilon'} \right) \right\|_{L^2(\Omega)} \\ &\leq \sqrt{6}\mu \max_{1 \leq i, j \leq 2} |k_{ij}^{-1}| \|\mathbf{u}\|_{H^1(\Omega)} \|\mathbf{w}\|_{H^1(\Omega)} + 2\mu \|\varepsilon'\|_{L^2(\Omega)} \left\| \frac{\mathbf{u}}{\varepsilon'} \right\|_{H^1(\Omega)} \left\| \frac{\mathbf{w}}{\varepsilon'} \right\|_{H^1(\Omega)} \\ &= \sqrt{6}\mu \max_{1 \leq i, j \leq 2} |k_{ij}^{-1}| \|\mathbf{u}\|_{H^1(\Omega)} \|\mathbf{w}\|_{H^1(\Omega)} + 2\mu \|\varepsilon'\|_{L^2(\Omega)} \frac{\|\mathbf{u}\|_{H^1(\Omega)} \|\mathbf{w}\|_{H^1(\Omega)}}{\|\varepsilon'\|_{H^1(\Omega)} \|\varepsilon'\|_{H^1(\Omega)}} \\ &\leq \sqrt{6}\mu \max_{1 \leq i, j \leq 2} |k_{ij}^{-1}| \|\mathbf{u}\|_{H^1(\Omega)} \|\mathbf{w}\|_{H^1(\Omega)} + \frac{2\mu}{\|\varepsilon'\|_{H^1(\Omega)}} \|\mathbf{u}\|_{H^1(\Omega)} \|\mathbf{w}\|_{H^1(\Omega)} \\ &\leq \max \left\{ \sqrt{6}\mu \max_{1 \leq i, j \leq 2} |k_{ij}^{-1}|, \frac{2\mu}{\|\varepsilon'\|_{H^1(\Omega)}} \right\} \|\mathbf{u}\|_{H^1(\Omega)} \|\mathbf{w}\|_{H^1(\Omega)} \\ &= Q_a \|\mathbf{u}\|_{H^1(\Omega)} \|\mathbf{w}\|_{H^1(\Omega)}, \end{aligned}$$

where  $Q_a = \max \left\{ \sqrt{6}\mu \max_{1 \leq i, j \leq 2} |k_{ij}^{-1}|, \frac{2\mu}{\|\varepsilon^l\|_{H^1(\Omega)}} \right\}$  and the inequality [14]

$$\|\mathbf{k}^{-1} \cdot \mathbf{u}\|_{L^2(\Omega)} \leq \sqrt{6} \max_{1 \leq i, j \leq 2} |k_{ij}^{-1}| \|\mathbf{u}\|_{L^2(\Omega)} \tag{4.5}$$

is applied to the third inequality. For the fifth inequality, we use the fact that  $\|\cdot\|_{L^2(\Omega)} \leq \|\cdot\|_{H^1(\Omega)}$ , so  $\frac{\|\cdot\|_{L^2(\Omega)}}{\|\cdot\|_{H^1(\Omega)}} \leq 1$ . Therefore,  $a(\mathbf{u}, \mathbf{w})$  is continuous.

To show that the bilinear form  $a(\cdot, \cdot)$  is coercive, we first proof Lemma 4.2, which will be used in the proof of coercivity presented in Theorem 4.3.

**Lemma 4.2.** *Let  $\mathbf{w} \in H^1(\Omega)$ . Then,*

$$\int_{\Omega} \mu \varepsilon^l \nabla \left( \frac{\mathbf{w}}{\varepsilon^l} \right) : \nabla \left( \frac{\mathbf{w}}{\varepsilon^l} \right) + \int_{\Omega} \mu \varepsilon^l \left( \nabla \left( \frac{\mathbf{w}}{\varepsilon^l} \right) \right)^T : \nabla \left( \frac{\mathbf{w}}{\varepsilon^l} \right) \geq \frac{\mu \sqrt{|V|}}{2n_r^2} \left\| \nabla \left( \frac{\mathbf{w}}{\varepsilon^l} \right) + \left( \nabla \left( \frac{\mathbf{w}}{\varepsilon^l} \right) \right)^T \right\|_{L^2(\Omega)}^2, \tag{4.6}$$

for some natural number  $n_r$ .

*Proof.* Let  $\mathbf{w} \in H^1(\Omega)$ . Since the porosity  $\varepsilon^l > 0$  is a real number, by the Archimedean property, there exists  $n_r \in \mathbb{N}$  such that  $\varepsilon^l \geq \frac{1}{n_r}$ . Given  $\mathbf{W} = \frac{\mathbf{w}}{\varepsilon^l}$ , then,

$$\begin{aligned} \int_{\Omega} \mu \varepsilon^l \nabla \left( \frac{\mathbf{w}}{\varepsilon^l} \right) : \nabla \left( \frac{\mathbf{w}}{\varepsilon^l} \right) + \int_{\Omega} \mu \varepsilon^l \left( \nabla \left( \frac{\mathbf{w}}{\varepsilon^l} \right) \right)^T : \nabla \left( \frac{\mathbf{w}}{\varepsilon^l} \right) &= \int_{\Omega} \mu \varepsilon^l \nabla \mathbf{W} : \nabla \mathbf{W} + \int_{\Omega} \mu \varepsilon^l (\nabla \mathbf{W})^T : \nabla \mathbf{W} \\ &= \int_{\Omega} \mu \varepsilon^l [\nabla \mathbf{W} : \nabla \mathbf{W} + (\nabla \mathbf{W})^T : \nabla \mathbf{W}] \\ &= \int_{\Omega} \mu \varepsilon^l [\nabla \mathbf{W} + (\nabla \mathbf{W})^T] : \nabla \mathbf{W} \\ &= \int_{\Omega} 2\mu \varepsilon^l \frac{1}{2} [\nabla \mathbf{W} + (\nabla \mathbf{W})^T] : \nabla \mathbf{W} \\ &= \int_{\Omega} 2\mu \varepsilon^l \mathbf{D} : \nabla \mathbf{W} \\ &= \int_{\Omega} 2\mu \varepsilon^l D_{ij} \frac{\partial W_i}{\partial x_j} \\ &= \int_{\Omega} 2\mu \varepsilon^l \left( D_{11} \frac{\partial W_1}{\partial x_1} + D_{12} \frac{\partial W_1}{\partial x_2} + D_{21} \frac{\partial W_2}{\partial x_1} + D_{22} \frac{\partial W_2}{\partial x_2} \right) \\ &= \int_{\Omega} 2\mu \varepsilon^l \left( D_{11}^2 + D_{12} \left( \frac{\partial W_1}{\partial x_2} + \frac{\partial W_2}{\partial x_1} \right) + D_{22}^2 \right) \\ &= \int_{\Omega} 2\mu \varepsilon^l \left( D_{11}^2 + 2D_{12} \frac{1}{2} \left( \frac{\partial W_1}{\partial x_2} + \frac{\partial W_2}{\partial x_1} \right) + D_{22}^2 \right) \\ &= \int_{\Omega} 2\mu \varepsilon^l (D_{11}^2 + 2D_{12}^2 + D_{22}^2) \\ &= \int_{\Omega} 2\mu \varepsilon^l (D_{11}^2 + D_{12}^2 + D_{21}^2 + D_{22}^2) \end{aligned}$$

$$\begin{aligned}
 &\geq 2\mu \int_{\Omega} (\varepsilon^l)^2 (D_{11}^2 + D_{12}^2 + D_{21}^2 + D_{22}^2) \\
 &= 2\mu \left( \int_{\Omega} (\varepsilon^l D_{11})^2 + \int_{\Omega} (\varepsilon^l D_{12})^2 + \int_{\Omega} (\varepsilon^l D_{21})^2 + \int_{\Omega} (\varepsilon^l D_{22})^2 \right) \\
 &= 2\mu \left( \|\varepsilon^l D_{11}\|_{L^2(\Omega)}^2 + \|\varepsilon^l D_{12}\|_{L^2(\Omega)}^2 + \|\varepsilon^l D_{21}\|_{L^2(\Omega)}^2 + \|\varepsilon^l D_{22}\|_{L^2(\Omega)}^2 \right) \\
 &\geq 2\mu \left( \|(\varepsilon^l D_{11})^2\|_{L^2(\Omega)} + \|(\varepsilon^l D_{12})^2\|_{L^2(\Omega)} + \|(\varepsilon^l D_{21})^2\|_{L^2(\Omega)} + \|(\varepsilon^l D_{22})^2\|_{L^2(\Omega)} \right) \\
 &\geq 2\mu \|(\varepsilon^l D_{11})^2 + (\varepsilon^l D_{12})^2 + (\varepsilon^l D_{21})^2 + (\varepsilon^l D_{22})^2\|_{L^2(\Omega)} \\
 &= 2\mu \left\| \sum_{i=1}^2 \sum_{j=1}^2 |\varepsilon^l D_{ij}|^2 \right\|_{L^2(\Omega)} \\
 &\geq 2\mu \|(\sigma_{\max}(\varepsilon^l \mathbf{D}))^2\|_{L^2(\Omega)} \\
 &= 2\mu \left( \int_{\Omega} (\sigma_{\max}(\varepsilon^l \mathbf{D}))^4 d\Omega \right)^{\frac{1}{2}} \\
 &= 2\mu \left( (\sigma_{\max}(\varepsilon^l \mathbf{D}))^4 \int_{\Omega} 1 d\Omega \right)^{\frac{1}{2}} \\
 &= 2\mu \left( (\sigma_{\max}(\varepsilon^l \mathbf{D}))^4 |V| \right)^{\frac{1}{2}} \\
 &= 2\mu \sqrt{|V|} (\sigma_{\max}(\varepsilon^l \mathbf{D}))^2 \\
 &= 2\mu \sqrt{|V|} \|\varepsilon^l \mathbf{D}\|_{L^2(\Omega)}^2 \\
 &= 2\mu \sqrt{|V|} \left\| \frac{\varepsilon^l}{2} (\nabla \mathbf{W} + (\nabla \mathbf{W})^T) \right\|_{L^2(\Omega)}^2 \\
 &\geq 2\mu \sqrt{|V|} \left\| \frac{1}{2n_r} (\nabla \mathbf{W} + (\nabla \mathbf{W})^T) \right\|_{L^2(\Omega)}^2 \\
 &= \frac{\mu \sqrt{|V|}}{2n_r^2} \|\nabla \mathbf{W} + (\nabla \mathbf{W})^T\|_{L^2(\Omega)}^2 \\
 &= \frac{\mu \sqrt{|V|}}{2n_r^2} \left\| \nabla \left( \frac{\mathbf{w}}{\varepsilon^l} \right) + \left( \nabla \left( \frac{\mathbf{w}}{\varepsilon^l} \right) \right)^T \right\|_{L^2(\Omega)}^2,
 \end{aligned}$$

where  $\mathbf{D} = \frac{1}{2}(\nabla \mathbf{W} + (\nabla \mathbf{W})^T)$  is symmetric with the indicial notation  $D_{ij} = \frac{1}{2} \left( \frac{\partial W_i}{\partial x_j} + \frac{\partial W_j}{\partial x_i} \right)$ . The variable  $D_{ij}$  is considered to be a real number for all  $i, j = 1, 2$ , and  $|V|$  is the volume of the domain  $\Omega$ . For the first inequality, we use the fact that the porosity  $\varepsilon^l \leq 1$ . For the second and third inequalities, we apply Hölder’s inequality and the triangle inequality, respectively. For the fourth inequality, we apply the spectral norm of a matrix  $\mathbf{E}$  [29], i.e.,

$$\|\mathbf{E}\|_{L^2(\Omega)} = \sigma_{\max}(\mathbf{E}) \leq \left( \sum_{i=1}^m \sum_{j=1}^s |a_{ij}|^2 \right)^{\frac{1}{2}}, \tag{4.7}$$

where  $\sigma_{\max}(\mathbf{E})$  represents the largest singular value of a matrix  $\mathbf{E}$ , and  $s$  and  $m$  are the dimensional numbers. For the last inequality, we use the Archimedean property [30]. Therefore,

$$\int_{\Omega} \mu \varepsilon^l \nabla \mathbf{W} : \nabla \mathbf{W} + \int_{\Omega} \mu \varepsilon^l (\nabla \mathbf{W})^T : \nabla \mathbf{W} \geq \frac{\mu \sqrt{|V|}}{2n_r^2} \|\nabla \mathbf{W} + (\nabla \mathbf{W})^T\|_{L^2(\Omega)}^2. \tag{4.8}$$

Hence, the proof is complete.

Next, we show the coercivity of the bilinear functional  $a(\cdot, \cdot)$ .

**Theorem 4.3.** *The bilinear functional  $a(\cdot, \cdot)$  is coercive, such that*

$$a(\mathbf{w}, \mathbf{w}) \geq Q_c \|\mathbf{w}\|_{H^1(\Omega)}^2, \quad \forall \mathbf{w} \in H^1(\Omega), \tag{4.9}$$

where  $Q_c = \min \left\{ \mu Q_k, \frac{\mu \sqrt{|V|}}{n_r^2 K} (N-1)^2 \right\}$  and  $Q_k$  is a positive number.

*Proof.* Let  $\mathbf{w} \in H^1(\Omega)$ . Then,

$$\begin{aligned} a(\mathbf{w}, \mathbf{w}) &= \int_{\Omega} \mu (\mathbf{k}^{-1} \cdot \mathbf{w}) \cdot \mathbf{w} + \int_{\Omega} \mu \varepsilon^l \nabla \left( \frac{\mathbf{w}}{\varepsilon^l} \right) : \nabla \left( \frac{\mathbf{w}}{\varepsilon^l} \right) + \int_{\Omega} \mu \varepsilon^l \left( \nabla \left( \frac{\mathbf{w}}{\varepsilon^l} \right) \right)^T : \nabla \left( \frac{\mathbf{w}}{\varepsilon^l} \right) \\ &= \int_{\Omega} \mu (\mathbf{k}^{-1} \cdot \mathbf{w}) \cdot \mathbf{w} + \int_{\Omega} \mu \varepsilon^l \nabla \mathbf{W} : \nabla \mathbf{W} + \int_{\Omega} \mu \varepsilon^l (\nabla \mathbf{W})^T : \nabla \mathbf{W} \\ &\geq \mu Q_k \|\mathbf{w}\|_{L^2(\Omega)}^2 + \frac{\mu \sqrt{|V|}}{2n_r^2} \|\nabla \mathbf{W} + (\nabla \mathbf{W})^T\|_{L^2(\Omega)}^2 \\ &= \mu Q_k \|\mathbf{w}\|_{L^2(\Omega)}^2 + \frac{\mu \sqrt{|V|}}{2n_r^2} \left( \|\nabla \mathbf{W} + (\nabla \mathbf{W})^T\|_{L^2(\Omega)}^2 + \|\nabla \mathbf{W} - (\nabla \mathbf{W})^T\|_{L^2(\Omega)}^2 \right. \\ &\quad \left. - \|\nabla \mathbf{W} - (\nabla \mathbf{W})^T\|_{L^2(\Omega)}^2 \right) \\ &\geq \mu Q_k \|\mathbf{w}\|_{L^2(\Omega)}^2 + \frac{\mu \sqrt{|V|}}{2n_r^2} \left[ 2\|\nabla \mathbf{W}\|_{L^2(\Omega)}^2 + 2\|(\nabla \mathbf{W})^T\|_{L^2(\Omega)}^2 - \left( \|\nabla \mathbf{W}\|_{L^2(\Omega)}^2 + \|(\nabla \mathbf{W})^T\|_{L^2(\Omega)}^2 \right) \right] \\ &= \mu Q_k \|\mathbf{w}\|_{L^2(\Omega)}^2 + \frac{\mu \sqrt{|V|}}{n_r^2} \left( \|\nabla \mathbf{W}\|_{L^2(\Omega)}^2 + \|(\nabla \mathbf{W})^T\|_{L^2(\Omega)}^2 \right) \\ &\geq \mu Q_k \|\mathbf{w}\|_{L^2(\Omega)}^2 + \frac{\mu \sqrt{|V|}}{n_r^2} \|\nabla \mathbf{W}\|_{L^2(\Omega)}^2 \\ &= \mu Q_k \|\mathbf{w}\|_{L^2(\Omega)}^2 + \frac{\mu \sqrt{|V|}}{n_r^2} \|\mathbf{W}\|_{H^1(\Omega)}^2 \\ &= \mu Q_k \|\mathbf{w}\|_{L^2(\Omega)}^2 + \frac{\mu \sqrt{|V|}}{n_r^2} \left\| \frac{\mathbf{w}}{\varepsilon^l} \right\|_{H^1(\Omega)}^2 \\ &\geq \mu Q_k \|\mathbf{w}\|_{L^2(\Omega)}^2 + \frac{\mu \sqrt{|V|}}{n_r^2 K} \left\| \frac{\mathbf{w}}{\varepsilon^l} \right\|_{H^1(\Omega)}^2 \\ &\geq \mu Q_k \|\mathbf{w}\|_{L^2(\Omega)}^2 + \frac{\mu \sqrt{|V|}}{n_r^2 K} \|(N-1) \mathbf{w}\|_{H^1(\Omega)}^2 \\ &= \mu Q_k \|\mathbf{w}\|_{L^2(\Omega)}^2 + \frac{\mu \sqrt{|V|}}{n_r^2 K} (N-1)^2 \|\mathbf{w}\|_{H^1(\Omega)}^2 \end{aligned}$$

$$\begin{aligned} &\geq \min \left\{ \mu Q_k, \frac{\mu \sqrt{|V|}}{n^2 K} (N-1)^2 \right\} (\|\mathbf{w}\|_{L^2(\Omega)}^2 + \|\mathbf{w}\|_{H^1(\Omega)}^2) \\ &\geq \min \left\{ \mu Q_k, \frac{\mu \sqrt{|V|}}{n^2 K} (N-1)^2 \right\} \|\mathbf{w}\|_{H^1(\Omega)}^2 \\ &= Q_c \|\mathbf{w}\|_{H^1(\Omega)}^2, \end{aligned}$$

where  $Q_c = \min \left\{ \mu Q_k, \frac{\mu \sqrt{|V|}}{n^2 K} (N-1)^2 \right\} > 0$ . The property [14]

$$\int_{\Omega} (\mathbf{k}^{-1} \cdot \mathbf{w}) \cdot \mathbf{w} \geq Q_k \|\mathbf{w}\|_{L^2(\Omega)}^2 \quad \text{where } Q_k > 0 \tag{4.10}$$

and inequality (4.8) are used in the first inequality. Parallelogram law [31]  $\forall \mathbf{u}, \mathbf{w} \in U$ ,  $\|\mathbf{u} + \mathbf{w}\|^2 + \|\mathbf{u} - \mathbf{w}\|^2 = 2(\|\mathbf{u}\|^2 + \|\mathbf{w}\|^2)$  and the fact that  $\|\mathbf{u} - \mathbf{w}\|^2 \leq \|\mathbf{u}\|^2 + \|\mathbf{w}\|^2$  are applied to the second inequality. Poincaré inequality [31]  $\exists K > 0$  such that  $\|\mathbf{w}\|_{H^m(\Omega)} \geq \frac{1}{K} \|\mathbf{w}\|_{H^m(\Omega)}$ ,  $\forall \mathbf{w} \in H_0^m(\Omega)$  where  $m \geq 0$ , is applied to the fourth inequality. For the fifth inequality, we apply Archimedean property [30]  $\forall r \in \mathbb{R}$ ,  $\exists N \in \mathbb{N}$  such that  $N - 1 \leq r \leq N$  and use the fact that  $\varepsilon^r$  is a positive real number. Hence, the proof of the coercivity of the bilinear form  $a(\mathbf{w}, \mathbf{w})$  is complete.

**5. The existence and uniqueness of the generalized Stokes-Brinkman model**

In this section, we provide the proof of the existence and uniqueness of the generalized Stokes-Brinkman equations. Before illustrating the proof of the well-posedness, we present the following proposition.

**Proposition 5.1.** *Let  $f \in L^2(\Omega)$  and  $s \in H^{1/2}(\partial\Omega)$ . Then, there exist  $\mathbf{u}_s \in H^1(\Omega)$  and a unique  $\mathbf{u}_0 \in V^\perp$  such that*

$$\|\mathbf{u}_s + \mathbf{u}_0\|_{H^1(\Omega)} \leq \frac{1}{\beta} \|f\|_{L^2(\Omega)} + \left( 1 + \frac{\sqrt{n}}{\beta} \right) Q_s \|s\|_{H^{1/2}(\partial\Omega)}, \tag{5.1}$$

where  $n$  is the dimensional number, and  $\beta$  and  $Q_s$  are positive constants.

*Proof.* Let  $f \in L^2(\Omega)$ , and  $s \in H^{1/2}(\partial\Omega)$ . Therefore, there exist  $\mathbf{u}_s \in H^1(\Omega)$ , a unique  $\mathbf{u}_0 \in V^\perp \subset H_0^1(\Omega)$  and  $Q_s > 0$  such that  $\mathbf{u}_s|_{\partial\Omega} = s$ ,  $f - \nabla \cdot \mathbf{u}_s \in L_0^2(\Omega)$ ,  $\nabla \cdot \mathbf{u}_0 = f - \nabla \cdot \mathbf{u}_s$ ,

$$\|\mathbf{u}_s\|_{H^1(\Omega)} \leq Q_s \|s\|_{H^{1/2}(\partial\Omega)}, \tag{5.2}$$

and there exists  $\beta > 0$  such that

$$\|\mathbf{u}_0\|_{H^1(\Omega)} \leq \beta^{-1} \|f - \nabla \cdot \mathbf{u}_s\|_{L^2(\Omega)}. \tag{5.3}$$

See Lemma A.4 for the details. Next, we show that  $\mathbf{u}_s + \mathbf{u}_0$  is bounded, as follows.

$$\begin{aligned} \|\mathbf{u}_s + \mathbf{u}_0\|_{H^1(\Omega)} &\leq \|\mathbf{u}_s\|_{H^1(\Omega)} + \|\mathbf{u}_0\|_{H^1(\Omega)} \\ &\leq Q_s \|s\|_{H^{1/2}(\partial\Omega)} + \frac{1}{\beta} \|f - \nabla \cdot \mathbf{u}_s\|_{L^2(\Omega)} \end{aligned}$$

$$\begin{aligned} &\leq Q_s \|s\|_{H^{1/2}(\partial\Omega)} + \frac{1}{\beta} \|f\|_{L^2(\Omega)} + \frac{1}{\beta} \|\nabla \cdot \mathbf{u}_s\|_{L^2(\Omega)} \\ &\leq Q_s \|s\|_{H^{1/2}(\partial\Omega)} + \frac{1}{\beta} \|f\|_{L^2(\Omega)} + \frac{\sqrt{n}}{\beta} \|\mathbf{u}_s\|_{H^1(\Omega)} \\ &\leq \frac{1}{\beta} \|f\|_{L^2(\Omega)} + \left(1 + \frac{\sqrt{n}}{\beta}\right) Q_s \|s\|_{H^{1/2}(\partial\Omega)}, \end{aligned}$$

where the fact that [16]  $\|\nabla \cdot \phi\|_{L^2(\Omega)} \leq \sqrt{n} \|\phi\|_{H^1(\Omega)}$ , where  $n$  is the dimensional number, is applied to the fourth inequality.

Next, we show the theorem of the well-posedness of the generalized Stokes-Brinkman equations.

**Theorem 5.2.** *Let  $\mathbf{f} \in H^{-1}(\Omega)$ ,  $f \in L^2(\Omega)$  and  $\mathbf{s} \in H^{1/2}(\partial\Omega)$ . There exist a unique  $\mathbf{u} \in H_s^1(\Omega)$  and  $p \in L_0^2(\Omega)$  satisfying Problem 1. Moreover,*

$$\|\mathbf{u}\|_{H^1(\Omega)} \leq \frac{1}{Q_c} \|\mathbf{f}\|_{H^{-1}(\Omega)} + \left(1 + \frac{Q_a}{Q_c}\right) \|\hat{\mathbf{u}}\|_{H^1(\Omega)}, \tag{5.4}$$

$$\|p\|_{L^2(\Omega)} \leq \frac{1}{\beta} \|\mathbf{f}\|_{H^{-1}(\Omega)} + \frac{1}{\beta} Q_a \|\mathbf{u}\|_{H^1(\Omega)}, \tag{5.5}$$

where  $\hat{\mathbf{u}} = \mathbf{u}_s + \mathbf{u}_0$ ,  $\beta > 0$ , as presented in Proposition 5.1, and  $Q_a$  and  $Q_c$  are defined in Theorem 4.1 and Theorem 4.3, respectively.

*Proof.* Let  $\mathbf{f} \in H^{-1}(\Omega)$ ,  $f \in L^2(\Omega)$  and  $\mathbf{s} \in H^{1/2}(\partial\Omega)$ . From Proposition 5.1, we have  $\mathbf{u}_s \in H^1(\Omega)$  and  $\mathbf{u}_0 \in V^1 \subset H_0^1(\Omega)$  such that  $\mathbf{u}_s|_{\partial\Omega} = \mathbf{s}$  and  $\nabla \cdot \mathbf{u}_0 = f - \nabla \cdot \mathbf{u}_s$ . Let  $\hat{\mathbf{u}} = \mathbf{u}_s + \mathbf{u}_0$  and  $L(\mathbf{w}) = c_1(\mathbf{w}) - a(\hat{\mathbf{u}}, \mathbf{w})$  for any  $\mathbf{w} \in V$ . By adopting the linearity and continuity of  $c_1(\cdot)$  and bilinearity and continuity of  $a(\cdot, \cdot)$  along with the coercivity of  $a(\cdot, \cdot)$ , we have that  $L(\cdot)$  is a linear and continuous function. Then, from the Lax-Milgram theorem, there exists a unique  $\tilde{\mathbf{u}} \in V \subset H_0^1(\Omega)$  such that  $a(\tilde{\mathbf{u}}, \mathbf{w}) = L(\mathbf{w})$ . Let  $\mathbf{u} = \tilde{\mathbf{u}} + \hat{\mathbf{u}}$ . Then,

$$\begin{aligned} \mathbf{u}|_{\partial\Omega} &= \tilde{\mathbf{u}}|_{\partial\Omega} + \mathbf{u}_s|_{\partial\Omega} + \mathbf{u}_0|_{\partial\Omega} \\ &= 0 + \mathbf{s} + 0 \\ &= \mathbf{s}. \end{aligned}$$

Therefore,  $\mathbf{u} \in H_s^1(\Omega)$ . Next, we show the uniqueness of  $\mathbf{u}$ . Since  $a(\tilde{\mathbf{u}}, \mathbf{w}) = L(\mathbf{w}) = c_1(\mathbf{w}) - a(\hat{\mathbf{u}}, \mathbf{w})$ , by using the bilinear property of  $a(\cdot, \cdot)$ , we have

$$a(\mathbf{u}, \mathbf{w}) = a(\tilde{\mathbf{u}} + \hat{\mathbf{u}}, \mathbf{w}) = c_1(\mathbf{w}). \tag{5.6}$$

Suppose that  $\mathbf{u}_1$  and  $\mathbf{u}_2$  are two such solutions satisfying

$$a(\mathbf{u}_1, \mathbf{w}) = c_1(\mathbf{w}) \text{ and } a(\mathbf{u}_2, \mathbf{w}) = c_1(\mathbf{w}). \tag{5.7}$$

Then, substituting  $\mathbf{w} = \mathbf{u}_1 - \mathbf{u}_2$  in Eq (5.7) and subtracting one equation from another equation, we get

$$0 = a(\mathbf{u}_1 - \mathbf{u}_2, \mathbf{u}_1 - \mathbf{u}_2) \geq Q_c \|\mathbf{u}_1 - \mathbf{u}_2\|_{H^1(\Omega)}^2 \geq 0,$$

where we apply the coercivity of  $a(\cdot, \cdot)$ , Theorem 4.3, at the first inequality. Since the constant  $Q_c > 0$ , it implies that  $\|\mathbf{u}_1 - \mathbf{u}_2\|_{H^1(\Omega)} = 0$ . Then,  $\mathbf{u}_1 = \mathbf{u}_2$ . Therefore,  $\mathbf{u}$  is unique, satisfying  $a(\mathbf{u}, \mathbf{w}) = c_1(\mathbf{w})$ , for all  $\mathbf{w} \in V$ .

Next, we show that  $\mathbf{u} = \tilde{\mathbf{u}} + \mathbf{u}_s + \mathbf{u}_0$  satisfies the continuity equation. Since  $\tilde{\mathbf{u}} \in V, \nabla \cdot \tilde{\mathbf{u}} = 0$ . Then,

$$\begin{aligned} \nabla \cdot \mathbf{u} &= \nabla \cdot (\tilde{\mathbf{u}} + \mathbf{u}_s + \mathbf{u}_0) \\ &= \nabla \cdot \tilde{\mathbf{u}} + \nabla \cdot \mathbf{u}_s + \nabla \cdot \mathbf{u}_0 \\ &= 0 + \nabla \cdot \mathbf{u}_s + f - \nabla \cdot \mathbf{u}_s \\ &= f, \end{aligned}$$

where  $\nabla \cdot \mathbf{u}_0 = f - \nabla \cdot \mathbf{u}_s$  is applied at the third equality. Hence,  $\mathbf{u}$  satisfies the continuity equation.

We prove the existence and uniqueness of  $p \in L_0^2(\Omega)$ . Define  $L_1$  such that  $\langle L_1, \mathbf{w} \rangle = \langle \mathbf{f}, \mathbf{w} \rangle = c_1(\mathbf{w})$ . Then, from Eq (5.6), we have

$$a(\tilde{\mathbf{u}}, \mathbf{w}) + a(\hat{\mathbf{u}}, \mathbf{w}) - \langle L_1, \mathbf{w} \rangle = 0, \quad \forall \mathbf{w} \in V. \tag{5.8}$$

By the definition of the linear operator, seen in Appendix A, we can rewrite Eq (5.8) in operator notation as  $A\tilde{\mathbf{u}} + A\hat{\mathbf{u}} - L_1 = 0$ . Then,  $A\tilde{\mathbf{u}} + A\hat{\mathbf{u}} - L_1 \in V^0$ , where  $V^0$  is the polar set of  $V$ ; see Appendix A for the definition. Given that  $B' : L_0^2(\Omega) \rightarrow V^0$  is an isomorphism **grad** operator, from Theorem A.2 and the property of isomorphism, there exists a unique  $p \in L_0^2(\Omega)$  such that  $B'p = A\tilde{\mathbf{u}} + A\hat{\mathbf{u}} - L_1 = A\mathbf{u} - L_1$ . Then,

$$A\mathbf{u} + B'p = L_1 = \mathbf{f}.$$

Therefore, there exist a unique  $\mathbf{u} \in H_s^1(\Omega)$  and  $p \in L_0^2(\Omega)$  satisfying Problems 1 and 2.

Next, we show the variables  $\mathbf{u}$  and  $p$  are bounded. We first illustrate that  $\tilde{\mathbf{u}}$  is bounded. Employing Eq (4.9), we have

$$\begin{aligned} Q_c \|\tilde{\mathbf{u}}\|_{H^1(\Omega)}^2 &\leq a(\tilde{\mathbf{u}}, \tilde{\mathbf{u}}) \\ &= c_1(\tilde{\mathbf{u}}) - a(\hat{\mathbf{u}}, \tilde{\mathbf{u}}) \\ &\leq \|\mathbf{f}\|_{H^{-1}(\Omega)} \|\tilde{\mathbf{u}}\|_{H^1(\Omega)} + Q_a \|\hat{\mathbf{u}}\|_{H^1(\Omega)} \|\tilde{\mathbf{u}}\|_{H^1(\Omega)}, \end{aligned} \tag{5.9}$$

where the second inequality is obtained from Theorem 4.1. Dividing both sides of Eq (5.9) by  $\|\tilde{\mathbf{u}}\|_{H^1(\Omega)}$  and  $Q_c$ , we get

$$\|\tilde{\mathbf{u}}\|_{H^1(\Omega)} \leq \frac{1}{Q_c} \|\mathbf{f}\|_{H^{-1}(\Omega)} + \frac{Q_a}{Q_c} \|\hat{\mathbf{u}}\|_{H^1(\Omega)}. \tag{5.10}$$

Thus,

$$\begin{aligned} \|\mathbf{u}\|_{H^1(\Omega)} &= \|\tilde{\mathbf{u}} + \hat{\mathbf{u}}\|_{H^1(\Omega)} \\ &\leq \|\tilde{\mathbf{u}}\|_{H^1(\Omega)} + \|\hat{\mathbf{u}}\|_{H^1(\Omega)} \\ &\leq \frac{1}{Q_c} \|\mathbf{f}\|_{H^{-1}(\Omega)} + \left(1 + \frac{Q_a}{Q_c}\right) \|\hat{\mathbf{u}}\|_{H^1(\Omega)}. \end{aligned}$$

To show that  $p$  is bounded, we first employ Eq (3.5):

$$b(\mathbf{w}, p) = c_1(\mathbf{w}) - a(\mathbf{u}, \mathbf{w})$$

$$\leq \|f\|_{H^{-1}(\Omega)} \|w\|_{H^1(\Omega)} + Q_a \|u\|_{H^1(\Omega)} \|w\|_{H^1(\Omega)}, \quad (5.11)$$

where inequalities (4.1) and (4.4) are applied to the inequality. Since

$$\sup_{w \in H_0^1(\Omega)} \frac{b(w, p)}{\|w\|_{H^1(\Omega)} \|p\|_{L^2(\Omega)}}$$

is independent of  $p$ , from Eq (A.11),

$$\|p\|_{L^2(\Omega)}^{-1} \sup_{w \in H_0^1(\Omega)} \frac{b(w, p)}{\|w\|_{H^1(\Omega)}} = \sup_{w \in H_0^1(\Omega)} \frac{b(w, p)}{\|w\|_{H^1(\Omega)} \|p\|_{L^2(\Omega)}} \geq \inf_{p \in L_0^2(\Omega)} \sup_{w \in H_0^1(\Omega)} \frac{b(w, p)}{\|w\|_{H^1(\Omega)} \|p\|_{L^2(\Omega)}} \geq \beta > 0. \quad (5.12)$$

Rearranging Eq (5.12), we obtain that

$$\begin{aligned} \|p\|_{L^2(\Omega)} &\leq \frac{1}{\beta} \sup_{w \in H_0^1(\Omega)} \frac{b(w, p)}{\|w\|_{H^1(\Omega)}} \\ &= \frac{1}{\beta} \sup_{w \in H_0^1(\Omega)} \frac{c_1(w) - a(u, w)}{\|w\|_{H^1(\Omega)}} \\ &\leq \frac{1}{\beta} \sup_{w \in H_0^1(\Omega)} \left( \frac{\|f\|_{H^{-1}(\Omega)} \|w\|_{H^1(\Omega)} + Q_a \|u\|_{H^1(\Omega)} \|w\|_{H^1(\Omega)}}{\|w\|_{H^1(\Omega)}} \right) \\ &= \frac{1}{\beta} \sup_{w \in H_0^1(\Omega)} (\|f\|_{H^{-1}(\Omega)} + Q_a \|u\|_{H^1(\Omega)}). \end{aligned}$$

Since  $\|f\|_{H^{-1}(\Omega)} + Q_a \|u\|_{H^1(\Omega)}$  is independent of  $w \in H_0^1(\Omega)$ ,

$$\sup_{w \in H_0^1(\Omega)} (\|f\|_{H^{-1}(\Omega)} + Q_a \|u\|_{H^1(\Omega)}) = \|f\|_{H^{-1}(\Omega)} + Q_a \|u\|_{H^1(\Omega)}.$$

Therefore,

$$\|p\|_{L^2(\Omega)} \leq \frac{1}{\beta} (\|f\|_{H^{-1}(\Omega)} + Q_a \|u\|_{H^1(\Omega)}).$$

Hence, the proof of existence and uniqueness of the generalized Stokes-Brinkman equations is complete.

## 6. Conclusions

In this research, we focus on the fluid movement in a porous medium induced by self-propelled solid phases and the adjacent free-fluid region. In the porous medium, we employ a macroscale equation derived from an upscaling technique called Hybrid Mixture Theory (HMT) because we consider a bundle of solid phases. Then, we apply a non-dimensionalization scheme to the macroscale equation to obtain the Brinkman equation. Our model is more general than the Brinkman equation in the literature because the porosity in our equation is considered as a function since the beginning of the derivation. Then, our model in the porous medium conserves the reality of the problem. In the free-fluid region, we

start with the generalized Navier-Stokes equation and use the non-dimensionalization method to derive the generalized Stokes equation. Our Brinkman and generalized Stokes equations can be matched at the free-fluid/porous-medium interface. We name them as the generalized Stokes-Brinkman equations. We also show that the discretized form of the mathematical model is a well-posed system with the use of a mixed finite element method. The weak formulation of the generalized Stokes-Brinkman equations is rewritten in linear and bilinear functional structures. We show that the bilinear form  $a(\cdot, \cdot)$  is continuous and coercive. Then, we present the well-posedness of the generalized Stokes-Brinkman equations in the last theorem. The system of equations can be useful for more complexity of a real problem in a macroscopic scale than a typical Stokes-Brinkman equation and can be applied to the fluid flow through the regions where fluid is driven by the moving solid phases such as hairlike structures and animal hair. The numerical research will be presented in the next study.

### Acknowledgments

This research is supported by RA/TA graduate scholarship from the School of Science, King Mongkut's Institute of Technology Ladkrabang, Thailand, grant number RA/TA-2563-D-003.

### Conflict of interest

The authors declare no conflict of interest.

### References

1. F. Basirat, P. Sharma, F. Fagerlund, A. Niemi, Experimental and modeling investigation of CO<sub>2</sub> flow and transport in a coupled domain of porous media and free flow, *Int. J. Greenhouse Gas Control*, **42** (2015), 461–470. <https://doi.org/10.1016/j.ijggc.2015.08.024>
2. N. Oangwacharaparkan, K. Wuttanachamsri, The flow in periciliary layer in human lungs with Navier-Stokes-Brinkman equations, *Tamkang J. Math.*, **54** (2021). <https://doi.org/10.5556/j.tkjm.54.2023.3738>
3. K. Khanafer, K. Cook, A. Marafie, The role of porous media in modeling fluid flow within hollow fiber membranes of the total artificial lung, *J. Porous Media*, **15** (2012), 113–122. <https://doi.org/10.1615/JPorMedia.v15.i2.20>
4. H. B. Ly, H. L. Nguyen, M. N. Do, Finite element modeling of fluid flow in fractured porous media using unified approach, *Vietnam J. Earth Sci.*, **43** (2020), 13–22. <https://doi.org/10.15625/0866-7187/15572>
5. K. Wuttanachamsri, L. Schreyer, Effects of cilia movement on fluid velocity: II numerical solutions over a fixed domain, *Transp. Porous Media*, **134** (2020), 471–489. <https://doi.org/10.1007/s11242-020-01455-4>
6. S. Poopra, K. Wuttanachamsri, The velocity of PCL fluid in human lungs with Beaver and Joseph boundary condition by using asymptotic expansion method, *Mathematics*, **7** (2019), 567. <https://doi.org/10.3390/math7060567>

7. K. Wuttanachamsri, Free interfaces at the tips of the cilia in the one-dimensional periciliary layer, *Mathematics*, **8** (2020), 1961. <https://doi.org/10.3390/math8111961>
8. M. Lesinigo, C. D'Angelo, A. Quarteroni, A multiscale Darcy-Brinkman model for fluid flow in fractured porous media, *Numer. Math.*, **117** (2011), 717–752. <https://doi.org/10.1007/s00211-010-0343-2>
9. T. Kasamwan, K. Wuttanachamsri, Unsteady one-dimensional flow in PCL with Stokes-Brinkman equations, *The 9<sup>th</sup> Phayao Research Conference*, (2020), 1949–1964.
10. N. Oangwatcharaparkan, K. Wuttanachamsri, Solutions of flow over periciliary layer using finite difference and n-dimensional Newton-Raphson methods, *J. Sci. Ladkrabang*, **29** (2020), 16–30.
11. S. Phaenchat, K. Wuttanachamsri, On the nonlinear Stokes-Brinkman equations for modeling flow in PCL, in *The 24<sup>th</sup> Annual Meeting in Mathematics*, (2019), 167–175.
12. R. Ingram, Finite element approximation of nonsolenoidal, viscous flows around porous and solid obstacles, *SIAM J. Numer. Anal.*, **49** (2011), 491–520. <https://doi.org/10.1137/090765341>
13. P. Angot, Well-posed Stokes/Brinkman and Stokes/Darcy coupling revisited with new jump interface conditions, *ESAIM: Math. Model. Numer. Anal.*, **52** (2018), 1875–1911. <https://doi.org/10.1051/m2an/2017060>
14. K. Chamsri, Formulation of a well-posed Stokes-Brinkman problem with a permeability tensor, *J. Math.*, **2014** (2014), 1–7.
15. P. Angot, On the well-posed coupling between free fluid and porous viscous flows, *Appl. Math. Lett.*, **24** (2011), 803–810. <https://doi.org/10.1016/j.aml.2010.07.008>
16. K. Chamsri, *Modeling the Flow of PCL Fluid Due to the Movement of Lung Cilia*, Ph.D thesis, University of Colorado at Denver, 2012.
17. L. Bennethum, J. Cushman, Multiscale, hybrid mixture theory for swelling systems—I: balance laws, *Int. J. Eng. Sci.*, **34** (1996), 125–145. [https://doi.org/10.1016/0020-7225\(95\)00089-5](https://doi.org/10.1016/0020-7225(95)00089-5)
18. K. Wuttanachamsri, L. Schreyer, Effects of cilia movement on fluid velocity: I model of fluid flow due to a moving solid in a porous media framework, *Transp. Porous Media*, **136** (2021), 699–714. <https://doi.org/10.1007/s11242-020-01539-1>
19. J. H. Cushman, L. S. Bennethum, B. X. Hu, A primer on upscaling tool for porous media, *Adv. Water Resour.*, **25** (2002), 1043–1067. [https://doi.org/10.1016/S0309-1708\(02\)00047-7](https://doi.org/10.1016/S0309-1708(02)00047-7)
20. L. S. Bennethum, Notes for Introduction to Continuum Mechanics, Continuum Mechanics Class Lecture, 2002.
21. A. E. Tilley, M. S. Walters, R. Shaykhiev, R. G. Crystal, Cilia dysfunction in lung disease, *Annu. Rev. Physiol.*, **77** (2015), 379–406. <https://doi.org/10.1146/annurev-physiol-021014-071931>
22. C. M. Smith, J. Djakow, R. C. Free, P. Djakow, R. Lonnen, G. Williams, et al., CiliaFA: a research tool for automated, high-throughput measurement of ciliary beat frequency using freely available software, *Cilia*, **1** (2012). <https://doi.org/10.1186/2046-2530-1-14>
23. M. Chovancov'a, J. Elcner, The pressure gradient in the human respiratory tract, *EPJ Web Conf.*, **67** (2014), 2–6. <https://doi.org/10.1051/epjconf/20146702047>

24. K. Chamsri, L. S. Bennethum, Permeability of fluid flow through a periodic array of cylinders, *Appl. Math. Modell.*, **39** (2015), 244–254. <https://doi.org/10.1016/j.apm.2014.05.024>
25. A. Karageorghis, D. Lesnic, L. Marin, The method of fundamental solutions for Brinkman flows. part II. interior domains, *J. Eng. Math.*, **127** (2021), 1–16. <https://doi.org/10.1007/s10665-020-10083-2>
26. T. F. Weinstein, *Three-phase Hybrid Mixture Theory for Swelling Drug Delivery Systems*, Ph.D thesis, University of Colorado at Denver, 2006.
27. T. F. Weinstein, L. S. Bennethum, On the derivation of the transport equation for swelling porous materials with finite deformation, *Int. J. Eng. Sci.*, **44** (2006), 1408–1422. <https://doi.org/10.1016/j.ijengsci.2006.08.001>
28. D. Braess, *Finite Elements: Theory, Fast Solvers, and Applications in Elasticity Theory*, Cambridge University Press, 2007.
29. R. A. Horn, C. R. Johnson, *Matrix Analysis*, Cambridge University Press, Cambridge, 2012. <https://doi.org/10.1017/CBO9780511810817>
30. R. G. Bartle, D. R. Sherbert, *Introduction to Real Analysis*, Wiley, New York, 2011.
31. S. C. Brenner, L. R. Scott, *The Mathematical Theory of Finite Element Methods*, Springer-Verlag, New York, 2008. <https://doi.org/10.1007/978-0-387-75934-0>
32. F. Brezzi, M. Fortin, *Mixed and Hybrid Finite Element Methods*, Springer-Verlag, New York, 1991. <https://doi.org/10.1007/978-1-4612-3172-1>
33. V. Girault, P. Raviart, *Finite Element Methods for Navier-Stokes Equations: Theory and Algorithms*, Springer-Verlag, Berlin, 1986. <https://doi.org/10.1007/978-3-642-61623-5>
34. E. G. Dyakonov, *Optimization in Solving Elliptic Problems*, CRC Press, 1996. <https://doi.org/10.1201/9781351075213>
35. G. B. Arfken, H. J. Weber, F. E. Harris, *Mathematical Methods for Physicists*, Academic Press, 2012. <https://doi.org/10.1016/C2009-0-30629-7>

## Appendix

### A. Fundamental definition and theorems

In this Appendix, we provide notations, definitions, theorems and lemmas used in the proof of the well-posedness of the generalized Stokes-Brinkman equations. They are all presented and proved in [14, 32–34].

#### Notations and spaces

In this section, we introduce some notations and spaces used in the proof of the well-posedness of the governing equations [14]. Define

$$L_0^2(\Omega) = \{q \in L^2(\Omega) : \int_{\Omega} q d\Omega = 0\}, \quad (\text{A.1})$$

$$H_0^1(\Omega) = \{\mathbf{w} \in H^1(\Omega) : \mathbf{w}|_{\partial\Omega} = 0\}, \quad (\text{A.2})$$

$$H_s^1(\Omega) = \{\mathbf{w} \in H^1(\Omega) : \mathbf{w}|_{\partial\Omega} = \mathbf{s}\}, \quad (\text{A.3})$$

$$H^{-1}(\Omega) = (H_0^1(\Omega))', \text{ the dual of } H_0^1(\Omega), \tag{A.4}$$

$$V = \{\mathbf{w} \in H^1(\Omega) : \mathbf{w}|_{\partial\Omega} = 0 \text{ and } \nabla \cdot \mathbf{w} = 0\}, \tag{A.5}$$

$$V^\perp = \{\mathbf{w}^\perp \in H_0^1(\Omega) : \int_\Omega \mathbf{w}^\perp \cdot \mathbf{w} = 0 \ \forall \mathbf{w} \in V\}, \tag{A.6}$$

$$V^0 = \{\mathbf{w}' \in H^{-1}(\Omega) : \langle \mathbf{w}', \mathbf{w} \rangle_{H^{-1}(\Omega) \times H_0^1(\Omega)} = 0 \ \forall \mathbf{w} \in V\}, \tag{A.7}$$

where  $\langle \cdot, \cdot \rangle_{H^{-1}(\Omega) \times H_0^1(\Omega)}$  denotes the duality pairing between  $H^{-1}(\Omega)$  and  $H_0^1(\Omega)$ . Notice that for  $n$  dimension,  $\mathbf{w} \in H^1(\Omega)^n$  and  $\nabla \mathbf{w} \in H^1(\Omega)^{n \times n}$ . In any case, for the sake of simplicity, we write  $\mathbf{w} \in H^1(\Omega)$ , and the implication comes from the context of the surrounding sentences.

Next, we provide the fundamental definition, theorems and lemma used in the proof of the existence and uniqueness of Problems 1 and 2 [12, 14, 31–35].

**Definition A.1.** Let  $\mathbf{u}, \mathbf{w} \in H^1(\Omega)$  and  $q \in L_0^2(\Omega)$ . Define linear operators  $A : H_0^1(\Omega) \rightarrow H^{-1}(\Omega)$  and  $B : H_0^1(\Omega) \rightarrow L_0^2(\Omega)$  by

$$\langle A\mathbf{u}, \mathbf{w} \rangle_{H_0^1(\Omega) \times H^{-1}(\Omega)} := a(\mathbf{u}, \mathbf{w}), \quad \forall \mathbf{u}, \mathbf{w} \in H_0^1(\Omega), \tag{A.8}$$

$$\langle B\mathbf{u}, q \rangle_{H_0^1(\Omega) \times L_0^2(\Omega)} := b(\mathbf{u}, q), \quad \forall \mathbf{u} \in H_0^1(\Omega), \forall q \in L_0^2(\Omega). \tag{A.9}$$

Let  $B' \in \mathcal{L}(L_0^2(\Omega); H^{-1}(\Omega))$  be the dual operator of  $B$ . Then,

$$\langle B'q, \mathbf{u} \rangle = \langle q, B\mathbf{u} \rangle := b(\mathbf{u}, q), \quad \forall \mathbf{u} \in H_0^1(\Omega), \forall q \in L_0^2(\Omega), \tag{A.10}$$

where the dual spaces of  $L_0^2(\Omega) = (L_0^2(\Omega))'$  and the dual spaces of  $H^{-1}(\Omega) = (H_0^1(\Omega))'$ .

**Theorem A.2.** Let  $\Omega$  be connected. Then,

1. the operator  $\text{grad}$  is an isomorphism of  $L_0^2(\Omega)$  onto  $V^0$ ,
2. the operator  $\text{div}$  is an isomorphism of  $V^\perp$  onto  $L_0^2(\Omega)$ .

Therefore, there exists  $\beta > 0$  such that

$$\inf_{q \in L_0^2(\Omega)} \sup_{\mathbf{w} \in H_0^1(\Omega)} \frac{b(\mathbf{w}, q)}{\|\mathbf{w}\|_{H^1(\Omega)} \|q\|_{L^2(\Omega)}} \geq \beta > 0 \tag{A.11}$$

and for any  $q \in L_0^2(\Omega)$ , there exists a unique  $\mathbf{u} \in V^\perp \subset H_0^1(\Omega)$  satisfying

$$\|\mathbf{u}\|_{H^1(\Omega)} \leq \beta^{-1} \|q\|_{L^2(\Omega)}. \tag{A.12}$$

**Theorem A.3.** There exist positive constants  $Q_t$  and  $Q_s$  such that, for each  $\mathbf{v} \in H^1(\Omega)$ , its trace on  $\partial\Omega$  belongs to  $H^{1/2}(\partial\Omega)$ , and

$$\|\mathbf{v}\|_{H^{1/2}(\partial\Omega)} \leq Q_t \|\mathbf{v}\|_{H^1(\Omega)}. \tag{A.13}$$

Conversely, for each given function  $\mathbf{s} \in H^{1/2}(\partial\Omega)$ , there exists  $\mathbf{u}_s \in H^1(\Omega)$  such that its trace on  $\partial\Omega$  coincides with  $\mathbf{s}$  and

$$\|\mathbf{u}_s\|_{H^1(\Omega)} \leq Q_s \|\mathbf{s}\|_{H^{1/2}(\partial\Omega)}. \tag{A.14}$$

**Lemma A.4.** Suppose that  $\mathbf{f} \in H^{-1}(\Omega)$ ,  $f \in L^2(\Omega)$  and  $s \in H^{1/2}(\partial\Omega)$ . Then, there exist  $\mathbf{u}_s \in H^1(\Omega)$ ,  $Q_s > 0$  and  $\beta > 0$  such that

$$\mathbf{u}_s|_{\partial\Omega} = \mathbf{s} \quad \text{and} \quad \|\mathbf{u}_s\|_{H^1(\Omega)} \leq Q_s \|s\|_{H^{1/2}(\partial\Omega)}, \quad (\text{A.15})$$

$$\exists! \mathbf{u}_0 \in V^\perp \subset H_0^1(\Omega) \quad \text{satisfying} \quad \nabla \cdot \mathbf{u}_0 = f - \nabla \cdot \mathbf{u}_s, \quad (\text{A.16})$$

and

$$\|\mathbf{u}_0\|_{H^1(\Omega)} \leq \beta^{-1} \|f - \nabla \cdot \mathbf{u}_s\|_{L^2(\Omega)}. \quad (\text{A.17})$$



AIMS Press

© 2023 the Author(s), licensee AIMS Press. This is an open access article distributed under the terms of the Creative Commons Attribution License (<http://creativecommons.org/licenses/by/4.0>)



## Appendix B

Two-dimensional fluid flow due to blade-shaped waving of cilia in human lungs



This material is reserved for educational use only, not allowed for commercial use.

Forbidden to modify the content, and cite the document when use.

Article

## Two-Dimensional Fluid Flow Due to Blade-Shaped Waving of Cilia in Human Lungs

Nisachon Kumankat and Nachayadar Kamolmitisom \* 

Department of Mathematics, School of Science, King Mongkut's Institute of Technology Ladkrabang, Bangkok 10520, Thailand; nisachon.kumankat@gmail.com

\* Correspondence: kanognudge.wu@kmitl.ac.th

**Abstract:** The mucociliary clearance system is an innate defense mechanism in the human respiratory tract, which plays a crucial role in protecting the airways from infections. The clearance system secretes mucus from the goblet cells, which scatters in the respiratory epithelium to trap foreign particles entering the airway, and then the mucus is removed from the body via the movement of cilia residing under the mucus and above the epithelium cells. The layer containing cilia is called the periciliary layer (PCL). This layer also contains an incompressible Newtonian fluid called PCL fluid. This study aims to determine the velocity of the PCL fluid driven by the cilia movement instead of a pressure gradient. We consider bundles of cilia, rather than an individual cilium. So, the generalized Brinkman equation in a macroscopic scale is used to predict the fluid velocity in the PCL. We apply a mixed finite element method to the governing equation and calculate the numerical solutions in a two-dimensional domain. The numerical domain is set up to be the shape of a fan blade, which is similar to the motion of the cilia. This problem can be applied to problems of fluid flow propelled via moving solid phases.

**Keywords:** periciliary layer; cilia; moving solid phase; Brinkman equation; mixed finite element method

**MSC:** 76-10; 76M10; 76S05



Received: 15 April 2025  
Revised: 20 May 2025  
Accepted: 20 May 2025  
Published: 22 May 2025

**Citation:** Kumankat, N.; Kamolmitisom, N. Two-Dimensional Fluid Flow Due to Blade-Shaped Waving of Cilia in Human Lungs. *Mathematics* **2025**, *13*, 1703. <https://doi.org/10.3390/math13111703>

**Copyright:** © 2025 by the authors. Licensee MDPI, Basel, Switzerland. This article is an open access article distributed under the terms and conditions of the Creative Commons Attribution (CC BY) license (<https://creativecommons.org/licenses/by/4.0/>).

### 1. Introduction

Cilia are hair-like structures located on the surfaces of many organisms, such as Paramecium, amoeba, and complex multicellular organisms. The human body contains numerous cilia that can be found both inside the body and on the human skin. Cilia, for example, help move eggs through the fallopian tubes into the uterus and move sperm in the reproductive system [1]. Cilia help pass food and waste through the digestive tract [2]. They also aid digestion and prevent intestine blockages [2]. Cilia in the respiratory system help move mucus and foreign particles out of the lungs and airways [3]. They are self-propelled structures that move in a way called metachronal motion. This protects the lungs and respiratory system from infection. This research focuses on the cilia found in the innate immune system in the human respiratory system, which play an important role in protecting the body from small particles contaminated with inhaled air, such as dust.

Figure 1 illustrates the human respiratory system (left) and a portion of the trachea in the respiratory tract (right). The system consists of the nose, pharynx, larynx, trachea, bronchus, bronchioles, and lungs. When closely inspecting the trachea, we can see that there are three main layers in the right figure: the periciliary layer (PCL), the mucus region, and the air at the top layer. In the respiratory tract, cilia are found in the PCL. The PCL also

contains fluid that is considered to be an incompressible Newtonian fluid because the PCL fluid is a fluid similar to water in its properties, such as viscosity [4]. The fluid in this layer is called PCL fluid. The area under the PCL is comprised of goblet cells scattering among the ciliated cells. The ciliated cell is the cell membrane where the cilia reside on the top of the cell. The goblet cells contain mucus granules, which secrete mucus to trap strange particles entering the human body. After capturing foreign particles, mucus forms a layer at the tips of cilia. To prevent the accumulation of mucus in the lungs, cilia beat forward and backward producing metachronal waves, which fully expand during the forward stroke and then bend close to the epithelium before rotating back to the beginning of the forward stroke to push mucus out of the lungs. This system is known as mucociliary clearance in human lungs. Above the mucus layer is the air row, which is the path for bringing oxygen in and sending carbon dioxide out of the body. In this research, we focus on the velocity of the fluid in the PCL moved via the movement of cilia, rather than a pressure gradient. Since the PCL consists of both solid phases (cilia) and the liquid phase (the PCL fluid) and the PCL has interconnected pores through which fluids can move, which is the characteristic of a porous medium, we consider the PCL a porous medium.

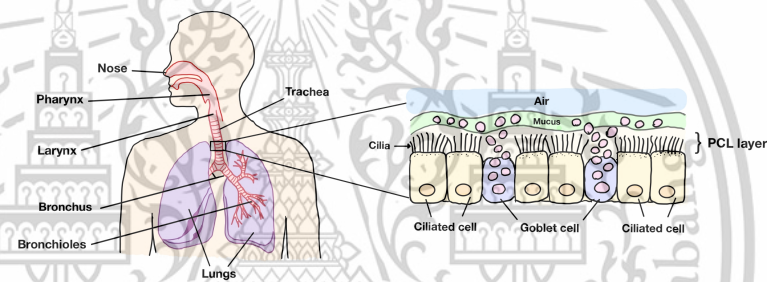


**Figure 1.** Left: human respiratory system. Right: a portion of the trachea in the human respiratory tract.

Problems of the PCL have been studied by several researchers [5–14]. For example, Zhu et al. [5] proposed a two-dimensional model to explore the migration law of particles due to cilium beat in the PCL of the human respiratory tract using the immersed boundary-lattice Boltzmann method. Poopra and Wuttanachamsri [6] provide boundary conditions at the top of the PCL due to the ciliary movement. Vanaki et al. [7] studied the fluid flow in the PCL driven by cilia using the finite difference method and the immersed boundary method. Jayathilake et al. [8] developed a three-dimensional numerical model to simulate human pulmonary cilia motion in the PCL and investigated the effects of the phase difference between cilia, the cilia beating frequency, the viscosity of PCL, the PCL height, and the ciliary length affecting the PCL fluid motion. Phaenchat and Wuttanachamsri [14] determined the velocity of the PCL fluid in a two-dimensional domain. They used the nonlinear Brinkman equation in the porous medium. The equation was solved using a mixed finite element method combined with Newton's method.

Many researchers have studied the fluid flow through porous domains using the Brinkman equation both analytically and numerically. For example, analytical studies focused on proving the well-posedness of the equation [15–21]. Conti and Giorgini [15] proved the existence and uniqueness of the Brinkman–Cahn–Hilliard system with logarithmic free energy density for the motion of binary fluids with different viscosities. Titi and Trabelsi [16] derived the existence and uniqueness of a three-dimensional Brinkman–Forchheimer–Bénard convection model for an incompressible fluid in a closed sample of a porous medium. For numerical solutions of the Brinkman equation, they were studied by

several researchers [22–31] in many aspects. For example, Wuttanachamsri [23] observed the velocity of the PCL fluid and the shape of the free boundary at the tips of cilia when the fluid was driven via cilia movement using a one-dimensional Brinkman equation with the Stefan problem. Basirat et al. [24] predicted the flow and transport of gaseous CO<sub>2</sub> in a porous medium using the Darcy–Brinkman equation with COMSOL software based on the finite element method. Wuttanachamsri and Schreyer [25] applied a mixed finite element method of the Taylor–Hood type to the Stokes–Brinkman equations to find the PCL fluid velocities due to the cilia beating in a three-dimensional domain. Nishad et al. [26] proposed a new Boundary Integral Equation (BIE) method and also investigated the two-dimensional Brinkman flow of incompressible Newtonian fluids through a porous channel. Cortez et al. [28] provided the exact and numerical solutions for the Brinkman equation in a three-dimensional domain where the incompressible flow was driven by regularized forces. Kanafiah et al. [30] investigated the numerical results of the Brinkman–viscoelastic fluid model for mixed convection transport via a horizontal circular cylinder saturated in a porous domain. Pranowo and Wijayanta [31] proposed the numerical solutions of the Darcy–Brinkman–Forchheimer model for forced–convective fluid flow in a porous medium using the Direct Meshless Local Petrov–Galerkin (DMLPG) method. Most of the previous literature had studied the numerical solutions of the Brinkman equation when the fluid moved by the pressure gradient. Although some works [6,11,12,14,23,25] considered the fluid velocity due to the movement of the solid phases, they assumed that the porosity was a constant, and they calculated the numerical results for a fixed angle  $\theta$  on a rectangular domain, as shown in Figure 2.

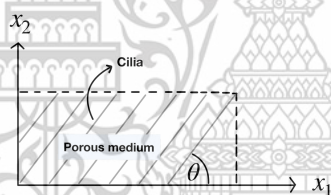
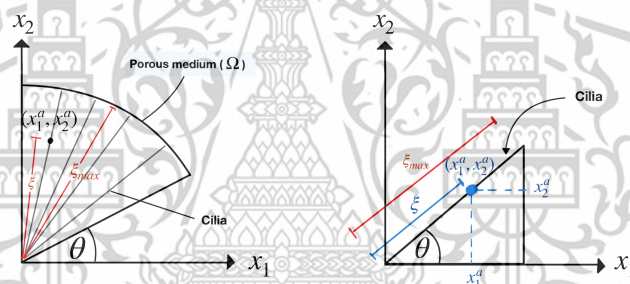


Figure 2. Rectangular domain.

Figure 2 illustrates a rectangular porous domain composed of cilia that make an angle  $\theta$  with the horizontal plane. In fact, the angle  $\theta$  and the porosity should be varied in the numerical domain because of the metachronal waves of cilia. Unlike the other researchers, in this work, we define the numerical domain in the shape of a fan blade, resembling the wave pattern of cilia, as shown on the left side of Figure 3, where the cilia are monitored as rigid cylinders because they have long and thin lines. Based on our information, this shape of the domain was not studied in the previous literature. The model designed is more closely to the actual beating pattern of cilia in that the cilia rotate as a clockwise pattern moving from left to right around their base. The movement of cilia generates the leftward flow of the PCL fluid. Figure 3 on the left shows our numerical porous domain with the angular movement of the cilia. The angle  $\theta$  represents the angle that the cilia make with the horizontal plane. In previous research, scholars have not studied various angles,  $\theta$ , in one fixed numerical domain. They considered only one angle,  $\theta$ , for one fixed numerical domain. Notice that there are numerous angles,  $\theta$ , in our one fixed numerical domain. Since there are several angles,  $\theta$ , in the domain, the porosity cannot be used as a constant. So, the porosity in this work is considered a function of the angle,  $\theta$ , not a constant. The variable  $\zeta$  is the dimensionless length along cilia, which is the distance from the roots of the cilia to a point  $(x_1^a, x_2^a)$  on the cilia divided by the length of the cilia, which is approximately  $7.5 \mu\text{m}$  [32]. Figure 3 on the right shows that, at each point  $(x_1^a, x_2^a)$  on

the cilia, we can calculate the variable  $\xi$  using the formula  $\xi = x_2^a / \sin \theta$  and the angle  $\theta = \arctan(x_2^a / x_1^a)$ , and the variable  $\xi_{\max}$  represents the dimensionless length of the cilia, which is one. Because we consider the movement of bundles of cilia affecting the movement of the PCL fluid, we use the generalized Brinkman equation [33] on a macroscopic scale to predict the velocity of the PCL fluid in the porous medium. The mathematical model we use is derived in [33], which is a macroscale equation determined from an upscaling technique called Hybrid Mixture Theory (HMT) [34–36] and the nondimensionalization method. This model is more general than the Brinkman equation in the literature because we choose to use the equation that the porosity in this equation is considered as a function since the beginning of the derivation starting from the conservation of momentum. The generalized Brinkman equation is not only derived in [33] but the authors have also proved the existence and uniqueness of the numerical solution when the equation is applied via a mixed finite element method. In [33], the authors used the Lax–Milgram theorem to prove the well-posedness of the equation. To the author’s knowledge, the generalized Brinkman equation was not solved numerically in any literature before. It is solved for the first time in this work. The aim of this research is to determine the velocity of the PCL fluid in the fan-blade shape of the porous domain using the generalized Brinkman equation, in which the fluid is driven by the beating of cilia.



**Figure 3.** Left: the fan-blade shape of the porous domain on the  $x_1x_2$  plane when cilia make angles with the horizontal plane. Right: the illustration of the length  $\xi$  along cilia at the point  $(x_1^a, x_2^a)$  and the variable  $\xi_{\max}$ .

Our mathematical model and boundary conditions are provided in Section 2. To determine the numerical solutions, we discretize the governing equation by using a mixed finite element method in Section 3. The velocity of cilia, permeability, and porosity are described in Section 4. The validation of the numerical solutions is presented in Section 5, and the numerical results are illustrated in Section 6. The validation and numerical results are computed from our own code using MatLab R2025a. The conclusions are drawn in Section 7.

## 2. Mathematical Model and Boundary Conditions

Because we consider the movement of a bundle of self-propelled cilia, rather than a single cilium in the fan-blade shape of the porous medium, the generalized Brinkman equation on the macroscopic scale is employed as our governing equation, which is shown in Section 2.1, and the boundary conditions are illustrated in Section 2.2.

### 2.1. Governing Equations

The mathematical model employed in this work is the generalized Brinkman equation on the macroscopic scale. The derivation of this equation has been proven in [33] using the Hybrid Mixture Theory (HMT) [34–36]. HMT is an upscaling technique that the averaging

theorem is used to upscale equations from a microscale equation to a macroscale equation. For example, consider the conservation of mass equation at the microscale,

$$\frac{\partial \rho}{\partial t} + \nabla \cdot (\rho \mathbf{v}) = 0, \tag{1}$$

where  $\rho$  is the density,  $t$  is time, and  $\mathbf{v}$  is the velocity. Multiplying Equation (1) by an indicator function for phase  $\alpha$ ,  $\gamma_\alpha$ , and then integrating the equation over a representative elementary volume (REV) and applying the averaging theorem [34,35],

$$\frac{1}{|\delta V|} \int_{\delta V} \frac{\partial F}{\partial t} \gamma_\alpha dv(\xi) = \frac{\partial}{\partial t} \left[ \frac{1}{|\delta V|} \int_{\delta V} F \gamma_\alpha dv(\xi) \right] - \sum_{\beta \neq \alpha} \frac{1}{|\delta V|} \int_{\delta A_{\alpha\beta}} F \mathbf{w}_{\alpha\beta} \cdot \mathbf{n}_\alpha da(\xi), \tag{2}$$

$$\frac{1}{|\delta V|} \int_{\delta V} \nabla_x F \gamma_\alpha dv(\xi) = \nabla_x \left[ \frac{1}{|\delta V|} \int_{\delta V} F \gamma_\alpha dv(\xi) \right] + \sum_{\beta \neq \alpha} \frac{1}{|\delta V|} \int_{\delta A_{\alpha\beta}} F \mathbf{n}_\alpha da(\xi), \tag{3}$$

to the integral equation, we have

$$\frac{\partial(\epsilon^\alpha \rho^\alpha)}{\partial t} + \nabla \cdot (\epsilon^\alpha \rho^\alpha \mathbf{v}^\alpha) = \sum_{\beta \neq \alpha} \epsilon^\alpha \rho^\alpha \dot{\epsilon}_{\beta}^{\alpha}, \tag{4}$$

which is the macroscale conservation of mass. Here,  $\delta V$  denotes the representative elementary volume (REV),  $|\delta V|$  is the magnitude of REV,  $F$  is the quantities in the field equations,  $\delta A_{\alpha\beta}$  is the portion of the  $\alpha\beta$  interface within  $\delta V$ ,  $\mathbf{w}_{\alpha\beta}$  is the microscopic velocity of interface  $\alpha\beta$ , and  $\mathbf{n}_\alpha$  is the outward unit normal vector to  $\delta V_\alpha$ . The variable  $\rho^\alpha$  is the macroscale density of phase  $\alpha$ ,  $\mathbf{v}^\alpha$  is the macroscale velocity of phase  $\alpha$ ,  $\dot{\epsilon}_{\beta}^{\alpha}$  is the rate of exchange of mass from phase  $\beta$  to phase  $\alpha$ , and  $\epsilon^\alpha$  is the volume fraction of phase  $\alpha$ .

Next, we briefly show the derivation of the generalized Brinkman equation [33]. We start with the multiphase equation [37], which is upscaled from the conservation of momentum using HMT when the porosity is a function. That is,

$$\epsilon^l \rho \frac{D^l \mathbf{u}^l}{Dt} + \epsilon^l \nabla p + p \nabla \epsilon^l - \nabla \cdot (\epsilon^l 2\mu \mathbf{d}^l) - \epsilon^l \rho \mathbf{g} = p \nabla \epsilon^l - \epsilon^l \mathbf{R} \cdot (\mathbf{u}^l - \mathbf{u}^s), \tag{5}$$

where the variables  $l$  and  $s$  mean the liquid and solid phases, respectively. The function  $\epsilon^l$  is the porosity, which is a variable in space,  $\mathbf{u}^l$  and  $\mathbf{u}^s$  are the velocities of the PCL fluid and solid phases (cilia), respectively,  $p$  is the pressure,  $\mu$  is the dynamic viscosity,  $\mathbf{d}^l = 0.5(\nabla \mathbf{u}^l + (\nabla \mathbf{u}^l)^T)$  is the rate of deformation tensor,  $\mathbf{g}$  is the gravity, and  $\mathbf{R}$  is a second-order tensor. Subtracting  $p \nabla \epsilon^l$  from both sides in Equation (5), dividing both sides by  $\epsilon^l$ , substituting  $\frac{D^l \mathbf{u}^l}{Dt} = \frac{\partial \mathbf{u}^l}{\partial t} + \mathbf{u}^l \cdot \nabla \mathbf{u}^l$ , which is the definition of the material time derivative for liquid phase [37], taking  $\mathbf{R} = \mu \epsilon^l \mathbf{k}^{-1}$ , where  $\mathbf{k}^{-1}$  is the inverse of the permeability tensor, and then rearranging the terms, we have

$$\rho \left( \frac{\partial \mathbf{u}^l}{\partial t} + \mathbf{u}^l \cdot \nabla \mathbf{u}^l \right) + \mu \mathbf{k}^{-1} \cdot (\epsilon^l \mathbf{u}^l - \epsilon^l \mathbf{u}^s) + \nabla p - \frac{\mu}{\epsilon^l} \nabla \cdot (2\epsilon^l \mathbf{d}^l) = \rho \mathbf{g}, \tag{6}$$

which is the conservation of momentum for the liquid phase. After that, the Equation (6) is normalized with dimensionless variables. So, some terms are neglected. Then, Equation (6) becomes

$$\mu \mathbf{k}^{-1} \cdot (\epsilon^l \mathbf{u}^l - \epsilon^l \mathbf{u}^s) + \nabla p - \frac{\mu}{\epsilon^l} \nabla \cdot (2\epsilon^l \mathbf{d}^l) = \rho \mathbf{g}, \tag{7}$$

which is called the generalized Brinkman equation in a macroscopic scale.

Let  $\Omega$  be the domain of the porous medium and  $\Gamma$  be the boundary of the domain  $\Omega$ . The generalized Brinkman equation, Equation (7), and the continuity equation [38] used in the PCL are

$$\mu \mathbf{k}^{-1} \cdot (\varepsilon^l \mathbf{u}^l) - \frac{\mu}{\varepsilon^l} \nabla \cdot (2\varepsilon^l \mathbf{d}^l) + \nabla p = \rho \mathbf{g} + \mu \mathbf{k}^{-1} \cdot (\varepsilon^l \mathbf{u}^s), \quad \text{in } \Omega \quad (8)$$

$$\nabla \cdot (\varepsilon^l \mathbf{u}^l) = f, \quad \text{in } \Omega \quad (9)$$

where  $f = \varepsilon^l / (1 - \varepsilon^l) + \nabla \cdot (\varepsilon^l \mathbf{u}^s)$  and  $\varepsilon^l = \partial \varepsilon^l / \partial t + \mathbf{u}^s \cdot \nabla \varepsilon^l$  is the material time derivative of the porosity with respect to the solid phase. Notice that the terms that have the inverse of the permeability in Equation (8) help in understanding the ability of the PCL fluid to flow through the PCL. The gravity term is the force exerted by Earth's gravity on the PCL fluid within the PCL. The pressure term represents the impact of pressure on fluid flow. The rate of deformation term refers to the change in velocity in different directions. The function  $f$  in Equation (9) tracks the rate of change of the porosity with respect to time. This term helps in understanding the change in porosity as we move along with the cilia. Define the vector

$$\mathbf{u} = \varepsilon^l \mathbf{u}^l. \quad (10)$$

Substituting Equation (10) into Equations (8) and (9), we obtain the system of equations

$$\mu \mathbf{k}^{-1} \cdot \mathbf{u} - \frac{\mu}{\varepsilon^l} \nabla \cdot (2\varepsilon^l \mathbf{d}^l) + \nabla p = \rho \mathbf{g} + \mu \mathbf{k}^{-1} \cdot \varepsilon^l \mathbf{u}^s, \quad \text{in } \Omega \quad (11)$$

$$\nabla \cdot \mathbf{u} = f, \quad \text{in } \Omega \quad (12)$$

which is used in this work. The unknowns of the system of equations are the fluid velocity,  $\mathbf{u}$ , and the pressure,  $p$ .

### 2.2. Boundary Conditions

In this work, we consider the forward stroke of cilia moving from the angle  $\theta = 90^\circ$  to  $40^\circ$ . The numerical domain and the boundaries are shown in Figure 4. The variable  $x_1^b$  is the length at which  $\xi_{\max}$  is projected on the  $x_1$  axis when the cilia make the angle  $\theta = 40^\circ$  with the horizontal plane. Then,  $x_1^b = \cos 40^\circ$  and  $0 \leq x_2 \leq 1$ . The variables  $\Gamma_i, i = 1, 2, 3$  are the boundaries of the domain  $\Omega$  and  $\Gamma = \Gamma_1 \cup \Gamma_2 \cup \Gamma_3$ . We let  $\mathbf{u} = (u_1, u_2)$  be the velocity vector, where  $u_1$  is the velocity in the rightward direction, and  $u_2$  is the velocity in the upward direction, in which the velocity these directions are considered to be positive numbers. If the cilia move in the downward direction, the velocity  $u_2$  becomes negative. At the boundary  $\Gamma_1$ , we let the fluid velocity be equal to the velocity of the cilia, provided in Section 4, when the angle  $\theta = 90^\circ$ . Since, from the experimental data, [39], the cilia move forward rapidly and stop moving at  $\theta = 40^\circ$ , approximately before having the reverse movement, in this work, we assume that the velocity of the cilia is zero at  $\theta = 40^\circ$ . So, the velocity at the boundary  $\Gamma_3$  is zero. For the boundary condition at  $\Gamma_2$ , since no one really knows the condition at  $\Gamma_2$ , we consider two cases for this problem.

Case 1: We employ the boundary conditions from [23], where they have determined the velocity at the tips of cilia when the cilia move forward and backward. They provide that the rate of change of the fluid velocities with respect to  $x_1$  and  $x_2$  depends on the exponential function of the angle  $\theta$ . So, our boundary conditions at  $\Gamma_1, \Gamma_2$ , and  $\Gamma_3$  are

$$u_1(0, x_2) = u^s(x_2), \quad \text{at } \Gamma_1 \quad (13)$$

$$\frac{\partial u_1}{\partial x_1} = c_1 e^\theta, \quad \frac{\partial u_1}{\partial x_2} = c_2 e^\theta, \quad \frac{\partial u_2}{\partial x_1} = c_3 e^\theta, \quad \frac{\partial u_2}{\partial x_2} = c_4 e^\theta, \quad \text{at } \Gamma_2 \quad (14)$$

$$u_1(x_1, x_2) = u_2(x_1, x_2) = 0, \quad \text{at } \Gamma_3 \quad (15)$$

where  $c_1, c_2, c_3$ , and  $c_4$  are constants.

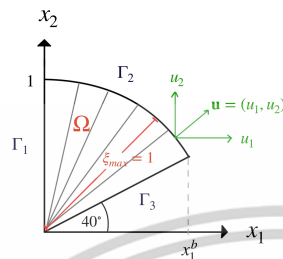


Figure 4. The boundary of our domain.

The constants  $c_i, i = 1, 2, 3, 4$ , can be positive, negative, or zero. It depends on the problems that one considers. For example, if  $c_1 = 0$ , then  $\frac{\partial u_1}{\partial x_1} = 0$ . Therefore, the rate of change of  $u_1$  with respect to  $x_1$  is zero. That is,  $u_1$  remains a constant even  $x_1$  has been changed.

Case 2: We assume that boundary conditions at  $\Gamma_2$  are unknown. So, to obtain the numerical solution, the velocities  $u_1$  and  $u_2$  at  $\Gamma_2$  are moved to the left-hand side of the equation and used to find the numerical solution, in order to determine  $u_1$  and  $u_2$  at  $\Gamma_2$ .

The governing equations, the generalized Brinkman equation, and the boundary conditions used in this work are now provided. Before we calculate the numerical results, we provide the discretized form of our mathematical model using a mixed finite element method in the next section.

### 3. Model Discretization

In this section, we discretize the system of equations, Equations (11) and (12) using a mixed finite element method. We begin with the generalized Brinkman equation in the indicial notation for two dimensions,

$$\mu k_{ij}^{-1} u_j - \frac{\mu}{\epsilon^l} \frac{\partial}{\partial x_j} (2\epsilon^l d_{ij}^l) + \frac{\partial p}{\partial x_i} = \rho g_i + \mu \epsilon^l k_{ij}^{-1} u_j^s, \quad \text{in } \Omega \tag{16}$$

for  $i, j = 1, 2$  and  $(g_1, g_2) = (0, -g)$  where  $g$  is gravity. The index  $i$  indicates the number of equations, and the repeated index  $j$  indicates summation. Let  $H^1(\Omega)$  be the Hilbert space and  $L_0^2(\Omega)$  be the Sobolev space, defined as follows,

$$L_0^2(\Omega) = \left\{ q \in L^2(\Omega) : \int_{\Omega} q \, d\Omega = 0 \right\} \text{ and } H_0^1(\Omega) = \left\{ \mathbf{w} \in H^1(\Omega) : \mathbf{w}|_{\partial\Omega} = 0 \right\}. \tag{17}$$

To find  $(\mathbf{u}, p) \in H^1(\Omega) \times L_0^2(\Omega)$ , we first provide the weak formulation of Equation (16). The weak formulation is the lower-order integral equations obtained from multiplying the higher-order differential Equation (16) by a weight function and then integrating over the domain and after that applying the Green's identity, which is integration by parts in one dimension, to the integral equation. To find the weak formulation, we multiply Equation (16) by a weight function,  $w_i \in H_0^1(\Omega)$ , and then we integrate over the domain  $\Omega$  both sides. Therefore, the Equation (16) becomes

$$\int_{\Omega} w_i \mu k_{ij}^{-1} u_j \, d\Omega - \int_{\Omega} w_i \frac{\mu}{\epsilon^l} \frac{\partial}{\partial x_j} (2\epsilon^l d_{ij}^l) \, d\Omega + \int_{\Omega} w_i \frac{\partial p}{\partial x_i} \, d\Omega = \int_{\Omega} w_i (\rho g_i + \mu \epsilon^l k_{ij}^{-1} u_j^s) \, d\Omega. \tag{18}$$

The repeated index  $i$  in Equation (18) means the equation number, not a summation. Applying Green’s identity to the second and third terms in Equation (18), we have

$$\int_{\Omega} \mu k_{ij}^{-1} w_i u_j d\Omega + \int_{\Omega} 2\mu \epsilon^l \frac{\partial}{\partial x_j} \left( \frac{w_i}{\epsilon^l} \right) d_{ij}^l d\Omega - \int_{\Omega} \frac{\partial w_i}{\partial x_i} p d\Omega = \int_{\Omega} w_i (\rho g_i + \mu \epsilon^l k_{ij}^{-1} u_j^s) d\Omega + \int_{\Gamma} 2\mu w_i d_{ij}^l n_j d\Gamma - \int_{\Gamma} w_i p n_i d\Gamma. \tag{19}$$

Substituting  $d_{ij}^l = 0.5 \left[ \frac{\partial}{\partial x_j} \left( \frac{u_i}{\epsilon^l} \right) + \frac{\partial}{\partial x_i} \left( \frac{u_j}{\epsilon^l} \right) \right]$  into Equation (19), we obtain the weak formulation of Equation (11), which is

$$\int_{\Omega} \mu k_{ij}^{-1} w_i u_j d\Omega + \int_{\Omega} \mu \epsilon^l \frac{\partial}{\partial x_j} \left( \frac{w_i}{\epsilon^l} \right) \frac{\partial}{\partial x_j} \left( \frac{u_i}{\epsilon^l} \right) d\Omega + \int_{\Omega} \mu \epsilon^l \frac{\partial}{\partial x_j} \left( \frac{w_i}{\epsilon^l} \right) \frac{\partial}{\partial x_i} \left( \frac{u_j}{\epsilon^l} \right) d\Omega - \int_{\Omega} \frac{\partial w_i}{\partial x_i} p d\Omega = \int_{\Omega} w_i (\rho g_i + \mu \epsilon^l k_{ij}^{-1} u_j^s) d\Omega + \int_{\Gamma} \mu w_i \frac{\partial}{\partial x_j} \left( \frac{u_j}{\epsilon^l} \right) n_j d\Gamma + \int_{\Gamma} \mu w_i \frac{\partial}{\partial x_i} \left( \frac{u_j}{\epsilon^l} \right) n_j d\Gamma - \int_{\Gamma} w_i p n_i d\Gamma, \tag{20}$$

where  $n_i$  is the outward unit normal vector,  $i = 1, 2$ .

To obtain the weak formulation of the continuity Equation (12), we apply the same process as we have done with Equation (11). We begin with the indicial notation of Equation (12)

$$\frac{\partial u_j}{\partial x_j} = \frac{-\epsilon^l}{1 - \epsilon^l} + \frac{\partial}{\partial x_j} (\epsilon^l u_j^s), \tag{21}$$

where, again, the repeated index  $j$  is the summation. Considering the term  $\epsilon^l$  in Equation (21), we have

$$\epsilon^l = \frac{\partial \epsilon^l}{\partial t} + \mathbf{u}^s \cdot \nabla \epsilon^l = \frac{\partial \epsilon^l}{\partial \theta} \frac{\partial \theta}{\partial t} + u_j^s \frac{\partial \epsilon^l}{\partial x_j}. \tag{22}$$

Using the angular velocity to determine  $\frac{\partial \theta}{\partial t}$ , we obtain  $\frac{\partial \theta}{\partial t} = \frac{-|u^s|}{\zeta}$  [25]. Then,

$$\epsilon^l = \frac{-|u^s|}{\zeta} \frac{\partial \epsilon^l}{\partial \theta} + u_j^s \frac{\partial \epsilon^l}{\partial x_j}, \tag{23}$$

where  $|u^s|$  is the speed of the solid velocity. Substituting Equation (23) into Equation (21) and applying the product rule to the last term of Equation (21), we obtain

$$\frac{\partial u_j}{\partial x_j} = \frac{|u^s|}{\zeta(1 - \epsilon^l)} \frac{\partial \epsilon^l}{\partial \theta} - \frac{\epsilon^l}{(1 - \epsilon^l)} u_j^s \frac{\partial \epsilon^l}{\partial x_j} + \epsilon^l \frac{\partial u_j^s}{\partial x_j}. \tag{24}$$

Multiplying a weight function  $q \in L_0^2(\Omega)$  to Equation (24) and then integrating the equation over the domain  $\Omega$  both sides, we obtain the weak formulation of the continuity equation, which is

$$- \int_{\Omega} q \frac{\partial u_j}{\partial x_j} d\Omega = - \int_{\Omega} q \left( \frac{|u^s|}{\zeta(1 - \epsilon^l)} \frac{\partial \epsilon^l}{\partial \theta} - \frac{\epsilon^l}{(1 - \epsilon^l)} u_j^s \frac{\partial \epsilon^l}{\partial x_j} + \epsilon^l \frac{\partial u_j^s}{\partial x_j} \right) d\Omega, \tag{25}$$

where we multiply  $(-1)$  both sides of the weak formulation in order to obtain the symmetric form of the stiffness matrix Equation (39), shown below. The well-posedness of the weak Formulations (20) and (25) is proven in [33]. Next, we discretize the domain  $\Omega$  into triangular elements and approximate the velocity and the pressure within each element using basis functions from the spaces  $U_h$  and  $H_h$ , respectively, defined below.

Let  $T_h$  be a triangulation of the domain  $\Omega$  and we define the finite-dimensional subspaces of  $H^1(\Omega)$  and  $L_0^2(\Omega)$  as [40]

$$U_h = \left\{ u \in H^1(\Omega) : u|_K \text{ is quadratic, } \forall K \in T_h \right\}, \quad (26)$$

$$H_h = \left\{ q \in L_0^2(\Omega) : q|_K \text{ is linear, } \forall K \in T_h \right\}, \quad (27)$$

respectively. Since  $\mathbf{u} = (u_1, u_2)$ ,  $\mathbf{u} \in U_h \times U_h$ . The solutions  $(u_1, u_2, p) \in U_h \times U_h \times H_h$  is approximated by the expansions of the forms

$$u_i(\mathbf{x}) = \sum_{m=1}^M \psi_m(\mathbf{x}) u_i^m = \mathbf{\Psi}^T \mathbf{U}_i, \quad (28)$$

$$p(\mathbf{x}) = \sum_{l=1}^L \phi_l(\mathbf{x}) p_l = \mathbf{\Phi}^T \mathbf{P}, \quad (29)$$

where  $i = 1, 2$ ,  $\mathbf{x} = (x_1, x_2)$ ,  $\psi_m \in H_0^1(\Omega)$  and  $\phi_l \in L_0^2(\Omega)$  are the basis functions, the vector  $\mathbf{\Psi}$  and  $\mathbf{\Phi}$  are their vector forms,  $\mathbf{U}_1, \mathbf{U}_2$ , and  $\mathbf{P}$  are vectors of the velocities and pressure, respectively, and the superscript  $T$  represents the transpose. The constants  $M$  and  $L$  are integers determined by the interpolation functions. For a triangular element, in this work, we use a quadratic function for the velocities  $u_i$  ( $M = 6$ ) and a linear function for the pressure  $p$  ( $L = 3$ ).

Substituting the vector form of the basis functions  $\mathbf{\Psi}$  into  $w_i$  and  $\mathbf{\Phi}$  into  $q$ , and substituting Equations (28) and (29) into Equations (20) and (25), we have

$$\begin{aligned} & \mu k_{ij}^{-1} \left( \int_{\Omega} \mathbf{\Psi} \mathbf{\Psi}^T d\Omega \right) \mathbf{U}_j + \mu \left( \int_{\Omega} \varepsilon^l \frac{\partial}{\partial x_j} \left( \frac{\mathbf{\Psi}}{\varepsilon^l} \right) \frac{\partial}{\partial x_i} \left( \frac{\mathbf{\Psi}^T}{\varepsilon^l} \right) d\Omega \right) \mathbf{U}_i \\ & + \mu \left( \int_{\Omega} \varepsilon^l \frac{\partial}{\partial x_j} \left( \frac{\mathbf{\Psi}}{\varepsilon^l} \right) \frac{\partial}{\partial x_i} \left( \frac{\mathbf{\Psi}^T}{\varepsilon^l} \right) d\Omega \right) \mathbf{U}_j - \left( \int_{\Omega} \frac{\partial \mathbf{\Psi}}{\partial x_i} \mathbf{\Phi}^T d\Omega \right) \mathbf{P} \\ & = \int_{\Omega} \mathbf{\Psi} \left( \rho g_i + \mu \varepsilon^l k_{ij}^{-1} u_j^s \right) d\Omega + \mu \left( \int_{\Gamma} \mathbf{\Psi} \frac{\partial}{\partial x_j} \left( \frac{\mathbf{\Psi}^T}{\varepsilon^l} \right) n_j d\Gamma \right) \mathbf{U}_i \\ & + \mu \left( \int_{\Gamma} \mathbf{\Psi} \frac{\partial}{\partial x_i} \left( \frac{\mathbf{\Psi}^T}{\varepsilon^l} \right) n_j d\Gamma \right) \mathbf{U}_j - \left( \int_{\Gamma} \mathbf{\Psi} \mathbf{\Phi}^T n_i d\Gamma \right) \mathbf{P}, \end{aligned} \quad (30)$$

and

$$- \left( \int_{\Omega} \mathbf{\Phi} \frac{\partial \mathbf{\Psi}^T}{\partial x_j} d\Omega \right) \mathbf{U}_j = - \int_{\Omega} \mathbf{\Phi} \left( \frac{u^s \varepsilon^l}{\zeta(1-\varepsilon^l)} \frac{\partial \varepsilon^l}{\partial \theta} - \frac{\varepsilon^l}{(1-\varepsilon^l)} u_j^s \frac{\partial \varepsilon^l}{\partial x_j} + \varepsilon^l \frac{\partial u_j^s}{\partial x_j} \right) d\Omega. \quad (31)$$

Let  $\Omega^e$  be the element domains, such that  $\Omega = \bigcup_e \Omega^e$ , where the interiors of the elements do not overlap. This decomposition enables the integral over the entire domain  $\Omega$  to be written as the sum of integrals over each element domain  $\Omega^e$ , that is

$$\int_{\Omega} f(x) d\Omega = \sum_{e=1}^n \int_{\Omega^e} f(x) d\Omega^e, \quad (32)$$

where  $n$  is the total number of elements. Applying Equation (32) to every integral term in Equations (30) and (31), we obtain the equations

$$\sum_{e=1}^n \left[ (\mu k_{ij}^{-1} \hat{\mathbf{A}} + \mu \hat{\mathbf{D}}_{ij}) \mathbf{U}_j + \mu \hat{\mathbf{K}}_{ij} \mathbf{U}_i - \hat{\mathbf{Q}}_i^T \mathbf{P} \right] = \sum_{e=1}^n \left[ \hat{\mathbf{F}}_i \right], \quad (33)$$

$$\sum_{e=1}^n \left[ -\hat{\mathbf{Q}}_j \mathbf{U}_j \right] = \sum_{e=1}^n \left[ \hat{\mathbf{F}}_3 \right], \quad (34)$$

where

$$\hat{\mathbf{A}} = \int_{\Omega^e} \boldsymbol{\Psi} \boldsymbol{\Psi}^T d\Omega^e, \quad \hat{\mathbf{K}}_{ij} = \int_{\Omega^e} \varepsilon^l \frac{\partial}{\partial x_j} \left( \frac{\boldsymbol{\Psi}}{\varepsilon^l} \right) \frac{\partial}{\partial x_i} \left( \frac{\boldsymbol{\Psi}^T}{\varepsilon^l} \right) d\Omega^e, \quad (35)$$

$$\hat{\mathbf{D}}_{ij} = \int_{\Omega^e} \varepsilon^l \frac{\partial}{\partial x_j} \left( \frac{\boldsymbol{\Psi}}{\varepsilon^l} \right) \frac{\partial}{\partial x_i} \left( \frac{\boldsymbol{\Psi}^T}{\varepsilon^l} \right) d\Omega^e, \quad \hat{\mathbf{Q}}_i^T = \int_{\Omega^e} \frac{\partial \boldsymbol{\Psi}}{\partial x_i} \boldsymbol{\Phi}^T d\Omega^e, \quad (36)$$

$$\begin{aligned} \hat{\mathbf{F}}_i &= \int_{\Omega^e} \boldsymbol{\Psi} (\rho g_i + \mu \varepsilon^l k_{ij}^{-1} u_j^s) d\Omega^e + \mu \left( \int_{\Gamma^e} \boldsymbol{\Psi} \frac{\partial}{\partial x_j} \left( \frac{\boldsymbol{\Psi}^T}{\varepsilon^l} \right) n_j d\Gamma^e \right) \mathbf{U}_i \\ &+ \mu \left( \int_{\Gamma^e} \boldsymbol{\Psi} \frac{\partial}{\partial x_i} \left( \frac{\boldsymbol{\Psi}^T}{\varepsilon^l} \right) n_i d\Gamma^e \right) \mathbf{U}_j - \left( \int_{\Gamma^e} \boldsymbol{\Psi} \boldsymbol{\Phi}^T n_i d\Gamma^e \right) \mathbf{P}, \quad i = 1, 2, \end{aligned} \quad (37)$$

$$\hat{\mathbf{F}}_3 = - \int_{\Omega^e} \boldsymbol{\Phi} \left( \frac{|u^s|}{\zeta(1-\varepsilon^l)} \frac{\partial \varepsilon^l}{\partial \theta} - \frac{\varepsilon^l}{(1-\varepsilon^l)} u_j^s \frac{\partial \varepsilon^l}{\partial x_j} + \varepsilon^l \frac{\partial u_j^s}{\partial x_j} \right) d\Omega^e. \quad (38)$$

Rewriting Equations (33) and (34) into matrix form for each element  $e$ , we have the element matrix of the system of Equations (33) and (34) in 2 dimension as follows,

$$\begin{pmatrix} \mu(k_{11}^{-1} \hat{\mathbf{A}} + \hat{\mathbf{D}}_{11} + \hat{\mathbf{K}}_{11} + \hat{\mathbf{K}}_{22}) & \mu(k_{12}^{-1} \hat{\mathbf{A}} + \hat{\mathbf{D}}_{12}) & -\hat{\mathbf{Q}}_1^T \\ \mu(k_{21}^{-1} \hat{\mathbf{A}} + \hat{\mathbf{D}}_{21}) & \mu(k_{22}^{-1} \hat{\mathbf{A}} + \hat{\mathbf{D}}_{22} + \hat{\mathbf{K}}_{11} + \hat{\mathbf{K}}_{22}) & -\hat{\mathbf{Q}}_2^T \\ -\hat{\mathbf{Q}}_1 & -\hat{\mathbf{Q}}_2 & \mathbf{0} \end{pmatrix} \begin{pmatrix} \mathbf{U}_1 \\ \mathbf{U}_2 \\ \mathbf{P} \end{pmatrix} = \begin{pmatrix} \hat{\mathbf{F}}_1 \\ \hat{\mathbf{F}}_2 \\ \hat{\mathbf{F}}_3 \end{pmatrix}. \quad (39)$$

To return to Equations (33) and (34), the local element matrices are assembled to a global matrix in order to get the numerical solution. From Equations (26)–(39), this demonstrates the discretization details. In the next section, we present the cilia velocity, permeability, and porosity used in this study.

#### 4. Permeability, Cilia Velocity, and Porosity

Regarding the numerical calculation, the values of the permeability, cilia velocity, and porosity that we use in our program are provided in this section.

##### 4.1. Permeability

For the permeability, we employ the values of the permeability tensor from [41], where they have calculated the permeability tensor when an array of rigid cylinders are parallel to each other and have a constant length, as shown in Figure 5. Figure 5 shows the parallel cylinders making the angle  $90^\circ$  to the horizontal plane, which is imitated from [41]. The cylinders are represented as cilia in this work. They have provided the permeability tensor when the parallel array of cylinders make angles  $\theta, 26^\circ \leq \theta \leq 90^\circ$ , to the horizontal plane in the fourth-order polynomial form, which is

$$\begin{aligned} \hat{k}_{ij} &= a_1 z^4 + a_2 z^3 \theta + a_3 z^3 + a_4 z^2 \theta^2 + a_5 z^2 \theta + a_6 z^2 + a_7 z \theta^3 + a_8 z \theta^2 \\ &+ a_9 z \theta + a_{10} z + a_{11} \theta^4 + a_{12} \theta^3 + a_{13} \theta^2 + a_{14} \theta + a_{15}, \end{aligned} \quad (40)$$

where  $i, j = 1, 2, 3$ , the coefficients  $a_k, k = 1, 2, \dots, 15$ , are given in Table 3 in [41], and  $z = r/d$ , where  $r$  is the cross-sectional radius of a cylinder and  $d$  is the distance between cylinders.

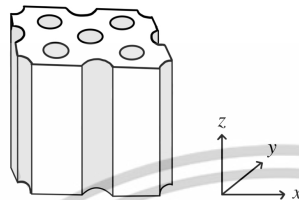


Figure 5. The geometric cells of the periodic array of five cylinders in three dimensions.

Note that, in three dimensions, the permeability

$$\hat{\mathbf{k}} = \begin{pmatrix} \hat{k}_{11} & \hat{k}_{12} & \hat{k}_{13} \\ \hat{k}_{21} & \hat{k}_{22} & \hat{k}_{23} \\ \hat{k}_{31} & \hat{k}_{32} & \hat{k}_{33} \end{pmatrix}. \tag{41}$$

So, the coefficients  $a_k, k = 1, 2, \dots, 15$  are different for each  $\hat{k}_{ij}, i, j = 1, 2, 3$ . In this work, we consider the two-dimensional problem, where the cilia move in  $x_1$  and  $x_2$  directions, which are  $x$  and  $z$  in Figure 5. So, the permeability used in our code comes from the first and third rows and columns of Equation (41). That is our permeability:

$$\mathbf{k} = \begin{pmatrix} k_{11} & k_{12} \\ k_{21} & k_{22} \end{pmatrix} = \begin{pmatrix} \hat{k}_{11} & \hat{k}_{13} \\ \hat{k}_{31} & \hat{k}_{33} \end{pmatrix}. \tag{42}$$

Since  $\hat{\mathbf{k}}$  is symmetric,  $k_{12} = k_{21}$ . Based on the laboratory data of cilia in human lungs provided in [42], the radius of cilia is  $0.1 \mu\text{m}$ , and the distance between cilia is  $0.3 \mu\text{m}$ . Then, substituting  $z = 1/3$  and  $\theta = \arctan(x_2/x_1)$  into Equation (40), we obtain  $k_{11}, k_{12} = k_{21}$  and  $k_{22}$ , which will be used in Sections 5 and 6.

#### 4.2. Velocity of Cilia

We provide the solid velocity  $\mathbf{u}^s$  used in this study employed from [25,39]. In [39], the authors experimentally provide the speed of cilia in lungs when cilia make angles  $40^\circ$  to  $140^\circ$  approximately with the horizontal plane. Next, Wuttanachamsri and Schreyer [25] convert the cilia speed into a polynomial form. The solid speed is approximated in the form of the eighth-order polynomial functions where the coefficients  $a_i, i = 1, 2, \dots, 8$  for the angles  $50^\circ, 60^\circ, 70^\circ, 80^\circ$  and  $90^\circ$  are given in Table 1 in [25]. That is the speed of cilia

$$s = a_1\zeta^8 + a_2\zeta^7 + a_3\zeta^6 + a_4\zeta^5 + a_5\zeta^4 + a_6\zeta^3 + a_7\zeta^2 + a_8\zeta, \tag{43}$$

where  $\zeta$  is the distance along cilia, as shown in Figure 3. The variable  $s$  in Equation (43) represents the solid speed along the cilia. To find the speed of the cilia at each point  $(x_1, x_2)$ , we substitute  $\zeta = x_2 / \sin \theta$  into the polynomial approximation (43). Because we consider the two-dimensional domain, let the cilia velocity  $\mathbf{u}^s = (u_1^s, u_2^s)$ . The components in the  $x_1$ -direction and the  $x_2$ -direction of the cilia velocity are  $u_1^s = s \sin \theta$  and  $u_2^s = -s \cos \theta$ , respectively.

From [39], they experimentally provide that, for the forward stroke of cilia, the cilia stop beating at  $\theta = 40^\circ$ , approximately. In this research, we assume the cilia start at  $\theta = 90^\circ$ , move forward with a decreasing angle, and stop beating at  $\theta = 40^\circ$ . Because the

angles used in this study are 5 degrees apart, we determine the cilia speed at the angles  $85^\circ, 75^\circ, \dots, 45^\circ$  by averaging the cilia speed of two adjacent angles. For example, we calculate the cilia speed at  $\theta = 85^\circ$  by averaging the cilia speed at  $\theta = 80^\circ$  and  $\theta = 90^\circ$ . We provide the coefficients of Equation (43) at  $\theta = 45^\circ, 55^\circ, 65^\circ, 75^\circ$  and  $85^\circ$  in Table 1, and the speed profiles of the angles are represented in Figure 6. Table 1 illustrates the coefficients  $a_i, i = 1, 2, \dots, 8$  of the terms of the polynomial in Equation (43), which are not provided in [25]. Figure 6 illustrates the speed along cilia from the roots to the tips of cilia from the angle  $\theta = 40^\circ$  to  $90^\circ$ . The black line is the velocity at  $\theta = 40^\circ, 50^\circ, 60^\circ, 70^\circ, 80^\circ$  and  $90^\circ$  presented in [25], and the red line is the speed at  $\theta = 45^\circ, 55^\circ, 65^\circ, 75^\circ$  and  $85^\circ$ , and also, we show the speed at  $\theta = 42.5^\circ, 47.5^\circ, 52.5^\circ, \dots, 87.5^\circ$ , as illustrated by the green line. The speed of the cilia is the maximum at the angle  $\theta = 90^\circ$ , and the speed is reduced when the angle  $\theta$  decreases until the cilia speed equals zero at  $\theta = 40^\circ$ .

Table 1. The coefficients of the eighth-order polynomial functions.

| Coefficients  | Degree      |             |             |             |             |
|---------------|-------------|-------------|-------------|-------------|-------------|
|               | $45^\circ$  | $55^\circ$  | $65^\circ$  | $75^\circ$  | $85^\circ$  |
| $\times 10^5$ |             |             |             |             |             |
| $a_1$         | 0.12489999  | 0.32704999  | -0.04719999 | -0.43174999 | -0.45169999 |
| $a_2$         | -0.53904999 | -1.37844999 | 0.22399999  | 1.84774999  | 1.89174999  |
| $a_3$         | 0.96449999  | 2.39729999  | -0.42229999 | -3.23804999 | -3.24839999 |
| $a_4$         | -0.92294999 | -2.22019999 | 0.40379999  | 2.98859999  | 2.94744999  |
| $a_5$         | 0.50664999  | 1.17564999  | -0.20744999 | -1.55564999 | -1.51859999 |
| $a_6$         | -0.15784999 | -0.35264999 | 0.05579999  | 0.45169999  | 0.44124999  |
| $a_7$         | 0.02519999  | 0.05444999  | -0.00659999 | -0.06549999 | -0.06434999 |
| $a_8$         | -0.00114999 | -0.00234999 | 0.00124999  | 0.00464999  | 0.00469999  |

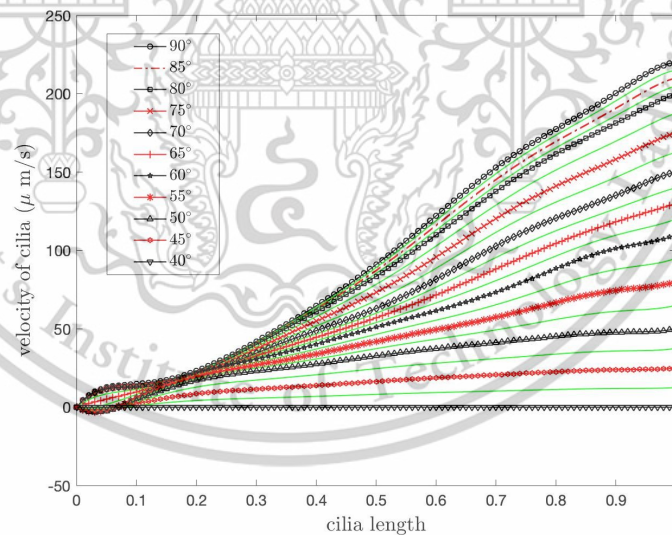


Figure 6. Speed of cilia along the cilia length.

#### 4.3. Porosity

For the value of the porosity  $\epsilon^l$ , we employ the value from [25], where they provide the porosity of a parallel array of cilia, making  $\theta = 90^\circ, 80^\circ, \dots, 40^\circ$  with a horizontal plane

in a cell domain. They approximate the porosity from [41] and present the porosity in a polynomial form. The fifth-degree polynomial function provided in [25] is

$$\varepsilon^l(\theta) = 0.5223\theta^5 - 3.0283\theta^4 + 7.0630\theta^3 - 8.4987\theta^2 + 5.5056\theta - 0.8627, \quad (44)$$

where  $\theta$  is the angle that cilia make with the horizontal plane given in radians. The values of other variables that are used in the code and the validation of the numerical solutions are presented in the next section. The numerical results of the velocities of the PCL fluid are provided in Section 6.

### 5. Numerical Validation

Before we provide our numerical results, we first validate our numerical solutions using the discretized model provided in Section 3, Equation (39). For this validation, we begin with the two-dimensional numerical domain, as shown in Figure 4. The domain is in the shape of a portion of a quarter circle. After that, we apply the mesh generator Netgen [43] to generate a triangular mesh, as shown in Figure 7. Figure 7 shows the example of our generated mesh with 5 degrees apart. To validate the numerical result, we use four different mesh refinements. The four discretized domains consist of 30, 45, 270, and 704 elements. For the constant variables, we let  $\mu = 3 \times 10^{-6} \text{ g}/(\mu\text{m}\cdot\text{s})$ ,  $\rho = 992.2 \times 10^{-15} \text{ g}/\mu\text{m}^3$ , the gravity  $g = 9.81 \times 10^6 \mu\text{m}/\text{s}^2$ , and the coefficient values  $c_1 = c_2 = c_3 = c_4 = 1$  in Equation (14). For the shape functions, we use quadratic triangular elements for the velocity and linear triangular elements for the pressure, confirming the stability of the method known as the Taylor–Hood elements [44]. Therefore, in Equations (28) and (29),  $M = 6$ , and  $L = 3$ . Next, we clarify the value of the inverse of the permeability tensor,  $\mathbf{k}^{-1}$ , used in our program. Because the polynomial function (40) used to approximate the permeability tensor is the function that depends on  $\theta$ , for each  $k_{ij}$  where  $i, j = 1, 2$ , we have six values per element. In this work, for each element, we average the 6 values of each  $k_{ij}$  and use the average value of each  $k_{ij}$  to find the numerical solutions. We then compute the inverse of the matrix  $\mathbf{k}$  to obtain  $k_{ij}^{-1}$  for each element.

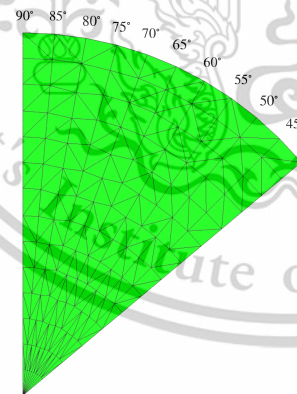


Figure 7. Generated mesh for the numerical domain.

For the solid velocity, we approximate the solid velocity in Equations (37) and (38) as

$$u_j^s(\mathbf{x}) = \sum_{m=1}^M \psi_m(\mathbf{x})(u_j^s)_m = \Psi^T \mathbf{U}_j^s. \quad (45)$$

where  $\mathbf{U}_j^s$  is the vector of solid velocities  $(u_j^s)_m$ ,  $m = 1, \dots, M$ ,  $j = 1, 2$ .

For the porosity, we use the same process of calculating the permeability tensor to compute the value of the porosity  $\varepsilon^l$  because the porosity  $\varepsilon^l$  is a function that depends on  $\theta$ . That is, we use the average value of the porosity  $\varepsilon^l$  for each element to find the numerical solutions. For the term  $\frac{\partial \varepsilon^l}{\partial x_j}$  in Equation (38), to compute the numerical solution, we approximate the derivative of the porosity as

$$\frac{\partial \varepsilon^l(\mathbf{x})}{\partial x_j} = \sum_{m=1}^M \frac{\partial \psi_m^T(\mathbf{x})}{\partial x_j} \varepsilon_m^l = \frac{\partial \Psi^T}{\partial x_j} \mathbf{Y}^l, \quad (46)$$

where  $\mathbf{Y}^l$  is the vector value of  $\varepsilon^l$ , consisting of six nodes per element. These values will be substituted into Equation (39) to calculate the numerical solutions.

To validate the code, we choose to present the velocity profile of the PCL fluid when  $\theta = 80^\circ$ . Since, in our work, we consider two cases of the boundary conditions, we provide our numerical results for the two cases. Figures 8 and 9 illustrate the PCL velocities for Case 1 and Case 2 boundary conditions, respectively. In both figures, the left graph shows the velocity,  $u_1$ , and the right graph presents  $u_2$ . The blue, orange, yellow, and purple lines represent the velocity of the PCL fluid obtained from the grid refinements containing 30, 45, 270, and 704 elements, respectively. In both figures, the numerical solutions obtained from the coarser grids converge to the numerical solutions obtained from the finest grid. Table 2 presents the  $L_2$ -norm errors of the velocities  $u_1$  and  $u_2$  of the PCL fluid at the angle  $\theta = 80^\circ$ , compared to the solutions obtained from the finest grid, 704 elements. The results show that the errors decrease as the number of elements increases, illustrating the convergence of the numerical solutions.

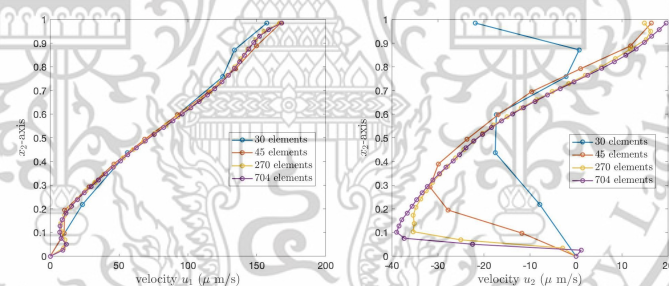


**Figure 8.** The velocities of the PCL fluid obtained from four different mesh refinements at the angle  $\theta = 80^\circ$  for the Case 1 boundary condition. The left graph is the velocity  $u_1$ , while the right graph is the velocity  $u_2$ .

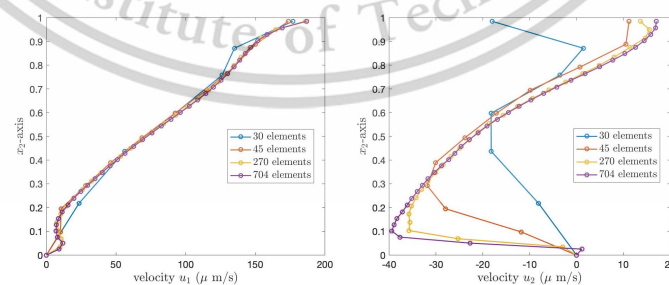


**Figure 9.** The velocities of the PCL fluid obtained from four different mesh refinements at the angle  $\theta = 80^\circ$  for the Case 2 boundary condition. The left graph is the velocity  $u_1$ , while the right graph is the velocity  $u_2$ .

**Table 2.** The  $l_2$ -norm errors of the PCL velocity obtained from the different mesh refinements at the angle  $\theta = 80^\circ$ .

| Number of Elements | $l_2$ -Norm Errors |         |         |         |
|--------------------|--------------------|---------|---------|---------|
|                    | Case 1             |         | Case 2  |         |
|                    | $u_1$              | $u_2$   | $u_1$   | $u_2$   |
| 30                 | 17.8755            | 52.3543 | 18.1664 | 47.3204 |
| 45                 | 8.8341             | 30.1146 | 15.3896 | 30.7428 |
| 270                | 8.8134             | 15.1360 | 9.7240  | 14.8701 |

## 6. Numerical Results

The numerical solutions of the generalized Brinkman equation and the continuity equation, Equations (11) and (12), are presented in this section. The existence and uniqueness of the numerical solution using the mixed finite element method have been proven in [33]. We use the two-dimensional finite element method to determine the velocities of the PCL fluid propelled via moving cilia in the porous medium. We present the velocity of the PCL fluid when cilia make an angle of  $90^\circ$  to  $40^\circ$  to the horizontal plane. Two cases of the boundary conditions are considered. The values of the dynamic viscosity, fluid density, gravity, and the coefficients  $c_i$ ,  $i = 1, 2, 3, 4$ , are the same as in Section 5.

We use the triangular mesh with 270 elements and 579 points generated via Netgen [43], as shown in Figure 7. The numerical domain  $\Omega$  is divided into 10 subdomains. The first subdomain starts from the leftmost vertical line, at  $\theta = 90^\circ$ , to the inclined line, at  $\theta = 85^\circ$ . The second subdomain is next to the right of the first subdomain, starting from  $\theta = 85^\circ$  to  $\theta = 80^\circ$ . Continuing the process until reaching  $\theta = 40^\circ$ , we have 10 different subdomains. By using the mixed finite element method of Taylor–Hood type, we obtain the numerical results, which are illustrated in Figure 10. The first row of Figure 10 shows the velocities of the PCL fluid using the Case 1 boundary condition. The top left graph represents the velocity  $u_1$  in the  $x_1$  direction, while the top right graph presents the velocity  $u_2$  in the  $x_2$  direction. The velocity of the PCL fluid decreases when the angle decreases. This is affected by the velocity of the cilia; see Figure 6. The velocity  $u_1$  is highest when  $\theta = 90^\circ$ , and the velocity is zero at  $\theta = 40^\circ$  because the velocity of cilia is highest at  $\theta = 90^\circ$ , and the cilia stop beating at  $\theta = 40^\circ$ . For the velocity  $v_2$ , when the angle decreases, the velocity  $u_2$  at the tips of cilia decreases from 110.74 to  $-36.64 \mu\text{m/s}$  and then increases slightly until the velocity approaches zero at  $\theta = 40^\circ$ . The velocity  $u_2$  is negative because, for the forward bend direction of cilia, the vertical velocity changes from the positive to the negative direction. The second row of Figure 10 illustrates the velocities  $u_1$  and  $u_2$  of the PCL fluid under the Case 2 boundary condition for the angles ranging from  $\theta = 90^\circ$  to  $40^\circ$ . The bottom left graph presents the velocity,  $u_1$ , and the bottom right graph represents the velocity,  $u_2$ . In this case, we assume that the boundary condition at  $\Gamma_2$ , at the tips of the cilia, is unknown. Similar to Case 1, the velocity  $u_1$  of the PCL fluid reduces as the angles decrease, and the maximum velocity of the PCL fluid occurs at the tips of cilia. The difference in  $u_1$  between Case 1 and Case 2 is that the velocity at the tips of cilia in Case 2 appears like a wave, moving up and down at the free interface. Similar to Case 1, the velocity  $u_2$  is highest at the tips of cilia at  $\theta = 90^\circ$ . As the angle decreases, the velocity  $u_2$  at the tips of cilia reduces from 90.39 to  $-37.06 \mu\text{m/s}$  before gradually increasing in the positive direction until it reaches zero at  $\theta = 40^\circ$ . We also observe that the velocity  $u_2$  at the tips of cilia in this case is smaller than the velocity  $u_2$  in Case 1 for all angles.

Next, we average the velocities  $u_1$  and  $u_2$  of the PCL fluid over the  $x_1$ -axis. The first row of Figure 11 shows the average velocities of the PCL fluid for the Case 1 boundary condition, while the second row illustrates the average velocities of the PCL fluid for the

Case 2 boundary condition. The top left graph shows the average velocity of  $u_1$ , while the top right graph shows the average velocity of  $u_2$ . The average velocities of  $u_1$  and  $u_2$  are almost the same for both cases. For the velocity  $u_2$ , near the root of cilia, the velocity has a negative value and the velocity gradually increases to a positive value along the cilia until the tips of the cilia. The highest average velocities are at the tips of cilia for all cases. The mean velocities of  $u_1$  for Case 1 and Case 2 are  $46.55$  and  $47.26$   $\mu\text{m/s}$ , respectively. The mean velocities of  $u_2$  for Case 1 and Case 2 are  $-13.95$  and  $-14.57$   $\mu\text{m/s}$ , respectively. The mean velocities for both cases of  $u_1$  are close to the velocity of the PCL fluid obtained from experimental data [45].

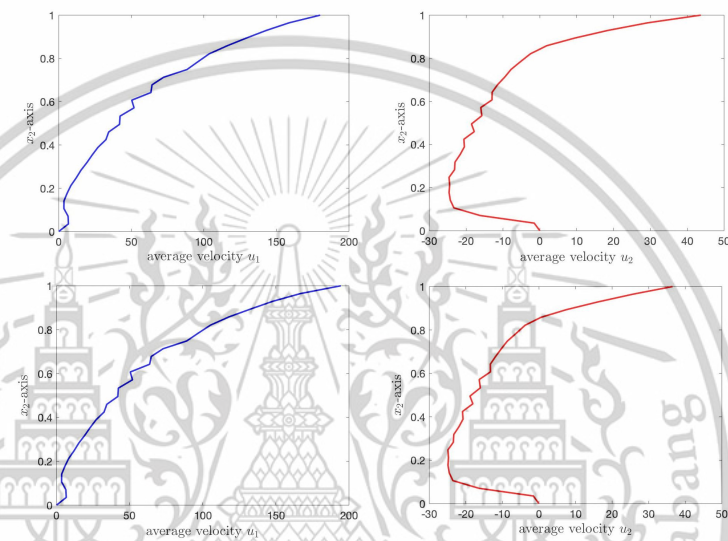


**Figure 10.** The velocities  $u_1$  (left) and  $u_2$  (right) of the PCL fluid for all angles. The first row shows the velocities for the Case 1 boundary condition while the second row shows the velocities for the Case 2 boundary condition.

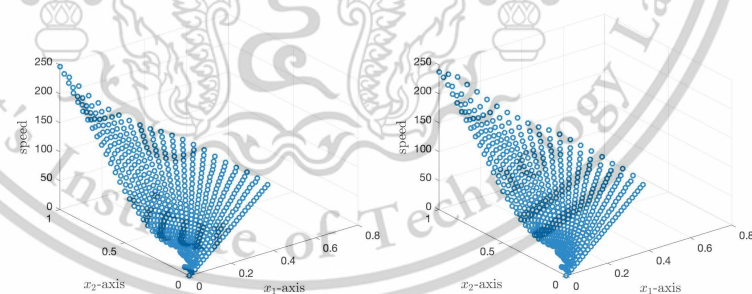
Researchers studied the movements of PCL and mucus in human tracheobronchial epithelial cell cultures using conventional and confocal microscopy of fluorescent microspheres. They found that the PCL fluid and mucus move at similar rates,  $39.2 \pm 4.7$  and  $39.8 \pm 4.2$   $\mu\text{m/s}$ , respectively, which is close to our mean velocity,  $u_1$ , for both cases.

Figure 12 shows the speed of the PCL fluid of both cases of the boundary conditions. The left and right graphs illustrate the speed of the PCL fluid for Case 1 and Case 2, respectively. The shapes of the graphs for both cases are similar to the velocity  $u_1$  except at the bottom of the representations. The difference comes from the effect of the negative value  $u_2$  near the root of cilia. It shows that the velocity  $u_1$  is more impactful to the PCL-fluid movement than  $u_2$ . The average speeds of the PCL fluid for Case 1 and Case 2 are  $54.68$   $\mu\text{m/s}$  and  $55.45$   $\mu\text{m/s}$ , respectively. The numerical results are compared with the numerical results provided in [13,14,25]. The authors determined the velocity of the PCL fluid due to the self-propelled cilia in one-dimensional, two-dimensional, and three-dimensional domains. In [13], the researchers used the finite element method to solve the nonlinear Stokes–Brinkman equations in a one-dimensional domain, and they discovered that the average speed of the PCL fluid was  $54.98$   $\mu\text{m/s}$ . In [14], the authors solved the nonlinear Brinkman equation in two dimensions using a mixed finite element method and Newton’s method to obtain the velocity of the PCL fluid. They found that the average

speed for all angles,  $40^\circ < \theta \leq 90^\circ$ , was  $52.52 \mu\text{m/s}$ . In [25], the researchers determined the velocity of the PCL fluid caused by cilia beating using a mixed finite element method of Taylor–Hood type to solve the Stokes–Brinkman equations in a three-dimensional domain. The average speed over angles,  $40^\circ < \theta \leq 90^\circ$ , was found to be  $52.52 \mu\text{m/s}$ . Comparing the numbers with our results reveals that the maximum difference is  $2.03 \mu\text{m/s}$  or about 3.6%. These comparisons demonstrate that the average speed for both cases obtained in our simulations is close to the average speed of the PCL fluid reported in the literature.



**Figure 11.** The average velocities  $u_1$  and  $u_2$  of the PCL fluid. The top left shows the average velocity  $u_1$  of Case 1, while the top right presents the average velocity  $u_2$  of Case 1. The bottom left shows the average velocity  $u_1$  of Case 2, while the bottom right presents the average velocity  $u_2$  of Case 2.



**Figure 12.** The left figure shows the speed of the PCL fluid for the Case 1 boundary condition, and the right figure presents the speed for the Case 2 boundary condition.

Next, we study the speed of the PCL fluid at the tips of cilia for different constants,  $c_i$ ,  $i = 1, 2, 3, 4$ , which are the coefficients in the boundary condition at  $\Gamma_2$  of Case 1. In the previous numerical results, we used  $c_i = 1$  for all  $i$ . For other values of  $c_i$ ,  $i = 1, 2, 3, 4$ , we present the speed of the PCL fluid at the tips of cilia in Figures 13 and 14. Figure 13 shows the speed at the tips of cilia when  $c_1 = c_2 = c_3 = c_4 = c$ , where  $c = 1, 10, 20, 30, 40, 50$ . From the graph, it can be observed that the different values of  $c_i$  result in slight variations

in speed. Figure 14 illustrates the speed of the PCL fluid at the tips of cilia when the values of  $c_i, i = 1, 2, 3, 4$ , are not equal. We also present the speed of the PCL fluid at the tips of cilia for Case 1 and Case 2 with different value of  $c_i, i = 1, 2, 3, 4$ . From the graph, we observe that the red and yellow lines are close to the line of Case 2. We also found that, despite different values of  $c_i$ , the shapes of all speed profiles in Figures 13 and 14 are similar.

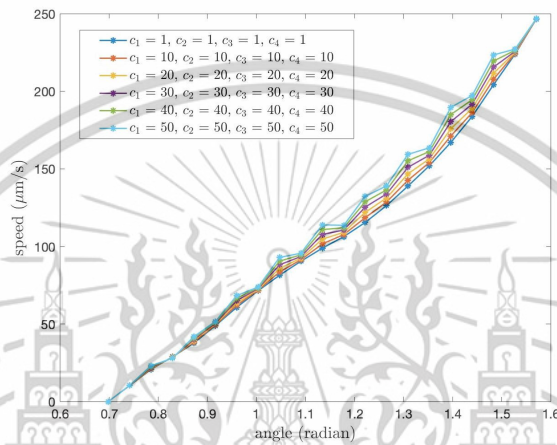


Figure 13. The speed of the PCL fluid at the tips of cilia for Case 1 boundary condition when  $c_1 = c_2 = c_3 = c_4 = c, c = 1, 10, 20, \dots, 50$ .

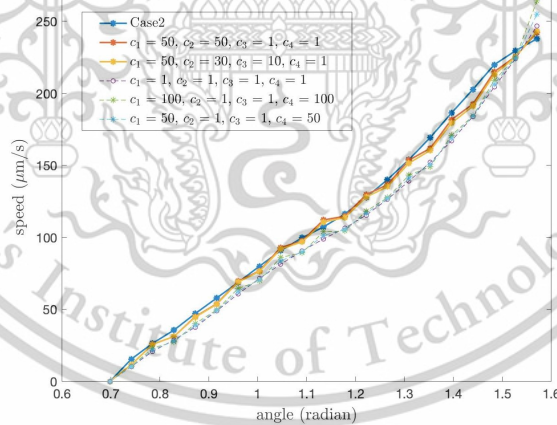
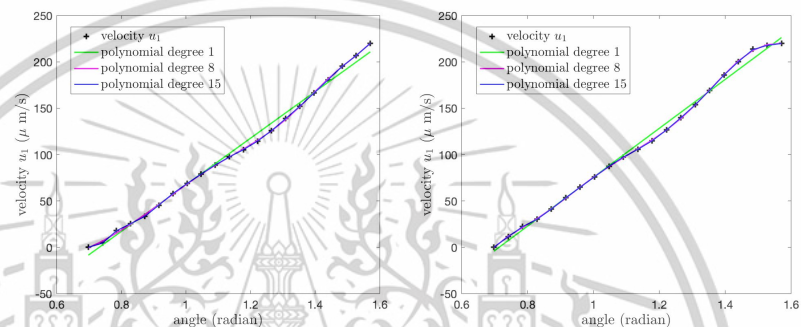


Figure 14. The speed of the PCL fluid at the tips of cilia with different values of  $c_i$  for  $i = 1, 2, 3, 4$ .

Because the velocity of the PCL fluid at the tips of cilia affects the velocity of mucus and the thickness of mucus can cause lung diseases, we focus on the velocity at the tips of cilia. We provide polynomial approximations of the velocities  $u_1$  and  $u_2$ , as well as the speed of the PCL fluid at the tips of cilia for both cases of the boundary conditions illustrated in Figures 15–17. We use  $c_1 = c_2 = c_3 = c_4 = 1$ . Here, we provide the polynomial approximations of degrees 1, 8, and 15 for the velocities  $u_1$  and the speed at the tips of cilia because the velocity  $u_1$  and the speed profiles at the tips of cilia can be approximated by

straight lines with an acceptable error, and sometimes it is convenient to use the first-degree polynomials for some problems. The polynomial approximations of degrees 8 and 15 are provided for  $u_2$ . In these figures, the horizontal axis represents the angle, measured in radians, ranging from  $40^\circ$  to  $90^\circ$ . The green, magenta, and blue lines represent the polynomial approximations of degrees 1, 8, and 15, respectively. Figure 15 shows the velocity  $u_1$  of the PCL fluid at the tips of the cilia and its polynomial approximations for Case 1 (left) and Case 2 (right) boundary conditions. We find that the velocity  $u_1$  at the tips of the cilia in both cases increases as the angle  $\theta$  increases from  $40^\circ$  to  $90^\circ$  and the maximum velocity occurs at the angle  $\theta = 90^\circ$ .

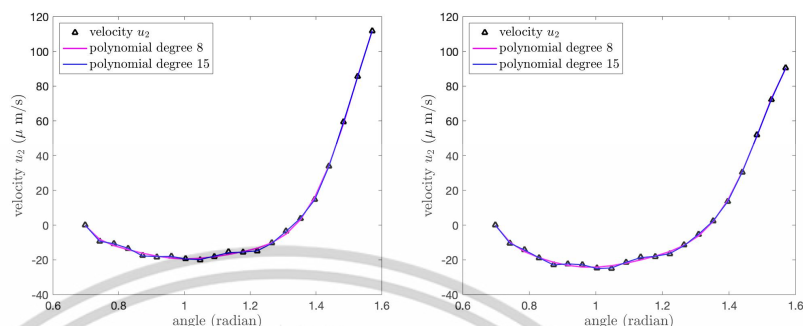


**Figure 15.** The velocity  $u_1$  of the PCL fluid at the tips of the cilia for Case 1 boundary condition (left) and for Case 2 boundary condition (right).

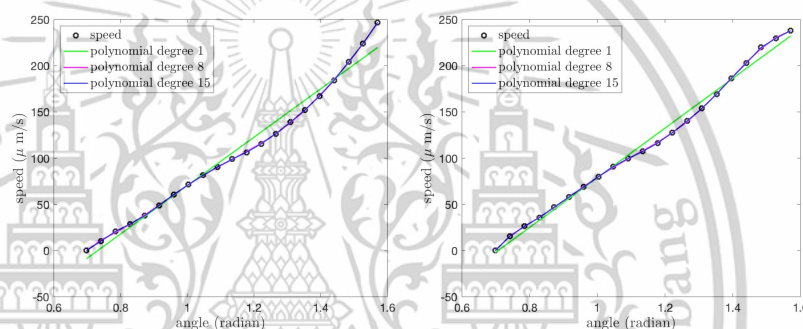
Figure 16 illustrates the velocity  $u_2$  of the PCL fluid at the tips of the cilia and its polynomial approximations for both cases of the boundary conditions. The velocity  $u_2$  for the Case 1 boundary condition (left) is greater than the velocity  $u_2$  for the Case 2 boundary condition (right), especially at  $\theta = 90^\circ$ . Although the shapes of the graphs in both cases have similar shapes, the values of the velocity  $u_2$  are different. The velocity  $u_2$  is the maximum at  $\theta = 90^\circ$ , and then it decreases as the angle decreases until  $\theta = 60^\circ$ . Then, the velocity increases until it reaches zero at  $\theta = 40^\circ$ .

Figure 17 shows the speed of the PCL fluid at the tips of cilia and the first-, eighth-, and fifteenth-degree polynomial approximations for Case 1 (left) and Case 2 (right) boundary conditions. We see that the shapes of the speeds at the tips of cilia are similar to the shapes of the velocity  $u_1$  for both cases; see Figure 15. This means the velocity  $u_1$  affects the motion of the PCL fluid more than the velocity  $u_2$ .

From physical perspectives, the PCL fluid appears to move similarly to the motion of the cilia. That is, the velocity of the PCL fluid increases progressively from the base to the tips of cilia. As the cilia angle decreases, indicating greater bending, the fluid velocity at the tips also decreases, implying that propulsion efficiency is reduced during the motion. Since cilia are self-propelled organelles that move forward speedily and back gently, they perform their power stroke to move fluids, and then they gradually back to their starting position, which is slower than the forward stroke. This pattern of acceleration and deceleration repeats periodically due to the nature of cilia. As a result, the PCL fluid moves faster when the cilia are upright (effective stroke), slows down during the bending, and then accelerates again when the cilia are in the upright position, resulting in a pulsatile flow pattern similar to metachronal waves.



**Figure 16.** The velocity  $u_2$  of the PCL fluid at the tips of cilia for Case 1 boundary condition (left) and for Case 2 boundary condition (right).



**Figure 17.** The speed of the PCL fluid at the tips of cilia for Case 1 boundary condition (left) and for Case 2 boundary condition (right).

The polynomial functions and their coefficients are given in Tables 3–5. Table 3 illustrates the coefficients of the first-degree polynomial function. Tables 4 and 5 show the coefficients of the eighth- and fifteenth-degree polynomial functions, respectively.

**Table 3.** The first-degree polynomial function:  $p(\theta) = a_1\theta + a_2$  estimates the speed and the velocities  $u_1$  at the tips of cilia for both cases of the boundary conditions, where  $\theta$  is the angle in radians.

| Coefficients  |             | Case 1 |                |
|---------------|-------------|--------|----------------|
| $10^2 \times$ | Speed       |        | Velocity $u_1$ |
| $a_1$         | 2.61877889  |        | 2.51367073     |
| $a_2$         | −1.91617185 |        | −1.83969272    |
| Coefficients  |             | Case 2 |                |
| $10^2 \times$ | Speed       |        | Velocity $u_1$ |
| $a_1$         | 2.68644586  |        | 2.64005346     |
| $a_2$         | −1.89878036 |        | −1.88461055    |

**Table 4.** The eighth-degree polynomial function:  $p(\theta) = a_1\theta^8 + a_2\theta^7 + a_3\theta^6 + a_4\theta^5 + a_5\theta^4 + a_6\theta^3 + a_7\theta^2 + a_8\theta + a_9$  estimates the speed and the velocities  $u_1$  and  $u_2$  at the tips of cilia for both cases of the boundary conditions, where  $\theta$  is the angle in radians.

| Coefficients  |                    | Case 1             |                    |
|---------------|--------------------|--------------------|--------------------|
| $10^6 \times$ | Speed              | $u_1$              | $u_2$              |
| $a_1$         | -0.012734118271167 | 0.057378313095743  | 0.008776158423867  |
| $a_2$         | 0.135670026652116  | -0.500821282568611 | -0.107483926304666 |
| $a_3$         | -0.617877401645130 | 1.885859004719336  | 0.527199931990443  |
| $a_4$         | 1.572260187763733  | -4.001363507459469 | -1.393202912554586 |
| $a_5$         | -2.445640591057800 | 5.233621138954125  | 2.203387221815350  |
| $a_6$         | 2.381652851245531  | -4.323269305568677 | -2.155213357695548 |
| $a_7$         | -1.418299927611897 | 2.204332823035274  | 1.280981336161525  |
| $a_8$         | 0.472589132393864  | -0.634706944987602 | -0.424880299024707 |
| $a_9$         | -0.067549690623399 | 0.079037225239463  | 0.060416408378815  |

| Coefficients  |                    | Case 2             |                    |
|---------------|--------------------|--------------------|--------------------|
| $10^6 \times$ | Speed              | $u_1$              | $u_2$              |
| $a_1$         | -0.010939237329981 | 0.015621983213058  | 0.008379732732943  |
| $a_2$         | 0.124622237256656  | -0.112413273633599 | -0.100340169104345 |
| $a_3$         | -0.597329420016729 | 0.319219155174230  | 0.484478291821826  |
| $a_4$         | 1.580853921698133  | -0.425346939699839 | -1.264833543315435 |
| $a_5$         | -2.535184997493686 | 0.184504901777252  | 1.980693486623330  |
| $a_6$         | 2.529299675528232  | 0.190169061295289  | -1.921683695840503 |
| $a_7$         | -1.536399388702010 | -0.289319521303333 | -1.134790516797084 |
| $a_8$         | 0.520744248609177  | 0.143704103345063  | -0.374654504988026 |
| $a_9$         | -0.075587763208465 | -0.026064000222104 | 0.053145691955595  |

**Table 5.** The fifteenth-degree polynomial function:  $p(\theta) = a_1\theta^{15} + a_2\theta^{14} + a_3\theta^{13} + a_4\theta^{12} + a_5\theta^{11} + a_6\theta^{10} + a_7\theta^9 + a_8\theta^8 + a_9\theta^7 + a_{10}\theta^6 + a_{11}\theta^5 + a_{12}\theta^4 + a_{13}\theta^3 + a_{14}\theta^2 + a_{15}\theta + a_{16}$  estimates the speed and the velocities  $u_1$  and  $u_2$  at the tips of cilia for both cases of the boundary conditions, where  $\theta$  is the angle in radians.

| Coefficients     |                    | Case 1             |                    |
|------------------|--------------------|--------------------|--------------------|
| $10^{13} \times$ | Speed              | $u_1$              | $u_2$              |
| $a_1$            | 0.000148633026563  | 0.000238695384065  | 0.000026480736805  |
| $a_2$            | -0.002550402419714 | -0.004115644913638 | -0.000605547516345 |
| $a_3$            | 0.020326208989479  | 0.032955135924412  | 0.006026245594933  |
| $a_4$            | -0.098800320623606 | -0.162544303017583 | -0.035447475762319 |
| $a_5$            | 0.337527285098084  | 0.55225554160010   | 0.139568160750811  |
| $a_6$            | -0.833149607242801 | -1.368720582565515 | -0.392545818489031 |
| $a_7$            | 1.549823716319571  | 2.556522729178357  | 0.18652144300971   |
| $a_8$            | -2.212460020243270 | -3.663952619805488 | -1.293279880109145 |
| $a_9$            | 2.443567136385676  | 4.061961701798492  | 1.563966870703912  |
| $a_{10}$         | -2.087818866919695 | -3.483132513082045 | -1.450226545717761 |
| $a_{11}$         | 1.368634146361897  | 2.291168271604290  | 1.024021239349936  |
| $a_{12}$         | -0.675937881127803 | -1.135256083953165 | -0.541256467049189 |
| $a_{13}$         | 0.243443136497010  | 0.410133386662197  | 0.207457763075095  |
| $a_{14}$         | -0.060357509441902 | -0.101981304210337 | -0.054469949954978 |
| $a_{15}$         | 0.009211069453411  | 0.015605585109138  | 0.008764590893595  |
| $a_{16}$         | -0.000652224105843 | -0.001107808266398 | -0.000651810809226 |

| Coefficients     |                    | Case 2             |                    |
|------------------|--------------------|--------------------|--------------------|
| $10^{13} \times$ | Speed              | $u_1$              | $u_2$              |
| $a_1$            | 0.000161729298700  | 0.000296703434881  | 0.000331043699638  |
| $a_2$            | -0.002663547237013 | -0.004991231500699 | -0.005772032762279 |
| $a_3$            | 0.020339099732280  | 0.038977801794141  | 0.046722649194728  |
| $a_4$            | -0.095508127683471 | -0.187426343684253 | -0.232891653324938 |
| $a_5$            | 0.308374706749317  | 0.620563020263077  | 0.799355226552687  |
| $a_6$            | -0.725042308960541 | -1.498477240355366 | -2.000992476154122 |
| $a_7$            | 1.282121070283650  | 2.725929439835820  | 3.773595128776208  |
| $a_8$            | -1.736005918233114 | -3.803798599185942 | -5.458846767793530 |
| $a_9$            | 1.814220029861536  | 4.104776739782694  | 6.106696174312163  |
| $a_{10}$         | -1.462981962075676 | -3.425342914369116 | -5.282486588179633 |
| $a_{11}$         | 0.902659332059763  | 2.192185648577189  | 3.504347199487991  |
| $a_{12}$         | -0.418360013949618 | -1.056619726773176 | -1.750716165522668 |
| $a_{13}$         | 0.140946840215663  | 0.371266424291172  | 0.637552371208820  |
| $a_{14}$         | -0.032574870988444 | -0.089776224139980 | -0.159766249185166 |
| $a_{15}$         | 0.00461166473962   | 0.01335853374243   | 0.024633814653303  |
| $a_{16}$         | -0.000302225539089 | -0.000922051337170 | -0.001761674965389 |

The  $l_2$ -norm errors of the polynomial approximations of the velocity  $u_1$  are presented in Table 6. Table 6 shows the errors of the first-, eighth-, and fifteenth-degree polynomials. When the degree of the polynomial increases, the error decreases. Although the 15th-degree polynomials provide the best fitting, we also present the lower-order approximations because, in some cases, one may need only a rough estimate.

**Table 6.**  $l_2$ -norm errors of the polynomial approximations of the velocity  $u_1$  for both cases of the boundary conditions.

| Order of Polynomial | $l_2$ - Norm Errors of Case 1 | $l_2$ - Norm Errors of Case 2 |
|---------------------|-------------------------------|-------------------------------|
| 1                   | 23.37590758                   | 22.60410473                   |
| 8                   | 4.49732994                    | 2.54515053                    |
| 15                  | 0.77551149                    | 0.67652906                    |

The  $l_2$ -norm errors of the polynomials approximating  $u_2$  are shown in Table 7. In Table 7, we present the errors of the eighth- and fifteenth-order polynomials. The 15th-order approximation has better error than the 8th-order polynomial, but we also present both of them here because the smaller degree of the polynomial may be useful for some rough study cases.

**Table 7.**  $l_2$ -norm errors of the polynomial approximations for both cases of the boundary conditions.

| Order of Polynomial | $l_2$ - Norm Errors of Case 1 | $l_2$ - Norm Errors of Case 2 |
|---------------------|-------------------------------|-------------------------------|
| 8                   | 4.22075638                    | 3.90055486                    |
| 15                  | 0.84113482                    | 1.05561499                    |

The  $l_2$ -norm errors of the polynomial approximations of the speed at the tips of cilia are provided in Table 8. The errors are small for the 15th-order approximation.

**Table 8.**  $l_2$ -norm errors of the polynomial approximations of the speed at the tips of cilia for both cases of the boundary conditions.

| Order of Polynomial | $l_2$ - Norm Errors of Case 1 | $l_2$ - Norm Errors of Case 2 |
|---------------------|-------------------------------|-------------------------------|
| 1                   | 45.26933528                   | 28.93285837                   |
| 8                   | 2.54321963                    | 2.58729001                    |
| 15                  | 0.49442221                    | 0.47532558                    |

## 7. Conclusions

In this research, we have studied the fluid flow problem in the periciliary layer (PCL) of the respiratory system in human lungs. We focused on the fluid moved via self-propelled bundles of cilia, rather than via pressure gradient. Here, we considered the PCL as a porous medium, which consists of the PCL fluid and cilia. To determine the velocity of the PCL fluid in the porous medium, we used the generalized Brinkman equation on a macroscopic scale with varied porosity for one fixed numerical domain. The numerical domain is designed to be the shape of a fan blade, imitating the actual beating pattern of cilia. The shape of the domain used in this study is closer to the pattern of the motion of cilia than the rectangular domain used in the previous literature. For the rectangular domain, authors have considered only one angle,  $\theta$ , for one fixed numerical domain. So, the porosity in their works was only a constant. In this work, our domain was designed to be aligned with the rotational movement of cilia, with which the cilia rotate around their roots. Therefore, the porosity used in the fan-blade domain is varied, depending on the angle,  $\theta$ , that the cilia make with the horizontal plane. We employ the mixed finite

element method of the Taylor–Hood type to discretize the mathematical model and find the numerical solutions in the two-dimensional domain. We consider the forward movement of cilia making the angle 90° to 40° with the horizontal plane. We provide the velocities  $u_1, u_2$  and the speed at the tips of cilia because it affects the velocity of mucus and then mucus thickness, which can cause diseases in the respiratory system in human lungs. At the tips of cilia, the velocity  $u_1$  for the Case 1 boundary condition is lower than the velocity  $u_1$  for Case 2, about 8.86%. Therefore, the boundary condition of Case 1 at the tips of cilia, which is expressed in the explicit form and is easy to apply to problems, may be used as a boundary condition at the free interface not only in this problem but also in other problems that are similar to this one, if the percentage difference is in an acceptable range of the problems. We provide the velocities and the speed of the PCL fluid for different values of  $c$ , so that they can be a guideline for those interested in applying this research to their works. We also present the first-, eighth-, and fifteenth-order polynomial functions for the velocities  $u_1$  and  $u_2$ , as well as the speed at the tips of the cilia, in order to apply them to future work and other similar efforts.

If the velocity of the solid phases in our governing equations is neglected, the system of equations can be applied to fluid-flow problems with immobile solids, such as natural rice fields or trees, glass rods, engine filters, filter pads, and underground oil. In future work, we will predict the PCL fluid velocity with the full forward stroke of cilia from the angles 130° to 40° [39], as well as extend the problem to two domains: a porous medium and an adjacent free-fluid region. We will use the result from this study as a lower boundary condition to find the mucus velocity.

**Author Contributions:** All authors contributed equally and significantly in writing this article. All authors have read and agreed to the published version of the manuscript.

**Funding:** This research was supported by the School of Science, King Mongkut’s Institute of Technology Ladkrabang, Thailand.

**Data Availability Statement:** The original contributions presented in this study are included in the article. Further inquiries can be directed to the corresponding author.

**Conflicts of Interest:** The authors declare no conflicts of interest.

**Nomenclature**

| Variables               | Definitions                                         | Units                                | Equations  |
|-------------------------|-----------------------------------------------------|--------------------------------------|------------|
| $a_k$                   | $k = 1, 2, \dots, 15$ , coefficients of polynomials | $[a_k] = 1$                          | below (40) |
| $\hat{\mathbf{A}}$      | a block matrix in the stiffness matrix              |                                      | (33)       |
| $c_1$                   | a constant                                          |                                      | (14)       |
| $c_2$                   | a constant                                          |                                      | (14)       |
| $c_3$                   | a constant                                          |                                      | (14)       |
| $c_4$                   | a constant                                          |                                      | (14)       |
| $d$                     | the distance between cylinder                       | $[d] = L$                            | below (40) |
| $\mathbf{d}^I$          | rate of deformation tensor                          | $[\mathbf{d}^I] = \frac{1}{T}$       | (5)        |
| $\hat{\mathbf{D}}_{ij}$ | a block matrix in the stiffness matrix              |                                      | (33)       |
| $e_{\beta}^{\alpha}$    | interactive quantity at the interface $\alpha\beta$ | $[e_{\beta}^{\alpha}] = \frac{1}{T}$ | (4)        |
| $f$                     | a source term                                       |                                      | (9)        |
| $F$                     | the quantities in the field equations               |                                      | (2)        |
| $\hat{\mathbf{F}}_3$    | a source term in an element matrix                  |                                      | (34)       |

|                             |                                                                               |                                                |
|-----------------------------|-------------------------------------------------------------------------------|------------------------------------------------|
| $\widehat{\mathbf{F}}_i$    | a block matrix in the stiffness matrix                                        | (33)                                           |
| $g$                         | gravity                                                                       | $[\mathbf{g}] = \frac{L}{T^2}$ below (16)      |
| $\mathbf{g}$                | $= (0, -g)$ gravity vector                                                    | $[\mathbf{g}] = \frac{L}{T^2}$ (5)             |
| $H^1(\Omega)$               | the Hilbert space                                                             | (17)                                           |
| $H_0^1(\Omega)$             | a Sobolev subspace of $H^1(\Omega)$                                           | (17)                                           |
| $H_h$                       | finite-dimensional subspace of $L_0^2(\Omega)$                                | (27)                                           |
| $k_{ij}^{-1}$               | a scalar of the inverse of a permeability tensor                              | $[k_{ij}^{-1}] = L^2$ (16)                     |
| $\mathbf{k}^{-1}$           | inverse of the permeability tensor                                            | $[\mathbf{k}^{-1}] = \frac{1}{L^2}$ below (5)  |
| $\hat{\mathbf{k}}$          | permeability tensor in 3 dimensions                                           | $[\hat{\mathbf{k}}] = L^2$ (41)                |
| $\hat{k}_{ij}$              | a scalar permeability, $i, j = 1, 2$                                          | $[\hat{k}_{ij}] = L^2$ (40)                    |
| $\widehat{\mathbf{K}}_{ij}$ | a block matrix in the stiffness matrix                                        | (33)                                           |
| $L_0^2(\Omega)$             | a Sobolev subspace of $L^2(\Omega)$                                           | (17)                                           |
| $L$                         | number of nodes of linear triangular elements                                 | (29)                                           |
| $M$                         | number of nodes of quadratic triangular elements                              | (28)                                           |
| $n$                         | total number of elements                                                      | (32)                                           |
| $\mathbf{n}$                | the outward unit normal vector                                                | $[\mathbf{n}] = 1$ (19)                        |
| $\mathbf{n}_\alpha$         | the outward unit normal vector to $\alpha\beta$                               | $[\mathbf{n}_\alpha] = 1$ (2)                  |
| $p$                         | pressure                                                                      | $[p] = \frac{M}{L \cdot T^2}$ (5)              |
| $\mathbf{P}$                | vector of pressure $p_l$ , $l = 1, 2, \dots, L$                               | (29)                                           |
| $q$                         | a weight function                                                             | (25)                                           |
| $\widehat{\mathbf{Q}}_i$    | a block matrix in the stiffness matrix                                        | (33)                                           |
| $r$                         | the cross-sectional radius of a cylinder                                      | $[r] = L$ below (40)                           |
| $\mathbf{R}$                | a second-order tensor                                                         | (5)                                            |
| $s$                         | solid speed along the cilia                                                   | $[s] = \frac{L}{T}$ (43)                       |
| $t$                         | time                                                                          | (1)                                            |
| $T_h$                       | a triangulation of the domain $\Omega$                                        | before (26)                                    |
| $\mathbf{u}$                | $= (u_1, u_2)$ , fluid velocity vector                                        | $[\mathbf{u}] = \frac{L}{T}$ (1)               |
| $u_1$                       | the velocity in the rightward direction                                       | $[u_1] = \frac{L}{T}$ Figure 4                 |
| $u_2$                       | the velocity in the upward direction                                          | $[u_2] = \frac{L}{T}$ Figure 4                 |
| $\mathbf{u}^l$              | velocity of the PCL                                                           | $[\mathbf{u}^l] = \frac{L}{T}$ (5)             |
| $\mathbf{u}^s$              | $= (u_1^s, u_2^s)$ , velocity of cilia                                        | $[\mathbf{u}^s] = \frac{L}{T}$ (5)             |
| $u_1^s$                     | the component of cilia velocity in the $x_1$ -direction                       | $[u_1^s] = \frac{L}{T}$ below (43)             |
| $u_2^s$                     | the component of cilia velocity in the $x_2$ -direction                       | $[u_2^s] = \frac{L}{T}$ below (43)             |
| $U_h$                       | finite-dimensional subspace of $H_0^1(\Omega)$                                | (26)                                           |
| $\mathbf{U}_i$              | vector of $u_i^m$ , $m = 1, 2, \dots, M$                                      | (28)                                           |
| $\mathbf{U}_j^s$            | vector of $(u_j^s)_m$ , $m = 1, 2, \dots, M$ , $j = 1, 2$                     | (45)                                           |
| $\mathbf{v}$                | mass-velocity                                                                 | $[\mathbf{v}] = \frac{L}{T}$ (1)               |
| $\mathbf{v}^\alpha$         | macroscale velocity of phase $\alpha$                                         | $[\mathbf{v}^\alpha] = \frac{L}{T}$ (4)        |
| $w_i$                       | a weight function                                                             | (18)                                           |
| $\mathbf{w}_{\alpha\beta}$  | microscopic velocity of interface $\alpha\beta$                               | $[\mathbf{w}_{\alpha\beta}] = \frac{L}{T}$ (2) |
| $\mathbf{x}$                | $= (x_1, x_2)$                                                                | (28)                                           |
| $x_1$                       | $x_1$ -axis in the physical coordinate system                                 | $[x_1] = L$ Figure 2                           |
| $x_2$                       | $x_2$ -axis in the physical coordinate system                                 | $[x_2] = L$ Figure 2                           |
| $x_1^a$                     | the $x_1$ -coordinate of an arbitrary point $(x_1^a, x_2^a)$ along the cilium | $[x_1^a] = L$ Figure 3                         |
| $x_2^a$                     | the $x_2$ -coordinate of an arbitrary point $(x_1^a, x_2^a)$ along the cilium | $[x_2^a] = L$ Figure 3                         |
| $x_1^b$                     | the $x_1$ -axis coordinate at the tip of the cilium when $\theta = 40^\circ$  | $[x_1^b] = L$ Figure 4                         |
| $z$                         | $= r/d$                                                                       | below (40)                                     |
| $\delta A_{\alpha\beta}$    | portion of $\alpha\beta$ interface within $\delta V$                          | $[\delta A_{\alpha\beta}] = L^2$ (2)           |
| $\delta V$                  | representative elementary volume                                              | $[\delta V] = L^3$ (2)                         |
| $\gamma_\alpha$             | indicator function for phase $\alpha$                                         | (2)                                            |
| $\Gamma$                    | $= \Gamma_1 \cup \Gamma_2 \cup \Gamma_3$ , boundaries of the domain           | $[\Gamma] = L$ Figure 4                        |

|               |                                                                              |                                 |             |
|---------------|------------------------------------------------------------------------------|---------------------------------|-------------|
| $\mu$         | dynamic viscosity                                                            | $[\mu] = \frac{M}{L^2 T}$       | (5)         |
| $\Omega$      | domain of the porous medium                                                  | $[\Omega] = L^2$                | Figure 3    |
| $\Omega^e$    | an element domain                                                            |                                 | before (32) |
| $\phi_i$      | linear basis function                                                        |                                 | (29)        |
| $\Phi$        | vector of the linear basis function                                          |                                 | (29)        |
| $\psi_m$      | quadratic basis function                                                     |                                 | (28)        |
| $\Psi$        | vector of the quadratic basis function                                       |                                 | (28)        |
| $\rho$        | density of fluid                                                             | $[\rho] = \frac{M}{L^3}$        | (1)         |
| $\rho^\alpha$ | macroscale density of phase $\alpha$                                         | $[\rho^\alpha] = \frac{M}{L^3}$ | (4)         |
| $\theta$      | angle between cilia and horizontal plane                                     | $[\theta] = \text{radian}$      | Figure 2    |
| $Y^l$         | vector of $\varepsilon_m^l$ , $m = 1, 2, \dots, M$                           |                                 | (46)        |
| $e^\alpha$    | volume fraction of phase $\alpha$                                            | $[e^\alpha] = 1$                | (4)         |
| $e^l$         | porosity                                                                     | $[e^l] = 1$                     | (5)         |
| $\dot{e}^l$   | the material time derivative of the porosity with respect to the solid phase |                                 | below (9)   |
| $\zeta$       | the dimensionless length along cilia                                         | $[\zeta] = 1$                   | Figure 3    |
| $\zeta_{max}$ | the dimensionless length of the cilia                                        | $[\zeta_{max}] = 1$             | Figure 3    |

## References

- Lyons, R.A.; Saridogan, E.; Djahanbakhch, O. The reproductive significance of human Fallopian tube cilia. *Hum. Reprod. Update* **2006**, *12*, 363–372. [\[CrossRef\]](#) [\[PubMed\]](#)
- Pechenik, J.A. *Biology of the Invertebrates*, 4th ed.; Tufts University: Medford, MA, USA; McGraw-Hill: New York, NY, USA, 1976; p. 305.
- Bustamante-Marin, X.M.; Ostrowski, L.E. Cilia and mucociliary clearance. *Cold Spring Harb. Perspect. Biol.* **2017**, *9*, a028241. [\[CrossRef\]](#) [\[PubMed\]](#)
- Walsh, D.; Bevan, J.; Harrison, F. How Does Airway Surface Liquid Composition Vary in Different Pulmonary Diseases, and How Can We Use This Knowledge to Model Microbial Infections? *Microorganisms* **2024**, *12*, 732. [\[CrossRef\]](#) [\[PubMed\]](#)
- Zhu, P.; Chen, D.; Xu, Y. Simulation study on the mass transport in PCL based on the ciliated dynamic system of the respiratory tract. *J. Phys. Conf. Ser.* **2019**, *1300*, 012068. [\[CrossRef\]](#)
- Poopra, S.; Wuttanachamsri, K. On the asymptotic boundary condition at the free-fluid/porous-medium interface in periciliary layer due to the ciliary movement. *Math. Probl. Eng.* **2022**, *2022*, 1390486. [\[CrossRef\]](#)
- Vanaki, S.M.; Holmes, D.; Jayathilake, P.G.; Brown, R. Three-dimensional numerical analysis of periciliary liquid layer: Ciliary abnormalities in respiratory diseases. *Appl. Sci.* **2019**, *9*, 4033. [\[CrossRef\]](#)
- Jayathilake, P.G.; Tan, Z.; Le, D.V.; Lee, H.P.; Khoo, B.C. Three-dimensional numerical simulations of human pulmonary cilia in the periciliary liquid layer by the immersed boundary method. *Comput. Fluids* **2012**, *67*, 130–137. [\[CrossRef\]](#)
- Sedaghat, M.H.; Sadrizadeh, S.; Abouali, O. Three-dimensional simulation of mucociliary clearance under the ciliary abnormalities. *J. Nonnewton. Fluid Mech.* **2023**, *316*, 105029. [\[CrossRef\]](#)
- Milosevic, M.; Stojanovic, D.B.; Simic, V.; Grkovic, M.; Bjelovic, M.; Uskokovic, P.S.; Kojic, M. Preparation and modeling of three-layered PCL/PLGA/PCL fibrous scaffolds for prolonged drug release. *Sci. Rep.* **2020**, *10*, 11126. [\[CrossRef\]](#)
- Oangwacharaparkan, N.; Wuttanachamsri, K. The flow in periciliary layer in human lungs with Navier-Stokes-Brinkman equations. *Tamkang J. Math.* **2023**, *54*, 107–120.
- Poopra, S.; Wuttanachamsri, K. The velocity of PCL fluid in human lungs with beaver and Joseph boundary condition by using asymptotic expansion method. *Mathematics* **2019**, *7*, 567. [\[CrossRef\]](#)
- Phaenchat, S. On the One-Dimensional Nonlinear Stokes-Brinkman Equations for Modeling Flow in PCL. Master's Thesis, King Mongkut's Institute of Technology, Ladkrabang, Thailand, 2019.
- Phaenchat, S.; Wuttanachamsri, K. Two-dimensional nonlinear Brinkman and steady-state Navier-Stokes equations for fluid flow in PCL. *Partial Differ. Equ. Appl. Math.* **2024**, *12*, 100961. [\[CrossRef\]](#)
- Conti, M.; Giorgini, A. Well-posedness for the Brinkman-Cahn-Hilliard system with unmatched viscosities. *J. Differ. Equ.* **2020**, *268*, 6350–6384. [\[CrossRef\]](#)
- Titi, E.S.; Trabelsi, S. Global well-posedness of a three-dimensional Brinkman-Forchheimer-Bénard convection model in porous media. *arXiv* **2022**, arXiv:2204.03531.
- Coclite, G.M.; Mishra, S.; Risebro, N.H.; Weber, F. Analysis and numerical approximation of Brinkman regularization of two-phase flows in porous media. *Comput. Geosci.* **2014**, *18*, 637–659. [\[CrossRef\]](#)
- Hansbo, P.; Juntunen, M. Weakly imposed Dirichlet boundary conditions for the Brinkman model of porous media flow. *Appl. Numer. Math.* **2009**, *59*, 1274–1289. [\[CrossRef\]](#)

19. Jia, J.; Lee, Y.J.; Feng, Y.; Wang, Z.; Zhao, Z. Hybridized weak Galerkin finite element methods for Brinkman equations. *Electron. Res. Arch.* **2021**, *29*, 2489–2516. [[CrossRef](#)]
20. Ouadefli, L.E.; Akkad, A.E.; Moutea, O.E.; Moustabchir, H.; Elkhalfi, A.; Scutaru, M.L.; Muntean, R. Numerical simulation for Brinkman system with varied permeability tensor. *Mathematics* **2022**, *10*, 3242. [[CrossRef](#)]
21. Chamsri, K. Formulation of a well-posed Stokes-Brinkman problem with a permeability tensor. *J. Math.* **2015**, *1*, 1–7.
22. Rinehart, A.; Lăciș, U.; Bagheri, S. The Brinkman viscosity for porous media exposed to a free flow. *arXiv* **2021**, arXiv:2106.01879.
23. Wuttanachamsri, K. Free interfaces at the tips of the cilia in the one-dimensional periciliary layer. *Mathematics* **2020**, *8*, 1961. [[CrossRef](#)]
24. Basirat, F.; Sharma, P.; Fagerlund, F.; Niemi, A. Experimental and modeling investigation of CO<sub>2</sub> flow and transport in a coupled domain of porous media and free flow. *Int. J. Greenh. Gas Control* **2015**, *42*, 461–470. [[CrossRef](#)]
25. Wuttanachamsri, K.; Schreyer, L. Effects of cilia movement on fluid velocity: II numerical solutions over a fixed domain. *Transp. Porous Media* **2020**, *134*, 471–489. [[CrossRef](#)]
26. Nishad, C.S.; Chandra, A.; Karmakar, T.; Raja Sekhar, G.P. A non-primitive boundary element technique for modeling flow through non-deformable porous medium using Brinkman equation. *Mechanica* **2018**, *53*, 2333–2352. [[CrossRef](#)]
27. Abo-Elkhair, R.E.; Mekheimer, K.S.; Moawad, A.M.A. Cilia walls influence on peristaltically induced motion of magneto-fluid through a porous medium at moderate Reynolds number: Numerical study. *J. Egypt. Math. Soc.* **2017**, *25*, 238–251. [[CrossRef](#)]
28. Cortez, R.; Cummins, B.; Leiderman, K.; Varela, D. Computation of three-dimensional Brinkman flows using regularized methods. *J. Comput. Phys.* **2010**, *229*, 7609–7624. [[CrossRef](#)]
29. Deo, S.; Ansari, I.A.; Srivastava, B.G. On the general stream function solution of Brinkman equation in the cylindrical polar coordinates. *Adv. Theo. Appl. Mech.* **2016**, *9*, 21–30. [[CrossRef](#)]
30. Kanafiah, S.F.H.M.; Kasim, A.R.M.; Zokri, S.M.; Shafie, S. Numerical solutions of convective transport on Brinkman-viscoelastic fluid over a bluff body saturated in porous region. *Case Stud. Therm. Eng.* **2021**, *28*, 101341. [[CrossRef](#)]
31. Pranowo, P.; Wijayanta, A.T. Numerical solution of Darcy-Brinkman-Forchheimer equation for forced-convective fluid flow through porous medium using DMLPG method. *AIP Conf. Proc.* **2020**, *2217*, 030171.
32. Sleigh, M.A. Ciliary adaptations for the propulsion of mucus. *Biorheology* **1990**, *27*, 527–532. [[CrossRef](#)]
33. Kumankat, N.; Wuttanachamsri, K. Well-posedness of generalized Stokes-Brinkman equations modeling moving solid phases. *Electron. Res. Arch.* **2023**, *31*, 1641–1661. [[CrossRef](#)]
34. Cushman, J.H.; Bennethum, L.S.; Hu, B.X. A primer on upscaling tools for porous media. *Adv. Water Resour.* **2002**, *25*, 1043–1067. [[CrossRef](#)]
35. Bennethum, L.S. *Multiscale, Hybrid Mixture Theory for Swelling Systems with Interfaces*; Lecture Note; University of Colorado: Denver, CO, USA, 2007.
36. Bennethum, L.S.; Cushman, J.H. Multiscale, hybrid mixture theory for swelling systems—I: Balance laws. *Int. J. Eng. Sci.* **1996**, *34*, 125–145. [[CrossRef](#)]
37. Wuttanachamsri, K.; Schreyer, L. Effects of cilia movement on fluid velocity: I model of fluid flow due to a moving solid in a porous media framework. *Transp. Porous Media.* **2021**, *136*, 699–714. [[CrossRef](#)]
38. Weinstein, T.; Bennethum, L.S. On the derivation of the transport equation for swelling porous materials with finite deformation. *Int. J. Eng. Sci.* **2006**, *44*, 1408–1422. [[CrossRef](#)]
39. Sears, P.R.; Thompson, K.; Knowles, M.R.; Davis, C.W. Human airway ciliary dynamics. *Am. J. Physiol. Lung Cell. Mol. Physiol.* **2012**, *304*, 170–183. [[CrossRef](#)] [[PubMed](#)]
40. Brenner, S.C.; Scott, L.R. *The Mathematical Theory of Finite Element Methods*; Springer: New York, NY, USA, 2008.
41. Chamsri, K.; Bennethum, L.S. Permeability of fluid flow through a periodic array of cylinders. *Appl. Math. Model.* **2015**, *39*, 244–254. [[CrossRef](#)]
42. ICRP. *Measurement: Human Respiratory Tract Model for Radiological Protection*; ICRP Publication 66. Ann. ICRP; ICRB: Ottawa, ON, Canada, 1994; Volume 24, pp. 1–3.
43. Schöberl, J. NETGEN An advancing front 2D/3D-mesh generator based on abstract rules. *Comput. Visual. Sci.* **1997**, *1*, 41–52.
44. Woodfield, J.; Alvarez, M.; Gómez-Vargas, B.; Ruiz-Baier, R. Stability and finite element approximation of phase change models for natural convection in porous media. *J. Comput. Appl. Math.* **2019**, *360*, 117–137. [[CrossRef](#)]
45. Matsui, H.; Randell, S.H.; Peretti, S.W.; Davis, C.W.; Boucher, R.C. Coordinated clearance of periciliary liquid and mucus from airway surfaces. *J. Clin. Investig.* **1998**, *102*, 1125–1131. [[CrossRef](#)]

**Disclaimer/Publisher's Note:** The statements, opinions and data contained in all publications are solely those of the individual author(s) and contributor(s) and not of MDPI and/or the editor(s). MDPI and/or the editor(s) disclaim responsibility for any injury to people or property resulting from any ideas, methods, instructions or products referred to in the content.

# Author Biography

|                       |                                                                                                                                                                                                                                                                                                                                                                                                                                                                                                                                                                                                                                                                                                   |
|-----------------------|---------------------------------------------------------------------------------------------------------------------------------------------------------------------------------------------------------------------------------------------------------------------------------------------------------------------------------------------------------------------------------------------------------------------------------------------------------------------------------------------------------------------------------------------------------------------------------------------------------------------------------------------------------------------------------------------------|
| Name                  | Miss Nisachon Kumankat                                                                                                                                                                                                                                                                                                                                                                                                                                                                                                                                                                                                                                                                            |
| Date of Birth         | 4 June 1995                                                                                                                                                                                                                                                                                                                                                                                                                                                                                                                                                                                                                                                                                       |
| Address               | 122 m.7 Maetha, Lamphun, 51170                                                                                                                                                                                                                                                                                                                                                                                                                                                                                                                                                                                                                                                                    |
| Education             | (2017) Bachelor of Science in Applied Mathematics, GPA 3.72<br>King Mongkut's Institute of Technology Ladkrabang<br>(2019) Master of Science in Applied Mathematics, GPA 3.94<br>King Mongkut's Institute of Technology Ladkrabang<br>(2024) Doctor of Philosophy in Applied Mathematics, GPA 4.00<br>King Mongkut's Institute of Technology Ladkrabang                                                                                                                                                                                                                                                                                                                                           |
| Scholarship           | The RA/TA graduate scholarship from the School of Science,<br>King Mongkut's Institute of Technology Ladkrabang,<br>grant number RA/TA-2563-D-003                                                                                                                                                                                                                                                                                                                                                                                                                                                                                                                                                 |
| Academic Publications | – Kumankat, N.; Pantaragphong, P.; Sabau, S.V. Finsler Metrics Induced by a Similarity Function. <i>Current Applied Science and Technology</i> , 2020, 2(2), 334-343.<br>– Kumankat, N.; Wuttanachamsri, K. Well-posedness of generalized Stokes-Brinkman equations modeling moving solid phases[J], <i>Electronic Research Archive</i> , 2023, 31(3): 1641-1661. doi:10.3934/era.2023085<br>2023, 31(3): 1641-1661. doi: 10.3934/era.2023085<br>– Kumankat, N.; Kamolmitisom, N. Two-Dimensional Fluid Flow Due to Blade-Shaped Waving of Cilia in Human Lungs. <i>Mathematics</i> , 2025, 13(11): 1703. <a href="https://doi.org/10.3390/math13111703">https://doi.org/10.3390/math13111703</a> |